Doctoral Thesis

Advancing Additive Manufacturing of Copper Alloys: Processing, Microstructure, and Property Optimisation

A thesis submitted in fulfilment of the requirements for the degree of Doctor of Philosophy, from the School of Aerospace, Mechanical and Mechatronic Engineering, Faculty of Engineering, The University of Sydney.

Kangwei Chen

2026

欲买桂花同载酒，终不似，少年游
但愿壮心尤未已，常无惧，少年游

I would buy osmanthus and share wine, yet it can never be the same as youthful wanderings.

I only hope my resolute heart remains unspent, ever unafraid, as in the journeys of youth.

Statement of Originality

This is to certify that to the best of my knowledge, the content of this thesis is my own work. This thesis has not been submitted for any other degree or purpose.

I certify that the intellectual content of this thesis is the product of my own work, and that all assistance received in preparing this thesis and all sources have been acknowledged.

Kangwei Chen

Authorship Attribution Statement

Chapter 6 of this thesis contains material from the published work:

Chen, K., Lim, B., Zhang, L., Koo, B. X., Ringer, S. P., & Nomoto, K. (2025). Formation mechanisms of Sn-rich δ phase and its role in strengthening Cu-10Sn manufactured by laser powder bed fusion. *Additive Manufacturing*, *102*, 104723.

Chapter 9 of this thesis contains material from work currently under peer review:

Chen, K., Cui, X. Y., Lim, B., Tran, T., Duguid, A., Camilleri, S., Ringer, S. P., & Nomoto, K. (2025). Age hardening response of Cu-30Ni alloys: The role of Si microalloying additions.

Supported by my supervisors, I participated in the design & conceptualisation of the study, implemented the methodology, performed the experimentation & data analysis, and wrote the paper, implementing corrections & suggestions from my co-authors and reviewers.

Kangwei Chen

As supervisors for the candidate upon which this thesis is based, we can confirm that the authorship attribution statements above are correct.

Simon P. Ringer

Keita Nomoto

Use of Generative AI statement

During the preparation of the thesis the author used ChatGPT for the purposes of text enhancement. The use of this generative AI tool includes paraphrasing, sentence structure and spelling. The author confirms that where text was modified by generative AI, the content was reviewed for possible errors, inaccuracies, and bias. The author takes full responsibility for the submitted thesis and ensures the work is their own and has used generative AI within the parameters of use.

Kangwei Chen

Abstract

Copper (Cu) and its alloys are indispensable to modern society due to their exceptional electrical and thermal conductivity, mechanical performance, and corrosion resistance. The transition towards Industry 4.0 and beyond, marked by digitalisation, electrification, and sustainability, has intensified demand for advanced Cu-based materials. Additive manufacturing (AM) offers the potential to realise these requirements through design flexibility, reduced material waste, and component customisation. However, its application to Cu alloys remains hindered by challenges intrinsic to Cu, such as high reflectivity and rapid heat dissipation. Unlike conventional processes such as casting or welding, AM imposes cyclic, spatially localised energy inputs that generate steep thermal and stress transients, producing microstructural phenomena not predicted by steady-state metallurgy. Consequently, the fundamental links between powder feedstock, processing conditions, microstructural evolution, post-processing and the resulting mechanical and functional properties are not yet well understood, limiting the widespread adoption of AM Cu alloys.

This thesis systematically investigates how AM process parameters, alloying strategies, and powder feedstock characteristics govern the microstructure and performance of three representative Cu alloys—Cu-10Sn, Cu-1Ti, and Cu30Ni. Through a combination of advanced microscopy, mechanical and electrical testing, computational fluid dynamics simulations, thermodynamic simulations, and density functional theory calculations, this thesis establishes quantitative links between processing conditions, microstructural features, and macroscopic properties. In Cu-10Sn, optimised printing parameters and scan strategies minimise porosity, the formation mechanism of a strengthening secondary phase is elucidated, and the critical role of powder characteristics in laser absorption and build quality is demonstrated. In Cu-1Ti, tailored moderate Ti and graphene additions enable a

balance of high strength and conductivity via controlled precipitation. In Cu-30Ni, the Si-driven precipitation response is mapped to guide heat-treatment optimisation. Collectively, the findings provide new insights into the solidification pathways, microstructural evolution, and strengthening mechanisms unique to AM Cu-based alloys and deliver practical guidelines for optimising alloy and process design. By bridging fundamental metallurgy with AM-specific processing, the thesis contributes to enabling Cu alloys as next-generation functional and structural materials for energy, transport, and digital technologies.

Acknowledgements

This thesis represents the culmination of three and a half years of effort during my doctoral journey. When I first set foot on the campus of the University of Sydney, I never imagined that I would one day pursue a path in academic research, yet here I am, still willing to devote myself to this endeavour and continue striving forward. Although many people describe the PhD process as gruelling, and some even abandon it midway, for me it has been a journey I have truly enjoyed from beginning to end: a journey of self-discovery, of steadily gaining confidence, and of personal growth. Along the way there have been moments of joy, frustration, and uncertainty, but ultimately this path has allowed me to see a different version of myself. It is with deep gratitude that I now extend my heartfelt thanks to all those who have supported and guided me, and who have helped me transform during this journey.

First and foremost, I would like to express my sincere gratitude to my supervisor, Prof. Simon P. Ringer. Everyone has their own image of what it means to be a gentleman, and from the moment I first met him, I felt he was the embodiment of that ideal. He has provided me with unparalleled opportunities, unconditional support, and steadfast guidance, while always championing my freedom as a researcher and my growth as a scientist. His comments, suggestions, and revisions on my papers, thesis, and discussions have benefited me immensely, and I still vividly remember my surprise when I first received his feedback, only then did I realise how differently and effectively a scientific paper could be written. I feel truly fortunate to have joined Ringer's group, which marked the beginning of my journey into scientific research. I would also like to thank Dr. Zibin Chen, without whom I would never have been introduced to the world of materials science research.

In addition, my heartfelt thanks go to Dr. Keita Nomoto, my supervisor, whose day-to-day guidance, advice, and many thoughtful and lively discussions have contributed greatly to the scientific achievements within this thesis. He is an exceptional mentor, intelligent, humble, patient, and always able to see things from another's perspective. Our conversations, whether on research or on life, often carried on effortlessly, as he quickly understood what I was trying to express and offered patient, meticulous guidance. I still remember those moments vividly: when he carefully revised my first presentation slides and explained why certain font sizes worked best; when he first showed me how to capture a dark-field image using a transmission microscope; when he explained how every sentence in a paragraph plays a distinct role in shaping a paper. He always asked me, "What do you think about doing it this way?" rather than instructing me, "You must do it this way." He would humbly say that he, too, was still learning, but through his actions, he set an example that taught me how to strive to become a better version of myself.

Beyond my supervisors, I am deeply grateful for the many discussions, advice, and support I have received from both current and former colleagues in Ringer's research group, including but not limited to: Dr. Hansheng Chen, Dr. Kay Song, Dr. Xiangyuan (Carl) Cui, Dr. Kevin Sisco, Dr. Suqin Zhu, Dr. Mengwei He, Mrs. Haoruo (Rosie) Zhou, Miss. Siyu Sun, Dr. Qi Wang, Dr. Bryan Lim, Dr William Davids, Dr. Andrew Breen, Dr. Hao wang, Dr. Zijian Yu, Dr. Majid Parvizi, Dr. Han Lin Mai, Dr. Apurv Yadav, Dr. Huma Bilal and Mr. James Dingle. It has been a true privilege and joy to work alongside you all. The times we spent talking, collaborating, sharing equipment, and enjoying drinks together have become some of my most treasured memories.

I am also truly thankful to my friends, including but not limited to Mr. Chao Huang, Mr. Fankai (Darren) Peng, Dr. Ranming Niu, Dr. Ying Liu, Dr. Jiangtao Qu, Dr. Feng Li, Dr.

Hanyu Li, Dr. Jinqiao Liu, Miss Heqing Li and Mr. Ruiqing Lu, whose companionship and encouragement have been an irreplaceable source of strength throughout my PhD journey. Whether it was sharing laughter over meals and coffees, offering comfort during challenging times, or simply being there to listen, your presence has made this experience far richer and more enjoyable. The moments we spent together, both in Sydney and beyond, are among my most cherished memories, and I feel deeply fortunate to have had your support along the way.

I would also like to express my gratitude for the scientific and technical support provided by the staff of Sydney Microscopy & Microanalysis (SMM) and the Sydney Manufacturing Hub (SMH) at the University of Sydney. A special thank you must be given to Dr. Hongwei Liu, Dr. Hongjian (Andy) Wang, Dr. Takanori Sato, Mr. Jacob Byrnes, Dr. Vijay Bhatia, Dr. Ashalatha I.K, Dr. Magnus Grrbrecht, Dr. Mattew Foley, Ms. Ellie Kable, Dr. Mehdi Eizadjou, Dr. Katja Eder, Dr. Wen Hao Kan and Mr. Patrick McCarthy. Your expertise, patience, and generous assistance have been invaluable, and without your support I would not have been able to carry out the extensive experimental work that underpins this thesis. I would also like to sincerely thank Prof. Xianghai An and Prof. Xiaozhou Liao for their generous guidance and support during my thesis examination process. I would also like to thank Prof. Anna Paradowska for her valuable guidance throughout our collaborations. I am grateful as well to Prof. Sophie Primig, Dr. Nana Kwabena Adomako, Dr Bosong Li, and Prof. Jay J. Kruzic from UNSW for their collaboration, and to ANSTO and AINSE for their generous scholarship support. I am grateful as well to my collaborators including Dr. Duyao Zhang (University of Bath), Dr. Ryan Brooke (RMIT University), and Prof. Mark Easton (RMIT University), for their valuable collaboration and discussions. My sincere thanks also go to Prof. Satoko Kuwano-Nakatani from Tohoku Gakuin University, whose collaboration and assistance

have been deeply appreciated. In addition, this research was supported by the Australian Government through the Australian Research Council Discovery Early Career Researcher Award (DE220100527).

I would also like to take a moment to thank myself. One of my favourite sayings is that in scientific research, we are constantly exploring and pushing the boundaries of human knowledge. It is only when we give our all and just barely touch that edge that we realise how small the world we know truly is, and why lifelong learning is so essential. I feel fortunate to have had the ability to learn while exploring this frontier. At the same time, I am grateful to the world itself, for there remain so many fascinating, undiscovered things that continue to inspire hope and anticipation.

Finally, I wish to thank my family for their unconditional love and support. Most importantly, I want to thank Muxuan Du. If you turn to the acknowledgements of my master's thesis, you will find her there as my girlfriend; today, she is my wife. We first met in middle school, when we were best friends, and over the course of sixteen years we grew from friends into partners for life, becoming each other's strongest support. She has always offered me selfless help in my most difficult times, and shared in my joy when I was happiest. Throughout my PhD, she has been at once a teacher, a friend, and the one who spent countless days and nights waiting for me, accompanying me through experiments, and staying up until dawn to revise my papers with me. As the final line of Dumas's The Count of Monte Cristo says: "All human wisdom is contained in these two words—wait and hope." She has waited with me for so long, and she is, and always will be, my hope.

Contents

Chapter 1 Introduction

Copper (Cu) and its alloys have played a pivotal role in human civilisation [1], primarily due to their exceptional thermal and electrical conductivity, together with their excellent mechanical properties and corrosion resistance [2, 3]. During the first industrial revolution, Cu was essential for steam-powered innovations, finding applications in boilers, engines, and other mechanical components. Its importance surged in the second industrial era with the advent of historical electrification, where Cu became indispensable for power generation, transmission, electrical wiring, and early telecommunications infrastructure. The digital revolution of Industry 3.0 further broadened its use in printed circuit boards, electrical connectors, and microelectronic devices. As we entered Industry 4.0, defined by automation, robotics, and cyber-physical systems, the demand for Cu and its alloys intensified due to their high electrical and thermal conductivity, mechanical robustness, and multifunctionality. Looking ahead to Industry 5.0, which prioritises sustainability, digital innovation, and electrification, the unmatched combination of high electrical and thermal conductivities, mechanical properties and recyclability positions Cu and its alloys to remain central to emerging technologies [4]. This enduring and expanding role is reflected in the projected growth of the global market of Cu and its alloys. As illustrated in Figure 1.1 [5], the market size is expected to rise steadily from USD 90 billion in 2018 to over USD 577 billion by 2032. This growth is not only driven by traditional infrastructure and electronics sectors but also by accelerating advancements in alloy design, technologies that extend Cu's functionality into high-performance, multi-functional applications across transportation, energy, and advanced manufacturing sectors.

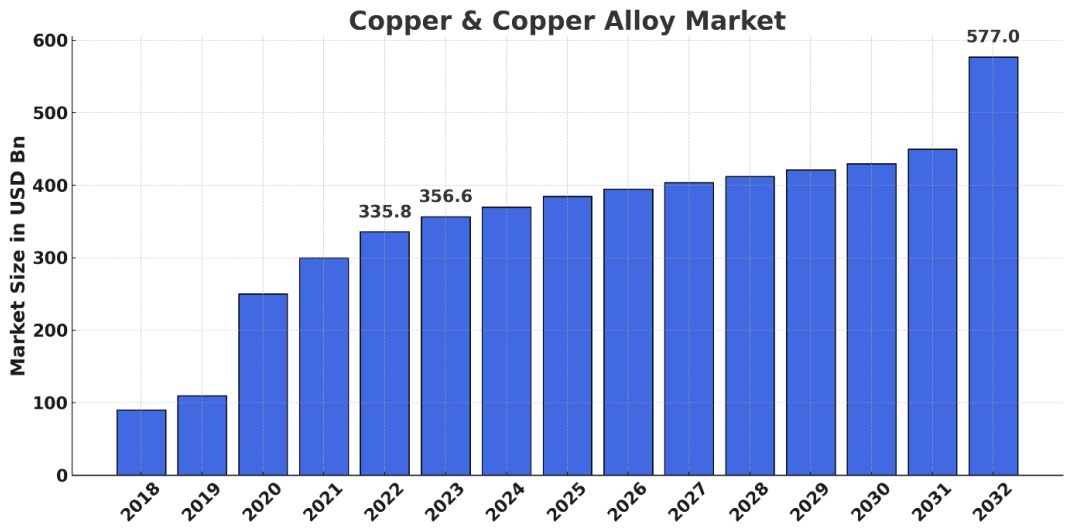

Figure 1.1: Global copper and copper alloy market Overview. The global copper and copper alloy market was valued at USD 356.61 billion in 2023. It is projected to grow from USD 378.73 billion in 2024 to approximately USD 577.03 billion by 2032. Reproduced from [5].

Underlying this projected market growth are the intrinsic properties of Cu, including exceptional electrical and thermal conductivity [3], making it indispensable to the global transition toward electrification as industries respond to growing environmental regulations and the expansion of renewable energy and electric transport systems. Electric vehicles (EVs), for instance, typically use approximately 60–80 kg of Cu per vehicle, significantly more than internal combustion counterparts, due to Cu's critical role in motors, wiring harnesses, battery interconnects, and high-speed charging infrastructure [6]. In response to increasing current densities and efficiency requirements in modern electrical systems, Cu alloys such as Cu-Cr-Zr, Cu-Ni-Si, and Cu-Ti have been developed to deliver superior mechanical strength, high electrical conductivity, and thermal stability, particularly in terms of resistance to grain growth and phase coarsening at elevated temperatures [7-13]. These materials are essential not only in the automotive sector but also across power generation and distribution systems, including wind turbines, solar photovoltaic arrays, and energy storage installations.

Beyond electrical applications, Cu and its alloys excel in thermal management. Their high thermal conductivity and favourable manufacturability make them ideal for use in heat exchangers, cooling systems, and electronic packaging. As digital technologies such as artificial intelligence (AI), cloud computing, and high-performance data centres grow increasingly power-intensive, the need for advanced thermal management becomes ever more critical. Cu-based materials now form the backbone of next-generation cooling solutions, including heat sinks, heat exchangers, and liquid cooling assemblies that effectively dissipate heat from CPUs, GPUs, and other components [14]. Alloys like Cu-Cr and Cu-Cr-Nb combine high thermal conductivity with mechanical strength [15, 16], enabling the fabrication of compact and complex cooling systems tailored for dense electronic environments. Particularly in data centres, Cu heat pipes and vapour chambers are employed to maintain thermal stability, ensuring high computing performance and device longevity.

In addition to its electrical and thermal properties, Cu's mechanical performance can be finely tuned through alloying and thermomechanical processing. Alloys such as bronze (Cu-Sn) and brass (Cu-Zn) offer an excellent balance of strength, ductility, wear resistance, and machinability [17-19], underpinning their widespread use in mechanical components, including bearings, gears, and valves, particularly where long service life is required under mechanical or corrosive loading. Specialised alloys such as Cu-Ag and Cu-Ni extend this functionality by providing enhanced resistance to corrosion and oxidation—qualities particularly vital for harsh environments involving exposure to seawater and corrosive chemicals [20, 21]. These attributes make Cu alloys ideal for marine and offshore engineering, where resistance to seawater-induced degradation significantly reduces maintenance costs while enhancing structural reliability and operational safety.

Traditional manufacturing methods, such as casting, forging, and machining, often struggle to deliver the complex geometries and custom designs required by modern applications, which demand compact, lightweight and highly efficient components. To address these challenges, additive manufacturing (AM) builds parts layer-by-layer via computer-aided design, enabling unparalleled design flexibility, reduced material waste, rapid prototyping, and part consolidation with fewer joints, capabilities often impractical or impossible with traditional methods [22, 23]. Additionally, unlike conventional casting, which typically involves slow cooling rates (10^1–10^2 K/s [24]) and near-equilibrium solidification, AM processes operate under extremely high cooling rates (10^3–10^6 K/s [25]) and steep thermal gradients. These non-equilibrium conditions promote rapid solidification, fine microstructural features, and unique phase selection pathways that are rarely achievable through traditional methods. Example metal AM techniques that have shown the successful balance of processability, density and property optimisation for Cu alloys include laser beam powder bed fusion (LB-PBF) and laser beam directed energy deposition (LB-DED). LB-PBF selectively melts thin powder layers with a focused scanning laser, enabling high-resolution, geometrically complex parts; however, the high reflectivity and thermal conductivity of Cu limit laser absorption, making it challenging to achieve full density [26, 27]. LB-DED feeds powder or wire feedstock into a laser-formed melt pool using a relatively large laser beam, enabling high deposition rates for large or functionally graded parts. It is also well-suited for repairs and multi-material applications [28]. In contrast to these melt-based approaches, cold spray additive manufacturing (CSAM) offers a fundamentally different pathway. Cold spray is a solid-state process in which a heated, pressurised gas accelerates feedstock powders to supersonic speeds. Upon powder particle impact, they plastically deform and bond without melting, making the process well-suited to Cu for dense coatings, repairs and structural build-ups [29].

Figure 1.2 illustrates the year-wise number of publications containing the keywords "Cu alloys" and "Cu alloys additive manufacturing", sourced from Scopus. Although Cu's industrial use and scientific applications have been well-documented since the late 20th century, its application to AM has only gained significant traction over the past decade (blue bars in Figure 1.2b), particularly with advances in laser technologies and powder development. However, AM-specific process conditions, including the rapid solidification, high thermal gradients, and layer-wise thermal cycling, which govern microstructure, and thus mechanical, electrical, and thermal properties, remain insufficiently understood and controlled. Consequently, knowledge derived from conventional metallurgy must be re-evaluated under AM-specific processing dynamics. Insights from welding disciplines are particularly valuable for understanding heat flow, solidification, and microstructure evolution. For metal AM broadly, industrial uptake is hindered by unresolved challenges, including the optimisation of pre-, in- and post-processing parameters, the development of powders with controlled characteristics and the design of alloys specifically tailored for AM. These issues apply across a wide range of alloys; however, they are particularly pronounced in Cu alloys. Equally important is the ability to deliberate microstructure control to achieve balanced combinations of strength, ductility and properties such as electrical and thermal conductivity, which requires a deep understanding of the interplay between processing conditions, alloy composition and microstructure-property relationships. These aspects form the central research focus of this thesis.

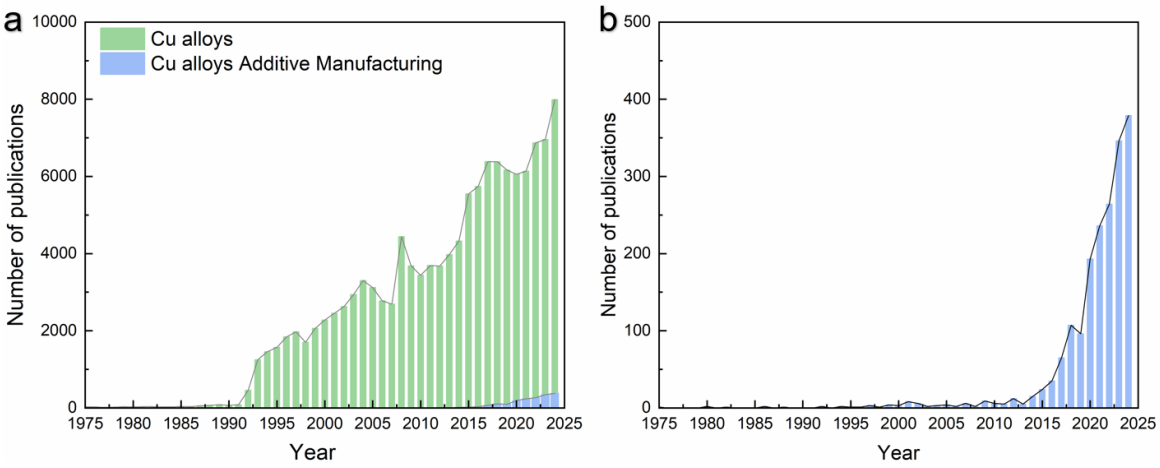

Figure 1.2: (a) Year-wise publication count for works containing key words: Cu alloys and Additive Manufacturing; and (b) a magnified view of blue bars in (a). Recorded using Scopus.

In this context, the thesis examines how AM process parameters and powder feedstock attributes control the microstructure of selected Cu alloys fabricated by LB-PBF and LB-DED, and explores routes to balance mechanical properties with electrical and thermal conductivity. While the emphasis is on AM processing-microstructure-property relationships, a significant component of the work employs ingot metallurgy to develop post-processing heat treatment strategies for microstructure reconfiguration, thereby bridging AM techniques with established metallurgical heat treatment approaches. By coupling multiscale characterisation, spanning from the macro to the atomic scale, with mechanical and electrical testing, this study establishes quantitative material-process-microstructure-property relationships and practical guidance for alloy and process design. The property emphasis is aligned with the dominant functional requirements of each system investigated. In Cu–Sn bronzes, mechanical robustness and wear resistance are prioritised due to their widespread use in load-bearing and tribological components. For precipitation-strengthened Cu–Ti alloys, optimisation of the strength–conductivity balance is a central objective. For Cu–Ni alloys, both mechanical performance and corrosion resistance,

together with ageing stability, are key considerations for reliable operation in aggressive service environments. This application-oriented framework provides the basis for the organisation of the subsequent chapters and guides the systematic exploration of processing–microstructure–property relationships across the different Cu alloy systems examined. The following chapters review selected AM techniques and Cu alloys (Cu-10Sn, Cu-30Ni and Cu-1Ti), articulate the rationale for their selections, and lead to the specific research questions and aims addressed in this study.

Chapter 2 Literature Review

This chapter reviews the literature important to this thesis and introduces key concepts in Cu alloys and metal AM. It further discusses the opportunities and challenges for AM Cu alloys, with a focus on three alloy systems: Cu-10Sn, Cu-30Ni and Cu-1Ti.

2.1 Significance of Cu and Cu alloys

Cu and its alloys have played a pivotal role in technological progress for thousands of years, from the early use of bronze in antiquity to high-performance applications in contemporary engineering [3, 30]. This long-standing relevance stems from a unique suite of properties, such as its relatively low melting point, ease of casting and forging, and the enhanced hardness of its alloys (e.g. bronze). With the advent of electrification in the late nineteenth century, the exceptional electrical and thermal conductivity of Cu came to the forefront [8, 31], further cementing its importance. The corrosion resistance of Cu further enhances its industrial utility in saline and industrial environments. Moreover, Cu is fully recyclable without loss of performance, aligning well with increasing global emphasis on sustainability and circular economy strategies. As modern industry transitions towards electrification, automation, and digital integration (Industry 4.0 and beyond), Cu and its alloys continue to serve as critical materials due to their multi-functionality, reliability, and eco-efficiency, as outlined by the International Energy Agency [32].

Among commercially available metals, Cu possesses the second-highest electrical conductivity, surpassed only by silver, as shown in Table 2.1 [33]. To standardise comparisons, the International Annealed Copper Standard (IACS) was established in 1913 [34], assigning annealed Cu a nominal conductivity of 100% IACS. On this scale, Ag

exhibits a conductivity of ~104% IACS, Al ~64% IACS, and Au ~76% IACS. This characteristic underpins its extensive use in electrical wiring, power transmission components, printed circuit boards, and connectors in various industries such as electronics, energy, transport, and marine engineering [8, 31]. Its high thermal conductivity (401 $W \cdot m^{-1} \cdot K^{-1}$) also enables efficient heat dissipation [35, 36], which is vital for heat exchangers, electronic devices, and thermal management in aerospace and automotive systems.

Table 2.1: Electrical conductivity of materials extracted from [33]. %IACS values were converted from electrical conductivity, where a nominal conductivity of 100% IACS is assigned to Cu, corresponds to the electrical conductivity of Cu. Thermal conductivity was extracted from [37].

Material	Electrical Conductivity (Sm^{-1})	IACS (%)	Thermal conductivity ($W \cdot m^{-1} \cdot K^{-1}$)
Silver	66.7×10^6	104.1	429
Copper	64.1×10^6	100.0	401
Gold	49.0×10^6	76.4	314
Aluminium	40.8×10^6	63.7	236
Rhodium	23.3×10^6	36.3	150
Zinc	18.2×10^6	28.4	116
Nickel	16.4×10^6	25.6	91
Iron	11.2×10^6	17.5	80
Platinum	10.2×10^6	15.9	72
Tin	8.7×10^6	13.6	67
Lead	5.3×10^6	8.3	35
Titanium	2.3×10^6	3.6	22
Mercury	1.0×10^6	1.6	8

The addition of alloying elements such as Sn, Ni, Si, and Ti allows tailoring of mechanical strength, wear resistance, and corrosion behaviour, thereby expanding the functional scope of Cu alloys. For instance, Sn increases hardness and wear resistance in bronzes [38], Ni contributes to the excellent corrosion resistance of cupronickel (Cu-Ni) alloys used in marine applications [39], and Si and Ti invoke an age hardening response, improving mechanical strength through the formation of precipitates [40, 41].

Recent research has aimed to enhance the mechanical strength and ductility of Cu without compromising its electrical and thermal performance—a challenging balance. Advances in alloy design, including grain refinement, precipitation hardening, and solid solution strengthening, have led to the development of novel Cu-based materials that meet the demands of next-generation technologies. These developments are especially significant in the context of AM, which, while offering considerable design freedom, introduces distinct challenges when applied to Cu and its alloys.

Accordingly, a comprehensive understanding of the behaviour, processing routes, and performance potential of Cu-based systems is crucial for advancing both conventional and advanced manufacturing technologies. The following sections examine the application of AM to Cu alloys, with a particular focus on Cu-10Sn, Cu-30Ni and Cu-1Ti alloy systems.

2.2 Additive manufacturing of Cu and Cu alloys

AM has become a transformative approach in materials processing, enabling the production of complex and high-performance components directly from digital models. For metallic systems, AM offers distinct advantages over traditional manufacturing, including the capability to fabricate near-net-shape parts, reduce material waste, and enable component customisation [42, 43]. In the context of Cu and its alloys, the same properties that make Cu attractive also pose unique challenges for AM, particularly with laser-based processes where Cu's high reflectivity and thermal conductivity result in unstable melt pools, poor bonding, and frequent defects [44, 45]. This section overviews three AM techniques, LB-PBF, LB-DED and CSAM, and explores the key challenges and recent advances associated with their application to Cu alloys.

2.2.1 Laser beam powder bed fusion

LB-PBF, also known historically as selective laser melting (SLM), is a subset of powder bed fusion AM where a high-power laser selectively melts regions of a fine metal powder bed according to the geometry defined by a digital CAD model [23], as shown in Figure 2.1. The process is carried out within an enclosed build chamber that is typically purged with inert gas, such as argon or nitrogen, to minimise oxidation and contamination [46]. A thin layer of powder (typically 20–100 μm) is spread uniformly across a metal build plate, which may be preheated depending on the process conditions, after which a focused fibre laser scans the surface according to a predetermined scan strategy, locally melting and fusing particles to form a dense layer. After each layer is completed, the build platform is lowered incrementally, and a fresh powder layer is spread by a recoater blade, continuing the layer-wise build process until the part is completed. LB-PBF offers high-resolution fabrication with minimal material waste and is compatible with a wide range of metals, including steel, Al, Ti, and Ni alloys [47-50], though the build volumes is relatively small (e.g. 100 × 100× 100 mm^3 in a Colibrium Additive MLab 200R LB-PBF machine).

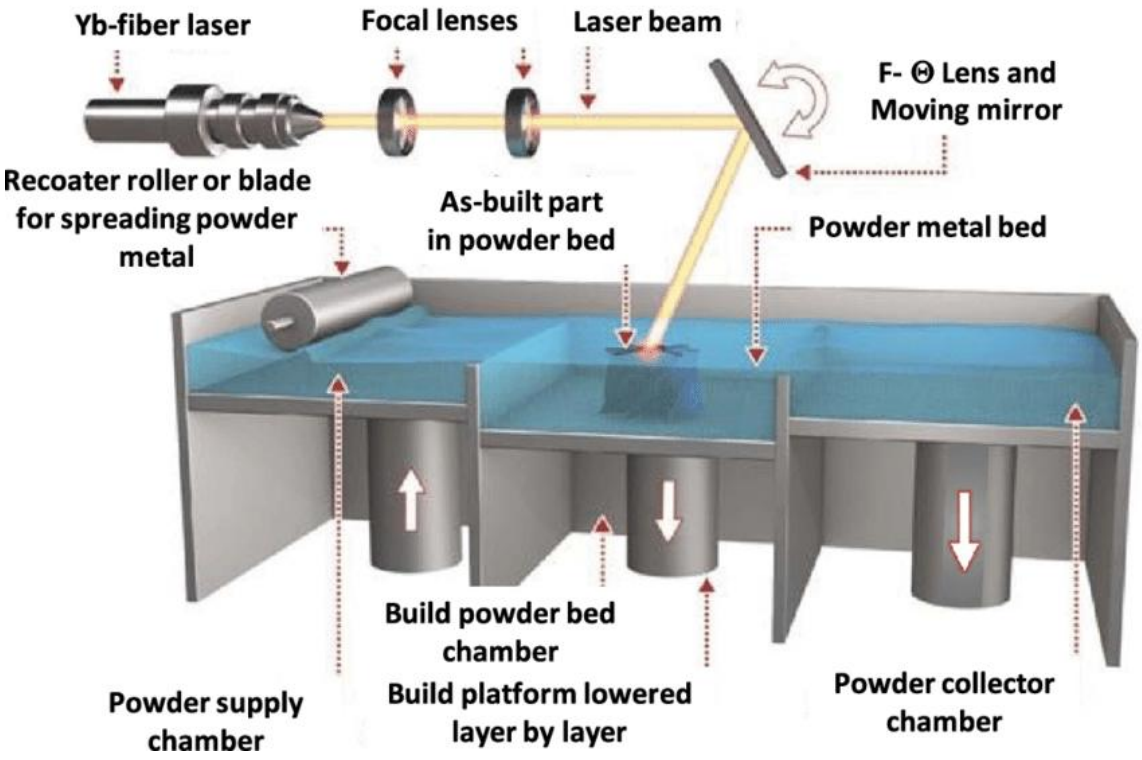

Figure 2.1: A schematic of a typical LB-PBF process. Adapted from [51].

However, fabricating pure Cu using LB-PBF is challenging primarily due to the high reflectivity and thermal conductivity of Cu, causing most of the laser energy to be reflected or rapidly diffused [52, 53]. Cu's high reflectivity at conventional laser wavelengths (especially near-infrared (NIR) at 1064 nm) leads to poor absorption of laser energy, often as low as 2% for pure Cu, as shown in Figure 2.2. As a result, insufficient energy coupling leads to incomplete melting, a lack of fusion between layers, and increased porosity [54]. Simultaneously, Cu's high thermal conductivity (~401 W/m·K) rapidly dissipates the energy delivered by laser or electron beams during AM, complicating the maintenance of a stable and sufficiently deep melt pool.

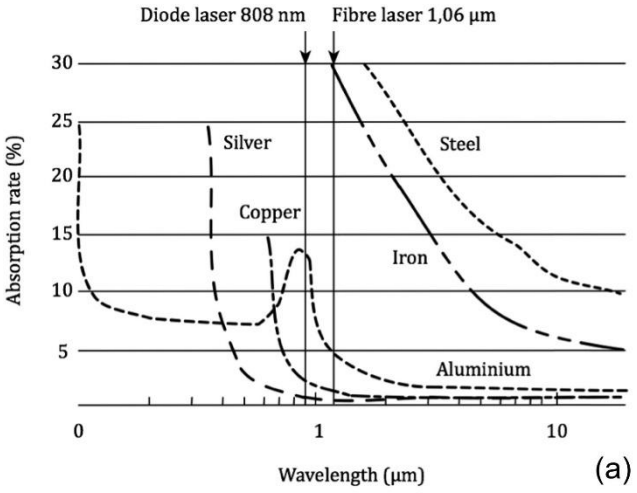

Figure 2.2: The absorption rate of common metals, adapted from [55].

In response, several strategies have been proposed to mitigate these processing issues. One widely explored approach is the use of alternative laser wavelengths. Green and blue lasers, with shorter wavelengths in the visible range, have been shown to substantially increase the absorptivity of Cu powders, thereby enhancing melt pool stability and part densification. For instance, the adoption of green lasers has enabled the fabrication of high-density Cu parts with relative densities exceeding 99% [56-58]. However, these laser sources are expensive, less mature, and not yet widely available in commercial AM systems, which limits their industrial scalability. Blue laser sources (~450 nm) have also been explored for Cu processing due to their even higher absorptivity compared with near-infrared lasers. The improved energy coupling can enhance melt pool stability and reduce the energy input required for Cu processing. However, high-power blue diode laser systems remain relatively expensive, and achieving very small and precisely controlled laser spot sizes can be more challenging compared with fibre-laser systems, which may influence process resolution and melt pool control.

An alternative approach involves alloying Cu with elements such as Cr, Zr, Co, Ni and Si. These alloying additions improve the laser absorption and also contribute to solid solution

and precipitation strengthening [59]. However, such alloying reduces electrical conductivity, as many solute elements exhibit significant solid solubility in Cu and act as electron scattering centres [59, 60]. To circumvent this conductivity-strength trade-off, recent studies have investigated the incorporation of non-soluble or immiscible nanoparticles into the α(Cu) matrix. For example, the addition of Fe particles [61], Co submicron particles[62], lanthanum hexaboride (LaB_6) [63] and copper oxide (Cu_2O) nanoparticles [64] has been demonstrated to enhance laser absorption, increase viscosity of the melt, and promote dynamic wetting behaviour, enabling the formation of fully dense, high-strength Cu with minimal loss of conductivity [60, 64].

The oxide dispersion strengthening (ODS) approach, in particular, offers a promising route for simultaneously enhancing both processability and mechanical performance. In a recent study [64], oxygen-assisted gas atomisation was used to embed nanoscale Cu_2O dispersoids into the powder feedstock. These particles not only facilitated energy absorption during laser melting but also contributed to grain refinement and solidification control. The resulting parts exhibited a yield strength (YS) of ~450 MPa, an ultimate tensile strength (UTS) of 524 MPa and a uniform elongation of ~11.5%, while retaining a high electrical conductivity (80%IACS), demonstrating the feasibility of this method for structural-functional integration. However, the approach presently relies on the oxygen-assisted gas atomised powder feedstock and a custom LB-PBF system rather than commercially available powders and off-the-shelf machines, which may constrain immediate reproducibility and broader adoption.

Other process-oriented strategies have also been explored. These include optimising laser parameters (e.g., power, scan speed, hatch spacing, and layer thickness) to establish a stable keyhole mode of melting without inducing porosity [65]. While high laser powers ($\geqslant$ 500 W) and small spot sizes have shown success in achieving near-full densification, the

narrow process window and risk of optical mirror damage due to laser back-reflections limit their robustness for broader industrial use [66]. Another study [26] shows that fully dense pure Cu can be fabricated on NIR by using high-precision settings, including a small laser spot (~25 μm), fine powder size (5–25 μm), and thin powder layers (10 μm), achieving 99.6% relative density and 76% IACS; however, the route often require customised optics and powders, run in narrow windows, and rely on thin layers that lower build rate. Furthermore, process enhancements such as hot isostatic pressing (HIP) post-treatment have been employed to eliminate residual porosity and improve ductility [66], though they introduce additional processing steps and costs. While the AM of Cu using laser-based methods remains technically challenging, substantial progress has been made through a variety of material and process innovations. Each approach, whether through laser wavelength modification, compositional tuning via alloying, oxide dispersion engineering, or parameter optimisation, offers distinct advantages and trade-offs. The field continues to evolve towards achieving a balance between high density, mechanical integrity, and retained electrical and thermal functionality, which is essential for realising the full potential of Cu components in demanding applications.

The use of LB-PBF for manufacturing Cu alloys offers unique advantages. The rapid cooling intrinsic to LB-PBF is central to producing non-equilibrium microstructures that can markedly enhance the mechanical response of Cu alloys relative to conventionally processed parts [67, 68]. This behaviour arises because LB-PBF accesses a far broader spatio-temporal thermal and stress parameter space via small melt pools, high power densities and fast scan speeds than conventional metallurgy can achieve [69-71]. The key parameters are the cooling rate ($\dot{T}$), the temperature gradient (G) and the solidification rate (R) with the relationship of $R = \dot{T}/G$ [72]. By controlling factors specific to the LB-PBF

process, including laser power, scan speed, and hatch spacing, G and R can be locally controlled, creating strong spatial and temporal heterogeneity in $\dot{T}$ [73].

The solidification mode is governed principally by the ratio G/R. R increases with scan speed, whereas G is controlled by the imposed heating and cooling conditions. The solidification morphology follows the widely used G-R map as shown in Figure 2.3 [74, 75]: the ratio G/R selects the morphology (planar → cellular → columnar dendritic → equiaxed dendritic as G/R decreases), while the product $G \cdot R$ (cooling rate $\dot{T}$) controls the size of the solidification structure. Higher cooling rates (shorter solidification times) therefore yield finer cells or dendrites. Therefore, precise control of processing parameters is necessary to attain the required microstructure features.

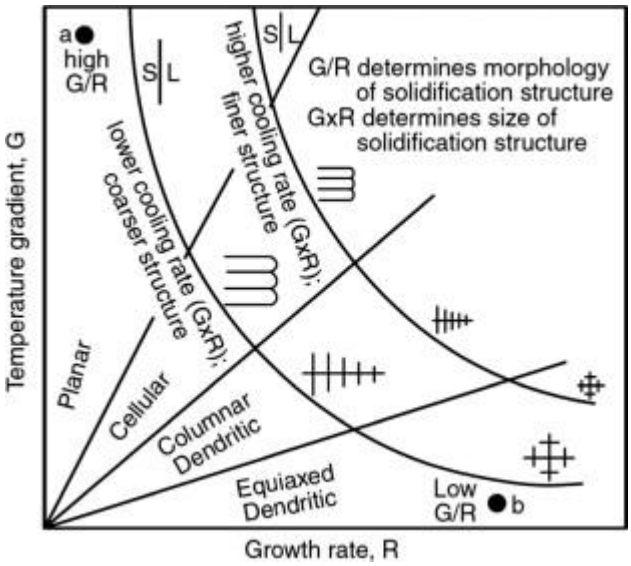

Figure 2.3: Effect of G and R on the morphology and size of microstructure upon solidification, adapted from [75].

2.2.2 Laser beam directed energy deposition

Directed energy deposition (DED) is an AM process in which focused thermal energy is used to melt and fuse material, such as metal powder or wire, simultaneously as it is being

deposited onto a substrate [89, 91]. Unlike LB-PBF, DED does not require a confined powder bed but instead utilises a coaxial or lateral feedstock delivery system with relatively high deposition rates, allowing for multi-directional deposition, part repair, and large-scale fabrication. DED systems can use various energy sources, including lasers, electron beams, and plasma arcs. LB-DED, often referred to as laser engineered net shaping (LENS) or laser metal deposition (LMD), is the most widely used variant due to its flexibility and compatibility with a broad range of alloys. In LB-DED (Figure 2.4), metal powder is delivered through nozzles, typically in a coaxial configuration, into the focal region of a high-power laser (typically 500 W to 3 kW [76]), which melts both the feedstock and a portion of the underlying substrate. The molten pool solidifies rapidly, and the process continues layer by layer to fabricate or repair a component according to the digital toolpath. The entire build is usually carried out in a sealed chamber filled with inert gas (e.g. argon or nitrogen) to minimise oxidation, which is particularly important for reactive metals such as Ti and Cu alloys. Compared to PBF, LB-DED achieves faster deposition rates and larger build volumes (e.g. > 1.2 m^3 for an Optomec LENS 850-R machine [77]) but typically offers lower resolution and poorer surface finish due to the broader melt pool and coarser metal powders (often 50–155 µm) [78, 79]. Nevertheless, LB-DED excels in gradient structures, multi-material builds, and the repair of high-value components such as turbine blades or moulds.

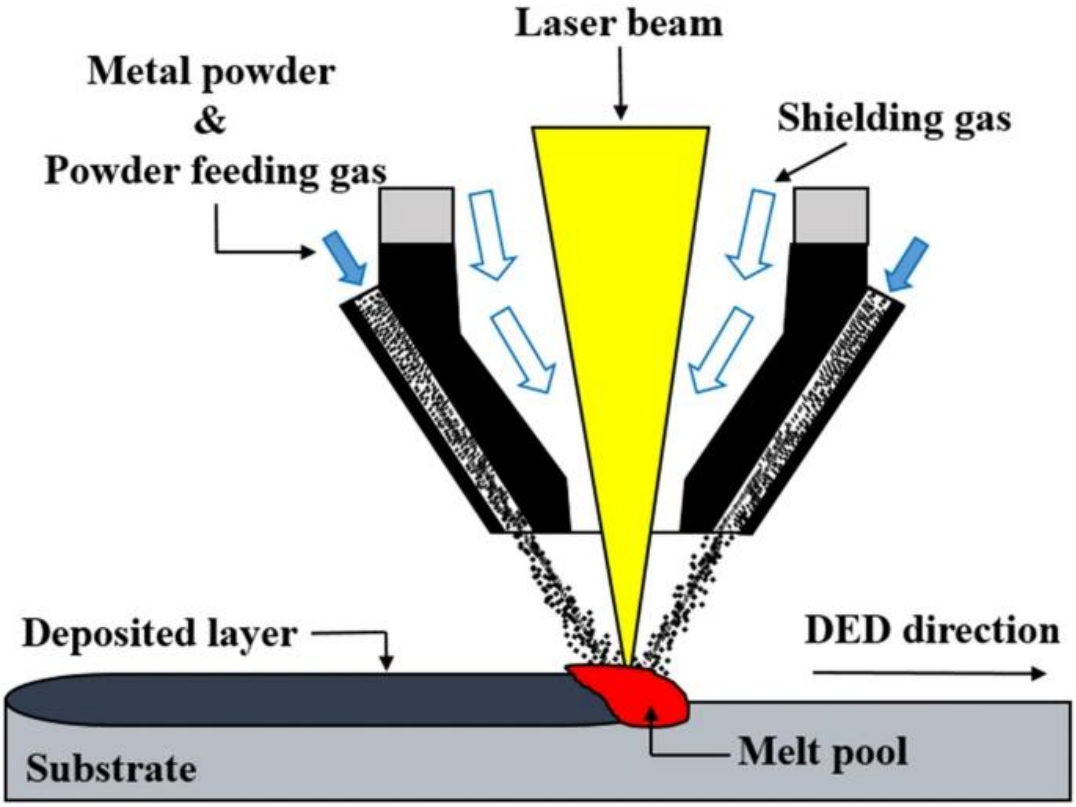

Figure 2.4: A schematic of LB-DED system. Adapted from [80].

When applied to Cu and its alloys, LB-DED faces similar challenges observed in LB-PBF, including high reflectivity at NIR laser wavelengths (~1064 nm) and rapid heat dissipation from the melt pool, which necessitate higher laser power and careful control of process parameters to ensure stable deposition and adequate fusion. To mitigate the processing challenges associated with Cu, several strategies have been explored, such as preheating the build platform, using low-thermal-conductivity substrates, and alloying Cu with elements such as Cr or Ni. For example, the addition of Cr in CuCr0.8 alloys not only improves mechanical properties through precipitation hardening but also reduces the thermal diffusivity, aiding in melt pool stabilisation during LB-DED [81]. Nevertheless, size effects remain prominent, particularly in thin-walled structures, where variable heat dissipation and solidification conditions strongly influence the build quality.

Advanced Cu alloys such as GRCop-42 (Cu-Cr-Nb) have been successfully fabricated via LB-DED for high-heat-flux applications in aerospace systems [82]. NASA-led developments have shown that rapid solidification associated with LB-DED refines the microstructure and minimises segregation, producing components with high hardness and thermal stability. While the material exhibits a strong crystallographic texture, mechanical anisotropy can be significantly reduced through surface treatments such as polishing, which alleviate surface-induced stress concentrations.

LB-DED also enables the fabrication of multi-material and bimetallic structures, such as Cu/stainless steel interfaces. These structures leverage the high conductivity of Cu and the mechanical strength of steel; however, the large mismatch in thermal expansion coefficients and melting points often results in interfacial cracking. Zhang et al. [83] reported that appropriate tuning of laser power and scan velocity is essential to achieve crack-free, metallurgically bonded interfaces, particularly when using Cu-Cr substrates.

In terms of industrial applications, LB-DED-processed Cu alloys have been utilised in components such as combustion chambers, regenerative cooling systems, electromagnetic railguns, and electrical contacts. These applications benefit from the ability of LB-DED to fabricate near-net-shape geometries with high thermal conductivity and tailored mechanical properties. For instance, LB-DED of Cu alloys has shown promise for producing large-scale functional components with complex geometries and site-specific property control [84]. However, key challenges remain, including the formation of porosity, oxidation during deposition, and the development of residual stresses, all of which can compromise the structural integrity and performance of LB-DED-fabricated components [85].

Despite these issues, recent innovations, such as the use of green and blue lasers, controlled thermal gradients, hybrid LB-DED systems, and machine-learning-assisted process optimisation, are progressively addressing these limitations. Moreover, the ability of LB-

DED to fabricate functionally graded materials offers exciting possibilities for creating components with spatially varying compositions and properties tailored to service conditions [86]. In summary, while LB-DED of Cu and its alloys remain technically demanding, continued advancements in laser optics, process control, and feedstock design have significantly expanded its feasibility and application scope. Ongoing research into microstructural control, interfacial engineering, and post-processing treatments will further unlock the full potential of this technology for high-performance, Cu-based systems.

2.2.3 Cold spray additive manufacturing

Cold spray (CS), also known as cold gas dynamic spraying, is a solid-state deposition process in which metallic powders are accelerated to supersonic velocities and bonded onto a substrate through high-strain-rate plastic deformation, without significant melting of the feedstock material. Originally developed as a coating and repair technology, CS has since been transferred into the AM space, where it is increasingly used to build fully dense three-dimensional (3D) metallic structures, commonly referred to as CSAM [87, 88]. Unlike fusion-based techniques such as LB-PBF or LB-DED, CSAM operates below the melting point of the materials, thereby avoiding issues related to solidification defects and residual thermal stresses. In a typical CSAM system (Figure 2.5), a compressed gas, commonly air, nitrogen, or helium, is heated and expanded through a converging-diverging (de Laval) nozzle, propelling powder particles (5–50 μm in diameter) at velocities exceeding 300 m/s [89]. Upon impact with the substrate, the particles undergo severe plastic deformation, resulting in mechanical interlocking and metallurgical bonding. CSAM offers several advantages, including high deposition rates, energy efficiency, and minimal thermal distortion. The growing demand for large-format AM technology makes CSAM well-suited

for the efficient, cost-effective production of large-scale metal components (e.g. a WarpSPEE3D printer is capable of producing components weighting up to 40 kg, with dimensions of 1 m by 0.7 m in diameter) [90]. For Cu and its alloys, CSAM is especially attractive due to the material's high thermal conductivity and oxidation tendency, which present challenges in conventional fusion-based AM processes. The absence of melting in CSAM prevents grain coarsening and maintains feedstock purity, enabling dense deposits with near-bulk properties, particularly when combined with post-deposition treatments such as hot isostatic pressing (HIP) or annealing.

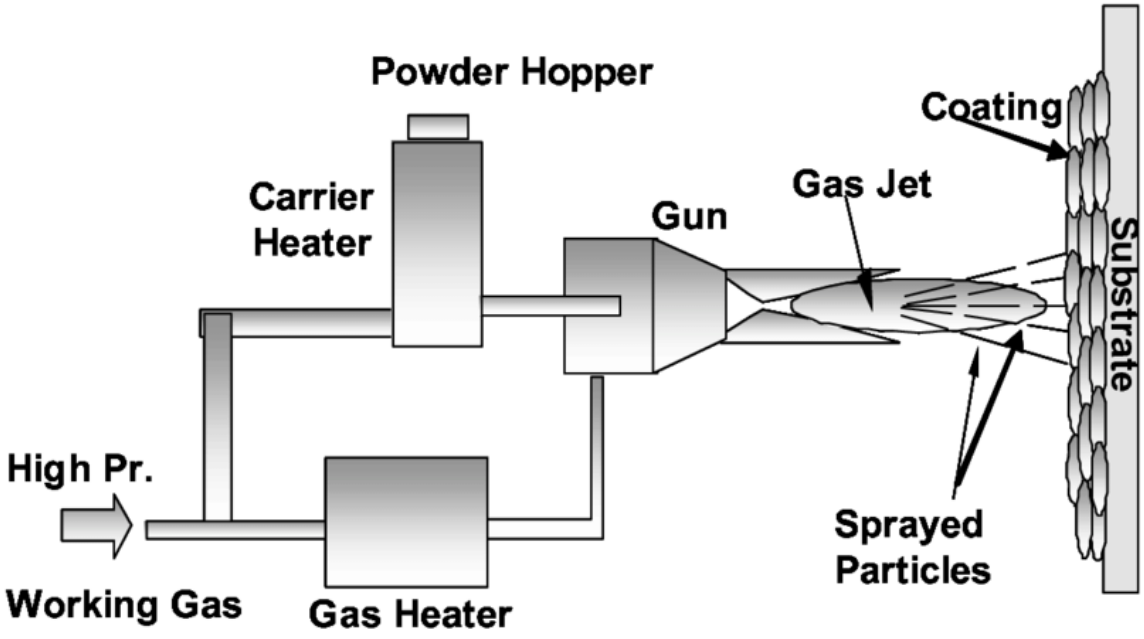

Figure 2.5: A schematic of cold spray process. Adapted from [91].

Cu is particularly well-suited to CSAM due to its excellent deformability. Numerous studies have demonstrated the fabrication of dense Cu components via CSAM with mechanical properties approaching or exceeding those of wrought Cu after suitable post-treatments [92, 93]. For example, Chen et al. [93] reported ultra-high strength and ductility in CSAM-deposited pure Cu, achieving an YS of 173 MPa and an elongation at fracture of

43.5% in the as-sprayed condition. These properties were attributed to a heterogeneous microstructure comprising bimodal grains and a gradient nanograined structure at the single splat level [93]. Notably, the builds employed pressurised helium as the propelling gas, which is comparatively costly and may limit scalability relative to nitrogen-based operation. Some challenges remain intrinsic to CSAM of Cu alloys, including poor inter-particle bonding in the as-deposited state, anisotropy arising from build orientation, and porosity networks that can compromise mechanical performance. Hutasoit et al. [94] reported that the Z-build orientation resulted in significantly lower strength and ductility compared to XY-builds, owing to disrupted bonding from altered spray angles. Post-build annealing at 400 °C improved recrystallisation and bonding but sintering at 1000 °C led to excessive grain growth and intergranular pores.

Powder characteristics and feedstock preparation play a critical role in CSAM component performance. Spherical gas-atomised powders offer better flowability and may result in higher deposition efficiency [95]. Mechanically milled powders, although more irregular in shape, can enhance deposition when paired with appropriate carrier gases and processing parameters, because rough morphologies promote better acceleration and anchoring upon impact [96]. The choice of carrier gas strongly influences the outcome; while helium provides superior particle acceleration and bond strength, it is cost-prohibitive. Nitrogen and compressed air are more economical alternatives, but the inter-particle bonding strength achieved with these gases is generally weaker than that obtained with helium.

Because CSAM builds form by solid-state, high-velocity impact, the as-deposited microstructure is highly strained and heterogeneous, with extensive work hardening, oxide-containing particle–particle interfaces, residual porosity and limited metallurgical diffusion across splat boundaries [90, 92, 97]. These features can reduce ductility, and in Cu-based systems, depress electrical/thermal conductivity. Post-heat treatments (e.g., annealing,

solutioning plus ageing) are therefore routinely applied to promote inter-particle diffusion, disrupt oxides, heal pores, relieve residual stresses via recovery/recrystallisation, and introduce precipitation strengthening. In doing so, they homogenise the deposit and allow tuning of the microstructure–property balance towards wrought-like performance. Thus, post-heat treatments remain essential for improving bonding and reducing porosity [98]. In the context of functional applications, CSAM has been extended beyond pure Cu to Cu alloys such as Cu-Ni systems. For instance, Tran et al. [99] demonstrated the successful fabrication of Cu-20Ni alloys via CSAM using mixed Cu and Ni powders, followed by solid-state annealing. The resulting parts displayed excellent corrosion and tarnish resistance, as well as antimicrobial properties, making them viable for public health hardware applications [99]. The successful CSAM fabrication of Cu-20Ni components points to a clear path for systematically exploring Cu–Ni alloys, but this work is restricted to a binary alloy and reports limited mechanical metrics and emphasises homogenisation rather than precipitation design. Subsequent studies should prioritise enhancing mechanical properties and optimising post-spray heat treatments.

In summary, CSAM still faces hurdles in the consistent formation of metallurgical bonds, removing defects, and tuning the microstructure-property balance. The Cu–20Ni demonstration by Tran et al. [99] confirms feasibility but leaves open how ageing treatments and minor alloying additions can affect microstructural evolution and mechanical properties, and how these treatments govern the strength–ductility–conductivity trade-off across the Cu–Ni space. Mapping the processing-microstructure-property relationship and advancing a heat-treatment-centred framework would be key steps for achieving high-performance CSAM alloys.

2.3 AM of Cu-Sn alloy system

2.3.1 Influence of scan strategy

Cu-Sn alloys, commonly referred to as bronzes, represent one of the oldest and most historically significant alloy systems, dating back to the Bronze Age. In modern engineering, Cu-Sn alloys continue to be widely used due to their excellent wear resistance, corrosion resistance, castability, and mechanical strength. According to market analysis in Figure 2.6 [100], bronze accounted for over 23.0% of the global Cu alloys market share in 2023, reflecting its continued industrial relevance across diverse sectors. These alloys are employed in marine components, bearings, gears, springs, and electrical connectors. Traditionally processed via casting, forging, and powder metallurgy, recent developments have explored their potential in AM, particularly with the aim of tailoring microstructures and properties through advanced processing techniques.

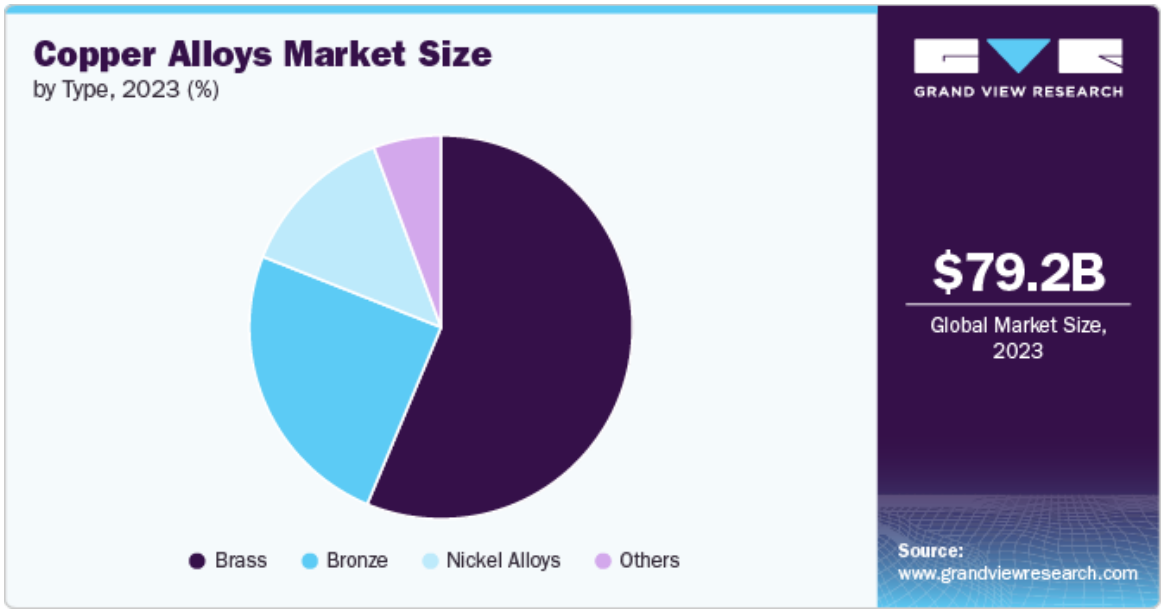

Figure 2.6: Copper alloys market size analysis report, by type (Brass, Bronze, Copper-Nickel and other Copper alloys). Adapted from [100].

In LB-PBF, the scan strategy, defined by the path and sequence of the laser beam across the powder bed, plays a crucial role in determining the thermal history of the melt pool and, consequently, the microstructure and mechanical properties of the fabricated component. Scan strategy encompasses parameters such as scan vector length, hatch spacing, scan rotation between successive layers, the use of stripe or chessboard segmentation, and scanning order. Extensive research on steels and Ni-based superalloys has demonstrated that these parameters significantly influence grain morphology, crystallographic texture, residual stress distribution, porosity formation, and mechanical anisotropy [101-104]. Figure 2.7 (adapted from Lam et al. [105]) presents common LB-PBF scanning strategies, including single-direction, alternating, rotation, and chessboard patterns. These schematics, together with associated microstructural features, highlight how changes in scan path and rotation can directly influence melt pool morphology, grain orientation, and defect formation.

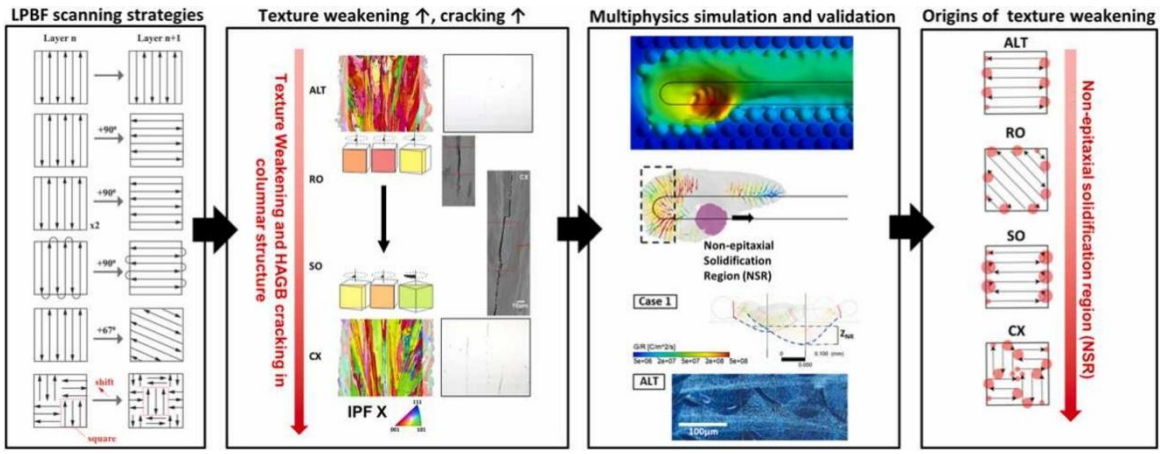

Figure 2.7: Graphical abstract showing the effect of different LB-PBF scanning strategies on texture weakening, cracking behaviour, and their correlation with non-epitaxial solidification regions in IN738LC superalloy [105].

Studies in other material systems show scan strategy strongly tunes melt-pool morphology, grain/cell size, porosity, texture and residual stresses. For example, in 316L stainless steel,

a stripe-with-contour pattern gave the finest cellular microstructure (~610 nm), highest strength (YS of 550 MPa, UTS of 1016 MPa) while checkerboard produced coarser cells, more porosity and higher residual stress [101]; in Inconel-718, alternating 67° rotational strategies weakened texture and lowered residual-stress gradients (i.e., less part shape distortion) [103]. In contrast to the well-established body of literature for steels and Ni-based systems, relatively little is known about the effects of scan strategy on Cu alloys fabricated via LB-PBF, particularly Cu-10Sn. While recent studies have explored the optimisation of laser power, scan speed, and hatch spacing for Cu-10Sn to achieve higher density and reduced porosity [106, 107], the influence of scan strategy in a broader sense, particularly the rotation of scan vectors between layers or the implementation of segmented scan patterns, remains unexplored.

Although process optimisation for LB-PBF Cu-10Sn has shown improved strength, one promising and underexplored avenue in LB-PBF Cu-10Sn lies in the control of the scan strategy. By modulating the scan path through changes in rotation between layers, segmenting patterns (e.g., chessboard vs. stripe), or vector length, as shown in Figure 2.7, it is possible to alter local thermal fields and solidification conditions. In low-conductivity alloys, these modifications have been used to reduce texture intensity, promote equiaxed grain formation, and relieve residual stresses [103]. Yet in Cu-10Sn, the effect of such strategies remains uncertain and largely untested. Given the high sensitivity of Cu-10Sn to thermal history, the scan strategy may influence both the grain structure and mechanical properties, highlighting the need for systematic investigation. Comprehensive parameter sweeps are particularly critical, as they allow the role of scan strategy in grain morphology and defect mitigation to be reliably established. Bridging these gaps will be essential for fully exploiting the potential of Cu-10Sn in AM applications, particularly where consistent microstructure, mechanical reliability, and functional performance are paramount.

2.3.2 Mechanical property and microstructure

This section examines mechanical property of the traditional versus AM processing of Cu-Sn alloys, their phase equilibria, microstructural characteristics, and the relationship between processing, microstructure, and final properties in AM contexts.

Numerous AM Cu-Sn alloys have been studied across a variety of industrial applications [108-111]. For instance, Scudino et al. [110] reported highly dense Cu-10Sn with ~83% higher YS (from 120 to 220 MPa), ~133% higher UTS (from 180 to 420 MPa) than those of equivalent samples in the as-cast condition, while ductility rises from 7% to 17% (Figure 2.8). This indicated the effectiveness of LB-PBF for producing Cu alloys with refined microstructures and outstanding mechanical properties. The representative stress-strain curves and a Cu-10Sn propeller fabricated by LB-PBF from this study are shown in Figure 2.8. Zeng et al. [111] examined the compositions, microstructures, and mechanical, thermal, and corrosion properties of LB-PBF-processed Cu-10Sn. The LB-PBF specimens also exhibit enhanced YS compare with those of as-cast specimens. Importantly, their study revealed a key difference between the properties of the as-built and vacuum-annealed specimens. Karthik et al. [112] fabricated Cu-13Sn with outstanding strength and ductility originating from nanoprecipitation. Similarly, Mao et al. [38] investigated high-Sn bronze (Cu-15Sn) and established a statistical correlation between AM process parameters and material density. They reported superior mechanical properties in Cu-15Sn, which are attributed to the fine grains comprising both cellular and dendritic morphologies. Yang et al. [113] elucidated the interplay between AM process parameters, surface roughness, density, and mechanical properties in Cu-5Sn, demonstrating improvements in the strength, ductility, and surface quality. Among Cu-Sn alloys produced via LB-PBF, Cu-10Sn has

attracted particular attention owing to its excellent mechanical properties and cost-effectiveness.

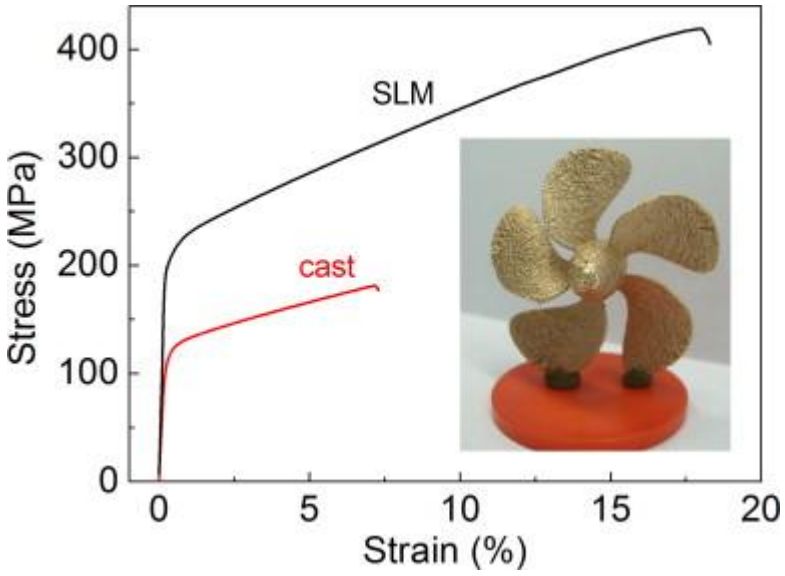

Figure 2.8: Stress–strain curves under tensile loading for the cast and as-built Cu–10Sn bronze and (inset) Cu–10Sn bronze propeller fabricated by LB-PBF. Adapted from [110].

Notwithstanding numerous studies on the properties and microstructures of additively manufactured Cu-Sn alloys, a fundamental gap in knowledge remains around the formation mechanism of secondary phases, particularly the Sn-rich face-cantered cubic (FCC) δ phase ($Cu_{41}Sn_{11}$, $F\bar{4}3m$, a = 1.783 nm). Traditionally, the hard and brittle δ phase occurs when the Sn content in Cu-Sn exceeds 10 wt.% [114]. The δ phase appears as a thick (~ in micrometres), interconnected region uniformly in as-cast samples, which leads to crack initiation and propagation upon loading, resulting in premature material failure. A previous study of as-cast Cu-Sn samples [115] showed that after primary α(Cu) starts to nucleate at approximately 990 °C, it reacts with the liquid phase to form β ($Cu_{17}Sn_3$) by a peritectic reaction at 798 °C. The newly formed β phase then undergoes a subsequent peritectic reaction to produce γ (Cu_3Sn) at 758 °C. Some peritectoid reactions involving ζ and ε also occur at 603–649 °C. With a further decrease in temperature, β decomposes to α + γ at

566 °C and γ decomposes to α + δ at 528 °C via eutectoid reactions. As the temperature reduces, the δ phase decomposes into the ε phase at approximately 350 °C through a sluggish eutectoid reaction, which rarely occurs in conventional castings [116]. However, the rapid cooling during LB-PBF results in a finer δ phase [106, 112], hindering dislocation motion and thereby enhancing instead of embrittling the ductility of the alloy. Mehta et al. [106] observed a fine dendritic microstructure consisting of two different FCC α(Cu) solid solutions with a space group of $F\bar{4}3m$, and δ phase. The lattice parameters of the two α(Cu), as a function of Sn concentration, were identified to be 0.364 nm and 0.368 nm. Subsequent mechanical testing revealed significantly better tensile strength and ductility of Cu-10Sn as compared to those reported in previous studies, likely arising from the contributions of the grain size (Hall-Petch) effects and dislocation strengthening mechanisms. Li et al. [117] have previously reported that when the cooling rate is higher than 1×10^4 °C/s, a metastable $Cu_{5.6}Sn$ phase with a simple tetragonal crystal structure (a = b = 0.985 nm and c = 1.103 nm [118, 119]) develops, whereas the δ phase does not occur. Overall, a detailed understanding of the properties and formation mechanism of the traditionally deleterious δ phase during LB-PBF remains elusive.

2.3.3 Powder-microstructure-property relationship

Although much attention has been paid to optimising process parameters in LB-PBF, powder characteristics are equally crucial as they influence build quality, including part density (i.e., pore formation), microstructure, and mechanical properties [120-122], as summarised in Figure 2.9 [123]. This highlights the necessity of further research into the role of powder characteristics, particularly particle size distribution (PSD), chemistry, and flowability, on microstructure and mechanical behaviour. PSD influences both the powder

bed packing density and energy absorption during laser scanning. For example, particle sizes outside the optimal range, such as large particles (>80 μm) or fine particles (<10 μm), can cause poor powder bed packing, incomplete melting, agglomeration [124], and balling [125], all of which result in significantly reduced part density. Recent work by Jin et al. [126] showed Cu-10Sn powders with a bimodal PSD improved both the density and strength of the as-built samples. However, while a particle size range of 15–60 μm is commonly accepted, the detailed influence of PSD variations within this range on microstructure and build quality remains insufficiently explored. Powder flowability is another essential factor for uniform powder spreading and is influenced by both PSD and mean particle size. A narrower PSD with a relatively larger particle size typically enhance flowability by minimising friction between particles [127]. In addition to particle size-related attributes, the chemical composition of the powder, including surface oxides [128], microalloying elements [129], and impurities [130], can significantly influence laser absorption [131], melting and solidification behaviour [128], phase formation [129], and dislocation and chemical cell wall formation [132]. While these powder characteristics have been studied individually [133-135], they are often interdependent, making it difficult to identify the key attributes that most directly impact the quality of the build, microstructure and mechanical properties. This complex interplay underscores the need for a systematic investigation to reveal how powder attributes collectively shape both the micro- and macro-scale structure and mechanical properties. These considerations suggest that a focused study of powder characteristics alone may offer a promising route to enhancing mechanical properties of LB-PBF alloys.

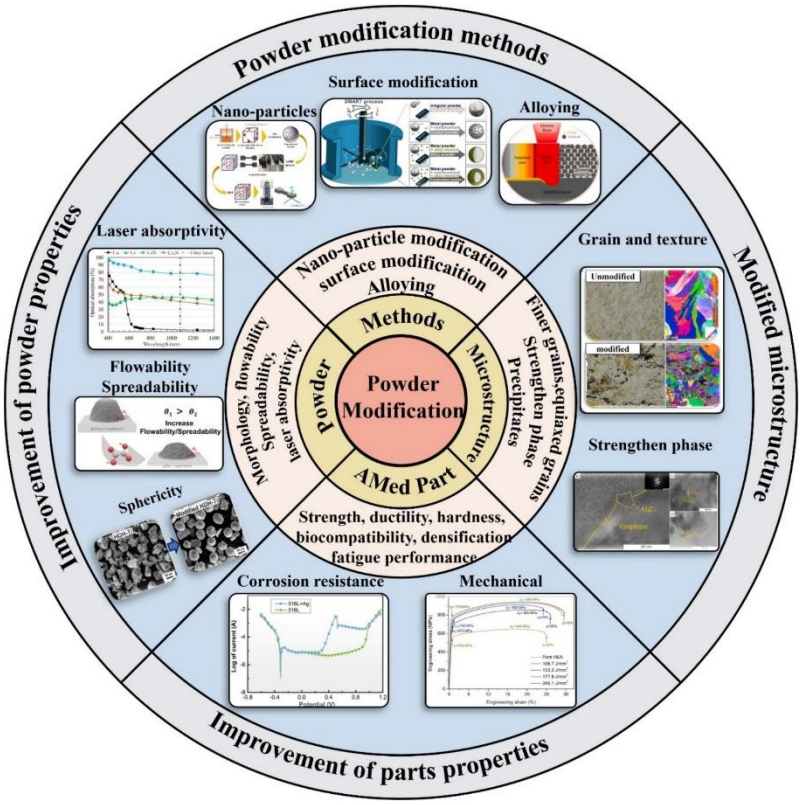

Figure 2.9: A summary of powder-microstructure-property relationship in AM. Adapted from [123].

As mentioned above, LB-PBF Cu-10Sn demonstrates significantly enhanced mechanical properties; however, the ductility remains modest across studies (13%–26% [106, 110, 136]), underscoring the need for further improvement in ductility while maintaining high strength. In recent years, a number of studies have explored the processing–structure–property relationships in LB-PBF Cu-Sn alloys. However, there remains a limited body of research directly connecting powder feedstock characteristics to mechanical performance and microstructural control in Cu-10Sn, despite its rising industrial relevance. Addressing this knowledge gap will be critical to moving beyond incremental improvements and towards a more predictive understanding of how powder design can be leveraged as a tool for tailoring both strength and ductility. Thus, future efforts aimed at systematically correlating powder attributes with process conditions and resulting mechanical properties

are expected to provide a more robust framework for advancing the performance of LB-PBF Cu-Sn alloys in demanding applications.

2.4 Cu-Ti alloys for AM

Achieving a simultaneous enhancement of mechanical strength and electrical conductivity remains one of the fundamental challenges in the AM of Cu alloys. According to Matthiessen's rule [137-139], at ambient temperature, solid-solution, grain boundary, dislocation, and precipitates all influence the material's electrical resistivity because of electrons' strong scattering by these factors, which indicate even small additions of alloying elements to improve strength often led to significant reductions in conductivity. Traditional alloying and oxide dispersion strategies have offered partial solutions, but a unified framework for designing Cu alloys that can deliver high strength without severely compromising conductivity is still underdeveloped.

The Cu–Ti alloy system has gained significant attention in recent years as a promising high-performance, precipitation-strengthened material for structural and electrical applications [40, 140]. Originally developed as a potential substitute for Cu–Be alloys, where the presence of Be poses serious toxicity and handling challenges, Cu–Ti alloy offers an appealing combination of high strength, good thermal stability, and moderate electrical conductivity [141, 142]. For a Cu–3Ti alloy processed by 95% cold rolling and aged at 450 °C for 1 h, Fu et al. [143] reported YS of 828 MPa, UTS of 895 MPa, total elongation at fracture of 13%, and conductivity of 13% IACS. Additionally, Nagarjuna et al. found that a Cu–4.5Ti–0.5Co alloy in the peak-aged state (400 °C) exhibited YS of 710 MPa, UTS of 890 MPa, total elongation at fracture of 25% and conductivity of 8% IACS. These properties are largely derived from its age-hardening response, which is governed by a

sequence of precipitation processes occurring upon thermal exposure. When aged at intermediate temperatures, typically between 400 °C and 450 °C, a supersaturated Cu solid solution decomposes via continuous precipitation to form fine, coherent, needle-shaped β′-Cu_4Ti precipitates [144, 145]. These precipitates, with a tetragonal D1a (Ni_4Mo-type, space group: $I4/m$) structure and lattice parameters of a = 0.585 nm and c = 0.365 nm, play a critical role in strengthening by impeding dislocation motion and generating coherent strain fields within the matrix. However, this metastable phase is thermodynamically less stable than the equilibrium β-Cu_4Ti phase [146], which possesses an orthorhombic (Au_4Zr-type, space group: $pnma$) structure and lattice parameters of a = 0.453 nm, b = 0.434 nm and c = 1.292 nm [147]. Prolonged or high-temperature ageing promotes the discontinuous precipitation of β-Cu_4Ti along grain boundaries, often forming coarse lamellar structures that consume the β′ phase and lead to a rapid decline in mechanical performance and conductivity [40, 148].

The precipitation sequence in Cu–Ti alloys is governed by the transformation from the metastable β′ (Cu_4Ti) to the stable β (Cu_4Ti) phase, a process primarily driven by Ti atom diffusion. This transformation is critically influenced by both thermodynamic and kinetic factors. Recent alloying strategies [149] supported by first-principles calculations and experimental studies have shown that the addition of Sc or Gd can effectively stabilise the β′ phase by forming substituted $Cu_4(Ti,Sc)$ or $Cu_4(Ti,Gd)$ structures. These solute elements increase the diffusion barrier for Ti and modify local bonding environments, thereby suppressing β-phase nucleation, reducing Ti mobility, and thus improving peak-aged hardness.

However, most existing studies focus on higher Ti concentrations (>2 wt.%), which despite offering increased hardness, often reduce electrical conductivity below 20% IACS. Furthermore, these alloys are typically produced by conventional casting or wrought

processes, where high grain boundary densities promote the rapid coarsening and transformation of the strengthening β′ phase into the equilibrium β phase, leading to premature over-ageing and a consequent decline in strength and conductivity. Moreover, although a recent study [150] demonstrated that in-situ alloying during LB-PBF improved the mechanical properties of Cu–3Ti alloys—achieving an UTS of 535 MPa and total elongation at fracture of 18.4%. To date, there has been limited exploration of Cu–Ti alloys processed via AM.

LB-DED presents a promising pathway for addressing these limitations. The process can produce large columnar grains with reduced grain boundary area, thereby mitigating β-phase formation and suppressing discontinuous precipitation. In addition, the high cooling rates inherent in LB-DED help retain a supersaturated solid solution, which is ideal for controlled post-deposition ageing to form fine β′ precipitates.

Despite these advantages, the potential of LB-DED for processing low-Ti Cu–1Ti alloys remains underexplored. At lower Ti contents, the thermodynamic driving force for β phase formation is reduced, potentially allowing better control over precipitation and improved retention of electrical conductivity.

2.5 Cu-30Ni alloy and implications for CSAM

Cu-Ni alloys are extensively used in maritime applications and chemical plant construction owing to their excellent strength and corrosion resistance [151, 152]. Among these, Cu-30Ni (wt.%), also known as cupronickel, alloyed with strategic additions of Fe, Mn, Nb, and Si, is widely used in harsh environments involving exposure to seawater and corrosive chemicals [152-154]. Early studies showed the benefit of microalloying in Cu-Ni alloys, with Barnett reporting in 1946 that Mn addition enhanced hardness [155], while Stewart

and LaQue summarising in 1952 that Fe addition could improve corrosion resistance [156]. In 1960, Shepherd investigated the effects of Nb and Si additions, and concluded that a modest amount of Si, combined with Nb, is crucial for improving weldability and mechanical strength [153] because these elements appeared to invoke an age hardening reaction. Gupta et al. later explored the optimisation of the age hardening process [157]. The precipitates in these alloys have been identified as face-centred cubic (FCC) ordered $L1_2$ Ni_3Si (γ') phase (space group 221 or $Pm\bar{3}m$), and their formation is sensitive to alloy composition, ageing temperature, and time [158, 159]. This ordered phase is referred to as γ'-Ni_3Si in some studies and as β-Ni_3Si in others [160]; both terms describe the same crystallographic structure. This γ' phase has been recognised for its significant role in enhancing the mechanical properties of Cu-Ni alloys [157, 161]. Despite these findings, the precise mechanisms by which Si contributes to precipitate formation remain unclear. Interestingly, the technology transfer for casting Cu-30Ni alloys has proven successful in the foundry industry [162], but there remains a notable deficiency in knowledge transfer with a limited number of publications, most of which were extensively studied over three decades ago (Figure 2.10a shows the result of a search of a publication database using keywords ‘Copper alloys’ and ‘Cupronickel/Cu-30Ni alloys’ over time on Scopus). Notably, studies specifically addressing ageing response account for only ~3% of the Cu-30Ni literature, highlighting a critical underexplored research area (Figure 2.10b). Since early 2000, the scientific literature has focused predominantly on alloy development, emphasising overall corrosion resistance and mechanical strength [154, 163, 164]. A significant gap in understanding of the evolution of the microstructure and properties during casting, homogenising, and age hardening remains. Moreover, the age hardening response, including the chemistry of γ' precipitates, how they are formed, and their effect on mechanical performance, has not been fully elucidated. Additionally, the effect of

different ageing methods, such as furnace ageing with furnace cooling versus salt bath ageing with water quenching, remains unclear, despite their potential to influence the age hardening response through differences in thermal history. Addressing these research gaps is vital for tailoring the Cu-30Ni alloy to specific application requirements, especially those requiring high-strength materials. Insights into the age hardening response can be applied to emerging fabrication technologies, most notably CSAM, where post-deposition heat treatments are required to enhance inter-particle bonding, homogenise microstructure, and simultaneously induce precipitation strengthening.

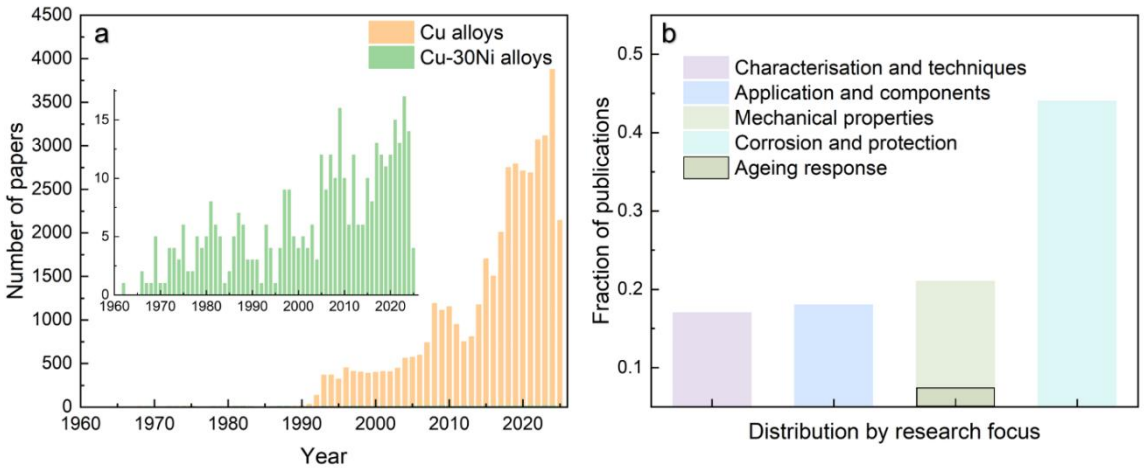

Figure 2.10: (a) The result of a search of a publication database using keywords 'Copper alloys' and 'Cupronickel/Cu-30Ni alloys' over time on Scopus (accessed 27/04/2025), and (b) the fraction of Cu-30Ni alloys with different research focus. Publications on Cu alloys have rapidly increased since the early 2000s. In contrast, studies specifically on Cu-30Ni alloys remain consistently limited, despite steady but modest growth over time. Notably, ageing response accounts for merely ~3% of the total Cu-30Ni-related literature.

2.6 Summary

This chapter has reviewed the significance of Cu and its alloys and recent developments in their processing via AM techniques, including LB-PBF, LB-DED, and CSAM, which offer transformative potential for high-performance applications due to Cu's superior electrical,

thermal, and corrosion-resistant properties. From this review, five key challenges and knowledge gaps can be identified as follows:

1. **Optimisation of printing parameters and scan strategy:** A comprehensive parameter sweep is a prerequisite not only for process optimisation but also as a foundation for fundamental investigations, such as scan strategy, particularly given the differences in powder characteristics and machine configurations used in this study compared to those reported in the literature. While scan path engineering has been effective in other alloy systems, the effect of laser scan strategy on thermal gradients, grain morphology, porosity formation, and mechanical properties in Cu-10Sn remains underexplored.
2. **Mechanism of Sn-rich δ phase formation in Cu-10Sn alloys:** Despite extensive studies on the microstructure and properties of additively manufactured Cu-Sn alloys, the fundamental mechanism underlying the formation of the Sn-rich face-centred cubic (FCC) δ phase ($Cu_{41}Sn_{11}$, $F\bar{4}3m$, a=1.783 nm) remains inadequately understood. The presence of the δ phase is of particular concern, as it can deteriorate mechanical properties, especially ductility, due to its intrinsic brittleness.
3. **Powder characteristics and their impact on microstructure-property relationship:** The influence of powder characteristics, such as particle size distribution, flowability, and chemical composition, on the resulting microstructure and mechanical properties in AM Cu alloys remains insufficiently understood. A deeper understanding of these correlations is essential for enhancing both strength and ductility, and for guiding rational powder selection and feedstock design for high-performance applications.
4. **Challenges in manufacturing high-strength, high-conductivity Cu:** Achieving a balance between mechanical strength and electrical conductivity remains a core

challenge in the development of AM Cu alloy. Although alloying strategies and oxide dispersion approaches have shown promise, a framework for designing alloys that retain high conductivity while improving strength remain challenging.

5. **Age hardening response of Cu-30Ni alloys:** While Cu-30Ni is widely used in corrosion-resistant applications, its age hardening behaviour, particularly in the presence of microalloying additions such as Si, remains insufficiently understood. These insights are highly relevant to solid-state processes such as CSAM, where post-deposition heat treatments can be used to optimise mechanical performance.

Collectively, this literature review highlights the urgent need for systematic, multiscale studies to address the fundamental and process-specific challenges associated with the AM of Cu-based systems. The insights gained from this review provide the basis for defining the specific aims outlined in the following chapter.

Chapter 3 Aim and Scope of this Thesis

Based on the literature review, considerable progress has been made in the AM of Cu alloys; however, critical challenges remain in process optimisation, microstructural control, and property enhancement. As outlined in Section 2.6, these unresolved issues underscore the need for systematic investigation of powder–process–microstructure–property relationships across Cu–Sn, Cu–Ti, and Cu–Ni systems. This thesis has five aims, each of which is addressed in a dedicated chapter. The aims were formulated to directly tackle the five specific research gaps identified in Section 2.6. The specific aims of this thesis are to:

Aim 1: Optimise printing parameters and investigate the effect of scan strategy in LB-PBF Cu-10Sn.

A comprehensive process parameter sweep is conducted to account for differences in machine configuration and powder feedstock compared to previous studies, and to identify the role of laser scan strategies in controlling microstructural development and mechanical properties. The optimised parameters established here are held constant in the following studies to eliminate process-related variation.

Aim 2: Elucidate the formation mechanism, distribution, and strengthening contribution of the Sn-rich δ phase ($Cu_{41}Sn_{11}$) in LB-PBF Cu-10Sn.

The δ phase has been widely recognised as a brittle intermetallic in conventionally processed alloys, yet its behaviour under rapid solidification remains poorly understood. The formation mechanism of the δ phase and its role in strengthening are unravelled through detailed microstructural and mechanical characterisation.

Aim 3: Enhance the mechanical property of LB-PBF Cu-10Sn by investigating powders with varying characteristics.

By evaluating powders with different PSD, chemical compositions, and flowability, this work investigates how feedstock properties influence melting and solidification behaviours, microstructure variations, and the resulting strength–ductility balance.

Aim 4: Develop processing strategies to balance high strength and electrical conductivity in Cu-based alloys, identifying composition and post-processing routes.

This work focuses on low-Ti Cu–1Ti alloys fabricated via LB-DED, where rapid solidification and subsequent heat treatment are employed to control β′ precipitation for strengthening while limiting conductivity degradation.

Aim 5: Investigate the age hardening response of Cu-30Ni alloys.

This study examines the evolution of the microstructure of Cu–30Ni alloys with and without Si, revealing how Si promotes precipitation during post-deposition heat treatments relevant to CSAM, with implications for strength retention and alloy design.

The scope of this thesis is defined by the selected materials, AM techniques, and characterisation methods employed. Three Cu-based alloy systems were studied: Cu–10Sn, Cu–1Ti, and Cu–30Ni. Two laser-based AM techniques, LB-PBF and LB-DED, were used to fabricate alloys, while a study in Cu–Ni is designed to optimise CSAM post-processing. A comprehensive suite of characterisation methods was employed to establish process–structure–property relationships, including microstructural analysis and property evaluation. Together, these approaches define the scope of this study, providing a focused

and multi-faceted exploration of how AM can be leveraged to optimise Cu alloys for advanced structural and functional applications.

The research objectives outlined in Aims 1–5 provide the framework for this thesis and are examined in detail across Chapters 5–9. Collectively, successful completion of these aims will provide: (i) validated process maps and scan-strategy guidelines for LB-PBF Cu-10Sn, (ii) a understanding and control strategy for δ-phase formation and strengthening, (iii) an evidence-based framework linking powder characteristics to defects formation, microstructural and mechanical response, (iv) a LB-DED route for Cu–1Ti that demonstrably balances strength with high electrical conductivity via controlled precipitation and heat treatment, and (v) an ageing/precipitation map for Cu-30Ni (with Si) tailored to CSAM heat treatments. Together, these outcomes will establish transferable design rules for powder–process–structure–property optimisation in AM Cu alloys, reduce trial-and-error in industrial implementation, and enable the engineering of high-performance, multifunctional Cu components for electrical, thermal and structural applications.

The structure beyond the aim-specific chapters is as follows. Chapter 4 describes the materials, fabrication methods, and experimental techniques used in this study. Chapter 10 presents the key conclusions drawn from the preceding chapters, and Chapter 11 outlines future research directions arising from this work.

Chapter 4 Material and Experimental Techniques

4.1 Material and fabrication

4.1.1 Cu-10Sn

This section describes fabrication methods for the studies of LB-PBF Cu-10Sn in Chapters 5, 6 and 7.

4.1.1.1 Powders

Three different batches of Cu-10Sn powder, manufactured by three different suppliers (denoted as A, B and C), are used in this study. All the powders were produced via gas atomisation, and they were stored in identical airtight containers and maintained in a controlled environment with a temperature of approximately 22 °C and a relative humidity of 45–50% throughout storage or testing. Initially, powder C supplied by Colibrium Additive was selected to perform a comprehensive printing parameter sweep, as the recommended parameters and scan strategy for the MLab 200R LB-PBF system used in this work are based on this powder, so the printing parameter sweep ensured reliable process stability and facilitated the identification of a robust set of printing parameters. Once the optimal processing window was established using powder C, these parameters were fixed for all subsequent builds. The experiments using powder C are presented in Chapters 5 and 6. To isolate the effects of powder characteristics, two additional Cu-10Sn powders (powder A from Eckart TLS GmbH and powder B from CNPC Powder Co., Ltd) with distinct particle size distributions and chemical compositions were sourced from separate suppliers. All three powders were printed under identical process parameters, and

their results focused on evaluating the influence of powder properties on the final as-built quality are detailed in Chapter 7.

4.1.1.2 Material fabrication

Samples were manufactured using an MLab 200R LB-PBF machine (Colibrium Additive) equipped with a 200 W Nd:YAG fibre laser (wavelength: 1064 nm) with a 75 µm spot size in an Argon atmosphere. Nine parameter sets were trialled with four samples for each parameter (totalling 36 samples simultaneously fabricated). The specimens had dimensions of 10 × 10 × 25 mm^3 (*X*-*Y*-*Z*, where *Z* is the build direction (BD)) and were fabricated with a support structure on top of a 316L stainless steel build plate at room temperature (22 °C). An alternating 90° rotation of the laser raster direction was employed between build layers (Figure 4.1), which serves as a standard (S)-scan strategy. A 25 µm layer thickness (*t*) and 75 µm hatch spacing (*h*) were maintained for all specimens.

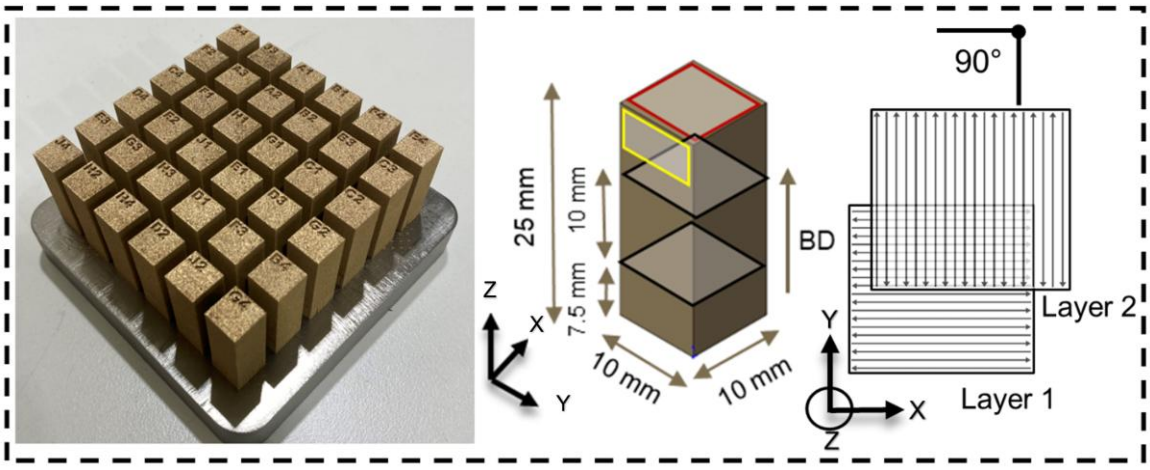

Figure 4.1: Image of the block samples on the build plate, with schematic bulk dimensions and alternating 90° laser scanning.

Relative densities of the LB-PBF Cu-10Sn samples were measured using Archimedes' principle, with each measurement repeated three times. All samples were ultrasonically cleaned in ethanol prior to measurement to remove residual powder. This parameter sweep

enabled identification of optimal processing conditions by revealing the transition from lack of fusion to keyhole-induced porosity across different energy regimes.

Commercial as-cast Cu-10Sn (Kormax LLC) was obtained for a comparison of the mechanical property, microstructure and conductivity. The composition of the as-built sample was determined by inductively coupled plasma atomic emission spectroscopy (ICP-AES) and a LECO combustion analyser, as shown in Table 4.1.

Table 4.1: Chemical compositions (wt.%) of the Cu-10Sn powder and as-built sample.

	Cu	Sn	P	Pb	O
Powder C	balance	10.3	0.29	0.04	0.05
As-built	balance	10.6	0.32	0.02	0.03

4.1.1.3 Scan strategies

To investigate the influence of scan strategy on the microstructure and defect formation in Cu-10Sn alloys processed via LB-PBF, a series of cubic samples (5 × 5 × 5 mm^3) and tensile test specimens were fabricated using four distinct scan strategies, as presented in Figure 4.2. Each strategy involved a unique laser scanning pattern and layer-wise BD. Unidirectional alternating (UA)-scan employed standard alternating uni-directional scanning using a consistent left-to-right path with a 90° rotation. Strip alternating (SA)-scan utilised a bidirectional strip exposure (1mm width) with 90° interlayer rotation and a 0.1 mm interlayer shift along *X* and *Y* direction. More complex scan strategies were explored in island alternating (IA)-scan and island shift (IS)-scan, which used island-based patterns with random 90° rotational changes. IA-scan utilised a 1 mm island size, while IS-scan applied a 0.1 mm shift along *X* and *Y* direction with the same island size. These strategies were chosen to assess the effects of energy distribution uniformity, melt pool

overlap, and scan vector rotation on the resulting microstructure. All samples were manufactured under identical processing parameters (*P* of 195 W, s of 860 mm/s, *t* of 25 µm and *h* of 75 µm), ensuring that only the scan strategy was varied. No post-processing heat treatment was applied; all specimens were analysed in the as-built condition.

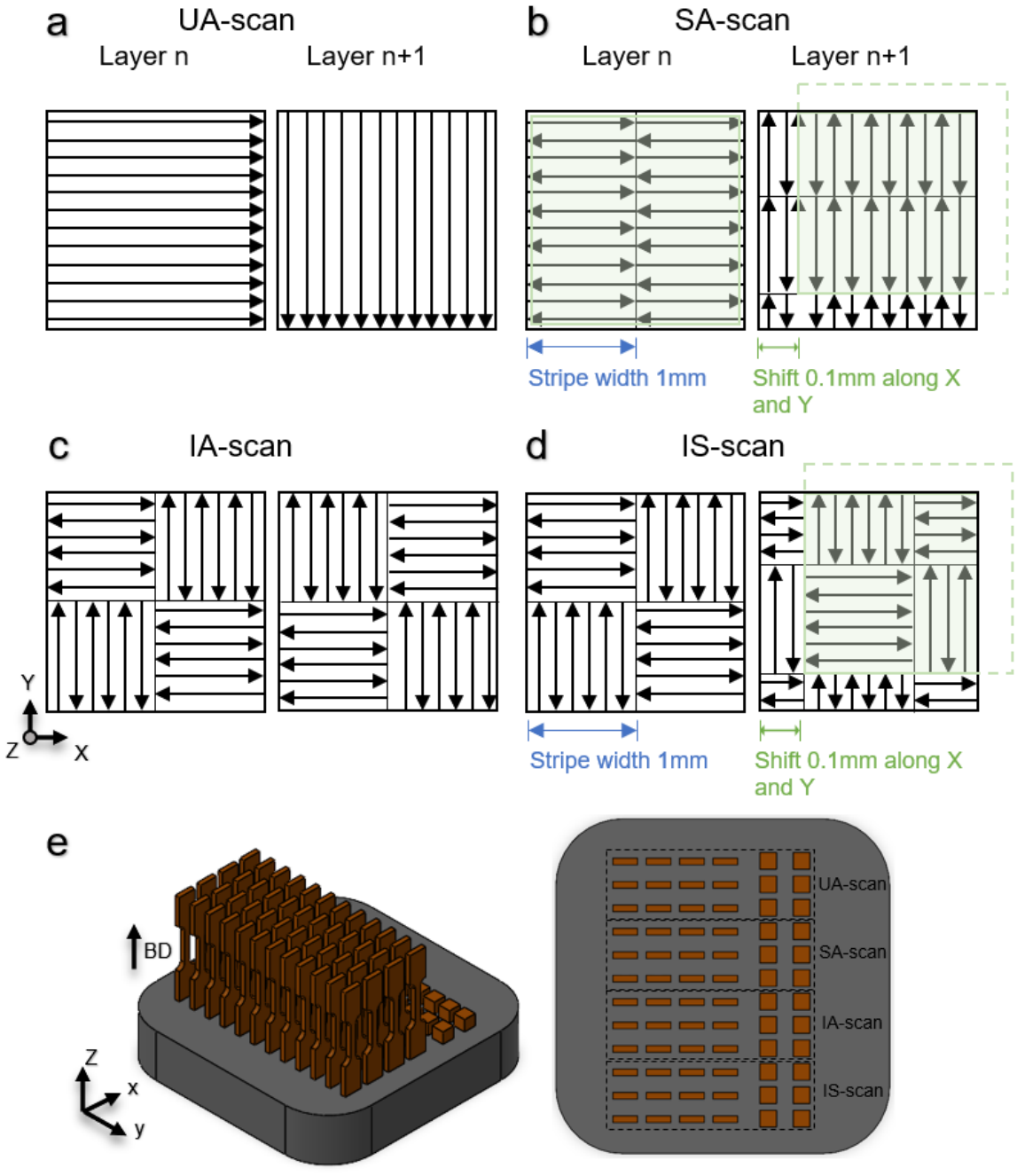

Figure 4.2: Schematic illustration of the four laser scan strategies used for LB-PBF Cu-10Sn. (a) unidirectional alternating (UA)-scan; (b) stripe alternating (SA)-scan; (c) island alternating (IA)-scan; and (d) island shifted (IS)-scan; and (e) shows the sample arrangement and build layout corresponding to each scan strategy.

4.1.1.4 Powder characterisation

The chemical composition of the three Cu-10Sn powders was determined using ICP-AES and a LECO combustion analysis. Surface chemical compositions were analysed by X-ray photoelectron spectroscopy (XPS) using a Thermo Fisher Scientific K-Alpha^{+} XPS system equipped with a monochromatic Al Kα X-ray source (1486.6 eV). The chamber pressure during analysis was maintained at approximately 10^{-7} mbar. XPS spectra were acquired over a binding energy range of 0–1350 eV, with a pass energy of 200 eV, a step size of 0.1 eV, a dwell time of 10 ms, and ten scans. Spectral deconvolution and fitting were performed using Avantage software.

Two methods were used to measure PSD of the Cu-10Sn powders. The first method utilised laser diffraction, evaluated using a Malvern Mastersizer 3000 laser diffraction particle size analyser. The second method used scanning electron microscopy (SEM). The metal powder was uniformly spread on conductive tape, and SEM images were captured at 20 kV in secondary electron imaging mode using a Zeiss ULTRA Plus field emission SEM. Image J v1.53k, an open-source software from the National Institutes of Health [165], was used for image processing using the 'Analyse Particles' function.

Powder flowability was assessed using a GranuDrum powder cohesion tester (Granutools). The powder was loaded into a drum, which was then placed inside the instrument and rotated at speeds ranging from 2 rpm to 20 rpm. A CCD camera captured multiple images at each angular velocity. For each rotation speed, the flowing angle (also known as the 'dynamic angle of repose' in the literature [166]) was calculated based on the average position of the powder-air interface. The dynamic cohesion index was subsequently

determined from the fluctuations of this interface, with higher cohesion index values indicating greater powder cohesiveness.

Laser absorbance of the powders was measured using a Shimadzu UV-VIS-NIR 3600 spectrophotometer over a wavelength range of 300–1650 nm. The absorbance was specifically evaluated at 1064 nm, corresponding to the laser wavelength used in LB-PBF.

4.1.2 Cu-1Ti

This section describes fabrication methods for the study of LB-DED Cu-1Ti in Chapter 8.

4.1.2.1 Powder mixing

Spherical Cu powder (99.5% purity, 50–100 μm diameter; Eckart TLS GmbH) and graphene nanoplatelets (99.99% purity, thickness 3 nm, diameter 1.5 μm; Nanografi) were dispersed in ethanol and mixed using a magnetic stirrer for 1 h. The suspension was then dried using a rotary evaporator (Büchi Rotavapor R-300) operated at 50 mbar, 80 rpm, with a 40 °C water bath and 4 °C condenser. ASTM Grade 1 titanium powder (45–100 μm spherical; Eckart TLS GmbH) was subsequently added, and the mixture was mechanically blended for 2 h in a TURBULA mixer to achieve the target composition of Cu-1Ti-0.05Graphene (wt.%) and ensure homogeneity.

4.1.2.2 Material fabrication

Rectangular bars (63 × 12 × 15 mm^3) were fabricated using a Trumpf TruLaser Cell 7020 system (Figure 4.3). The Yb:YAG solid-state laser (wavelength: 1030 nm, Gaussian beam profile) was operated in continuous mode. All samples were built on a 316L stainless steel substrate using the following optimised process parameters: laser power of 800 W, scan speed of 800 mm/min, laser spot size of 1.0 mm, layer height of 0.3 mm, hatch spacing of

0.7 mm, powder feed rate of ~2.9 g/min, shielding Argon gas flow rate of 16 L/min, and an interlayer dwell time of 20 s. A raster hatching strategy with a 71° rotation between successive layers was employed, and the outer geometry was finalised with a border scan. These parameters were selected to promote high densification and minimise defect formation. The actual chemical compositions of the manufactured samples were determined by ICP-AES; the results are summarised in Table 4.2. The as-built samples were aged at 470 °C for various durations (0.1, 0.5, 1, and 3 h) in the furnace, followed by quenching. This ageing temperature and time regime was selected based on Thermo-Calc simulations to promote controlled precipitation, while avoiding excessive coarsening observed at higher temperatures.

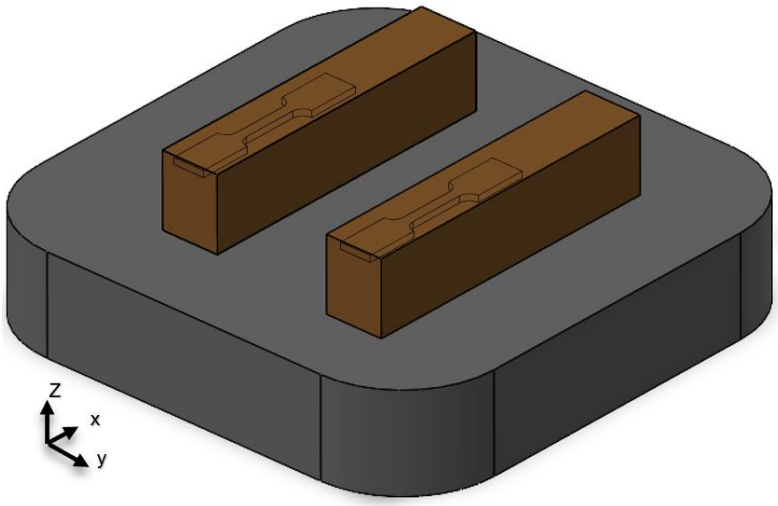

Figure 4.3: Schematic of two Cu-1Ti rectangular bars with dimensions of 63 × 12 × 15 mm³ fabricated on the build plate via LB-DED. The tensile specimens for mechanical testing were subsequently sectioned from these bars.

Table 4.2: Chemical compositions (wt.%) of the LB-DED Cu-1Ti sample.

	Cu	Ti	C	Si	O
As-built	balance	1.00	0.01	0.02	0.01

4.1.3 Cu-30Ni

This section describes fabrication and heat treatment methods for the study of Cu-30Ni in Chapter 9.

Alloys with 0 and 0.5 wt.% Si, designated as alloys 0Si and 0.5Si, were prepared per ASTM B369/B369M–20 using an AM500 arc-melter (Edmund Bühler) in Argon atmosphere. The chemical compositions, shown in Table 4.3, were analysed using ICP-AES The arc-melted samples were homogenised at 1000 °C for 16 h in a Nabertherm furnace with Argon gas, followed by water-quenching. Subsequently, the alloys were aged at 650 °C for various durations (0.1, 0.5, 1, 6, 24 and 100 hours (h)) in the furnace, followed by furnace cooling (denoted as FA-FC). These temperatures and times were selected based on Thermo-Calc simulations to ensure homogenisation and age hardening, as detailed in the results section. Additionally, to compare the effect of various age hardening heat treatments, salt bath ageing followed by water quenching (SB-Q), and furnace ageing followed by water quenching (FA-Q) were applied at the selected ageing condition. The specific conditions are detailed in Figure 4.4 and 4.5.

Table 4.3: Chemical compositions (wt.%) of the as-arc-melted Cu-30Ni alloys with and without Si.

Sample	Cu	Ni	Fe	Mn	Nb	Si
0Si	Bal	29.30	0.55	0.73	0.41	0.02
0.5Si	Bal	29.50	0.60	0.76	0.66	0.42

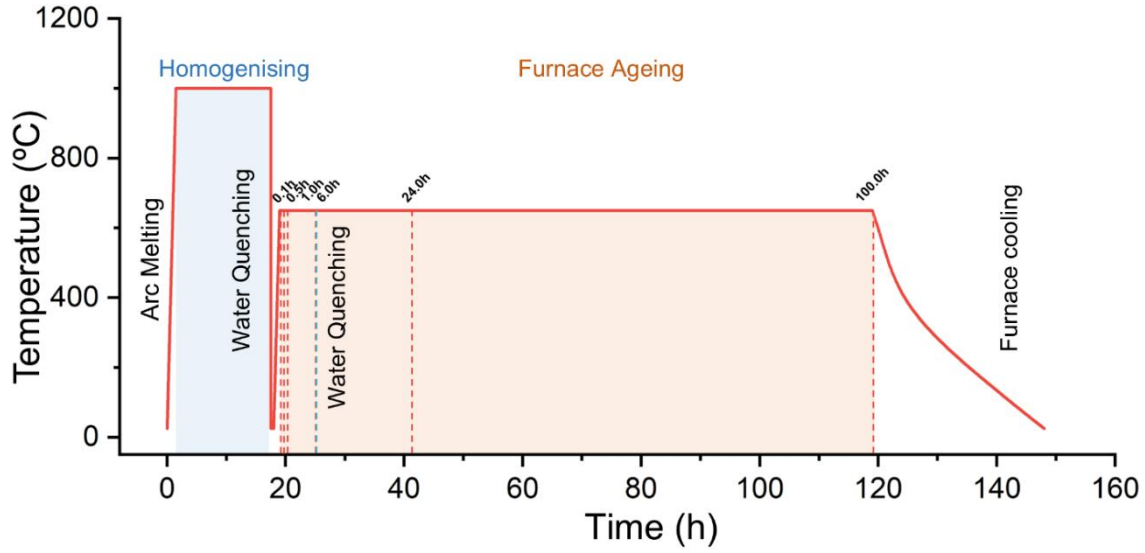

Figure 4.4: Time-Temperature schedule for ageing of Cu-30Ni alloy in furnace. The time in hours for ageing was indicated.

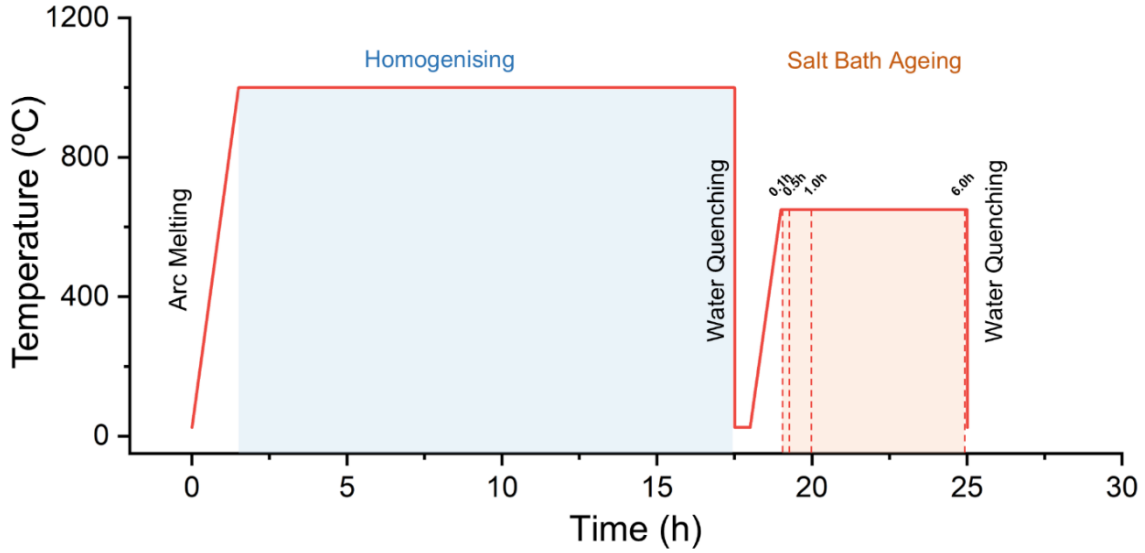

Figure 4.5: Time-Temperature schedule for ageing of Cu-30Ni alloy in salt bath. The time in hours for ageing was indicated.

4.2 Microscopy and microanalysis

4.2.1 Cu-10Sn

For the Cu-10Sn sample, both of the cuboid samples shown in Figure 4.1 (10 × 10 × 25 mm^3) and in Figure 4.2 (5 × 5 × 5 mm^3) were sectioned using an Accutom-50 diamond saw

(Struers) to prepare cross-sections in two planes: the *YZ* plane (parallel to BD in Figures 4.1 and 4.2) and the *XY* plane (perpendicular to BD in Figures 4.1 and 4.2). Specimens from the *YZ* plane were used for microstructure characterisation and hardness tests, and those from the *XY* plane were used for phase analyses, microstructure characterisation and wear property tests. Specimens used for microstructural characterisation were mounted in epoxy and mechanically polished to a 0.25 μm surface finish, using a combination of silicon carbide papers followed by diamond suspension polishing. Subsequently, the samples were further polished using a VibroMet 2 vibratory polisher (Buehler) with 0.04 μm colloidal silica surface finish followed by broad Ar-ion surface polishing using a PECS II system (Gatan) at 4 kV. Moreover, a LEXT 5000 confocal laser microscope (Olympus) was used to examine the melt pool morphology and the surface roughness at the top surface of the as-built samples.

X-ray diffraction (XRD) patterns were acquired from bulk samples (*XY* plane) using a PANalytical X'Pert (Malvern) with a Cu-K_α source. A scan rate of 4 °/min and step size of 0.01° with diffraction angle (2θ) ranging from 20 to 100° was used. Phase quantification was carried out by Rietveld refinement using GSAS-II software [167]. The refinement process incorporated a least-squares approach to optimise the weighting in the model, and refinement was performed until a close fit between the experimental and calculated patterns was achieved. The refinement's accuracy was evaluated using the statistical parameters, including the weighted R-profile (Rwp $\leqslant$ 10) [168].

Electron backscatter diffraction (EBSD) was performed using a Zeiss ULTRA field emission SEM equipped with an EBSD detector (Oxford Instruments) at an accelerating voltage of 30 kV. EBSD data was acquired with a step size of 0.1 μm and processed using Oxford Instruments' AZtecCrystal 3.0 software. Grains were defined by a minimum of 10 pixels and a misorientation of at least 5° relative to adjacent grains. The raw EBSD data

were processed to remove wild spikes, and iterations were performed up to the fifth nearest neighbour to refine zero solutions. The projection direction used for the inverse pole figure (IPF) maps corresponds to the reference axis specified in each figure. For additively manufactured samples, the IPF maps are typically plotted with respect to the BD (Z direction), unless otherwise stated. For areal porosity analysis, post-processed SEM images were analysed using ImageJ v1.53k via greyscale thresholding.

Transmission electron microscopy (TEM) was performed using a Spectra and Themis-Z (Thermo Fisher Scientific), both operated at an accelerating voltage of 300 kV, coupled with energy-dispersive X-ray spectroscopy (EDXS). Site-specific TEM samples were prepared by standard lift-out techniques [169] from polished EBSD specimens using a Helios G4 plasma focused ion beam (PFIB) SEM (Thermo Fisher Scientific). The PFIB was operated at 30 kV, with beam currents reduced from 15 nA down to 30 pA during coarse milling process, followed by fine milling at reduced acceleration voltage of 5kV with a beam current of 30 pA.

Atom probe tomography (APT) was conducted using an INVIZO 6000 (CAMECA) equipped with a dual 257.5 nm UV laser system. Site-specific APT specimens were also lifted-out from polished EBSD specimens via standard APT lift-out techniques [170] in the Helios G4 PFIB SEM. APT was performed at ~50 K and ~2.6×10^{-11} Torr. A laser power of 400 pJ and laser pulse repetition rate of 200 kHz with a detection rate of 2% were used. APT reconstruction and analysis were performed in CAMECA's AP Suite 6.3 software, with the default values for field factor and image compression factor of 4 and 1.4, respectively. Over 700 million ions were collected for the compositional analysis.

Differential scanning calorimetry (DSC) was performed on as-built samples and an equivalent commercially as-cast sample (Kormax LLC) using STA 449 Jupiter

(NETZSCH). The mechanically polished sample from *XY* plane (~5 μm surface finish) with a mass of ~200 mg was placed in an alumina crucible pan with a lid and heated to 1200 °C at 10 °C/min.

4.2.2 Cu-1Ti

For Cu-1Ti sample, thin slices from the as-built rectangular bar were cut parallel to the BD (*YZ* plane) for heat treat, microstructural characterisation and hardness test according to Figure 4.3 using an Accutom-50 diamond saw (Struers). Specimens sectioned from the *YZ* plane were prepared for microstructural characterisation and hardness testing. *YZ*-plane specimens were prepared for SEM analysis following the polishing procedure described in Section 4.2.1. A Zeiss Ultra SEM equipped with EDXS and EBSD detectors was used for microstructural analysis with a step size of 1 μm, with EBSD analysis performed using Oxford Instruments' AZtecCrystal 3.0 software as outlined in Section 4.2.1. TEM was conducted using a Themis-Z double-aberration-corrected microscope (Thermo Fisher Scientific), operated at 300 kV and coupled with EDXS detectors. TEM micrographs were analysed with Velox 3.5.0 software. APT was conducted using a CAMECA INVIZO 6000 equipped with a dual 257.5 nm UV laser system (a laser power of 200 pJ and laser pulse rate of 200 kHz) at ~50 K. The APT datasets were reconstructed via CAMECA's AP suite 6.3 software using the 3D reconstruction protocol described in [174], with self-consistent values for the image compression factor of 1.40 and field reduction factor of 4. The TEM and APT specimens were extracted from polished EBSD specimens via standard lift-out techniques [169, 170], as described in Section 4.2.1 , using a Helios G4 PFIB SEM (Thermo Fisher Scientific).

Precipitates were analysed using the protocol developed by [170] and [171]. The search for precipitates was conducted by using the cluster algorithm in CAMECA's IVAS software

with the following parameters applied to the solute element Ti: the distance between solute ions (d_{max}), the number of other solute ions (Order), the minimum number of solute ions in a cluster (N_{min}) [171-173], the distance from each solute ion in a cluster (L) and the distance from ions that are not included in the cluster ($d_{erosion}$). These parameters were optimised according to the method outlined by Williams et al. [174], and the cluster finding approach described in [171] was applied. The value of d_{max} was chosen heuristically by comparing the histogram of nearest neighbour distance distribution (distance between closest solute atoms in 3D space) between the experimental and random labelling data and choosing the distance at which there is the greatest difference from random, an approach similar to [175]. The N_{min} parameter was determined from a comparison of the experimental and random cluster size distribution plots [176], where this value was chosen to be greater than the maximum cluster size given by the random plot. Additionally, a large N_{min} value was chosen to isolate the obviously large features corresponding to precipitates, while effectively filtering out the small features [171]. In Chapter 8, features containing more than 70 atoms are regarded as precipitates. This discrimination was based on stereological comparisons of the volumes and spacing of the precipitates observed in the TEM and the APT 3D atom maps. The sizes and volume fractions precipitates were calculated based on the fraction of clustered atoms in the matrix.

4.2.3 Cu-30Ni

The samples subjected to different heat treatments were prepared using the polishing procedure described in Section 4.2.1, which included mechanical polishing, vibratory polishing (Buehler), and broad Ar-ion surface polishing (PECS II, Gatan). Microstructural characterisation was performed using SEM, EBSD, TEM, and APT following the same

protocols outlined in Section 4.2.1, with the following differences: APT was conducted using a CAMECA INVIZO 6000 equipped with a dual 257.5 nm UV laser system (200 pJ, 200 kHz, ~50 K). APT datasets were reconstructed using AP Suite 6.3 with an image compression factor of 1.40 and field reduction factor of 4.0.

Solute atom clustering and precipitates were analysed using the protocol developed by [170] and [171]. The search for clusters and precipitates was conducted by using the cluster algorithm in CAMECA's IVAS software with the following parameters applied to the solute element Si: d_{max}, Order, N_{min}, L and $d_{erosion}$. These parameters were optimised as mentioned in Section 4.2.2, and the cluster finding approach described in [171] was applied. In Chapter 9, solute aggregations containing less than 200 atoms have been considered as solute nanoclusters, and features containing more than 200 atoms are regarded as precipitates. This discrimination relied on stereological comparisons of the volumes and spacing of the precipitates measured in the TEM and the APT 3D atom maps. The sizes and volume fractions of the clusters and precipitates were quantified based on the fraction of clustered atoms in the matrix.

4.3 Mechanical and electrical property testing

Small-scale Cu-10Sn tensile test samples with gauge lengths, widths, and thicknesses of 10, 2.4, and 2 mm, respectively, were printed as per American Society for Testing and Materials (ASTM) E8 standard [177]. Cu-1Ti tensile specimens with the same gauge dimensions were machined perpendicular to the BD (*XY* plane in Figure 4.3) using electrical discharge machining. The tensile specimens in Chapter 5 were printed in the vertical orientation (*YZ* plane), and tensile tests were performed in the direction parallel to BD at ambient conditions. All tensile specimens in Chapter 6 and 7 were printed in the horizontal

orientation (*XY* plane), and tensile tests were performed in the direction perpendicular to BD at ambient conditions. Tensile test samples were mechanically polished using silicon carbide papers, and each sample underwent three repetitions using an Instron 3366 tensile tester equipped with a clip-on extensometer. For all tensile tests, the crosshead speed was fixed at 0.6 mm/min based on ASTM E8 standards [177].

Ball-on-disc sliding was performed on the Cu-10Sn sample from *XY* plane using a commercial tribometer (NANOVEA-MT/60/NI) to assess the coefficient of friction [178]. Tungsten carbide balls with diameters of 2.38 mm were used, and each test was conducted under 1 N for 30 min at a sliding speed of 0.1 m/s in the air at room temperature. The depth of the wear track was determined to assess the wear resistance of the builds using a LEXT 5000 confocal laser microscope (Olympus).

In Chapter 5, 6, 8, and 9, Vickers hardness tests were also performed on the EBSD polished specimens using a Struers Duramin-40 hardness tester under a load of 1 kg and dwell time of 10 s. These were performed in regions sufficiently far from prior nanoindentations. A minimum distance of 500 µm was maintained between neighbouring indentation points, ensuring the elimination of any influence caused by prior indentations [179]. An average of six indentations per sample was recorded for the Vickers hardness. In Chapter 7, Vickers hardness tests were conducted on the *XY*-plane of the as-built samples using a Struers Durascan-80 automated hardness tester. A load of 0.1 kg was applied with a dwell time of 10 s. To minimise interference of indent deformation zones, the distance between indents was set to 85 µm, equivalent to 2.5 times the Vickers diagonal length (~33 µm), in accordance with ASTM standards E384 [180]. Hardness values were averaged over 121 indents within a square area of 0.85×0.85 mm^2.

Compression tests were performed on Cu-10Sn samples in their as-built condition using an Instron 8852 dynamic testing machine equipped with a 100 kN calibrated load cell. The specimens with dimensions 4 × 8 × 4 mm^3 (*X-Y-Z*, Z is the BD) were cut from as-built sample. The tests for compression were carried out along the horizontal direction (perpendicular to BD) under ambient environmental conditions, setting the rate of the displacement to 2 μm/s.

Differential scanning calorimetry (DSC) was performed on as-built samples and an equivalent commercially as-cast sample (Kormax LLC) using STA 449 Jupiter (NETZSCH). The mechanically polished sample from XY plane (~5 μm surface finish) with a mass of ~200 mg was placed in an alumina crucible pan with a lid and heated to 1200 °C at 10 °C/min.

Electrical resistivity was measured via a linear four-probe technique using a Physical Property Measurement System (Quantum Design). A 99.99% Cu (Metalminotti) with an electrical resistivity of 1.72 × 10^{-8} Ω·m at 20 °C was used as a calibration sample, corresponding to 100.2% IACS. Electrical resistivity of the as-cast (Kormax LLC), LB-PBF Cu-10Sn and LB-DED Cu-1Ti alloys was measured at 20 °C, and their electrical conductivity was calculated by taking the reciprocal of the electrical resistivity to the IACS.

4.4 Thermo-Calc and FLOW-3D Simulations

CALculation of PHAse Diagram (CALPHAD) simulations were performed with Thermo-CALC 2021b and the TCCu4 database to predict solidification conditions for the Cu-10Sn phase, while the precipitate conditions and CALPHAD simulations of Cu-30Ni were predicted using Thermo-Calc 2021b with the TCCU4 database and DICTRA with MOBNI5 database. Additionally, Thermo-Calc 2025a precipitation module with CUDEMO database

was used to predict precipitation Cu-1Ti alloy. Computational fluid dynamics (CFD) simulations of the powder printing process were conducted using FLOW-3D AM (release 7, update 3, Flow Science). Detailed parameter models, including the powder settling, powder spreading, melt and solidification, are described in the Appendix A.

4.5 Density functional theory (DFT) calculations

In Chapter 9, DFT calculations employed the generalised gradient approximation [181] and the projector augmented-wave method [182] in the Vienna Ab initio Simulation Package (VASP) [183]. A cutoff energy for plane-wave basis sets of 500 eV was applied. The $4s^1 3d^{10}$, $3d^8 4s^2$, $3s^2 3p^2$ and $4s^2 4p^6 5s^1 4d^4$ electrons were treated as valence electrons for Cu, Ni, Si, and Nb, respectively. The algorithm used for ionic relaxation was the conjugate gradient algorithm. The Monkhorst-Pack k-points were meshed by 3 × 3 × 3 for the 256-atom ($4a$ × $4a$ × $4a$) a-Cu supercell. Atomic relaxation was allowed until the forces converged to less than 0.1 eV/nm. Solute diffusivity was evaluated via *ab initio* molecular dynamic (AIMD) simulations using a 500-atom supercell, containing 5 Ni, 5 Si and 5 Nb atoms, with a time step of 2 fs in the canonical ensemble. Using the Nose-Hoover thermostat [184] the temperature was controlled at 427 °C and 627 °C, separately.

Chapter 5 Influence of Scan Strategy on Microstructural Evolution and Mechanical Properties of Cu-10Sn Manufactured by Laser Beam Powder Bed Fusion

This chapter addresses Aim 1 by exploring printing parameters and scan strategy as a tool for microstructural engineering in LB-PBF Cu-10Sn. Cu-10Sn are widely employed in applications where wear resistance, mechanical reliability, and structural integrity are of primary importance, including bearings, bushings, and marine components. Optimising printing parameters is essential to achieve high-density, defect-minimised builds suitable for subsequent microstructural and property evaluation. By evaluating a set of scan strategies under constant optimised printing parameters, this study focuses on how variations in scan path affect melt pool morphology, grain structure, and ultimately mechanical properties. The findings will provide essential insights into the microstructure–property relationships governed by scan strategy in Cu-10Sn and offer practical guidance for tuning both strength and formability in future high-performance components.

5.1 Results

5.1.1 Printing parameter sweep

A systematic parameter sweep was conducted by varying laser power, P (95 W, 145 W, and 195 W) and scan speed, s (between 360 and 860 mm/s). Figure 5.1a, b, and c show the band contrast in the YZ planes of the Cu-10Sn parts as functions of P and s. The

corresponding volume energy densities (VEDs) ranged from 120 to 140 J/mm³, calculated using the relation [185]:

$$VED = \frac{P}{s \cdot t \cdot h}$$

In Figure 5.1d, it is evident that increasing *P* can effectively enhance the density of the samples, despite a decrease in density observed when the VED and *P* are set at 140 J/mm^3 and 195 W. Figure 5.1e demonstrates the dependence of relative density on VED for different *P*. At *P* = 95 W, the density initially increases with VED, reaches a maximum, and then decreases. At *P* = 145 W, the density increases over the VED range examined. At *P* = 195 W, the density decreases with increasing VED. To map the process window, an additional set of samples was built across a broadened parameter space. The relative density of the LB-PBF Cu-10Sn samples was measured using the Archimedes method. Each scan strategy was repeated three times (n = 3), and the results are reported as the mean density with standard deviation, as summarised in Table 5.1. The measured densities of these samples are presented in Figure 5.1f, showing a bell-shaped dependence on VED, bounded by lack of fusion porosity at low VED [186-188] and keyholing at high VED [189, 190].

At *P* = 95 W, samples #A, #B, and #C have densities under 97.5% and show an evident lack of fusion defects (hexagons in Figure 5.1a). However, at 145 W, all samples surpassed 97.5% density. Notably, #F has a higher density than #D and #E, and reveals smaller, circular gas pores (circles in Figure 5.1c). This indicates a shift from lack of fusion to a transitional state, and then to keyhole formation with increasing laser energy, consistent with observations reported in [191]. At 195 W, #G achieves an impressive density of over 99.9%. The band contrast images show more trapped gas pores with increased energy, marking a progression to the keyhole state of melting.

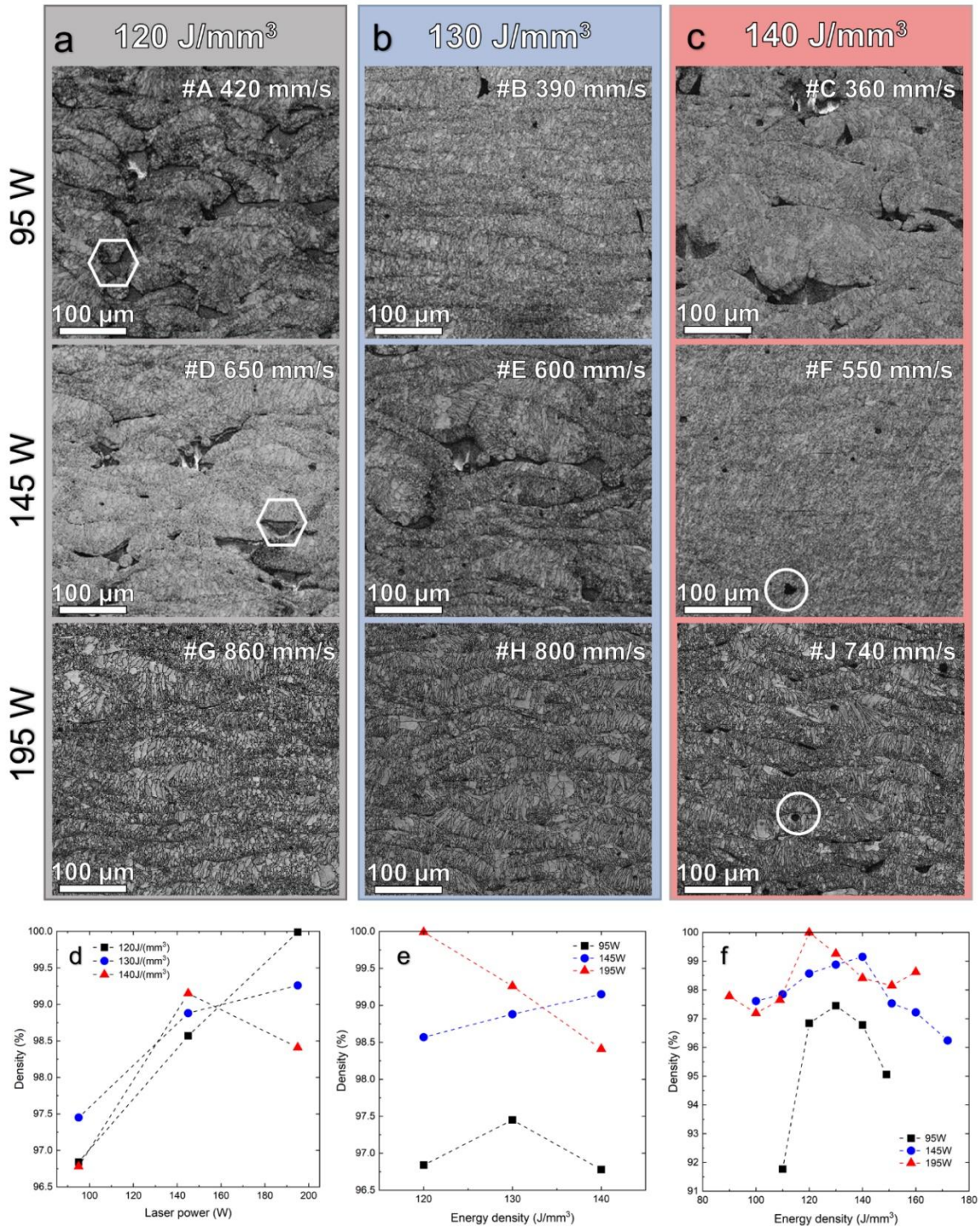

Figure 5.1: Relative density analysis of the as-built Cu-10Sn samples. Band contrast images of as-built samples as a function of volume energy density (VED) (a) 120 J/mm3, (b)130 J/mm3, and (c) 140 J/mm3; relative density of as-built samples as a function of laser power (d) and VED (e); (f) relative density of as-built samples with enlarged parameter window. The lack of fusion defects were marked by hexagons, and the gas pores were marked by circles.

Consequently, a *P* of 195 W and *s* of 860 mm/s with a standard scan strategy led to the highest material density of 99.90 ± 0.07%, as measured by using Archimedes' principle. Accordingly, an identical, optimised processing parameters was employed for the samples presented in Chapters 5, 6 and 7.

Table 5.1: The relative density of as-built LB-PBF Cu-10Sn samples.

Sample	Relative density (%)
A	96.84 ± 0.12
B	97.45 ± 0.07
C	96.78 ± 0.07
D	98.56 ± 0.19
E	98.88 ± 0.09
F	99.15 ± 0.03
G	99.93 ± 0.07
H	99.26 ± 0.11
J	98.41 ± 0.06

5.1.2 Density and surface morphology

Relative density and surface morphology of the LB-PBF Cu-10Sn specimens built with four different scan strategies are presented in this section. Among them, UA-scan specimen exhibits the highest densification at 99.98%, followed by IS-scan, SA-scan, and IA-scan with densification of 99.28%, 98.97%, and 98.87%, respectively.

The 3D surface morphology of LB-PBF Cu-10Sn samples under different scan strategies is illustrated in Figure 5.2. UA-scan strategy (Figure 5.2a) shows the smoothest surface with a surface roughness (Sa) of 8.74 μm, while the SA, IA, and IS-scan strategies exhibit higher Sa values of 12.73 μm, 13.81 μm, and 13.34 μm, respectively (Figure 5.2b–d).

Notably, island-based strategies tend to generate more irregular and coarser topographies, consistent with their higher Sa values.

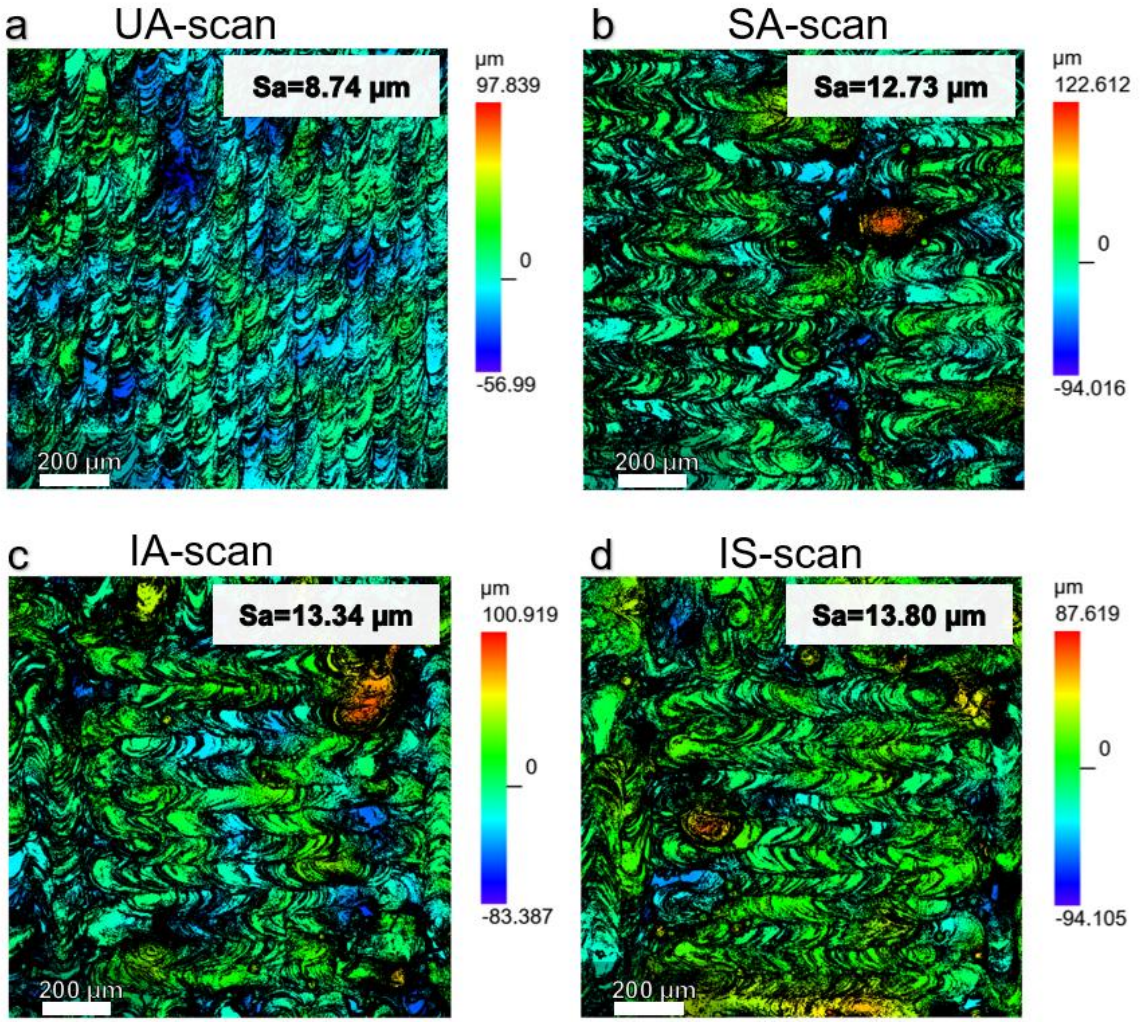

Figure 5.2: Surface morphology of LB-PBF Cu-10Sn under different scan strategies. Surface roughness (Sa) is shown for each sample.

5.1.3 Melt pool and microstructural analysis

The SEM images in Figure 5.3 show the top-surface (*XY* plane) melt pool morphologies for specimens processed with four different scan strategies. In the UA-scan (Figure 5.3a), the melt pools are densely packed with regular, continuous semicircular tracks aligned along a single direction. The SA-scan (Figure 5.3b) exhibits melt pools with clearly defined

boundaries and visible lap regions between adjacent scan tracks. The IA-scan (Figure 5.3c) shows segmented melt pool structures within well-defined island boundaries, along with evident overlapping regions where defects are concentrated. In the IS-scan (Figure 5.3d), the melt pool morphology features alternating patterns within each island, with inner and outer boundaries aligned in different directions. Compared to IA-scan, fewer defects are observed at island boundaries, suggesting partial remelting of the underlying layer due to the shifted pattern. However, the new layer still contains irregularities, and the melt pool boundaries appear less distinct.

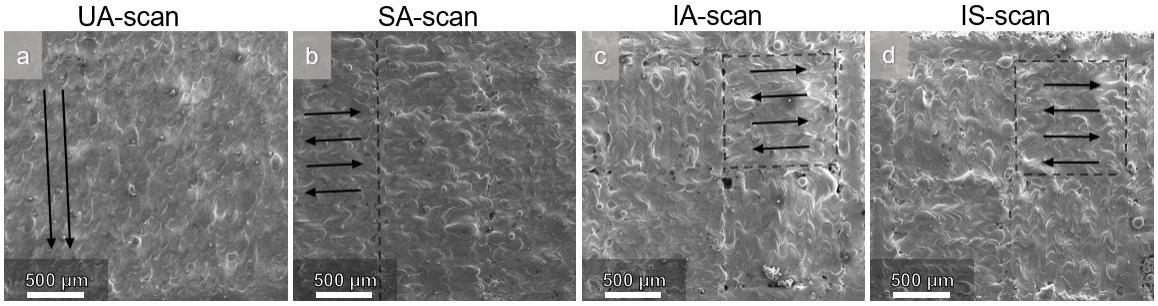

Figure 5.3: SEM images demonstrating the top-surface melt pools of LB-PBF Cu-10Sn processed with different scan strategies, where the laser scan directions are indicated by black arrow, and boundaries of the scan pattern are indicated by black dash line.

The EBSD IPF maps (*YZ* plane) in Figure 5.4 (a1–d1) reveal distinct melt pool morphologies associated with each scan strategy. The UA-scan exhibits shallow, closely spaced, and uniformly overlapping melt pools, forming a regular fish-scale pattern that promotes fine, equiaxed grains. In contrast, the SA-scan shows deeper, arc-shaped melt pools with wider spacing. The IA-scan presents segmented, island-confined melt pools with inward-curved boundaries. The IS-scan features dual-boundary melt pools within each island. Fragmented grain structures with a mix of columnar and finer grains near island edges can also be observed. These variations in melt pool geometry strongly influence grain

morphology and reflect the complex thermal dynamics imposed by each scan strategy, discussed further in Section 5.2.2.

The grain boundary character maps (Figure 5.4 (a2–d2)) distinguish between low-angle grain boundaries (LAGBs, $2° < \theta < 15°$; blue) and high-angle grain boundaries (HAGBs, $\theta > 15°$; red), revealing differences in boundary networks across the four scan strategies. The UA-scan sample (a2) exhibits the lowest HAGB fraction at 77.2%, indicating a comparatively lower degree of grain subdivision and potential for dislocation accumulation. In contrast, the SA-scan (b2), IA-scan (c2), and IS-scan (d2) samples show higher HAGB fractions of 81.6%, 81.7%, and 81.3%, respectively. Among these, the IA-scan sample displays the most disrupted grain boundary network, particularly near the island boundaries.

The grain size distributions (Figure 5.4 (a3–d3)) confirm the impact of scan strategy on microstructural refinement. The UA-scan sample shows the finest grains with a mean grain size of 3.18 μm, followed closely by the IS-scan (3.28 μm). In contrast, the IA-scan and SA-scan samples exhibit slightly coarser average grain sizes of 3.74 μm and 3.47 μm, respectively. The broader tail in the IA-scan histogram shows the presence of larger, columnar grains.

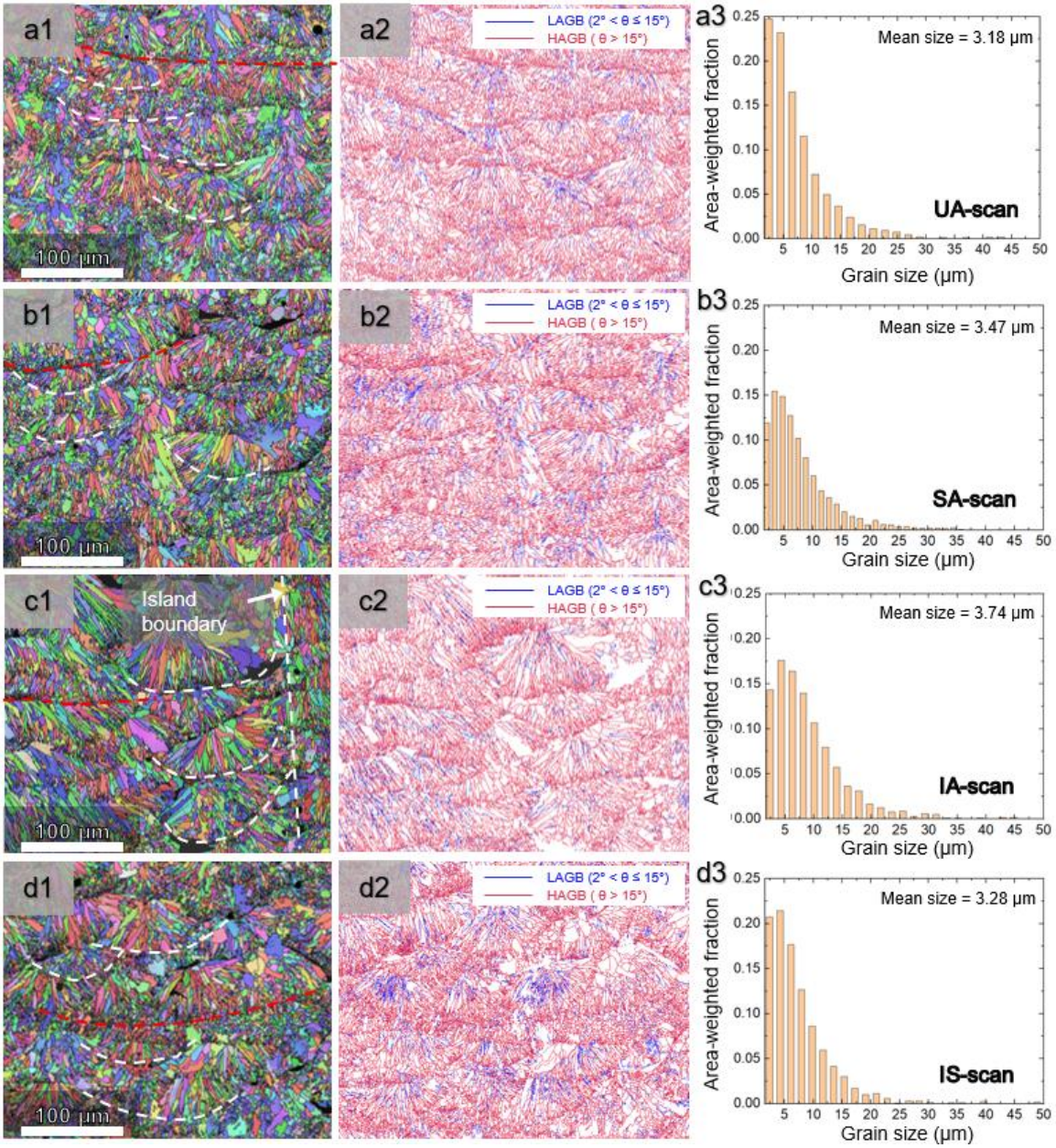

Figure 5.4: EBSD results showing melt pool morphology, grain boundary character and grain size distribution of LB-PBF Cu-10Sn alloy processed with (a1-3) UA-scan strategy, (b1–3) Sa-scan strategy, (c1–3) IA-scan strategy, and (d1–3) IS-scan strategy. Selected melt pool boundaries associated with the laser scanning tracks in the Y direction are highlighted with white dashed lines and the melt pools formed during scanning in the X direction are highlighted with red dashed lines.

To further characterise the microstructure features, Figure 5.5 presents EBSD IPF maps and corresponding pole figures, which reveal noticeable differences in crystallographic texture. Among the four samples, UA-scan condition exhibits the highest texture intensity among the scan strategies studied, showing a <100> fibre texture approximately parallel to the BD,

as indicated by the concentration in the {100} pole figure with a maximum intensity of 1.31. This result suggests a relatively higher degree of crystallographic alignment compared with the other scanning conditions. In comparison, SA-scan and IA-scan samples still maintain a moderate <100> fibre texture but with slightly decreased intensity (1.16 and 1.26, respectively). IS-scan sample, however, exhibits the weakest texture overall, with a highly dispersed pole figure, indicating minimal preferred orientation. Thus, varying the scan strategy significantly influences the resulting crystallographic texture, ranging from strong <100> fibre texture alignment to nearly random grain orientation distributions. It should be noted that the EBSD texture analysis presented here was conducted on bulk samples rather than the tensile specimens themselves. Although the overall scan strategy is identical, slight differences in thermal conditions may occur due to the smaller scanning length of the tensile specimens. Future work could examine the texture directly within tensile specimens to further clarify the relationship between scan strategy, texture, and mechanical properties.

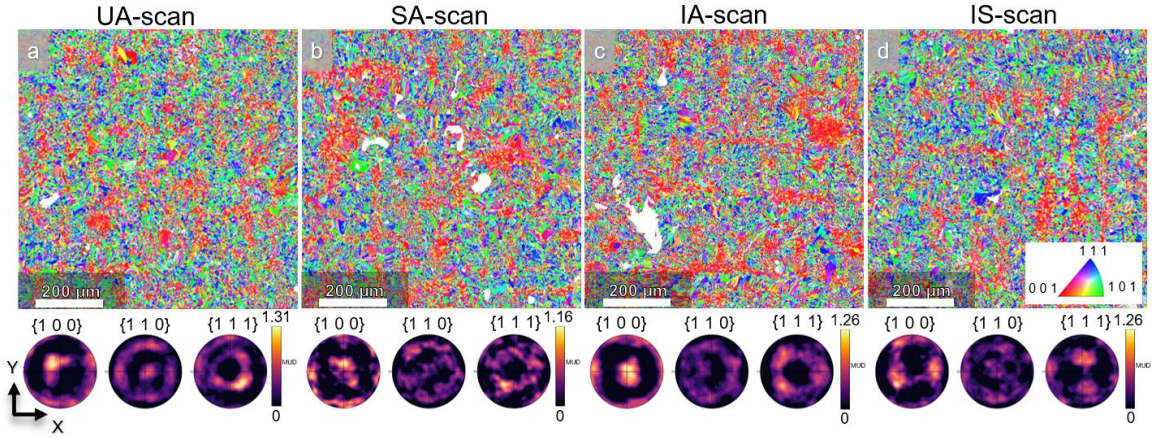

Figure 5.5: The EBSD IPF maps and corresponding pole figures showing texture of LB-PBF Cu-10Sn alloy processed with different scan strategies.

5.1.4 Mechanical performance under various scan strategies

Figure 5.6 presents the engineering stress–strain curves for LB-PBF Cu-10Sn samples produced using four different scan strategies. The corresponding tensile properties and hardness values are summarised in Table 5.2. The results indicate that the mechanical properties are broadly comparable across the different scan strategies, with minor variations observed in strength, hardness, and ductility. The UA-scan sample demonstrates a YS of 408 MPa, an UTS of 512 MPa, and the highest hardness value of 175 ± 10.0 HV_1. The SA-scan sample shows comparable strength (YS: 412 MPa, UTS: 514 MPa) with a slightly lower hardness of 167 ± 4.0 HV_1. The IS-scan sample exhibits a YS of 410 MPa and a hardness of 167 ± 13.2 HV_1, but its UTS decreases to 497 MPa, indicating a moderate drop in tensile strength compared to UA-scan and SA-scan samples. In contrast, the IA-scan sample shows the lowest strength (YS: 399 MPa, UTS: 493 MPa) and the lowest hardness of 156 ± 5.7 HV_1. Despite these variations, all four samples display similar ductility, with elongation at fracture ranging from 9.3% to 10.4%.

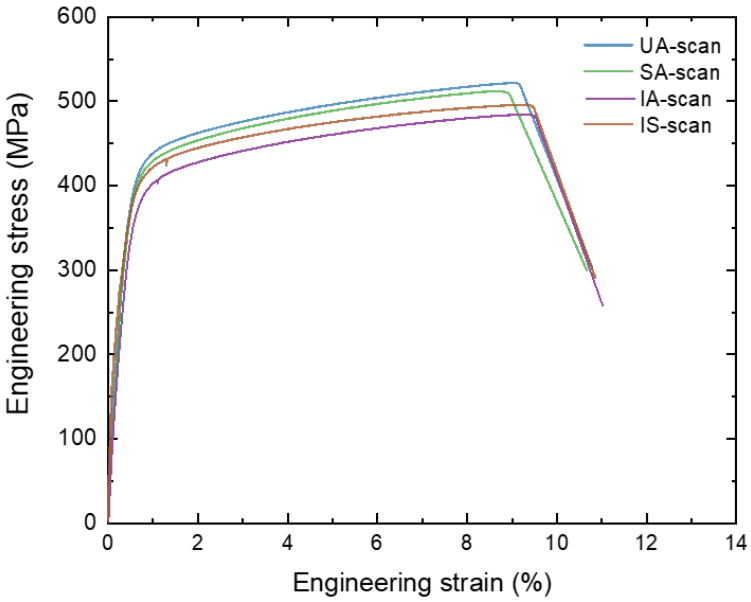

Figure 5.6: The representative tensile stress-strain curves of LB-PBF Cu-10Sn alloy processed with various scan strategies.

Table 5.2: Summary of yield strength, ultimate tensile strength, ductility and Vickers hardness for LB-PBF Cu-10Sn samples in Figure 5.6.

Sample	YS (MPa)	UTS (MPa)	Elongation (%)	Vickers Hardness (HV_1)
UA-scan	408 ± 4	512 ± 14	9.4 ± 1.5	175 ± 10.0
SA-scan	412 ± 5	514 ± 9	9.3 ± 0.5	167 ± 4.0
IA-scan	399 ± 2	493 ± 8	10.4 ± 0.8	156 ± 5.7
IS-scan	410 ± 5	497 ± 4	9.8 ± 1.5	167 ± 13.2

5.1.5 Fractography

The tensile fracture surfaces of the Cu-10Sn samples were examined using SEM, as shown in Figure 5.7. All samples exhibit ductile fracture characteristics with dimple features, though notable differences are observed among them. UA-scan sample shows micro-cracks and small dimples; while SA-scan sample is dominated by dimples, some unmelted regions and macro-cracks can be observed. In contrast, IA and IS-scan samples contain macro-cracks, unmelted particles, and striations around the macro-cracks.

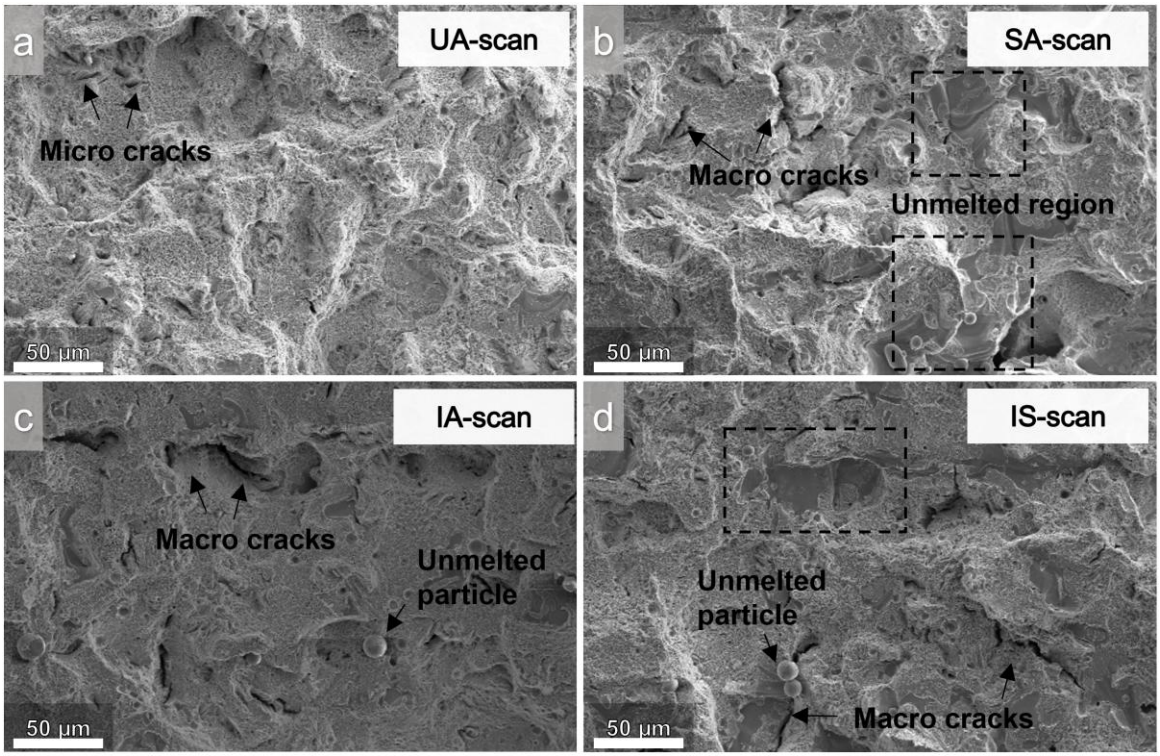

Figure 5.7: Fracture surface morphology of LB-PBF Cu-10Sn samples with different scan strategies. The cracks and unmelted particles are indicated by arrows, and the unmelted regions are marked with squares.

5.2 Discussion

5.2.1 Influence of laser scan strategy on defects of LB-PBF Cu-10Sn

The laser scan strategy directly impacts the thermal history, melt pool behaviour and solidification, which in turn influence the formation of defects, including pores, lack of fusion defects, and uneven remelting. In this study, the relative densities across all strategies remain within a narrow range; however, notable differences in defect distribution and density were observed among specimens fabricated using four distinct scan strategies.

The UA-scan strategy produced the highest densification, with minimal porosity or cracking. This can be attributed to the continuous scanning path, which maintains a stable melt pool, uniform thermal gradients, and consistent layer remelting, thereby suppressing the surface roughness, lack-of-fusion pores and reducing crack initiation. Similar effects of

uninterrupted scanning in promoting densification and microstructural homogeneity have been reported in Al alloys [192]. In contrast, the IA-scan strategy resulted in the poorest densification, exhibiting the highest concentration of lack-of-fusion defects, particularly along island boundaries. The segmented nature of the island pattern causes each region to experience independent thermal cycles, leading to inconsistent heat distribution, which may promote surface undulations and the accumulation of balling defects [193, 194]. The overlap zones between islands, subjected to repeated and differently oriented thermal inputs, undergo non-uniform melting and rapid solidification, which often results in poor bonding and increased surface roughness, and promotes gas pore formation [195]. The SA-scan strategy showed moderate porosity levels, with defects mainly concentrated along the boundaries between adjacent stripe bands. Although this strategy offers more continuous scanning than the island pattern, the presence of stripe overlap regions introduces areas of variable remelting and uneven thermal gradients. This can result in incomplete fusion, localised porosity, and increased surface roughness, though to a lesser extent than in the IA-scan. The IS-scan strategy, which incorporates a layer-wise lateral shift of island positions, demonstrated an improvement in densification relative to the unshifted IA-scan. This configuration allows partial remelting of the previous layer's island edges, enhancing inter-island bonding and reducing the density of boundary-related defects. However, while the overall porosity and crack density were lower than IA-scan, some residual defects originating from previous layers, such as lack-of-fusion defects and partially melted regions, still persisted in the microstructure, though a portion of them was remelted during subsequent laser passes.

These findings highlight the critical influence of scan strategy on relative density and surface roughness, where complex or discontinuous scanning paths increase the likelihood of defects. While strategies such as island scanning have the potential to reduce residual

stresses and warping [196, 197], they may also introduce additional defects if not optimised for the specific thermal and material behaviour of the alloy system. For Cu-10Sn, scan strategies promoting uniform energy input and consistent remelting, such as UA-scan, are more effective in minimising defect formation and achieving high-density builds.

5.2.2 Influence of laser scan strategy on the microstructure of LB-PBF Cu-10Sn

The chosen laser scan strategy sets the melt pool geometry, thermal gradient distribution, and solidification behaviour in LB-PBF Cu-10Sn, thereby dictating the resultant microstructural features such as grain morphology, grain boundary character, and crystallographic texture.

The UA-scan strategy generated shallow, regularly overlapping melt pools with uniform fish-scale patterns, reflecting stable heat flow and directional solidification. This configuration promotes rapid, uniform cooling and a high degree of epitaxial grain growth along the BD, yielding fine equiaxed grains in the overlap regions and a relatively low mean grain size (3.18 μm). The high uniformity of heat flow also explains the relatively lower HAGB fraction (77.2%), as fewer interruptions to columnar growth occur. These findings are consistent with prior reports in Cu-Cr-Zr and Al-Li alloys [198, 199], where continuous scan paths maintained a strong thermal gradient aligned with the preferred <100> growth direction, thereby producing strong textures and fine grain structures.

In contrast, the IA-scan strategy generated segmented, island-confined melt pools with pronounced curvature at island boundaries (Figure 5.4). The localised heat accumulation within each island altered the G/R ratio, encouraging competitive grain growth and coarser columnar structures, reflected in the largest mean grain size (3.74 μm) and the highest

HAGB fraction (81.7%). The locally higher heat accumulation may cause more pronounced lack-of-fusion defects, as shown in Figure 5.3 and 5.4, along island boundaries due to incomplete overlap and uneven remelting. The pole figures reveal a moderate <100> fibre texture with reduced intensity relative to UA-scan, indicative of more isotropic grain orientations arising from frequent disruption of epitaxial growth. Similar phenomena have been observed in island-scanned Inconel 718 and stainless steel [103, 200], where scattered thermal gradient vectors in non-epitaxial solidification regions weakened texture and increased HAGB density, thereby promoting microstructural heterogeneity.

The SA-scan strategy, employing long stripe bands, exhibited intermediate behaviour. Melt pools were deeper and more widely spaced than in UA-scan, indicating higher energy input and directional heat flow, which leads to more elongated grains (Figure 5.4). With clear lap regions between stripes, these overlapping zones experienced variable remelting and altered local cooling rates, producing slightly coarser grains (3.47 μm) and a higher HAGB fraction (81.6%) compared to UA-scan. The texture intensity was weaker than UA-scan but stronger than IA-scan, reflecting partial retention of directional solidification in stripe interiors, disrupted primarily at stripe boundaries.

The IS-scan strategy offered partial improvement over the unshifted island approach. By laterally offsetting islands in successive layers, partial remelting of boundary regions occurred, leading to finer grains (3.28 μm) than IA-scan and a modest reduction in texture disruption. Nevertheless, the presence of dual-boundary melt pool patterns, caused by the shifted scan pattern between layers, still introduced irregularities and lowered texture intensity relative to UA-scan. Similar improvements in grain refinement and texture alignment through shifted island scans have been reported in Al-Li [198] and IN738LC alloy [105], attributed to enhanced inter-island bonding and reduced localised heat accumulation.

Crystallographic texture analysis indicates that the UA-scan condition exhibits the highest pole figure intensity among the scan strategies studied. The orientation distribution is consistent with a <100>-type fibre that is approximately aligned with the build direction (BD), but with a slight deviation from BD as observed in Fig. 5.5; therefore, the present results support stronger crystallographic concentration rather than strictly stronger <001> alignment along BD. The intensity decreases progressively in SA-scan, IA-scan, and IS-scan, paralleling the increase in thermal gradient misalignment and grain orientation scattering. As observed in previous alloy systems [105, 201], frequent changes in scan vector direction and discontinuous melt pool formation disrupt the competitive growth of favourably oriented grains, promoting randomly oriented grains and weakening the overall texture. The slight deviation of the {100} poles from the build direction (BD) is attributed to the asymmetric melt pool geometry produced by unidirectional laser scanning. The resulting tilt of the local thermal gradient towards the downstream scanning direction causes epitaxial grain growth to align slightly away from BD, consistent with the EBSD observations in Fig. 5.5.

5.2.3 Influence of laser scan strategy on mechanical properties of LB-PBF Cu-10Sn

The laser scan strategy affects the mechanical performance of LB-PBF Cu-10Sn by altering densification behaviour, defect distribution, and microstructural characteristics. In this study, the four investigated strategies produced comparable ductility values (9.3–10.4%), but showed variations in strength and hardness, reflecting the dominant influence of defect content and grain morphology on strength-related properties.

The UA-scan strategy achieved the highest overall mechanical performance, combining a UTS of 512 MPa, YS of 408 MPa, and the highest hardness (175 HV_1). This superior strength is consistent with its highest relative density, minimal porosity, and fine grains. The low defect content minimises stress concentration sites, while the finer grains contribute to strength through grain boundary strengthening. The SA-scan specimen displayed mechanical properties close to those of UA-scan (UTS 514 MPa, YS 412 MPa) but with a lower hardness (167 HV_1). The slightly reduced hardness is primarily attributed to the marginally coarser grains (3.47 μm) and the presence of localised defects at stripe overlap regions, which can partially offset grain boundary strengthening effects. Defects were more localised at stripe overlap regions, where incomplete fusion occasionally occurred. While the mechanical performance remains competitive, the presence of these defects slightly reduces the load-bearing cross-section, preventing further strength gains. The IS-scan strategy exhibited intermediate performance (YS 410 MPa, UTS 497 MPa, hardness 167 HV_1). Although the shifted island arrangement improved densification relative to IA-scan and promoted grain refinement compared to unshifted islands, residual boundary-related defects persisted.

The IA-scan strategy recorded the lowest strength (YS 399 MPa, UTS 493 MPa) and hardness (156 HV_1), despite having ductility slightly higher than the other strategies. The reduced strength is directly correlated with the highest defect content, particularly lack-of-fusion defects and boundary cracks concentrated along island interfaces. These features act as microstructural weak points that initiate premature fracture under tensile loading. The coarser columnar grains further diminish strength by reducing grain boundary strengthening.

Notably, the ductility values across all strategies remain in a narrow range (9.3–10.4%), suggesting that the modest differences in grain boundary character and texture do not

significantly alter the alloy's capacity for plastic deformation in the as-built state. Although defects such as cracks, unmelted powders, and lack of fusion are generally expected to reduce ductility by serving as stress concentrators, their influence in this study appears muted. This likely reflects the fact that the overall defect content at the achieved densification levels (> 98.80%) is below a critical threshold where elongation would be strongly compromised. In this way, while defects and grain morphology strongly affect strength and hardness, their contribution to ductility is comparatively minor. This behaviour differs from observations in some LB-PBF Ni-based superalloys [202, 203], where ductility has been reported to vary more strongly with processing-induced microstructural changes, including variations in texture and grain structure, but aligns with previous findings in high-conductivity Cu alloys [199], where strength is more sensitive than elongation to variations in defect content and microstructural refinement.

5.3 Summary and Processing Recommendations

This study systematically explored the influence of printing parameters and laser scan strategy on the densification, microstructure, and mechanical performance of LB-PBF Cu-10Sn. Through a parameter sweep, the optimal processing window was identified at 195 W laser power and 860 mm/s scan speed, yielding a maximum relative density of 99.90 ± 0.07%, which was adopted for all subsequent builds. Within this optimised condition, different scanning approaches were compared, showing that the choice of scan path strongly influences defect distribution, microstructural evolution, and mechanical performance, even when relative densities remain high.

Overall, continuous and uniform energy input proved most effective in producing high strength, hardness, and surface quality. Such conditions typically promote strong

crystallographic textures; however, in this study the resulting texture intensity remained relatively low. Importantly, ductility was found to be relatively insensitive to processing variations, reflecting the robust plastic response of the alloy once a critical densification level is achieved.

Processing recommendations:

(1) Maintain processing within the identified optimal energy density window to balance the high thermal conductivity of Cu, which rapidly dissipates heat and can otherwise lead to insufficient melt pool stability and lack-of-fusion defects at low energy input.
(2) Prioritise scan strategies that promote stable melt pool formation and consistent remelting, which is particularly important for Cu alloys due to their rapid heat conduction and the resulting sensitivity of melt pool geometry to local energy input.
(3) Avoid overly complex or discontinuous scan patterns that may disrupt directional heat flow and epitaxial grain growth in Cu alloys, as frequent changes in scanning direction can amplify thermal gradient fluctuations and increase the likelihood of defect formation.

In summary, careful control of printing parameters and energy input pathways is critical for achieving defect-minimised, high-performance LB-PBF Cu-10Sn components, while the relatively low texture observed here suggests additional processing flexibility for balancing strength, conductivity, and formability in future applications.

Chapter 6 Formation Mechanisms of Sn-rich δ phase and its Role in Strengthening Cu-10Sn Manufactured by Laser Beam Powder Bed Fusion

Aim 2 seeks to clarify the formation and strengthening mechanisms of the Sn-rich δ phase in LB-PBF Cu-10Sn. To address this aim, the properties of the Sn-rich δ phase in LB-PBF Cu-10Sn are investigated via a suite of multi-scale microscopy and microanalysis techniques. Mechanical properties, including tensile and compression strength, hardness, and wear resistance, were measured and correlated with detailed microstructural analyses. The investigation reveals new observations of the existence of two types of δ phase, each with a distinct size range, morphology, and dispersion. These variations are attributed to the unique rapid solidification conditions occurring at the boundary and the interior of the melt pools formed during LB-PBF. Moreover, the findings shed light on the transformation pathway of Sn-rich metastable phase to δ during cyclic heating inherent in LB-PBF Cu-10Sn. To elucidate the thermal conditions governing phase evolution during LB-PBF processing of Cu-10Sn, numerical simulations were conducted using FLOW-3D. The simulations provide insight into the spatial and temporal temperature distributions within the melt pool and surrounding heat-affected zones, thereby quantifying the cyclic heating and cooling histories experienced during layer-by-layer fabrication. The significance of the findings on the phase formation mechanism, particularly the identification of two distinct types of Sn-rich δ phase, advances the understanding of microstructural engineering in AM Cu-Sn alloys, thereby enabling the optimisation of mechanical properties in applications across the automotive, aerospace, and machinery industries.

6.1 Results

6.1.1 Mechanical and electrical properties

Figure 6.1a provides a representative engineering stress–strain curve of the LB-PBF Cu-10Sn using the S-scan (standard scan strategy, defined in Section 4.1.1.2) with the optimised printing parameters defined in Chapter 5. The sample exhibits a YS of 422 ± 7 MPa and UTS of 521 ± 2 MPa with a total elongation to fracture of 7.2 ± 0.4%. Figure 6.1b shows a compression stress–strain curve, showing a compressive YS of 414 ± 7 MPa and a compressive strength higher than 750 MPa at a strain level of ~25%. The present LB-PBF Cu-10Sn demonstrates superior YS as compared to the previously reported properties for LB-PBF Cu, LB-PBF Cu-10Sn, and conventional cast Cu-10Sn, as shown in Figure 6.1c [45, 63, 106, 107, 110, 204-212]. Based on the manufacturer's data, the commercial as-cast Cu-10Sn shows a YS of 170 MPa and elongation to the fracture of 10%. The YS of LB-PBF Cu-10Sn increases by approximately 148% compared to conventionally cast Cu-10Sn alloys. The average Vickers hardness is measured as 172.4 ± 1.5 HV_1 (Table 6.1), which is demonstrably harder by 22% than conventionally cast Cu-10Sn alloys, and 8% than those values of LB-PBF Cu-10Sn reported in previous studies [106, 211]. Figure 6.1d shows the cross-sectional profiles of the wear tracks for the as-built and as-cast samples. The wear track depth of the as-built sample (~0.5 μm) was ~four times shallower than that of the as-cast sample (~2 μm). The coefficient of friction (COF) for the as-built sample reached a steady state of 0.4 after 5 minutes. In contrast, the COF for the as-cast sample increased to 0.6 and then decreased to 0.3 over a period of 15 minutes (Figure 6.2). The IACS of the LB-PBF Cu-10Sn was measured to be 9.7%, similar to that of the as-cast Cu-10Sn (10.3%, also in [59]).

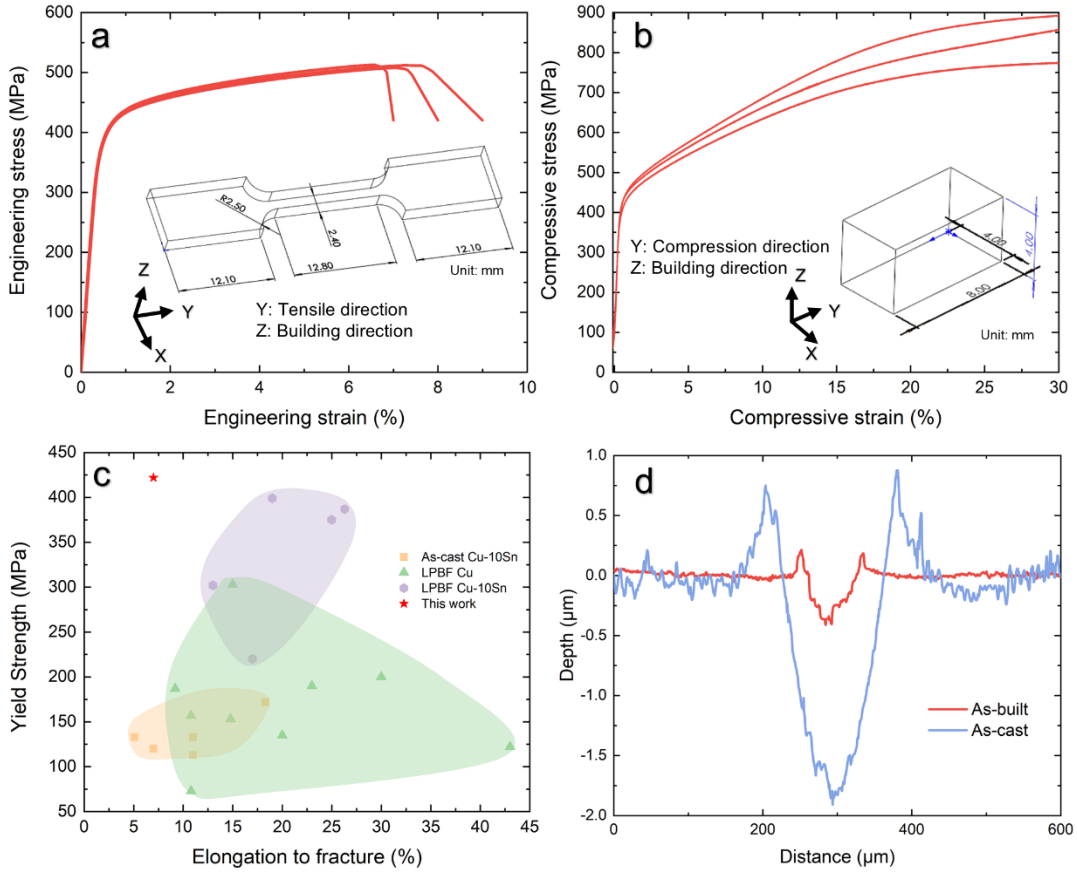

Figure 6.1: Mechanical properties of LB-PBF Cu-10Sn sample. (a) stress–strain curve obtained from uniaxial tensile testing; (b) stress–strain curve obtained from compression testing; (c) comparison of the tensile yield strength of the present as-built Cu-10Sn alloy studied in this work compared to results from previous reports [45, 63, 106, 107, 110, 204-212]; and (d) wear track dimensions of the as-built sample as compared to that of the as-cast sample.

Table 6.1: Hardness of as-built LB-PBF Cu-10Sn in this study compared with values from other studies and as-cast sample.

Sample	Vickers Hardness (HV_1)
As-built in this study	172.4 ± 1.5
As-cast in this study	140.8 ± 2.8
LB-PBF Cu-10Sn [106]	158.2 ± 2.4
LB-PBF Cu-10Sn [211]	159.8

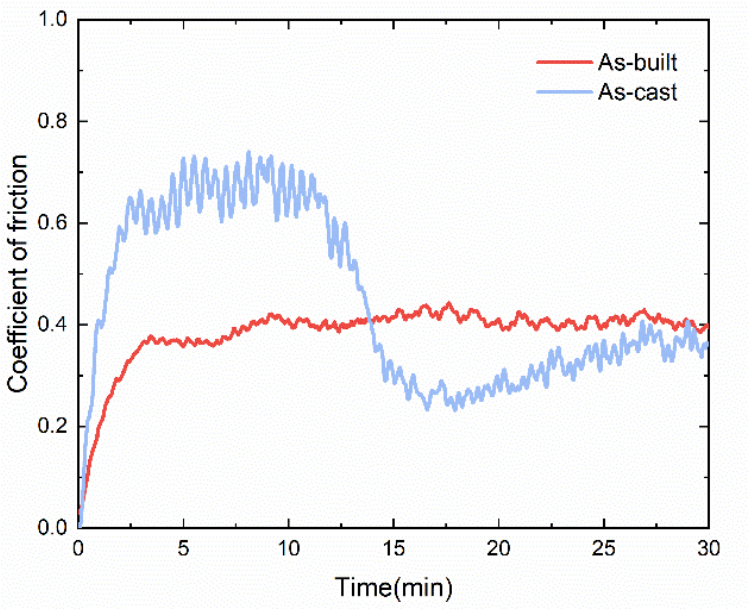

Figure 6.2: Coefficient of friction of as-built samples compared with as-cast sample.

6.1.2 Microstructural analysis

Figure 6.3 shows the representative microstructural information of the as-built LB-PBF Cu-10Sn. SEM and optical micrographs depict the top layer (Figure 6.3a) and the cross-section of the as-built sample (Figure 6.3b), respectively, showing a typical melt pool profile. Figure 6.3c shows the cross-sectional crystallographic analysis of the as-built sample. In the EBSD IPF map, columnar grains were observed along the BD. These grains originate from the melt pool boundaries (indicated by white dashed lines), and their epitaxial growth toward the melt pool centres is evident. Furthermore, smaller equiaxed grains with diameters less than 3.5 µm are decorating melt pool boundaries, common in LB-PBF alloys [213, 214]. Based on the EBSD results, the mean grain size was estimated to be 4.9 ± 2.3 µm. The comparative examination of the as-cast sample in Figure 6.3d reveals that it possesses much larger grains (> 200 µm). The IPF map of the as-built sample (Figure 6.3c) was decorated with randomly oriented grains indicating an absence of a prominent texture.

This was further supported by the low texture intensity in the BD observed in the pole figure (PF) (Figure 6.3e).

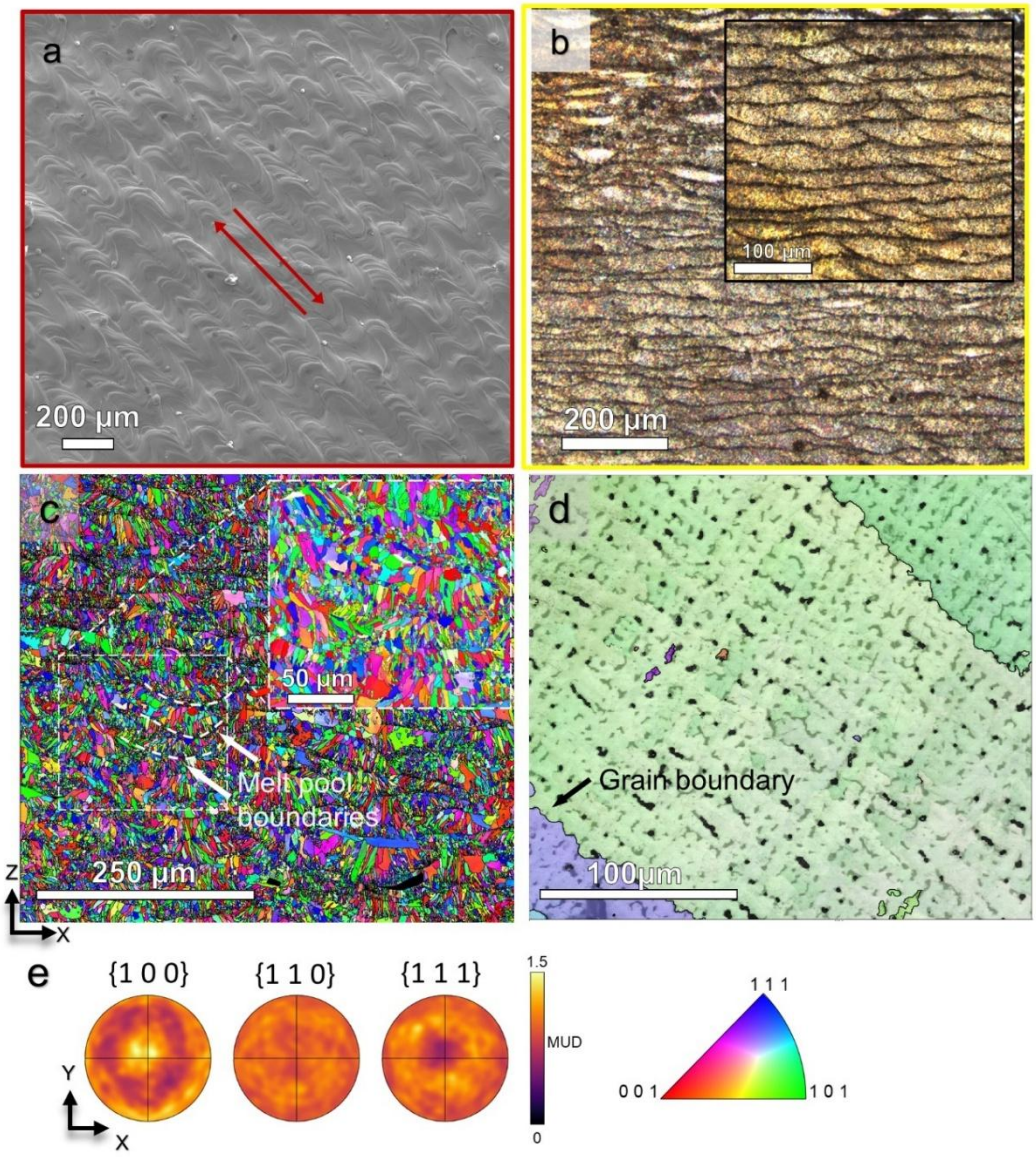

Figure 6.3: Microstructural information of the as-built Cu-10Sn sample (P: 195 W and s: 860 mm/s) and as-cast sample. (a) SEM image demonstrating the melt pool at the top layer, where the laser scan directions are indicated by red arrows; (b) optical micrograph with a high magnification inset depicting the melt pool of the as-built sample in the YZ plane; (c) EBSD IPF map of the as-built LB-PBF sample along the BD with a high magnification inset; (d) EBSD IPF map of the as-cast sample; and (e) pole figures corresponding to the IPF maps in (c).

To further rationalise the observed hardness variations, the microstructures of the as-built sample were examined using XRD and EBSD. The XRD results verified the existence of

two distinct solid solutions of FCC α(Cu): α1 (a = 0.366 nm) and α2 (a = 0.369 nm) as well as the δ phase (Figure 6.4), same as the observations in [106]. The fractions of the α1, α2, and δ phase were determined to be 56.5, 33.2, and 10.3 wt.%, respectively via Rietveld refinement (Figure 6.5). The reliability factors of the weighted profiles R_{wp} were less than 10%, suggesting that the refinements fit well with the observed values [215]. Table 6.2 provides a comparison between the cooling rates and the δ fractions of the samples studied here and those reported in the literature. The cooling rate can be estimated as follows [74]:

$$\dot{T} = 2\pi ks(T - T_0)^2 / Q$$

where k is the thermal conductivity (38.5 W/mK) estimated from electrical conductivity based on the Wiedemann–Franz equation [216], T is the melting point of the alloy (1005 °C [217]), T_0 is the build plate temperature (25 °C), and Q is the input energy that can be predicted from P (195 W) and laser absorption coefficient (0.547 measured from powder laser absorbance with a laser wavelength of 1064 nm). The result indicates that the fraction of the δ phase increases with an increase in the cooling rate, as compared to the findings reported in [111].

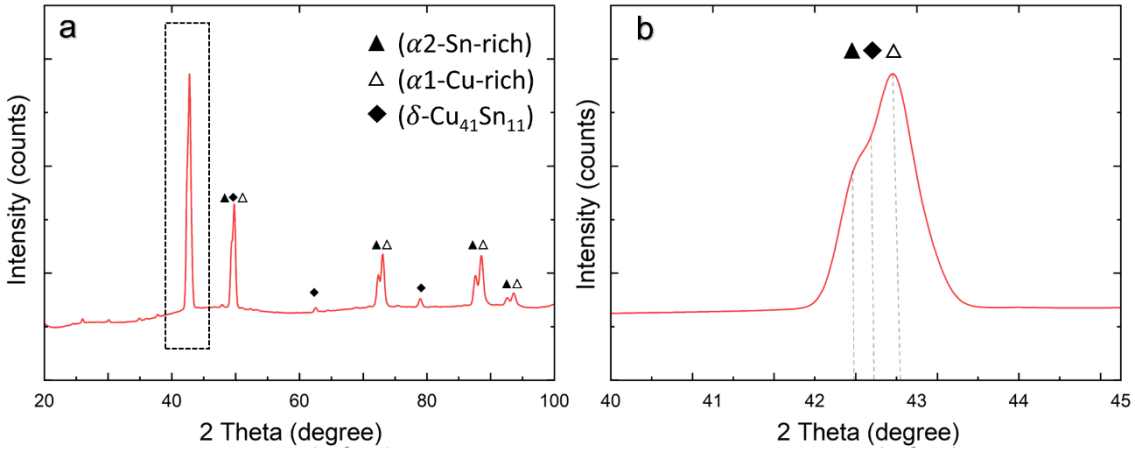

Figure 6.4: (a) XRD diffraction patterns of the as-built sample, and (b) the magnified region of the dotted frame in (a).

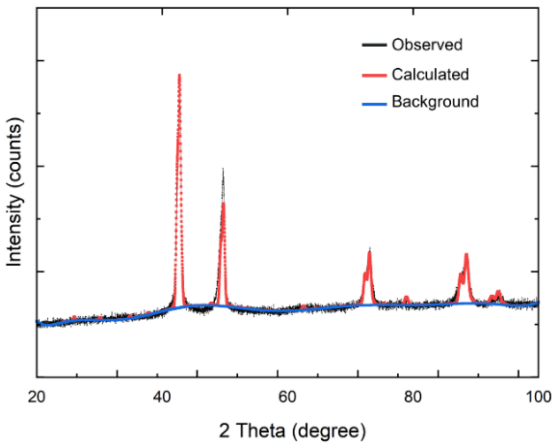

Figure 6.5: Rietveld refinement analysis of the as-built Cu-10Sn sample (195 W & 860 mm/s).

Table 6.2: Summary of Rietveld analysis of the XRD patterns of the as-built samples and samples reported in the literature along with a comparison of the calculated cooling rates of these samples.

Sample	Cooling rate ($\times 10^6$ °C/s)	α1 (wt.%)	α2 (wt.%)	δ (wt.%)	R_{wp} (%)
As-built (195 W and 860 mm/s)	1.88	56.5	33.2	10.3	5.71
Ref. [111] (95 W and 1200 mm/s)	4.58	-	-	25.9	8.78

Figure 6.6a is an EBSD band contrast micrograph of the as-built sample where the δ phase is highlighted in yellow by using ImageJ. Figure 6.6b is an image of the magnified area across the melt pool boundary in Figure 6.6a. The presence of the spot-like instances of the δ phase indicates a sub-micron scale dispersion. In contrast, the EBSD phase map of the as-cast sample reveals a micron-scale dispersion of the δ phase located around the inter-dendritic regions (Figure 6.6c). Figure 6.6d provides a summary of the size distributions of the grains observed in Figure 6.6a. The grain size value of 3.5 μm was arbitrarily set to

distinguish between small equiaxed and large columnar grains and, on this basis, it was found that the larger columnar grains constitute approximately 80% of all grains.

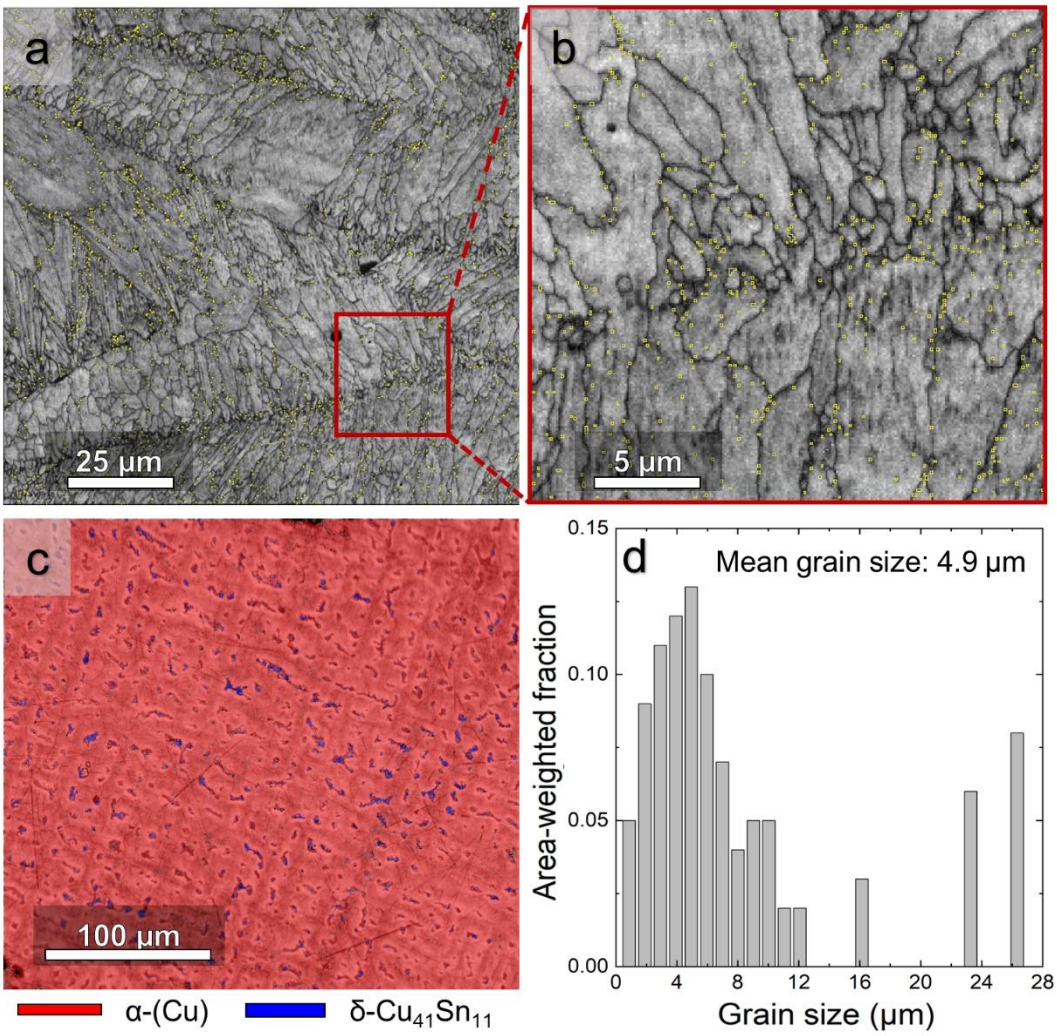

Figure 6.6: SEM microstructural characteristics of the as-built and as-cast sample. (a) EBSD band contrast images with yellow highlighted δ phase; (b) magnified image showing the grain morphology and δ distribution for the area marked in (a); (c) EBSD phase map of the as-cast sample; and (d) grain size distribution of the as-built sample.

High-resolution TEM (HRTEM) specimens were prepared from the middle layer and excised specifically from the interior of the melt pool. Figure 6.7a-b are the high-angle annular dark-field scanning TEM (HAADF-STEM) image, along with the STEM-EDXS maps of Cu, Sn, and P for the specific region. Globular regions with distinct dark contrasts (~200 nm) are visible. The corresponding EDXS elemental mapping in Figure 6.7b

confirmed that these regions were enriched with Sn and P. Figure 6.7c is a selected area electron diffraction (SAED) pattern from the area circled in Figure 6.7b. Diffraction analysis verified that the Sn-rich particle observed in Figure 6.7b was the δ phase, oriented along $[1\ 1\ 1]_{\delta}$ // $[0\ 1\ 1]_{\alpha(Cu)}$. Figure 6.7d depicts a representative HRTEM image of the Sn-rich region in Figure 6.7b. The HRTEM and fast Fourier transform (FFT) images in the insets of Figure 6.7d further confirmed that the Sn-rich region was the FCC δ phase with characteristic lattice parameter of 1.73 nm. The sub-micron δ phase (Figure 6.7d) was assessed as being semi-coherent with matrix phase because the interface between α and δ phase was not perfectly aligned. The misfit dislocations can be observed in Figure 6.8, which is the inverse FFT image of the δ in Figure 6.7d.

A further TEM specimen was extracted from across a melt pool (Figure 6.7e). The melt pool boundary, characterised by equiaxed grains ≤ 3.5 μm, is delineated by a yellow dashed line, with BD marked by a black arrow. On the right side of the melt pool boundary, the interior of the melt pool contains larger columnar grains. Notably, the sub-micron δ phase is observed in this region (red square), exhibiting similar sizes and shapes as those observed in Figure 6.7a. Their areal fraction was estimated at 8.5%, which is closely aligned with the volume fraction of the δ phase derived from the XRD. However, along the melt pool boundary, larger irregularly shaped δ phase with sizes ranging in the micron-scale are evident (yellow square). The analysis demonstrates that two different allotropes of the δ phase are present at the centre and boundary of the melt pool.

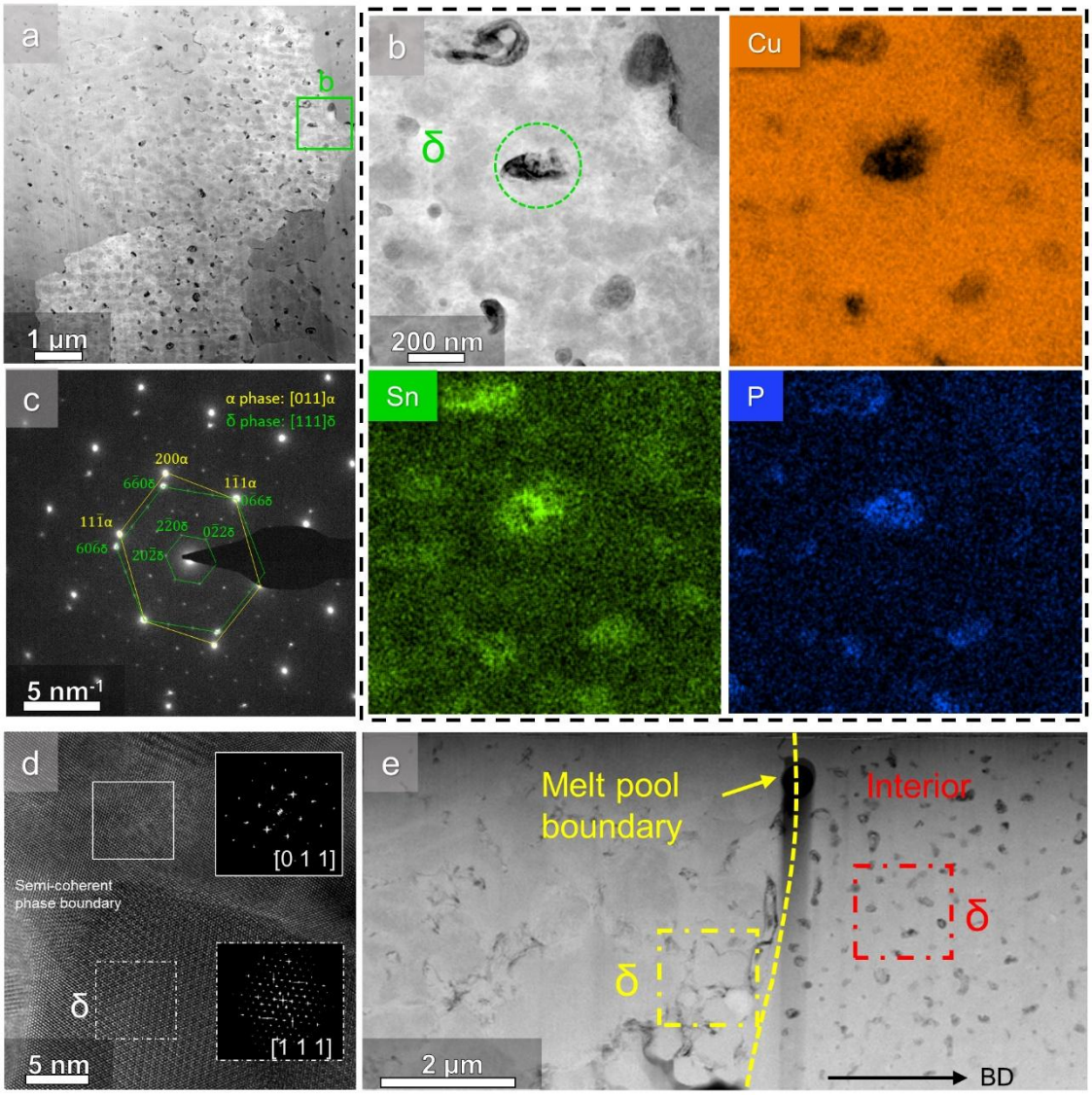

Figure 6.7: TEM based microstructural characterisation of the as-built sample. (a) HAADF-STEM image showing the microstructure of the melt pool interior; (b) magnified image of the region marked with green square in (a) and EDXS elementary maps (Cu, Sn, and P); (c) selected area electron diffraction pattern obtained from green annotated area in (b); (d) bright field HRTEM image showing phase interface between δ and matrix; insets show the FFT images of the matrix and δ phase; and (e) HAADF-STEM image demonstrating the microstructure across the melt pool boundary, two distinct types of the δ phase are indicated by yellow and red squares.

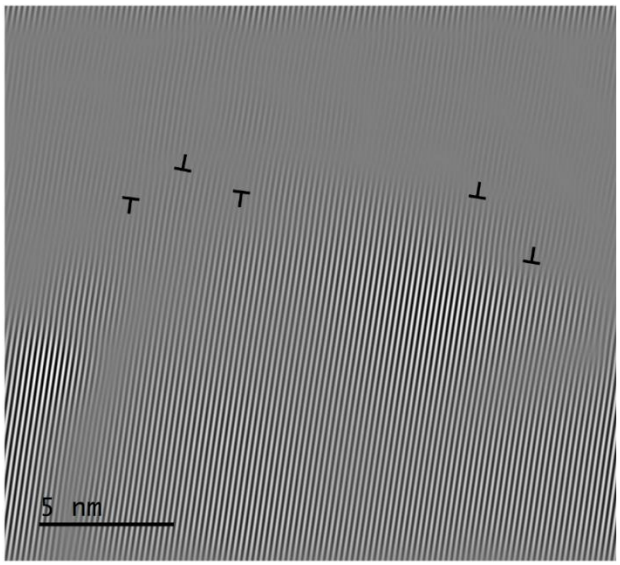

Figure 6.8: Inverse FFT pattern of the δ interface in Figure 6.7d filtered by [$\bar{6}$ 0 6] *and* [6 0 $\bar{6}$] *reflections.*

The composition of the δ phase in the as-built sample was further investigated via APT, and a tomographic atom map of a region containing this phase is provided in Figure 6.9a. Iso-concentration surfaces are mapped ≥20 at.% Sn (green) and ≥5 at.% P (blue) with a voxel size of 3 nm and delocalization value of 5 nm. The cylindrical one-dimensional (1D) elemental concentration profile for the region between the Sn-rich regions provided in Figure 6.9b confirms that the Sn concentration is ~20 at.% in the δ phase and ~5–10 at.% in the α(Cu) matrix. Notably, high concentrations of P are observed in the Sn-rich regions, implying that P tends to segregate to the α/δ interface or perhaps forms a Cu phosphide compound around the δ phase. The APT-measured elemental concentration of the Sn-rich regions is broadly consistent with TEM EDXS results presented in Figure 6.7b.

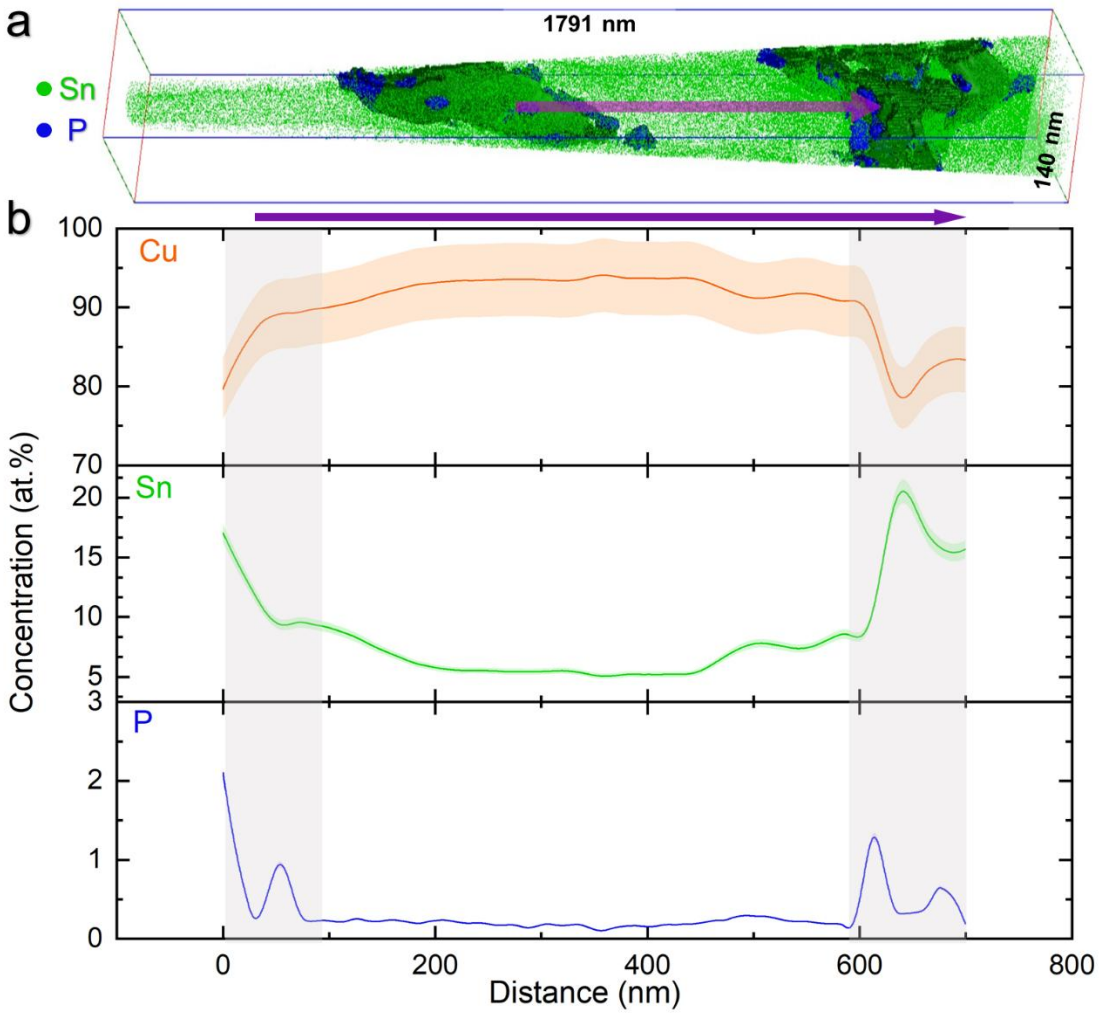

Figure 6.9: Atom probe tomography of the as-built sample. (a) 3D reconstructed atom map of a region containing δ; (b) 1D concentration profiles of Cu, Sn, and P corresponding to the arrow indicated in the atom map in (a). The shaded area represents a statistical error of one standard deviation.

Additional TEM samples were analysed by sectioning individual Cu-10Sn metal powder C particles used in our LB-PBF AM process. Figure 6.10a provides a STEM-HAADF image and the corresponding EDXS maps for Cu, Sn and P, revealing the presence of large, irregularly shaped Sn-rich phase in the powder particles. The EDXS maps also indicate the existence of P in this Sn-rich phase. Figure 6.10b is the phase interface as viewed by HRTEM, and its FFT image is shown in the inset. The indexing of the FFT pattern verified that the Sn-rich phase was a metastable $Cu_{5.6}Sn$ [117]. The composition of the different Sn-rich phase was examined by STEM-EDXS over a total of 75 Sn-rich regions in each of the

as-built and powder samples, as shown in Figure 6.10c. For simplicity, the observed phases are classified into three classes: $Cu_{5.6}Sn$, δ phase ($Cu_{41}Sn_{11}$), and others. The Sn-rich phase of the powder sample contained more $Cu_{5.6}Sn$, while that of the as-built sample contained more δ. The other phases contained a significantly higher Sn fraction (>25 at.%) and were observed in both samples.

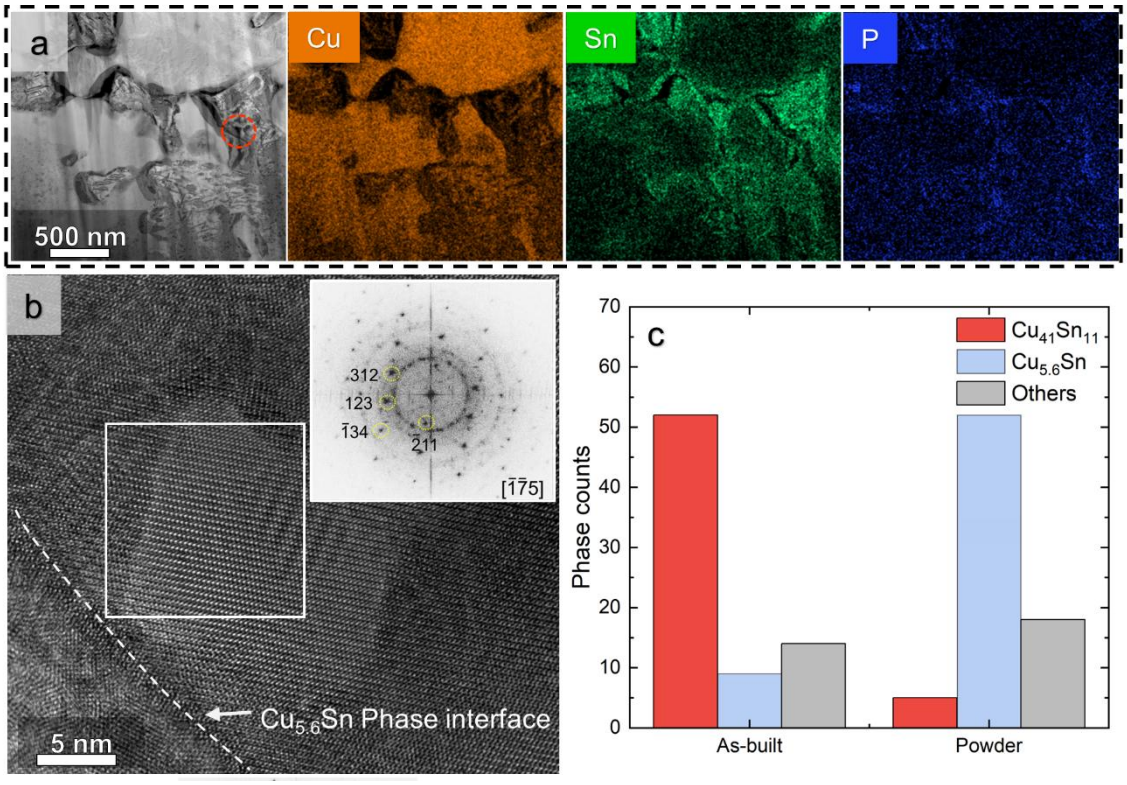

Figure 6.10: TEM microstructural characteristics of the Cu-10Sn powder C. (a) HAADF-STEM image showing the microstructure of the powder particle interior and EDXS elemental maps (Cu, Sn, and P); (b) HRTEM image depicting the phase interface with the inset showing the FFT image of $Cu_{5.6}Sn$; and (c) STEM-EDXS results demonstrating the phase fractions of different phases in the as-built and powder samples.

6.1.3 Phase transformations during LB-PBF Cu-10Sn

To further investigate the phase transformations in the Cu-10Sn alloy during LB-PBF, the volume fractions of the equilibrium phases were calculated as a function of temperature, Figure 6.11a, and the non-equilibrium Gulliver-Scheil solidification model examined, Figure 6.11b. During equilibrium solidification such as is assumed in Figure 6.11a, primary

α(Cu) nucleates and grows from the liquid phase at temperatures below 990 °C. As the temperature reduces, the δ phase occurs below ~450 °C and transforms to the ε phase at approximately 365 °C. However, during non-equilibrium solidification such as in Figure 6.11b, the phase transformation sequence of Cu-10Sn is L → α(Cu) → β ($Cu_{17}Sn_3$) → γ (Cu_3Sn). After the liquid phase solidifies as α(Cu) below 990 °C, β and γ begin to come out of the melt at approximately 750 and 700 °C, respectively, until the total mole fraction of the solid phase reaches 0.95 at ~650 °C. This suggests that the microstructure of LB-PBF Cu-10Sn is mainly composed of a large amount of α(Cu) and small amounts of β and γ at 650 °C.

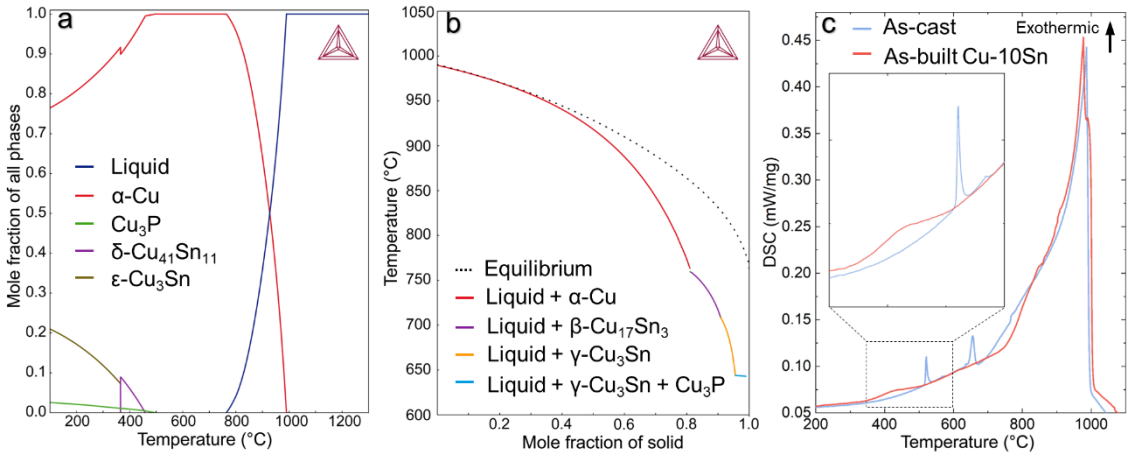

Figure 6.11: Phase analysis of Cu-10Sn using Thermo-Calc simulation and DSC. (a) volume fractions of the stable phases as functions of temperature; (b) non-equilibrium Gulliver-Scheil solidification model; (c) DSC heating curves of the as-cast and LB-PBF samples heated up to 1200 °C at a rate of 10 °C/min and inset magnified image showing the peaks for the region marked in (c).

DSC heating curves of the as-cast and LB-PBF Cu-10Sn samples are shown in Figure 6.11c. These curves demonstrated four major exothermic reactions with the onset temperatures of 527, 645, 763, and 980 °C for the as-cast sample. These suggest the following phase transformation sequence: γ ↔ α + δ at 527 ºC, β + L ↔ γ at 763 ºC, and a liquidus temperature of 980 °C, consistent with [115]. The exothermic peak at 645 °C can be ascribed to the reaction γ + ε ↔ ζ, where ζ is a $Cu_{10}Sn_3$ [115] or Cu phosphide such as

Cu_3P [218]. In comparison, the onset temperatures of 350 °C and 758 °C were observed for LB-PBF Cu-10Sn, which are the transformation temperatures of δ and γ/β, respectively. These broad peaks are considered to be caused by the fraction of the δ phase being too small to be detected by DSC [112], as supported by XRD and microstructural analysis, together with the influence of rapid solidification and non-equilibrium microstructures on transformation kinetics under the applied heating rate.

Another crucial aspect of the LB-PBF process is cyclic heating and cooling. These temperature excursions were assessed using simulations in FLOW-3D AM. Figure 6.12a-b are cross-sectional images after three sequential laser scans (1, 2 and 3), with black arrows depicting the scan direction. We monitored the temperature during the laser scan at points A, B, and C. Figure 6.12c is the temperature profile at each point when the second laser scan passes. The temperature increased to approximately 520 °C at the set point B when the laser approached. In contrast, it decreased to approximately 300 °C when the laser moved away from the set points.

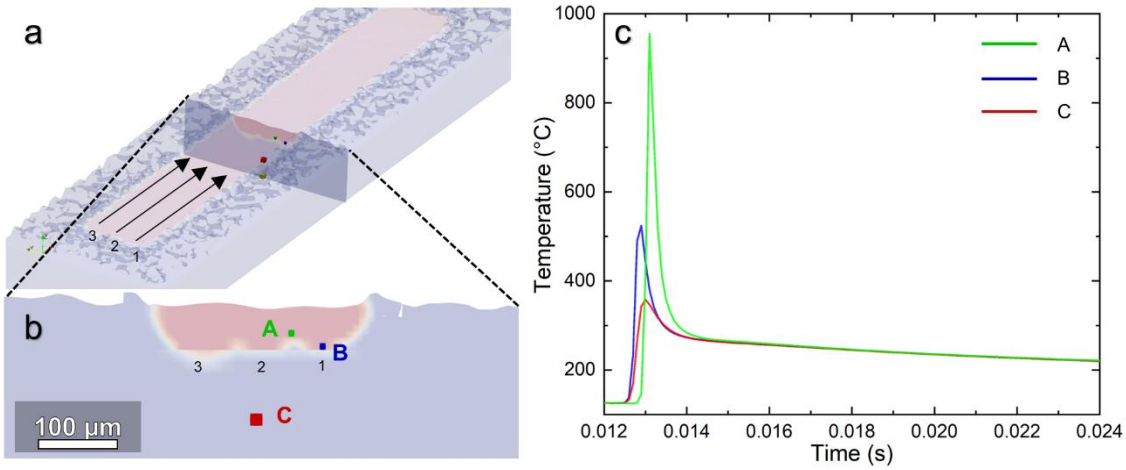

Figure 6.12: FLOW-3D AM simulations. (a) and (b) are the profiles of the melt pool of Cu-10Sn alloy along the scan direction (arrowed); (c) the temperature versus time profile for the three designated points.

6.2 Discussion

The present work revealed the existence of two distinct types of δ with different sizes, shapes, and spatial distributions depending on their location in the melt pool boundary versus interior, as described in Figure 6.7 This section discusses the formation mechanisms of the Sn-rich δ phase, Sn segregation with the unique morphology and distribution, and the contribution to the mechanical property.

6.2.1 Mechanisms of Sn-rich δ phase formation

During LB-PBF, Cu-10Sn powder particles are fused and solidified by a laser scan, initially forming α(Cu) and a Sn-rich phase. The Sn-rich phase is considered metastable, identified as $Cu_{5.6}Sn$, due to the rapid solidification. This has been previously observed in rapidly solidified samples [117] and is further supported by our phase identification in rapidly cooled metal powder particles (Figure 6.10c). Given the close chemical compositions of the metastable $Cu_{5.6}Sn$ and β ($Cu_{17}Sn_3$) phases, we consider that the metastable phase develops from the parent β phase via a martensitic phase transformation during rapid solidification, as suggested by Li et al. [117]. While δ phase formation from γ near the eutectoid transformation temperature may occur, determining the parent phase, whether γ or β, requires further investigation, such as in-situ synchrotron XRD during a single laser track experiment. Nevertheless, the limited fraction of γ observed under non-equilibrium conditions and the dominance of $Cu_{5.6}Sn$ in this study lead us to prioritise the β and $Cu_{5.6}Sn$ pathway in explaining δ phase formation. The phase transformation from $Cu_{5.6}Sn$ to δ in the as-built sample is likely driven by cyclic heating during the multiple laser scans, coupled with a diffusion process. The FLOW-3D AM simulation presented in Figure 6.12 revealed that the surrounding melt pool region, where metal particles were rapidly

solidified, experiences repeated cyclic heating and cooling at the temperature range between 300 °C to 520 °C. This temperature range corresponds to the onset transformation temperature for δ as described in Figure 6.11c. Collectively, these results indicate that rapid cooling during LB-PBF initially leads to the formation of the metastable $Cu_{5.6}Sn$, which subsequently transitions to the equilibrium δ phase following cyclic heating. Specifically, the formation of metastable δ is rationalised in terms of rapid solidification under high cooling rates and steep thermal gradients within individual melt pools, whereas the equilibrium δ is associated with cyclic reheating arising from subsequent layer deposition, which enables diffusion-mediated phase transformation toward thermodynamic stability.

6.2.2 Origin of the Sn segregation with the unique morphology and distribution

Among the two types of the δ phase observed in Figure 6.7, one type appears as a small globular structure distributed within the melt pool interior. The other type, which exhibits an irregular shape and larger size, is located around the fine grains at the melt pool boundary. This variation in the distribution of the grain structure and Sn-rich phase can be attributed to the different thermal gradient (*G*) and solidification rate (*R*) at the centre (lower *G/R* ratio) and boundary of the melt pool (higher *G/R* ratio) during LB-PBF [73], where the following unique solidification sequence in each region play a role.

Figure 6.13 depicts a series of schematics of the solidification pathway in a single melt pool during the synthesis of LB-PBF Cu-10Sn. In the initial stage of the solidification at the melt pool boundary (Figure 6.13a and c), α(Cu) with high Cu concentration starts to grow due to its partitioning coefficient being less < 1, as indicated in the Cu-Sn phase diagram [115]. With a decrease in temperature, the Sn atoms are rejected into liquid, resulting in a region

of Sn-rich liquid ahead of the interface. Concurrently, equiaxed dendrites may nucleate near the melt pool boundary where local solidification conditions favour heterogeneous nucleation, often facilitated by intermetallic particles or inclusions, as reported in previous studies [219, 220], the Sn-rich liquid can be expected to migrate to the edges of the dendrites. The *R* at the melt pool boundary is slower due to minimal local undercooling, as the temperature decreases gradually from above to just below the melting point. In this region, the motion of the solid-liquid interface is primarily governed by directional heat flow into the unmelted area, rather than by the rapid dissipation of heat alone. Moreover, the low solidification front velocity at the melt pool boundaries would likely provide sufficient time for the aggregation of Sn atoms at solid-liquid interface, resulting in the heterogenous nucleation of the metastable Sn-rich $Cu_{5.6}Sn$ phase. This Sn-rich phase can also serve as a nucleation site for the solidification of the remaining liquid, and will also have an inhibiting effect on subsequent grain growth. An earlier study [221] observed similar equiaxed microstructures at melt pool boundaries in LB-PBF-made Al-Cu-Mg alloy, attributed to the formation of precipitates at melt pool boundaries. As described in the previous section, the results suggest that the metastable $Cu_{5.6}Sn$ phase transforms into the equilibrium δ phase following cyclic heating during the multiple laser scans (Figure 6.13e). This microstructural evolution at the melt pool boundaries results in relatively large δ phase at the grain boundaries of what ultimately is a fine and equiaxed grain structure, Figure 6.13g.

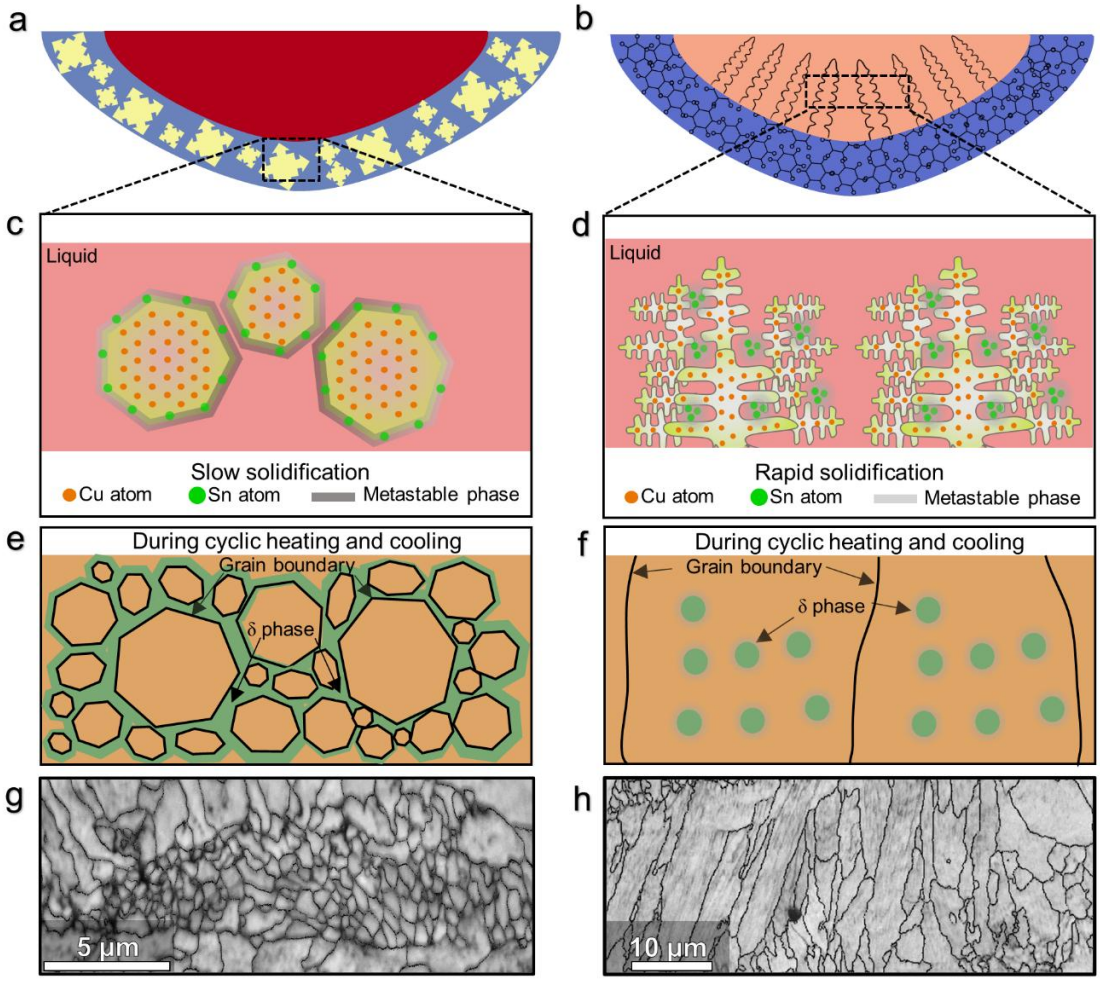

Figure 6.13: Schematics of solidification at a single melt pool. (a) growth of equiaxed grains at the initial stage of solidification at the melt boundary; (b) growth of columnar dendrites at the later stage of solidification within the melt pool; (c) atomic distribution and Sn-rich metastable phase formation at a slow solidification rate at the melt pool boundary; (d) atomic distribution and Sn-rich metastable phase production at a rapid solidification rate within the melt pool; (e) generation of large and irregularly shaped δ during cyclic heating at the melt pool boundary; (f) formation of small globular δ during cyclic heating within the melt pool; (g) and (h) are EBSD band contrast images of as-built sample showing microstructure of melt pool boundary and interior region respectively.

As the solidification interface progresses toward the centre of the melt pool (Figure 6.13b and d), *R* significantly increases while *G* decreases [222-224], forming a columnar dendritic microstructure. Herein, the dendrite arms grow fast, and multiple dendrites with many primary, secondary, and tertiary arms can develop in one columnar grain [225] (Figure 6.13f and h). The last drop of the Sn-rich liquid can be trapped within the dendrite arms, leading to their incorporation into the α(Cu) matrix. Consequently, small and globular Sn-rich $Cu_{5.6}Sn$ phase particles formed within the columnar grains (Figure 6.7). Previous

studies have also suggested that dendritic growth will take place when the supercooling is large, where the newly nucleated grains grow epitaxially in the opposite direction to the heat flux, thereby generating columnar grains [225-227]. Similar to the case of the melt pool boundary, finally, $Cu_{5.6}Sn$ transforms into the equilibrium δ phase facilitated by the cyclic heating during the printing of additional layers (Figure 6.13f).

6.2.3 Contribution of the δ phase to yield strength, electrical conductivity, and wear resistance

The YS of the as-built sample is more than two times higher than that of the as-cast sample [110]. A methodology described in the literature is adopted [106, 228] to estimate the δ phase contribution to the YS. The δ observed in Figure 6.7 is semi-coherent with the matrix due to the large difference between the lattice parameters. Thus, the main source of the precipitation strengthening (σ_{PS}) is the dislocation-particle interaction by the Orowan process [229]. In this case, the δ phase particles act as dispersoids, requiring dislocations to bow around them, resulting in an increase in YS [230]. Therefore, the σ_{PS} contribution can be calculated by the Ashby–Orowan equation [231]:

$$\sigma_{PS} = \frac{0.81 M G_s b}{2\pi(1 - v)^{1/2}} \frac{\ln(d_p / b)}{(\lambda - d_p)}$$

where M is the Taylor factor of Cu (3.1) [232], Gs is the shear modulus (48.3 GPa) [233], b is the Burgers vector of Cu (2.56×10^{-10} m) [228], v is the Poisson's ratio of Cu (0.34) [232] and d_p is the average diameter of δ, which is 160 nm according to Figure 6.7a. Furthermore, λ is the interspacing between precipitates and related to their diameters (d_p) and volume fractions (f_p) as follows [234]:

$$\lambda = \frac{1}{2} d_p \sqrt{\frac{3\pi}{2f_p}}$$

The volume fraction was estimated to be 9.63 vol.% according to the densities of α1 (8.59 g/cm^3), α2 (8.38 g/cm^3), and δ (9.18 g/cm^3) and their weight fractions (Table 6.2). As a result, the δ phase contribution to the YS, or σ_{PS} was calculated at 96.6 MPa.

The observed strengthening of LB-PBF Cu-10Sn is further explained in the Appendix B, where we sum the contributions from the intrinsic YS of the Cu matrix (σ_0) (52 MPa), the solid-solution strengthening (σ_{SSS}) (10.2 MPa), the grain boundary strengthening (σ_{GBS}) (81.3 MPa), the dislocation strengthening (σ_{DS}) (175.8 MPa), and the σ_{PS} (96.6 MPa). The overall YS of LB-PBF Cu-10Sn is calculated to be 416 MPa, which is consistent with the experimentally observed YS (422 MPa). While the contribution of the dislocation density is the highest, the fine grains and sub-micron dispersed δ significantly contribute to the superior YS.

The spatial distribution of the δ phase, along with the columnar and equiaxed grain structures in different regions of the melt pool, significantly influences the alloy's mechanical behaviour. This microstructural heterogeneity arises from the unique thermal gradients and solidification dynamics of the LB-PBF process. The UTS and elongation at failure determined in this work are 8% and 265% lower, respectively, than those reported by [106], while the YS is 9% higher. Compared to [136], the UTS observed in this work is similar, but the YS is 10% higher. The low ductility in the as-built samples may be attributed to the small amount of porosity introduced during the LB-PBF process, or variations in the dislocation density, which governs the material's strain-hardening capability. Reducing porosity and manipulating dislocation density through optimisation of powder characteristics and printing parameters, such as laser power, scanning speed, and

hatch spacing, could potentially enhance ductility while maintaining the strength benefits conferred by the δ phase.

The electrical behaviour of LB-PBF Cu-10Sn is influenced by a complex interplay of microstructural features, which collectively determine its conductivity and resistance. Despite the unique microstructure of the LB-PBF sample, including refined grains, high dislocation density, and dispersed δ phase precipitates, the IACS values (9.7% for LB-PBF and 10.3% for as-cast) remain nearly identical. This similarity can be attributed to the predominant influence of solute atoms, specifically Sn, on electrical resistivity. Solute atoms significantly reduce the concentration of conducting electrons and dominate electron scattering effects, outweighing the contributions of grain boundaries and dislocations [235]. While features such as high dislocation density and grain boundary area in LB-PBF Cu-10Sn could increase resistivity, and the fine δ phase precipitates may locally disrupt electron flow, their impact is minimal compared to solute scattering. Moreover, the fine and dispersed δ phase precipitates contribute positively to mechanical strength without negatively affecting electrical resistivity, resulting in a balance that maintains similar conductivity between LB-PBF and as-cast samples.

The δ phase also contributes to the wear resistance in the LB-PBF sample. The test conditions resulting in the highest volume loss are expected to yield the deepest wear track [236], suggesting that the as-cast sample is likely to demonstrate higher volume losses and inferior wear resistances. Generally, adhesive wear has been reported as the main active mechanism in Cu alloys in former studies [237, 238]. Adhesive wear usually causes a higher COF and increases material loss [239], as observed in the as-cast sample. However, the dispersion of δ and enhanced hardness in the LB-PBF Cu-10Sn can be responsible for abrasive wear mechanism, with the hard δ phase particles reducing material adhesion and instead promoting micro-cutting and plowing actions, which are characteristic of abrasive

wear as in the literature [240]. The steady COF observed for the LB-PBF sample aligns with the abrasive wear mechanism, as it reflects stable interaction at the surface, minimising adhesion. Moreover, note that the COF of the LB-PBF sample is lower and more rapidly reaches a steady state as compared to the case of as-cast samples (Figure 6.2). This behaviour can also contribute to the superior wear resistance of the LB-PBF Cu-10Sn [241].

6.3 Summary

A Cu-10Sn was manufactured via LB-PBF, and its microstructural characteristics and mechanical properties were investigated, with a specific focus on the properties and formation mechanisms of the Sn-rich δ phase. The key conclusions drawn from this study are as follows:

(1) Two distinct types of δ were observed in the as-built samples. The variations in the size and shape of δ were due to differing solidification conditions occurring at the melt pool boundary versus those at the interior of the melt pool. The relatively slow solidification rate at the melt pool boundary led to the formation of large, irregularly shaped Sn-rich δ phase intermixed with finer α(Cu) grains. In contrast, rapid solidification within the melt pool interior resulted in the emergence of the sub-micron, globular, and dispersed Sn-rich δ phase with coarser α(Cu) columnar grains.

(2) A phase transformation pathway of the Sn-rich Cu5.6Sn metastable phases to the equilibrium δ phase during cyclic heating in LB-PBF is proposed. The temperature range during the multiple laser scans corresponds to the onset transformation temperature that the δ phase develops.

(3) This study demonstrates that LB-PBF Cu-10Sn exhibits a higher YS and hardness compared to conventionally cast Cu-10Sn alloys. The improvements to these

mechanical properties are approximately at 148% and 22%, respectively. Additionally, their wear resistance significantly improves when compared to conventionally cast alloys, as evidenced by a fourfold reduction in wear track dimensions and a steadier COF. We attribute these improved properties to the combined contributions of grain boundary strengthening, dislocation strengthening, and additional contributions from the δ phase. Interestingly, and as discussed in detail, the δ phase is traditionally regarded as a deleterious phase in these alloys.

Chapter 7 Enhancing Strength and Ductility of As-Built Cu-10Sn via Powder–Structure–Property Control in Laser Beam Powder Bed Fusion

Chapter 6 demonstrated the formation mechanisms of the Sn-rich δ phase as a key strengthening mechanism of LB-PBF Cu-10Sn alloys. However, the ductility of this sample remained relatively low, with elongation at fracture of approximately 7 %, underscoring the need for further improvement in the ductility. To address Aim 3 and enhance the mechanical properties, particularly ductility, three powders with distinct PSD, chemical compositions, and flowability were processed under identical LB-PBF parameters, and their role on the microstructure and mechanical properties of the as-built sample was systematically investigated. This controlled design allows us to assess how the variations in powder characteristics alone affect the microstructure and mechanical properties of the as-built parts. Multi-length-scale microscopy and microanalysis reveal that even slight variations in the powder characteristics can significantly influence melting and solidification behaviour, resulting in microstructural variations that directly impact mechanical performance. PSD variations affect powder packing and melt uniformity, while differences in surface oxygen modify laser energy coupling and melt pool stability. Flowability governs layer homogeneity during recoating and thus the likelihood of lack-of-fusion defects. Most critically, the measured absorptance values show a clear ranking among the powders. With all processing parameters held constant, these differences directly alter effective energy input and local thermal history, thereby controlling melt pool morphology, porosity, microstructural evolution, and ultimately the strength–ductility response of the as-built material. By identifying the most influential power properties, this

work establishes critical relationships between powder characteristics, microstructure, and mechanical properties, thereby enhancing the reliability and reproducibility of Cu-10Sn components manufactured by LB-PBF.

7.1 Results

7.1.1 Mechanical properties

Figure 7.1a shows engineering tensile stress–strain curves for samples A, B and C. Sample C, used in Chapter 6, serves as the benchmark, showing a YS of 422 ± 5 MPa, UTS of 522 ± 2 MPa, and a total elongation at fracture of 7.2 ± 0.5%. In comparison, as summarised in Table 7.1, samples A and B exhibit comparable YS to sample C but show a substantial enhancement in total elongation at fracture (15.1 ± 1.3% and 17.4 ± 1.0% respectively), more than double that of sample C, without compromising strength. This improvement was achieved solely by varying powder characteristics, without the need for post-processing. Figure 7.1b compares the tensile properties of the Cu-10Sn alloys in this study with previously reported values for other LB-PBF Cu-10Sn [18, 106, 136, 209, 210, 242-244] and conventionally cast Cu-10Sn alloys [205, 206, 242, 245]. The LB-PBF Cu-10Sn samples presented here exhibit superior YS and UTS with ductility comparable to previously reported LB-PBF Cu-10Sn. Overall, the mechanical properties of the as-built LB-PBF Cu-10Sn in this study exceed those of conventional as-cast Cu-10Sn.

Figure 7.1c presents the compression stress–strain curves for samples A, B, and C. The compressive YS (CYS) is measured as 429 ± 1 MPa for sample A, 422 ± 4 MPa for sample B, and 418 ± 3 MPa for sample C, reflecting a similar trend to the tensile YS. All samples exhibit good plasticity under compression. At approximately 30% strain, the compressive strength (CS) reaches 869 ± 62 MPa, 788 ± 52 MPa, and 819 ± 61 MPa for samples A, B and C, respectively.

The average Vickers hardness values are 181.0 ± 8.6 $HV_{0.1}$, 175.7 ± 4.3 $HV_{0.1}$, and 176.6 ± 5.0 $HV_{0.1}$ for samples A, B and C, respectively, with the corresponding microhardness maps provided in Figure 7.2. Sample A exhibits slightly higher hardness (~3%) than samples B and C. This modest variation is consistent with the small differences observed in YS (Table 7.1). A summary of all mechanical properties measured in this study is presented in Table 7.1.

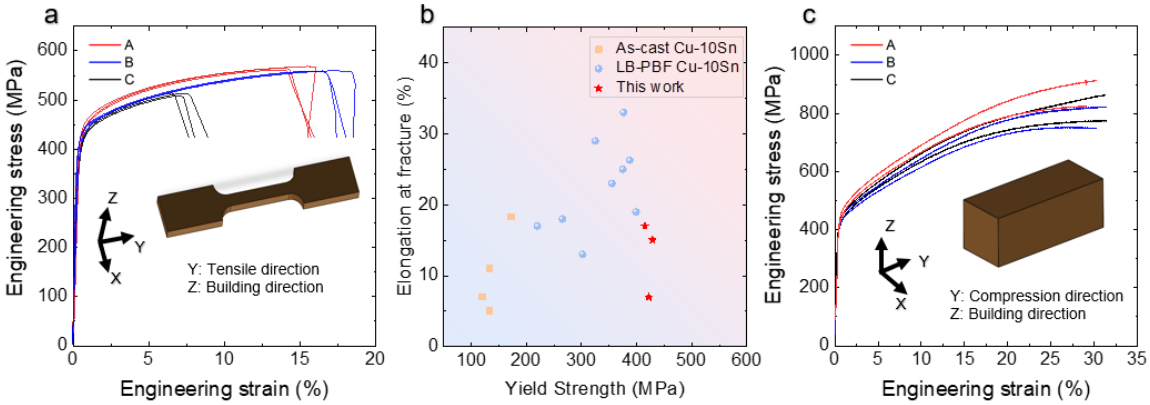

Figure 7.1: Mechanical properties of LB-PBF Cu-10Sn alloys. (a) tensile engineering stress-strain curves of samples A, B and C; (b) comparison of total elongation at fracture and YS of present LB-PBF Cu-10Sn alloys with previously published results, including other LB-PBF Cu-10Sn [18, 106, 136, 209, 210, 242-244] and conventionally cast Cu-10Sn [205, 206, 242, 245]); and (c) compressive engineering stress-strain curves of samples A, B and C.

Table 7.1: Summary of Vickers hardness, yield strength, ultimate tensile strength and ductility for LB-PBF Cu-10Sn samples A B and C.

Sample	YS (MPa)	UTS (MPa)	Compressive YS (MPa)	CS (MPa)	Ductility (%)	Vickers Hardness ($HV_{0.1}$)
A	429 ± 7	563 ± 4	429 ± 1	869 ± 62	15.1 ± 1.3	181.0 ± 8.6
B	415 ± 9	558 ± 1	422 ± 4	788 ± 52	17.4 ± 1.0	175.7 ± 4.3
C	422 ± 5	522 ± 2	418 ± 3	819 ± 61	7.2 ± 0.5	176.6 ± 5.0

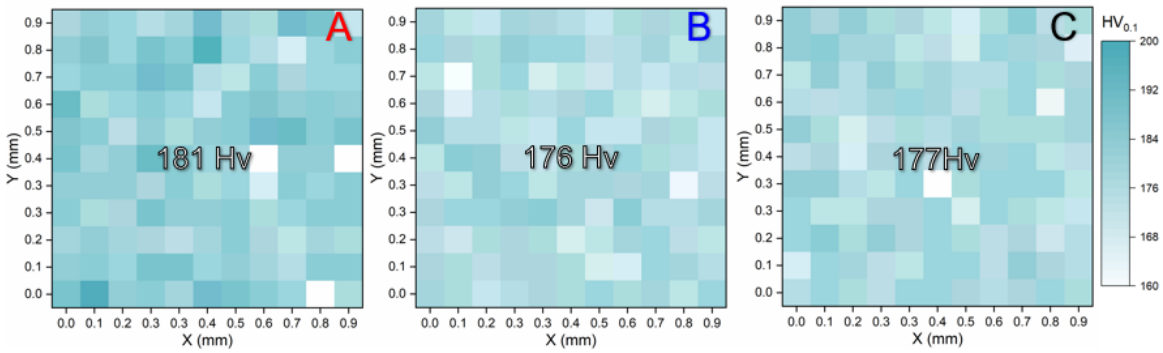

Figure 7.2: Vickers hardness maps of LB-PBF Cu-10Sn as-built sample A, B and C, showing average hardness values of 181 Hv, 176 Hv, and 177 Hv, respectively.

7.1.2 Powder characteristics

To understand the distinct mechanical properties resulting from the use of three different powders, extensive powder characterisations were performed, covering chemical compositions (bulk and surface), geometric properties (size, PSD, morphology, and flowability), and additional attributes such as laser absorbance, microstructure and thermal conductivity. The results presented below highlight the key differences among the powders.

The chemical compositions of the three powders are summarised in Table 7.2. Among the bulk compositions, powder C has the highest Sn content at 10.30%, compared to 9.90% in powder A and 9.57% in powder B. Phosphorus (P) is absent in powder A but is present in powders B and C at 0.16% and 0.29%, respectively. Notably, powder B contains 0.44% zinc (Zn), while Zn is below 0.01% in powders A and C. The surface composition reveals more significant differences. Powder B has a high Zn content of 21.87%, which is absent in the other powders. Surface Sn content is highest in powder A (9.09%), followed by B (7.00%) and C (5.00%). Oxygen (O) is more prevalent on the surface of powders C (8.78%) and B (8.39%) compared to A (5.30%).

Table 7.2: Bulk and surface chemical compositions (wt.%) of the three powders.

Bulk chemical composition / Powder	Cu	Sn	P	Zn	O
A	Bal	9.90	0.01	<0.01	0.08
B	Bal	9.57	0.16	0.44	0.12
C	Bal	10.3	0.29	<0.01	0.05
Surface chemical composition / Powder	**Cu**	**Sn**	**P**	**Zn**	**O**
A	84.19	8.94	-	-	5.21
B	60.89	6.79	-	21.22	8.14
C	83.44	4.92	0.78	-	8.63

PSD of the three powders, measured by the laser diffraction, is shown in Figure 7.3a. Powder C shows the smallest particles, with D50 and D90 values of 21.8 µm and 34.7 µm, respectively. While powders A and B have nearly identical D10 values, powder A exhibits a broader size distribution and a slightly larger D90.

Figure 7.3b shows PSD obtained from SEM image analysis, which reveals finer-scale variability in particle sizes not captured by the laser diffraction method. All powders exhibit a bimodal PSD, characterised by distinct peaks corresponding to fine and coarse particle sizes. The size ratio, defined as the ratio of the coarse particle peak to the fine particle peak, is significantly higher in powders A and B (16 and 15, respectively), compared to powder C (2). Additionally, powder A contains approximately twice the number of fine particles as powder B.

Figure 7.3c shows the laser absorbance of the three powders measured at a wavelength of 1064 nm–the same wavelength as the laser used in the LB-PBF process. Powder A has the highest absorbance at 63%, compared to 58% for powder B and 55% for powder C.

Figure 7.3d presents the dynamic cohesion index of the powders as a function of rotating speed. For all powders, the cohesion index increases with increasing rotation speed, indicating that they are non-cohesive powders, as described in a previous study [246]. This behaviour is primarily governed by particle size and morphology. While powders A and B exhibit comparable cohesion index values, powder C consistently shows higher values, suggesting increased cohesiveness relative to the other powders.

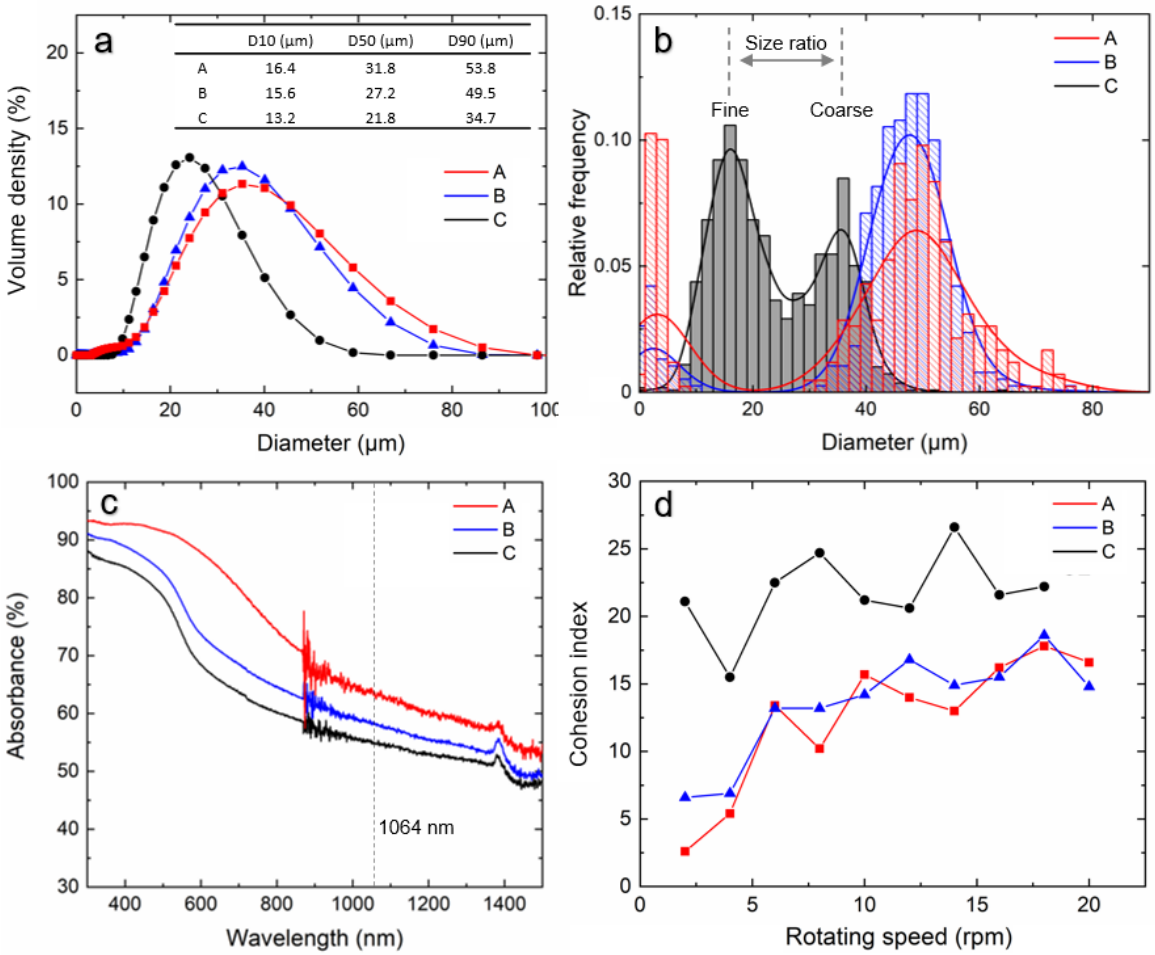

Figure 7.3: Powder characterisations highlighting key differences among powders. (a) PSD measured by laser diffraction, with an inset table showing particle diameters at D10, D50, and D90 percentiles; (b) PSD measured by SEM imaging analysis; (c) laser absorbance as a function of wavelength (1064 nm corresponds to the laser wavelength used in LB-PBF process); and (d) dynamic cohesion index measured by rotating drum as a function of rotating speed.

7.1.3 Microstructure

Figure 7.4 shows representative EBSD cross-sectional crystallographic information (*YZ*-plane) of the as-built samples. The IPF maps reveal a bimodal grain structure in all samples, with fine grains decorating the melt pool boundaries, while the columnar grains grow toward the melt pool centres. The mean grain size of samples A, B and C is measured as 3.4 μm, 3.4 μm, and 3.7 μm, respectively, with the grain size distributions presented in Figure 7.5. These distributions exhibit generally consistent profiles, each showing a high fraction of fine grains (<10 μm), followed by a gradual decline toward coarser grains. The melt pool shapes, marked by representative white dashed lines in Figure 7.4, were characterised using the melt pool geometry analysis method described in [247]. The estimated melt pool dimensions (mean width {depth}) are 116 {30} μm for sample A, 116 {19} μm for sample B, and 113 {11} μm for sample C. Notably, sample A shows a melt pool depth approximately two times deeper than that of sample C. Although a weak texture along BD is observed in all samples, as shown in the pole figures in Figure 7.4, the low pole figure intensities and the randomly oriented grains in the IPF maps indicate the absence of a strong crystallographic texture.

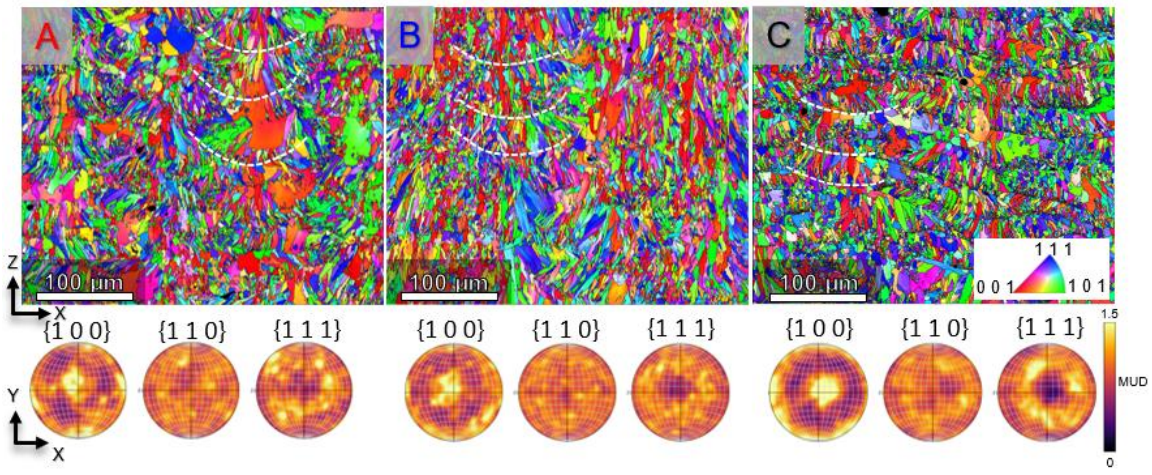

Figure 7.4: EBSD IPF maps showing the microstructural information of LB-PBF Cu-10Sn samples A, B and C, along with their corresponding pole figures. Selected melt pool boundaries are highlighted with white dashed lines.

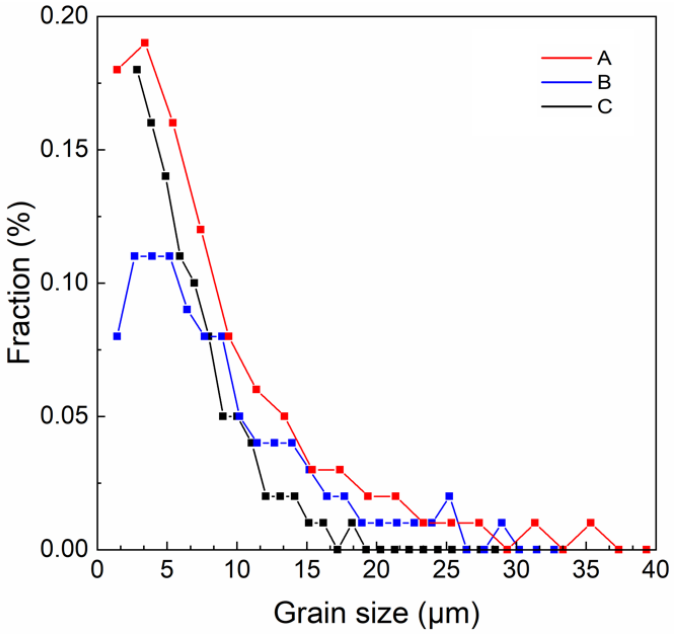

Figure 7.5: The grain size distribution of LB-PBF Cu-10Sn samples A, B and C obtained from the EBSD data in Figure 7.4.

Total geometrically necessary dislocation (GND) density maps (Figure 7.6a–c) were computed from the same EBSD dataset shown in Figure 7.4, with a magnified view. The calculations were based on the Burgers vector, ***b***, along the slip direction of the face-centred cubic (FCC) α(Cu) matrix, where ***b***= (*a*/2) <110> and *a* is the lattice constant of the Cu unit cell. The analysis considered randomly textured low angle grain boundaries (LAGB), with a maximum misorientation of 5° [248]. The total GND density varies among the three samples, as shown in the histogram in Figure 7.7. The mean GND densities for samples A, B, and C are 6.27 ± 2.6, 6.15 ± 3.0, and 5.26 ± 2.1 ($\times 10^{14}$ m^{-2}), respectively. Samples A and B show approximately 18% higher GND densities than sample C. Regions of the high GND density are predominantly located within the melt pool interior, corresponding to columnar grains observed in Figure 7.4.

To further investigate the dislocation distribution within the melt pool interior, TEM lamella specimens were extracted from the columnar grains located at the melt pool centre. Figure 7.6d–f shows annular bright-field STEM (ABF-STEM) images of samples A, B, and C, along with the corresponding STEM-EDXS maps of Cu and Sn. The ABF-STEM images reveal a cellular dislocation structure within columnar grains in all samples, with a high density of dislocations forming dislocation walls (indicated by yellow arrows). The elemental distribution maps reveal the enrichment of Sn along the cellular walls, with a local Sn concentration at the cell wall of approximately 15 wt.%. Based on a series of TEM images similar to those shown in Figure 4d–f, the average size of the cellular structures was estimated using the line intercept method [249] to be approximately 287 ± 10 nm, 342 ± 15 nm, and 407 ± 30 nm for samples A, B and C, respectively. These values were determined from five intercept lines measured across three representative TEM micrographs per sample. The average thickness of the dislocation walls ranges between 50 and 100 nm.

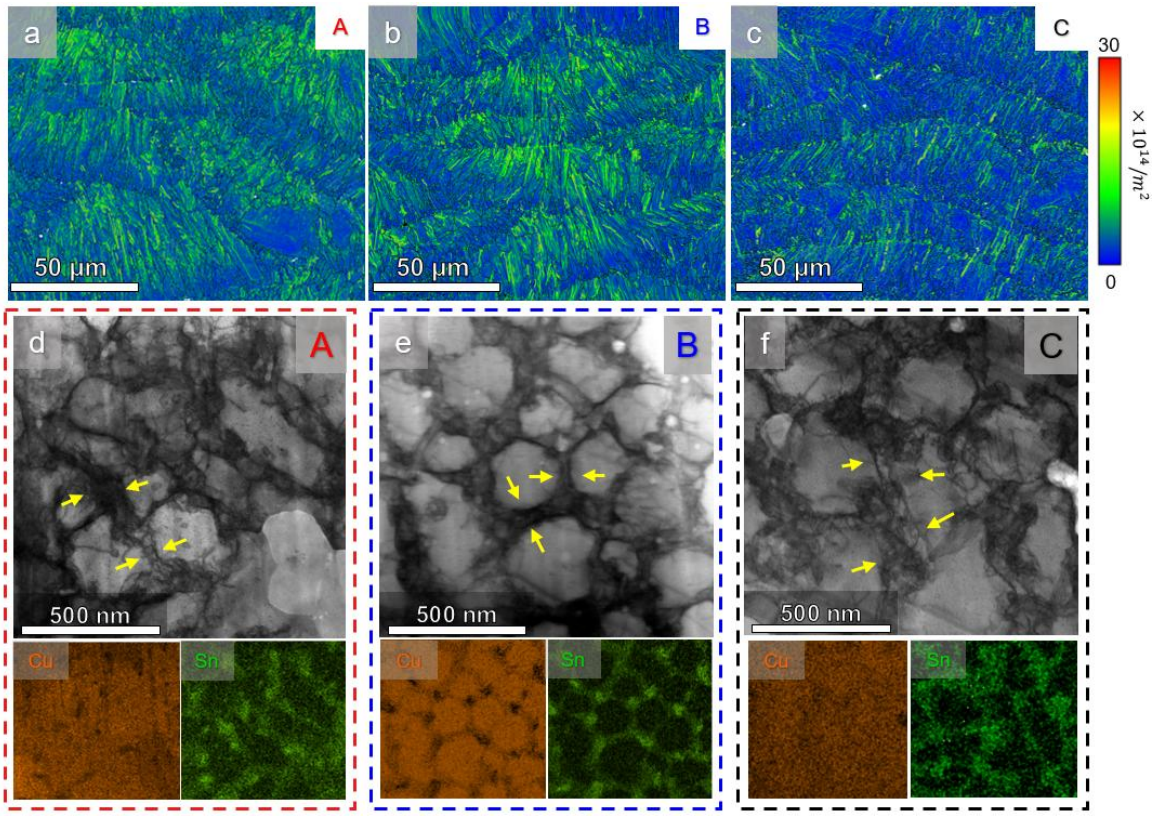

Figure 7.6: SEM and TEM microstructural characterisation of LB-PBF Cu-10Sn samples A, B and C. (a–c) GND density maps derived from EBSD data, corresponding to magnified regions from Figure 3; and (d–f) ABF-STEM images and the corresponding EDXS elemental maps (Cu and Sn) of LB-PBF Cu-10Sn samples A, B and C, respectively, showing the cellular microstructure. TEM specimens were extracted from the melt pool centres. The dislocation cell walls, marked by yellow arrows, coincide with Sn-rich regions, indicating an overlap between dislocations and chemical cell walls.

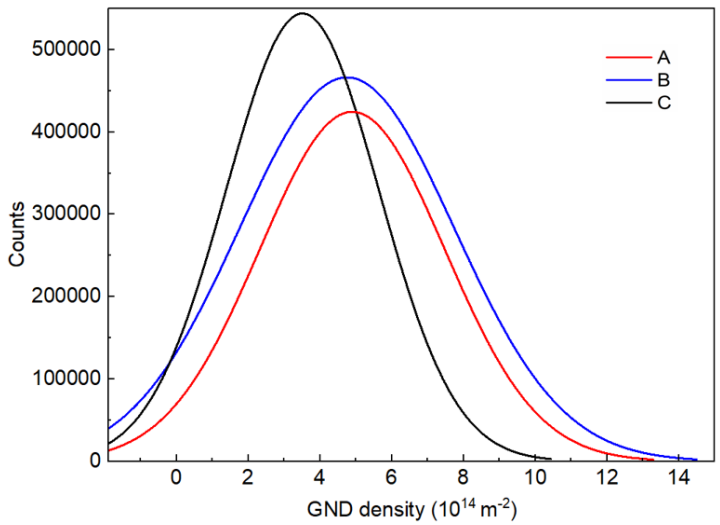

Figure 7.7: The GND density distributions LB-PBF Cu-10Sn samples A, B and C obtained from the EBSD data in Figure 7.6

.

To investigate secondary phase formation in the as-built microstructure, HAADF-STEM imaging and corresponding EDXS analysis were performed, as shown in Figure 7.8a–c. Precipitates were observed in all samples, with average diameters of 121 ± 19 nm for sample A, 118 ± 24 nm for sample B, and larger precipitates of 176 ± 28 nm for sample C. These precipitates were identified as the Sn-rich δ phase as previously reported [106]. In sample A, the δ precipitates exhibit relatively uniform Sn enrichment, with the Sn concentration approximately 29 wt.%. In sample B, while a majority of δ precipitates are predominantly Sn-rich, approximately half of them exhibit additional enrichment in Zn, P, and O, with composition ranges of 1–3 wt.% Zn, 1–2 wt.% P, and 1–5 wt.% O. This precipitate composition, consisting of both purely Sn-rich and multi-element-enriched δ phases, is unique to Sample B. In contrast, the δ precipitates in sample C are more uniformly enriched in both Sn and P, with the P concentration approximately 1–4 wt.%. While the EDXS maps reveal distinct differences in the chemical composition of these δ phases among the samples, their crystal structure remains consistent, as confirmed by high-resolution TEM images and the corresponding fast Fourier transform (FFT) patterns (Figure 7.8d–f). The volume fraction of the δ phase was quantified by Rietveld analysis of XRD patterns, showing an increasing trend, 7.1 vol.% in sample A to 8.0 vol.% in sample B, and 9.6 vol.% in sample C, as summarised in Table 7.3.

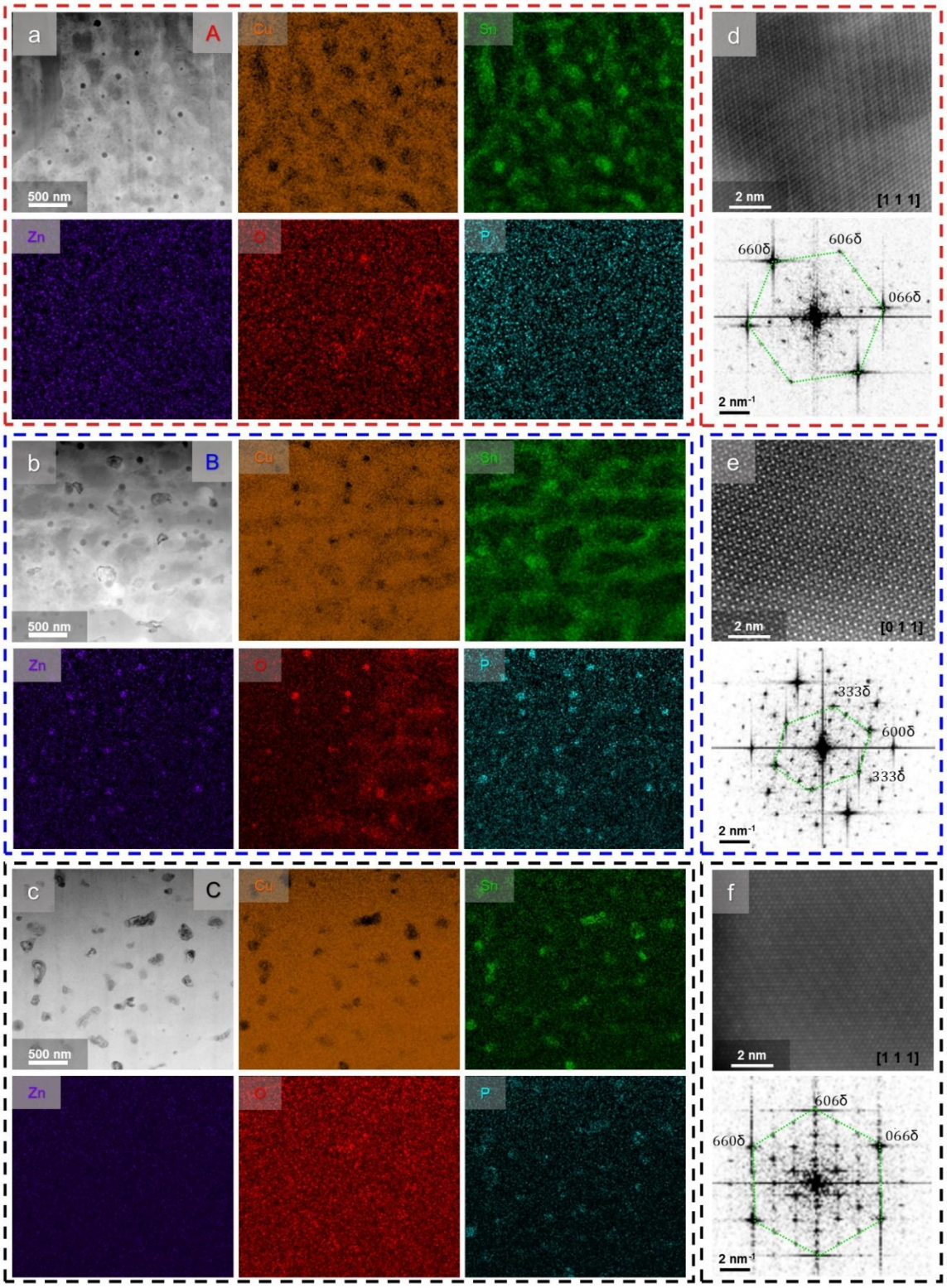

Figure 7.8: TEM microstructural characteristics of LB-PBF Cu-10Sn samples A, B, and C. (a–c) HAADF-STEM images and the corresponding EDXS elemental maps (Cu, Sn, Zn, O and P) showing the distribution and composition of δ precipitates in samples A, B and C, respectively; (d-f) atomic-resolution HAADF-STEM images with FFT patterns, confirming the consistent crystal structure of δ precipitates in all samples. Sample A shows uniformly Sn-rich precipitates. In Sample B, both Sn-rich and Zn, P and O-enriched δ phases are observed, indicating compositional variation. Sample C contains larger δ precipitates mainly enriched in Sn and P.

Table 7.3: Summary of δ precipitate diameter and volume fraction in LB-PBF Cu-10Sn samples A, B, and C.

Sample	Precipitates size in diameter (nm)	Precipitates volume fraction (wt. %)
A	121 ± 19	7.1
B	118 ± 24	8.0
C	176 ± 28	9.6

7.1.4 Fractography and as-built part density

The tensile fracture surfaces of the as-built Cu-10Sn samples were examined using SEM, as shown in Figure 7.9a–c. All samples exhibit ductile fracture characteristics with dimple features, though notable differences are observed among them. Sample A shows micro-cracks and relatively small dimples, while sample B is dominated by larger, well-defined dimples. In contrast, sample C contains macro-cracks, unmelted particles, and striations around the macro-cracks. Density measurements using the Archimedes method indicate that samples A, B, and C all exhibit nearly full densification, with relative densities of 99.99%, 99.98%, and 99.90%, respectively. However, the areal porosity analysis in Figure 7.9d–f reveals greater variation: sample C has the highest areal porosity at 0.73%, compared to 0.32% in sample A and 0.21% in sample B. Sample C contains a higher concentration of unmelted regions and lack-of-fusion voids, whereas sample B primarily features small gas pores, and sample A shows the presence of some large gas pores.

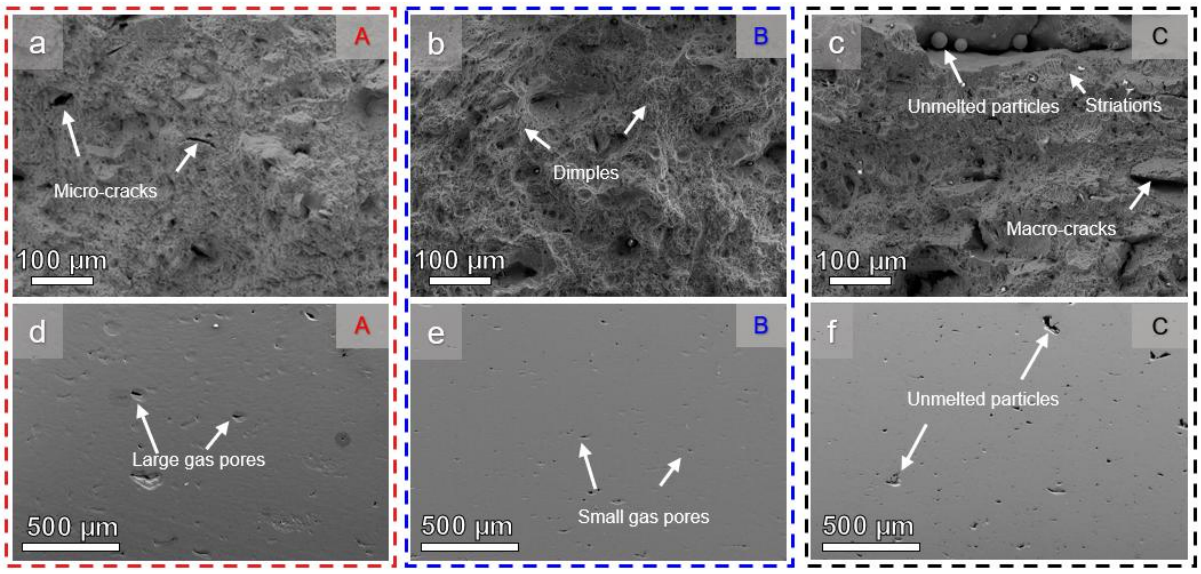

Figure 7.9: SEM microstructural characterisation of LB-PBF Cu-10Sn samples A, B and C. (a–c) fracture surface morphologies after tensile testing; and (d–f) cross-sectional (YZ plane) images used for areal porosity analysis.

7.1.5. FLOW-3D simulation

Figure 7.10 presents computational fluid dynamics simulation results using FLOW-3D, showing the single-track melt pool dimensions for samples A, B and C. The G and $\dot{T}$ at the melt pool centre (marked by a star in Figure 7.10) when the laser scan passes were extracted from the simulations, and the R was then calculated using the formula $R = \dot{T}/G$ [72]. The results are summarised in Table 7.4.

Sample A exhibits the widest and deepest melt pool, followed by sample B, which has a deeper melt pool than sample C. Regarding the thermal history at the melt pool centre, $\dot{T}$ remains nearly consistent across all three samples, whereas G decreases in the order A > B > C. Since R is inversely proportional to G, it follows the opposite trend, C > B > A. The simulation model used in the present work has been validated by experimental data, as demonstrated by the consistent trends in the melt pool dimensions, and agreement with previously reported thermal history data [72, 250, 251].

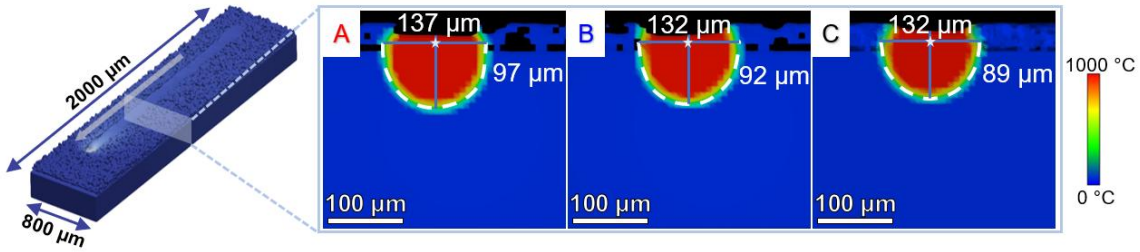

Figure 7.10: Schematic of the single-track FLOW-3D simulations and the resulting melt pool geometries for samples A, B and C. The star symbol indicates the location at the melt pool centre where thermal history parameters (temperature gradient G and cooling rate $\dot{T}$) were extracted.

Table 7.4: Cooling rate, temperature gradient and solidification rate for samples A, B and C extracted from the FLOW-3D simulations.

Sample	Cooling rate, $\dot{T}$ (°C/s)	Temperature gradient, G (°C/m)	Solidification rate, R (m/s)
A	9.51×10^5	1.11×10^7	0.09
B	1.09×10^6	7.70×10^6	0.14
C	1.08×10^6	5.70×10^6	0.19

7.2 Discussion

The present work demonstrates that the ductility of as-built LB-PBF Cu-10Sn alloys can be enhanced, while maintaining their strength, by varying powder characteristics among three powders, while maintaining the same printing parameters. This section discusses the critical powder characterisations that influence the microstructure and the resulting mechanical properties, aiming to understand the correlation between powder characteristics, structure and mechanical properties of the Cu-10Sn alloy in LB-PBF.

7.2.1 Influence of powder characteristics on laser absorbance

Variations in energy input can influence the melting behaviour during LB-PBF, leading to structural defects or increased microstructural complexity in the as-built part [252]. Since laser absorbance serves as a practical, measurable indicator of a powder's ability to absorb

laser energy during the LB-PBF process, it is essential to understand how differences in powder characteristics affect this property.

At a wavelength of 1064 nm, powder A showed the highest laser absorbance (63%), followed by powder B (58%) and powder C (55%) (Figure 7.3c). Given the similarity in bulk compositions among the powders, the discussion focuses on differences in their surface chemical compositions. The enhanced laser absorbance observed for powder A is attributed to its higher Sn composition (9.09%), compared to powders B (7.00%) and C (5.00%), as shown in Table 7.2. Sn is known to significantly increase laser absorbance; for example, coating pure Cu powder with just 0.28% Sn layer increased the absorbance from 19% to 51% at a laser wavelength of 1080 nm, as reported in [253]. Zn also contributes to the higher laser absorbance, as seen in the comparison between powders B and C: powder B contains 21.87% Zn on its surface, and Zn is known to exhibit higher laser absorbance than Cu [254]. Given the very low bulk Zn content, this elevated surface concentration is likely due to Zn surface segregation during processing [255], driven by its lower surface energy, combined with the shallow analysis depth of XPS . Although oxide layers on particle surfaces can also assist in absorbing laser energy [131], this effect appears less dominant in the Cu-10Sn system because powder A, despite having the lowest oxygen content, exhibited the highest laser absorbance. These observations suggest that surface-enriched Sn and Zn are the primary contributors to improved laser absorbance in these powders.

In addition to the surface composition, laser absorbance is also influenced by the PSD and the geometrical arrangement of powder particles. This is because laser beams can be scattered repeatedly between neighbouring particles, leading to additional laser absorbance through multiple scattering [256, 257]. Tran et al. [258] reported that a bimodal PSD enhances laser scattering and absorbance by increasing powder bed packing density. In this

case, both powders A and B showed a similar bimodal PSD, while finer particles (diameter of <10 μm) account for 20% of the total number of particles in powder A, compared to 9% in powder B (Figure 7.3b). The presence of fine particles promotes multiple internal reflections when the laser beam interacts with clusters of small particles [259], which explains the higher laser absorbance observed in powders A and B relative to powder C. The superior laser absorbance of powder A is attributed to its greater proportion of fine particles.

7.2.2 Influence of powder characteristics on as-built porosity

PSD influences not only laser absorbance but also powder bed packing density, especially in the case of bimodal PSD. Fine particles can fill the interstitial spaces between coarse particles, thereby improving packing efficiency and contributing to higher as-built part density, as demonstrated in [258]. This likely explains the lower areal porosity in samples A and B compared to sample C (Figure 7.9). Greater frequency of micro-cracks and slightly higher areal porosity were observed in sample A compared to sample B (Figure 7.9a and d). These defects are likely related to the highest laser absorbance and energy input in powder A, which results in higher G and promotes a strong Marangoni effect that can promote pore formation and incomplete fusion, as previously reported [260, 261].

During LB-PBF, each powder layer is uniformly spread over the previously fused layer by the recoating system, making powder flowability a key factor influencing the porosity of the as-built part [133]. Powder C exhibited the highest cohesive index (Figure 7.3d), indicating poor powder flowability due to the difficulty of transitioning from a static consolidated state to a dynamic flow state. Unlike PSD, the dynamic cohesion index is primarily governed by mean particle size [262], and cohesive powder C tends to form large

agglomerates, which reduce flowability due to increased interparticle friction during spreading. In comparison, powders A and B showed nearly identical and significantly lower cohesive index values (Figure 7.3d), corresponding to superior flowability attributed to their optimised particle sizes. The poor flowability of powder C is clearly linked to its smaller particle size. Such insufficient flowability causes the formation of macrostructural defects, including macro-cracks and unmelted particles, as observed in Figure 7.9c, and correlates with the higher areal porosity measured in sample C compared to samples A and B. We found that larger particle sizes (D50 = ~30 μm and D90 = ~50 μm in powders A and B) are optimal under the current process parameters, as they reduce interparticle friction and enhance powder flowability. These results highlight the importance of optimising powder flowability through control of both particle size and PDS to minimise porosity and defects in LB-PBF parts. The optimal particle size and PSD, however, should be tailored to specific process parameters such as laser spot size and layer thickness.

7.2.3 Influence of powder characteristics on as-built microstructure

Despite differences in powder characteristics, a similar bimodal grain structure was observed for all samples, with fine equiaxed grains decorating melt pool boundaries and columnar grains growing toward the melt pool centres, as shown in the EBSD IPF maps in Figure 7.4. However, notable differences were found in dislocation density and δ phase precipitates. While dislocation cell wall structures were present in all samples, a higher GND density was measured in samples A and B compared to sample C (Figure 7.6 and Section 7.1.3). Additionally, variations in the size, composition, and volume fraction of the δ phase were also observed (Figure 7.8 and Table 7.3). The underlying reasons for these differences are discussed in the following paragraphs.

In general, the as-built microstructure in LB-PBF forms through complex melting and solidification processes [18, 62], which is strongly influenced by the dynamically evolving R and G during laser scanning. During solidification—particularly at high R toward the centre of the melt pool—Sn atoms are ejected into the liquid phase due to the partitioning coefficient of Sn being less than one, forming Sn-rich regions ahead of the solid-liquid interface. This results in constitutional undercooling, which induces instability at the solidification front and causes repeated Sn rejection and redistribution, forming periodic Sn-rich chemical cell wall structures within a single columnar grain [263].

In parallel with the formation of the Sn-rich cell wall structures, the high G during solidification causes local thermal stress from uneven thermal expansion. When these stresses exceed the local YS, a solidified material undergoes plastic deformation to accommodate them [264]. In FCC metals, plastic deformation primarily occurs through dislocation slip along specific crystal planes. As dislocations glide and interact, they become entangled and rearranged into dislocation cell walls [265]. Notably, the pre-formed Sn-rich cell walls can serve as strong pinning sites for dislocation motion, resulting in the spatial overlap between chemical and dislocation cell walls, as reported in [266]. Such cellular dislocation structures have also been observed in metallic materials fabricated by AM [132, 267, 268].

Building on this understanding, the results indicate that samples A and B experienced relatively higher energy inputs than sample C, which results in higher G and lower R, as shown in Table 7.4 and supported by previous studies [269, 270]. The lower R allows more time for Sn atoms to diffuse into the liquid, enhancing solute partitioning and leading to strong Sn segregation at the cell walls. Simultaneously, the high G causes greater thermal stresses, which promote dislocation formation, particularly along the Sn-rich cell walls, as evidenced by the higher GND density in samples A and B. In contrast, sample C

experienced slightly lower G and higher R and exhibited reduced thermal stresses and weaker Sn segregation at the cell walls, resulting in fewer dislocation pinning sites and lower dislocation density.

In some regions, the final fraction of liquid enriched in Sn can be trapped within dendrite arms and subsequently solidifies as Sn-rich δ precipitates, as demonstrated in Chapter 6. In the present work, two types of the δ phase were identified: purely Sn-rich and multi-element-enriched variants (Figure 7.8). The results suggest that impurity or inclusion in the powder, such as Zn, O and P**,** affect the formation of these δ phase precipitates. In sample B, the enrichment of Zn and O within the δ phase indicates their possible involvement in modifying phase stability or refining the precipitate structure. This could occur through the formation of Zn and O clusters that increase the nucleation rate while limiting precipitate growth [271]. In contrast, the presence of P in sample C appears to contribute to precipitate coarsening by reducing nucleation and promoting the growth of existing δ phase precipitates. Due to its low solubility in Cu and Sn, P tends to segregate at grain boundaries and interfaces, which can reduce the number of nucleation sites and facilitate the growth of existing δ phase precipitates. This interpretation is supported by the larger δ phase precipitates observed in sample C (176 ± 28 nm) compared to those in samples A (121 ± 19 nm) and B (118 ± 24 nm). Furthermore, the increasing volume fraction of the δ phase from sample A (7.1 wt.%) to B (8.0 wt.%) and C (9.6 wt.%) indicates that both Zn and P influence not only the formation kinetics but also the thermodynamic stability of the δ phase. Despite these compositional differences, the crystal structure of the δ phase precipitates remained consistent across all samples (Figure 7.8d–f). It should be noted that the proposed roles of Zn and P in modifying δ-phase nucleation and growth are based on compositional trends observed by EDXS and correlations with precipitate size and volume fraction; however, the present data do not permit definitive quantification of solute partitioning or

direct assessment of thermodynamic stability, and therefore these interpretations should be regarded as mechanistically plausible but not conclusively established without higher-resolution techniques such as atom probe tomography.

7.2.4 Interplay between microstructure and mechanical properties

A simultaneous improvement in both strength and ductility was achieved in samples A and B compared to C. Based on the analysis of previous studies [62, 106, 272], this enhancement is attributed to multiple strengthening mechanisms, including grain boundary strengthening (σ_{GBS}), precipitation strengthening (σ_{PS}), and dislocation strengthening (σ_{DS}), as summarised in Table 7.5 (see Appendix C for analytical procedures). According to the classical Hall-Petch relationship, reducing grain size enhances strength through σ_{GBS}. In this study, all samples exhibited refined grain structures with mean grain sizes of 3.4–3.7 μm (Section 7.1.3), which are markedly finer than those of conventionally cast Cu-10Sn. This results in a consistent σ_{GBS} contribution of 149 ± 2 MPa across all three samples. Another major strengthening mechanism arises from the interaction between δ precipitates and dislocations via the Orowan mechanism [273], making dislocation-precipitate interaction the primary source of σ_{PS}. The σ_{PS} correlates with the precipitate size and volume fraction (Table 7.3), with sample B showing the highest precipitation strengthening (110 MPa), followed by sample A (101 MPa) and sample C (93 MPa). This indicates that finer δ precipitates in samples A and B contributed to superior strengthening. The σ_{DS} values were estimated using the Baily-Hirsh relationship, based on the GND densities quantified from EBSD (Section 7.1.3). The calculated values were 192, 190, and 176 MPa for samples A, B and C, respectively (Table 7.5), with samples A and B showing approximately 8% higher σ_{DS} than sample C. Since σ_{DS} contributes to the flow strength

after yielding [274], this aligns with experimental observations where samples A and B exhibited approximately 9% higher UTS compared to sample C.

Table 7.5: Summary of estimated precipitation strengthening, grain boundary strengthening and dislocation strengthening for LB-PBF Cu-10Sn samples A B and C.

Sample	σ_{GBS} (MPa)	σ_{PS} (MPa)	σ_{DS} (MPa)
A	150	101	192
B	150	110	190
C	146	93	176

This work demonstrates that the dislocation cell structure significantly contributes to the enhanced strength and ductility observed in samples A and B, while the stabilised cellular substructure enables stable plastic deformation and helps retain ductility. The high dislocation density associated with dislocation cell wall structure (Figure 7.6) impedes dislocation motion and thereby enhances strength. As deformation progresses, dislocations initially impeded by these cell walls gradually pass through them. At the same time, segregated Sn atoms exert a pinning effect that stabilises the dislocation cell walls, preserving their structure during plastic deformation and promoting stable plastic flow. Consequently, the dislocation cell walls, overlapping with Sn-rich cell walls, serve as stable yet "soft" barriers: they resist dislocation motion to enhance strength, while allowing the transmission of dislocations, ensuring continuous plastic flow. This behaviour is consistent with findings from in-situ TEM studies reported in [267].

Another factor that affects the ductility of the as-built sample is the presence of macrostructural defects formed during LB-PBF process. Sample C showed the lowest ductility, likely due to the presence of lack-of-fusion defects (Figure 7.9), which were

caused by lower energy input, reduced powder bed packing efficiency, and insufficient melting. Poor powder flowability can cause uneven powder bed packing to localised temperature variations during melting. These variations generate internal stresses that may ultimately form large pores or unmelted regions. The striations visible along the fracture surface of sample C (Figure 7.9) indicate the incremental crack growth and reveal the direction of crack propagation. The large gas pores observed in sample A are attributed to the higher energy input. While these defects are less severe than those in sample C, they still act as stress concentrators and contribute to the reduced ductility of sample A compared to sample B.

7.2.5 Powder-microstructure-property relationship

The LB-PBF Cu-10Sn fabricated using the three different powders showed distinct mechanical properties, despite being processed with identical printing parameters. Remarkably, the ductility of samples A and B was more than twice that of sample C, achieved solely through variations in powder characteristics. As discussed earlier, these powder characteristics influence the resulting microstructure and the mechanical properties. This section provides a summary of the relationship between powder characteristics, structure, and mechanical properties.

Key powder properties, including PSD and chemical composition, are intrinsic, while the laser absorbance and flowability are process-relevant outcomes derived from these intrinsic powder properties, determining how well the powder interacts with LB-PBF processes. Based on our results, the laser absorbance significantly impacts energy input, which directly influences melt pool dynamics and subsequent microstructural features such as dislocation/Sn-rich cell wall structures and δ phase precipitates.

A bimodal PSD and relatively larger particle sizes contribute to improved powder bed packing density and flowability, both of which reduce porosity and enhance the macrostructural integrity of the printed parts, critical factors for enhancing ductility. Additionally, the chemical composition of the powder affects the formation and distribution of dislocation/Sn-rich cell wall structures and δ phase precipitates. The combined effect of these factors explains the superior strength and ductility observed in samples A and B compared to sample C. These results underscore the importance of optimising and controlling powder characteristics. By tailoring PSD, flowability, laser absorbance, and chemical composition, it is possible to push the performance boundaries of LB-PBF alloys, achieving simultaneous improvements in both strength and ductility.

7.3 Summary

This study demonstrated that enhanced strength and ductility can be achieved in as-built Cu-10Sn alloys via LB-PBF by investigating how powder characteristics influence both macrostructure and microstructure. The conclusions of this study are summarised as follows:

(1) Powders with a bimodal PSD, comprising both fine and coarse particles, and higher surface concentrations of alloying elements such as Sn and Zn exhibit enhanced laser absorbance. This leads to improved energy input and more favourable melting and solidification behaviour during LB-PBF. The bimodal PSD also facilitates higher powder bed packing density and optimises powder flowability, promoting uniform layer distribution. These key powder characteristics collectively minimise the formation of macroscopic defects, such as porosity and unmelted

particles, and contribute significantly to the enhanced strength and ductility of the as-built Cu-10Sn alloys.

(2) The formation of dislocation cell wall structures in conjunction with Sn-rich chemical cell walls, is a key microstructural feature contributing to the enhancement of strength and ductility. These structures result from high temperature gradients and strong thermal stresses generated during the rapid solidification process in LB-PBF. A high laser absorption of the powders promotes higher dislocation density. The stable dislocation networks, together with δ phase precipitates, increase YS and resistance to deformation while enabling continuous plastic flow, thereby achieving a balance between strength and ductility.

(3) In practical terms, the optimum LB-PBF powder for Cu-10Sn should combine: (i) a highly bimodal PSD with a fine-to-coarse particle size ratio that maximises powder packing density and flowability; (ii) relatively larger mean particle sizes tuned to process parameters to minimise cohesion; and (iii) deliberate surface element modification, such as Sn enrichment and Zn addition, to enhance laser absorbance, while minimising contamination or oxide levels to avoid defect formation. Achieving this combination ensures efficient energy absorption, stable melt pool dynamics, defect minimisation, and microstructural refinement, thereby maximising the strength–ductility balance in the final build.

These findings underscore the importance of both macro- and microstructural control, enabled through the optimisation of powder characteristics, such as PSD with a high coarse-to-fine particle ratio, surface chemical composition, and flowability, to minimise structural defects and tailor the microstructure for maximising the mechanical properties of LB-PBF Cu-10Sn alloys. This study provides practical insights for enhancing material properties

through strategic powder design and process adjustments, offering a pathway toward superior AM outcomes.

Chapter 8 Manufacturing High-Strength, High-Conductivity Cu via Directed Energy Deposition

To address Aim 4, developing processing strategies to balance high strength and electrical conductivity in Cu alloys, a novel alloy design strategy combining moderate Ti additions with graphene nanoplatelets is explored to enhance both processability and performance in Cu-based alloys processed by LB-DED. The graphene addition offsets Cu's high infrared reflectivity, enabling stable melt-pool formation, while Ti is supersaturated in the Cu matrix during rapid solidification and subsequently precipitates as fine β′-Cu_4Ti on ageing, thereby strengthening the alloy at minimal solute content and limited conductivity penalty. Systematic ageing at 470 °C reveals a clear precipitation-hardening response: YS increases from 167 MPa in the as-built state to a higher of 315 MPa at 3 h, accompanied by significant improvements in UTS from 334 to 463 MPa), while with a reduction in ductility (31 % → 17 %). Multi-scale characterisation including EBSD, TEM and APT demonstrates that the strengthening arises from the formation of coherent β′ precipitates (~4 nm, 0.12 vol.%). Concurrently, electrical conductivity improves from 11.8 % IACS in the as-built state to 25.4 %IACS after ageing due to solute depletion of Ti in the Cu matrix. These findings establish the efficacy of moderate-Ti/graphene design in enabling laser processing of Cu and provide fundamental insights into the microstructure–property relationships governing precipitation-strengthened Cu alloys. The results lay the foundation for developing high-strength, high-conductivity Cu-based components for electrical and thermal management applications.

8.1 Design strategy

The key feature of the design strategy is to combine a moderate Ti addition with graphene, which (i) enables melting of Cu powders using a standard 1030 nm infrared laser despite Cu's high reflectivity and thermal conductivity, (ii) supersaturates the Cu matrix with Ti during rapid solidification, and (iii) yields fine precipitates on heat treatment that strengthen while preserving high electrical conductivity at low Ti content. The design principles are as follows:

(1) Solubility and conductivity: A moderate Ti addition is selected for its low solid solubility in Cu at ambient temperatures, ensuring minimal electron-scattering and thus limited impact on conductivity, while still enabling age-hardening via fine Cu–Ti precipitates at low overall Ti (~1%).

(2) Absorptivity: Graphene nanoplatelets are introduced specifically to offset Cu's high near-IR reflectance, enhancing laser energy coupling to the powder feedstock and promoting stable melt-pool formation.

(3) Ti dissolution and precipitation: Ti should dissolve sufficiently in the transient melt pool and precipitate on solidification/ageing as a fine, well-dispersed precipitates, maximising strengthening at minimal volume fraction.

8.2 Results

8.2.1 Microstructural characterisation

Figure 8.1 presents Thermo-Calc simulations for the Cu–1Ti system. The equilibrium phase diagram (Figure 8.1a) indicates that the alloy solidifies into α-Cu around ~1050 °C, with β precipitating below ~600 °C. Precipitation simulations reveal the mean radius of β as a function of time under isothermal ageing at 470 °C (Figure 8.1b) and 570 °C (Figure 8.1c).

At 470 °C, the precipitate radius grows slowly from ~1 nm to ~10 nm over 3 h, whereas at 570 °C, rapid coarsening occurs, reaching nearly 20 nm with a pronounced two-stage growth regime. Based on these results, 470 °C was selected as the optimal ageing temperature to suppress excessive coarsening of β and maintain a fine precipitate distribution.

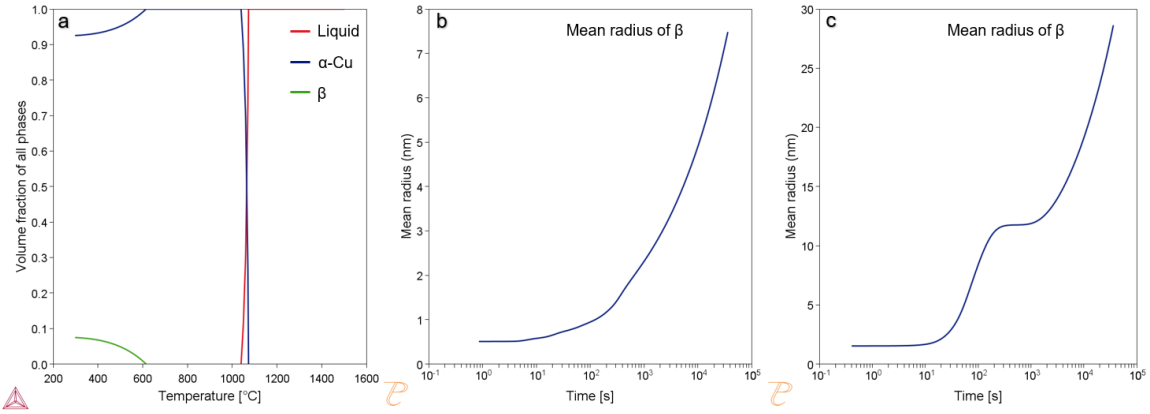

Figure 8.1: Phase analysis of Cu-1Ti using Thermo-Calc simulations. (a) volume fraction of the stable phases as functions of temperature; (b) the variations in mean size (radius) of β phase with ageing time at 470 °C; and (c) the variations in mean size (radius) of β phase with ageing time at 570 °C.

Figure 8.2 shows the EBSD IPF maps of the as-built, 0.5 h aged, and 3 h aged Cu–1Ti samples. The as-built sample (Figure 8.2a) exhibits elongated columnar grains, characteristic of directional solidification during the LB-DED process. After short-term ageing for 0.5 h at 470 °C (Figure 8.2b), the grain morphology remains largely unchanged, although slight recovery features can be observed within individual grains. With prolonged ageing for 3 h (Figure 8.2c), the microstructure evolves towards a more homogeneous appearance, with reduced intragranular contrast indicative of annealing effects. Due to the large grain size in all conditions, no strong crystallographic texture is observed.

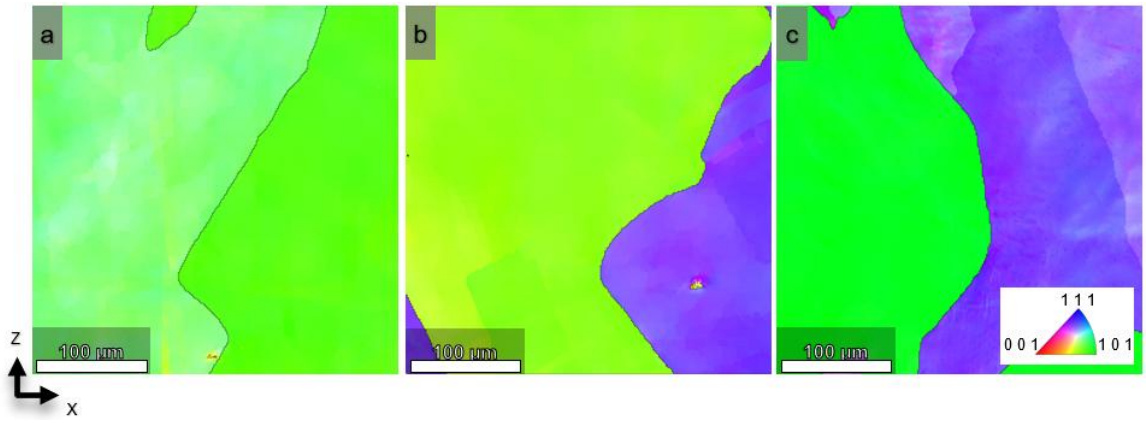

Figure 8.2: Microstructure analysis of the as-built and heat-treated LB-DED Cu-1Ti samples. EBSD IPF maps of (a) the as-built sample; (b) the aged sample at 470 °C for 0.5 h; and (e) the aged sample at 470 °C for 3 h.

Figure 8.3 presents the TEM microstructural observations of LB-DED Cu-1Ti samples aged at 470 °C for 0.5 h and 3 h, representing the early stage of ageing and a condition near the highest observed hardness, respectively. After a short ageing time of 0.5h, the HAADF-STEM image (Figure 8.3a) reveals a mottled contrast throughout the matrix, which corresponds to a moderate chemical fluctuation (Ti-rich and Ti-lean regions) associated with the early stages of spinodal decomposition. A magnified region (Figure 8.3b) highlights these nanoscale modulations, and the FFT pattern (Figure 8.3c) exhibits only fundamental reflections of the α(Cu) matrix, confirming the absence of ordered β′ precipitates at this stage. In contrast, after 3 h ageing, the ABF-STEM image (Figure 8.3d) reveals the presence of uniformly distributed and disk-shape precipitates with lengths of several tens of nanometres. The magnified view in Figure 8.3e shows their coherent morphology, and the FFT pattern (Figure 8.3f) contains additional superlattice reflections indexed to β′ (space group: I4/m and lattice parameters of a = 0.585 nm and c = 0.365 nm). These results indicate that that precipitation commences between 0.5 h and 3 h of ageing at 470 °C, following the sequence of compositional modulation (clustering) in the solid solution to the ordering in the Ti-rich regions and finally to the nucleation of

β′ precipitates. Importantly, only the metastable β′ phase is detected under these conditions, with no evidence of the stable β phase.

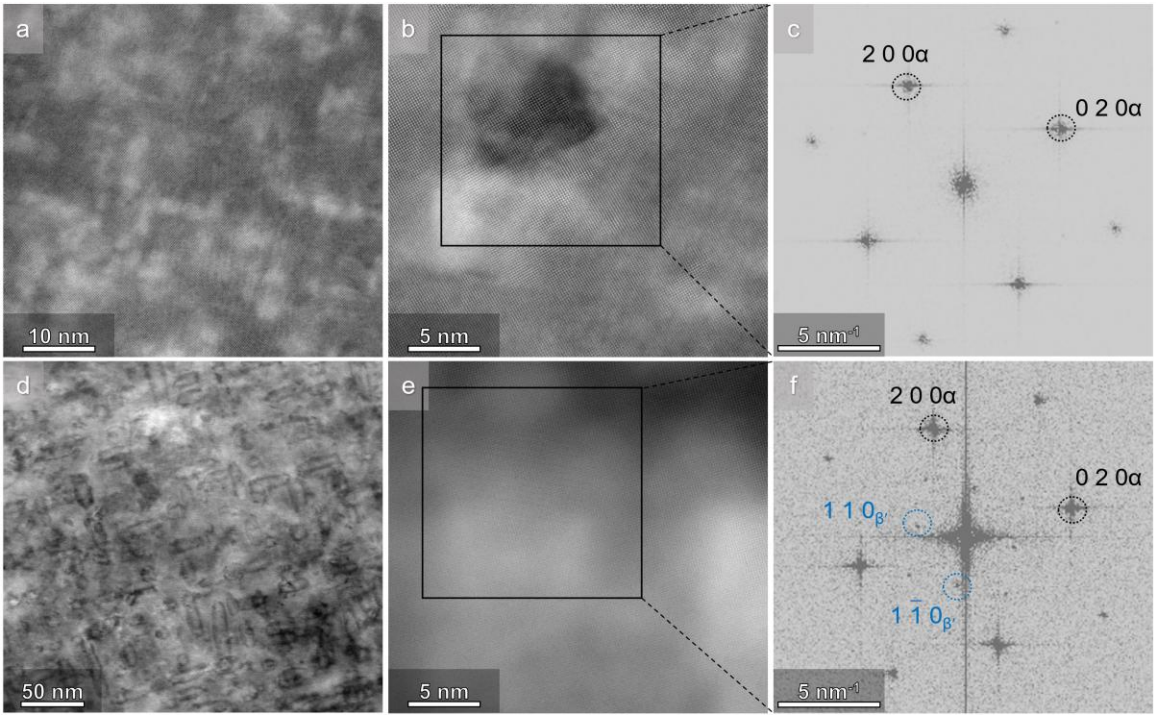

Figure 8.3: TEM microstructural observations of the LB-DED Cu-1Ti samples aged at 470 °C for 0.5h and 3h. (a) HAADF-STEM image showing microstructure of the sample aged for 0.5 h; (b) corresponding magnified region from (a); (c) FFT pattern converted from the region marked in (b); (d) ABF-STEM image showing the precipitates in the sample aged for 3 h; (e) corresponding magnified region from (d); and (f) FFT pattern of β′ precipitate, converted from the region marked in (e).

To gain insights into the chemistry of the β′ and their volume fraction, APT was performed on the LB-DED Cu-1Ti sample aged at 470 °C for 3h. The iso-concentration surfaces of Ti visualise the β′ precipitates (Figure 8.4a), which have an average diameter of 4.2 nm. The volume fraction, calculated as the number of atoms within the precipitates divided by the total number of atoms in APT datasets, is 0.12%. Proxigram analysis reveals the composition in the β' precipitate (Figure 8.4b), which contains 81.3 at.% of Cu and 18.7 at.% of Ti. It should be noted that the precipitate volume fraction estimated from APT reconstruction represents a highly local measurement and may not fully reflect bulk

statistics; therefore, future work will incorporate multiple APT regions and independent mass-balance estimations based on bulk composition and precipitate stoichiometry, supported by TEM quantification, to provide a more comprehensive evaluation.

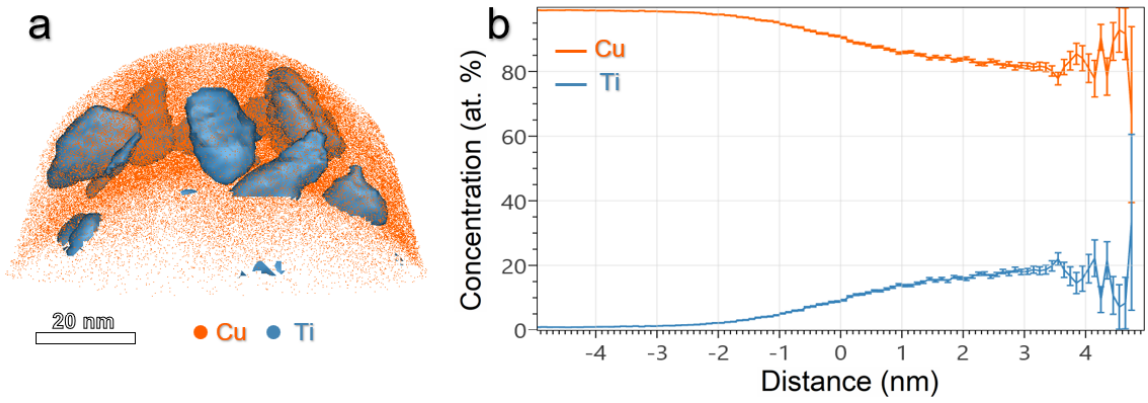

Figure 8.4: Atom probe tomography reveals the three-dimensional atom map reconstruction (a) with proxigram-based composition profile (b) derived from the Ti iso-concentration surface for the LB-DED Cu-1Ti aged at 470 °C for 3h.

8.2.2 Mechanical response and electrical conductivity

Figure 8.5 shows the hardness evolution of the LB-DED Cu–1Ti as a function of ageing time at 470 °C. The as-built sample exhibits a baseline hardness of 108 ± 15.6 HV_1. Upon ageing, the hardness progressively increases with time, rising from 109 ± 8.3 HV_1 at 0.1 h to 144 ± 27.0 HV_1 at 1 h, and further to the highest value in this dataset of 161 ± 22.7 HV_1 at 3 h.

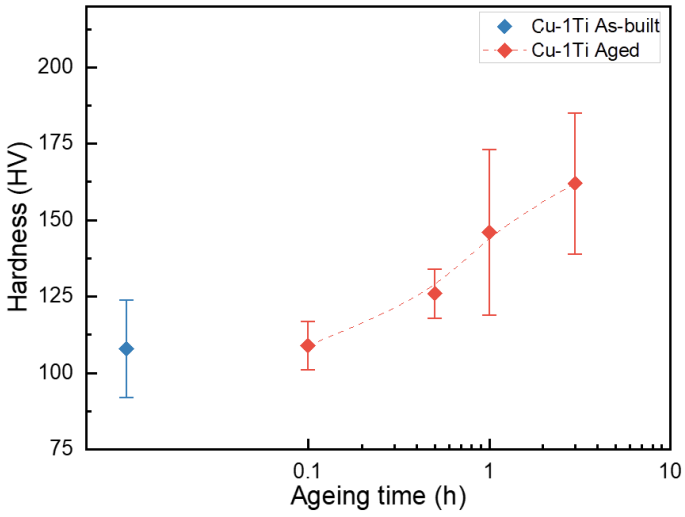

Figure 8.5: The age hardening response of the LB-DED Cu-1Ti samples and the variations in hardness with ageing time at 470 °C.

The tensile properties of the LB-DED Cu-1Ti alloy in the as-built and aged conditions are presented in Figure 8.6a. The as-built sample exhibits a YS of 167 MPa, UTS of 334 MPa, and a total elongation at fracture of 31%. After ageing at 470 °C for 0.5 h, YS increases to 209 MPa and a UTS to 399 MPa, while a slight reduction in elongation at fracture to 26%. Ageing at 470 °C for 3 h further strengthens the alloy, with YS reaching 315 MPa and UTS 463 MPa, but elongation declines to 17%.

The electrical conductivity of the as-built alloy was measured as 11.8 % IACS. Ageing at 470 °C for 0.5 h and 3 h increases the electrical conductivity to 20.9 % and 25.4 % IACS, respectively. As shown in Figure 8.6b, although the conductivity values remain below those of the LB-PBF pure Cu, the concurrent strengthening and conductivity improvement during ageing demonstrates a favourable trend. The combined strength–conductivity properties of the Cu-1Ti alloy achieved in this work surpass the Cu alloys such as CuNiSi, CuSn, CuCr, and CuCrZr, and are competitive with more advanced Cu containing nano-carbon or oxide reinforcements.

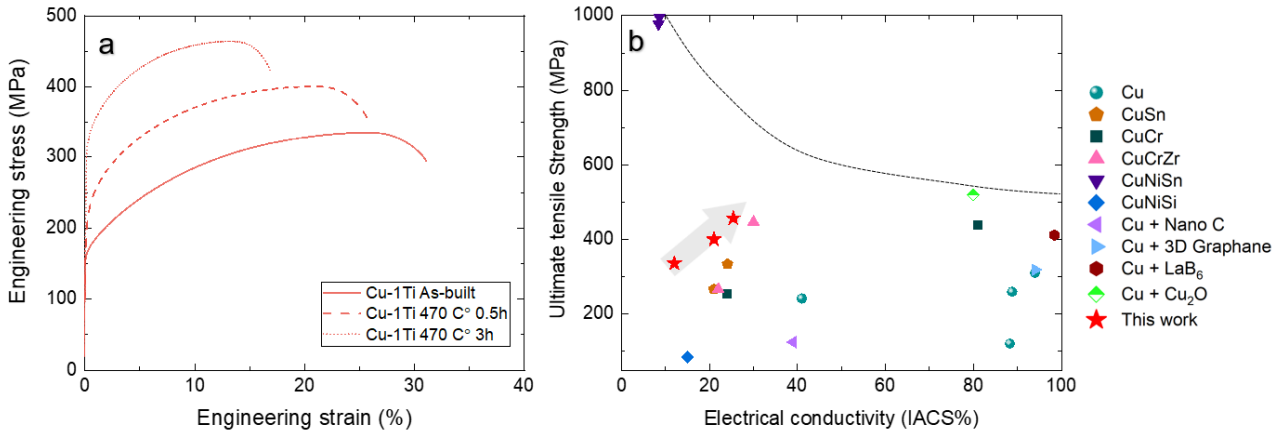

Figure 8.6: Tensile property and electrical conductivity of LB-DED Cu-1Ti alloys. (a) tensile engineering stress-strain curves of as-built samples and samples aged at 470 °C for 0.5h and 3h; and (b) comparison of UTS and electrical conductivity of the Cu-1Ti sample in this work with previously reported Cu and Cu alloys produced by LB-PBF [45, 63, 64, 208, 275-283].

8.3 Discussion

8.3.1 Strengthening mechanisms

The increased strengthening observed in the LB-DED Cu–1Ti alloy can be rationalised by considering the possible contributions from grain boundary (σ_{GBS}), solid solution (σ_{SSS}), dislocation (σ_{DS}), and precipitation mechanisms (σ_{PS}) [106, 228]. EBSD (Figure 8.2) confirms that grain morphology remains largely unchanged during ageing, indication negligible σ_{GBS}. No evidence of additional dislocation multiplication during ageing is observed in TEM images (Figure 8.3). Therefore, dislocation strengthening is not a major contributor in this system.

By contrast, TEM and APT analyses (Figure 8.3 and 8.4) confirm the presence of nanoscale, coherent β′ precipitates (with average diameter of 4.2 nm and volume fraction of 0.12%), which are uniformly dispersed after 3 h ageing at 470 °C. The early stage of ageing (0.5 h) is characterised by chemical modulations and clustering, with no ordered precipitates, consistent with the moderate strengthening observed in hardness and tensile

testing (Figure 8.5 and 8.6). After 3 h, however, the formation of coherent β′ precipitates accounts for the highest hardness (161 HV_1) and strength (YS 315 MPa, UTS 463 MPa). Importantly, no evidence of the stable β phase is observed, indicating that precipitation hardening [284] is the primary strengthening mechanism enabled by β′ precipitates.

In general, the Orowan bypass mechanism becomes operative once precipitates grow beyond a critical radius or lose coherency with the matrix, whereas sufficiently small and coherent precipitates are primarily strengthened through shearing [285]. To evaluate the precipitation-strengthening mechanisms, the strength increments from shearing, taken as the sum of coherency($\Delta\sigma_{coh}$) and modulus ($\Delta\sigma_{mod}$)strengthening, and strengthening by the orowan bypass mechanism ($\Delta\sigma_{or}$) were calculated using the methodology outlined in [285, 286] and are listed in Table 8.1. These predicted values are compared to the experimental strength increment ($\Delta\sigma$) 148 MPa (Table 8.1), which is the increase in YS from the as-built to the 3 h aged state.

The increase in the YS due to the coherency strengthening is given by [286]:

$$\Delta\sigma_{coh} = M\alpha_{\varepsilon}(G\varepsilon)^{\frac{3}{2}}\left(\frac{rf}{0.5Gb}\right)^{\frac{1}{2}}$$

where M is the Taylor factor of Cu (3.1) [232], α_{ε} is a constant (2.6) [287], G is the shear modulus (48.3 GPa) [233], ε is the constrained lattice parameter mismatch (taken to be that of β′ in Cu, 0.0164) [288], r is the average radius of β′, and f is the volume fraction of β′, and b is the Burgers vector of Cu (2.56×10^{-10} m) [228].

The increase in the YS due to the modulus mismatch is given by [286]:

$$\Delta\sigma_{mod} = 0.0055M\,(\Delta G)^{\frac{3}{2}}\left(\frac{2f}{Gb^2}\right)^{\frac{1}{2}} b\left(\frac{r}{b}\right)^{(\frac{3m}{2}-1)}$$

where ΔG is the shear modulus mismatch between the matrix and the precipitates (13.4 GPa) [288], and m is a constant (0.85) [287].

The increase in the YS for the Orowan bypass mechanism is estimated using the same equation as shown in Section 6.2.3.

Table 8.1: Experimental observed and calculated strengthening for the LB-DED Cu-1Ti sample aged at 470 °C for 3 h.

Sample	Experimental strengthening $\Delta\sigma$ (MPa)	Calculated Coherency and modulus strengthening $\Delta\sigma_{coh} + \Delta\sigma_{mod}$ (MPa)	Calculated Orowan strengthening $\Delta\sigma_{or}$ (MPa)
3 h aged	148	126	133

The close agreement between the experimentally observed strength increment (148 MPa) and the calculated contributions from both coherency/modulus strengthening (126 MPa) and Orowan bypass strengthening (133 MPa) suggests that the precipitate size in this study lies near the critical size at which the operative deformation mechanism transitions from precipitate shearing to bypass. With an average β′ precipitate diameter of 4.2 nm, the strengthening effect appears to be at the boundary between these two regimes, where either shearing or Orowan looping could be activated depending on local variations in precipitate size and distribution. This is consistent with the notion that at small precipitate radii, dislocation shearing dominates, whereas at larger sizes, bypass becomes energetically favourable.

Although the primary strengthening mechanism in the aged condition arises from β′ precipitation, solid-solution strengthening from Ti should also be considered, particularly in the as-built state. A simple Fleischer-type estimate suggests that 1 wt.% Ti dissolved in the Cu matrix can contribute approximately 70–95 MPa to the yield strength [289]. This estimate is consistent with the experimentally observed difference between the yield strength of the as-built Cu–1Ti alloy (~167 MPa) and that of pure Cu (typically 60–80 MPa). During ageing, Ti atoms progressively partition from the matrix into β′ precipitates, reducing the solute concentration in solid solution. Consequently, the contribution of solid-solution strengthening decreases, while the observed increase in strength is primarily governed by precipitation strengthening from β′ precipitates.

8.3.2 Origination of the high electrical conductivity

The electrical conductivity of alloys is generally governed by multiple scattering contributions that restrict the movement of conductive electrons, including the resistivity originating from pure Cu (1.75 μΩ·cm), grain boundaries, dislocations, dissolved solute atoms, and precipitates, as outlined by Matthiessen's rule [137-139]. In the present LB-DED Cu-1Ti system, several of these factors can be considered negligible. Firstly, dissolved solute atoms are minimal because the Ti concentration is very low and majority of Ti atoms are consumed during precipitation reactions, particularly after ageing, leaving little solute in the Cu matrix. Secondly, the dislocation density in the as-built alloy, although measurable, contributes only marginally to resistivity: reported values indicate that a dislocation density on the order of 10^{-14} m^{-2} would yield resistivity of only approximately 10^{-3} μΩ·cm [290], well below the resistivity of pure Cu. Similarly, the effect of grain boundary scattering is also limited. With a grain size in the order of tens of

micrometres, compared to the electron mean free path of 40 nm [138], the resistivity from grain boundaries is considered as insignificant according to the relationship between mean free path of conductive electrons and grain size in [138, 291].

Consequently, the dominant factor influencing electrical conductivity is the precipitation behaviour of Ti. As confirmed by TEM and APT, ageing at 470 °C produces a fine distribution of coherent β′ precipitates with nanometre-scale dimensions. Because these precipitates remain coherent with the Cu matrix, the lattice strain fields are localised and electron scattering is limited, in contrast to incoherent or coarse equilibrium β precipitates that are known to cause significant conductivity reductions in Cu alloys with higher Ti addition [292, 293]. The observed rise in electrical conductivity during ageing is therefore attributed to two concurrent effects: the removal of Ti atoms from solid solution, which reduce the resistivity from solute atoms, and the coherent nature of the β′ precipitates, which minimises the resistivity from precipitates.

Therefore, the origin of high electrical conductivity in LB-DED Cu–1Ti is closely linked to its microstructural characteristics, including coarse grain size suppressing the resistivity from grain boundaries, minimal retained Ti in matrix lowering the resistance from solute atoms, and predominance of coherent β′ precipitates that act as relatively weak scattering centres. These features collectively explain the progressive recovery of conductivity during ageing, reaching values above 25% IACS, while maintaining significant precipitation strengthening. This microstructural balance enables the alloy to achieve a combination of improved mechanical strength and retained electrical conductivity, distinguishing it from conventional Cu-Ti alloys where conductivity losses are severe. Although the conductivity remains below that of conventional high-conductivity Cu alloys, this balance between strength and conductivity represents a promising outcome for AM Cu–Ti. Further optimisation of alloy composition and heat

treatment is expected to mitigate conductivity losses more effectively and enhance its suitability for electrical-structural applications.

8.4 Summary

In summary, this chapter established a viable strategy for manufacturing high-strength, high-conductivity Cu alloys by combining moderate Ti additions with graphene nanoplatelets in the LB-DED process. The central principle of this approach is to simultaneously overcome the intrinsic processing difficulties of Cu and to exploit controlled precipitation strengthening. Graphene enhances laser absorptivity, enabling stable melt-pool formation, while rapid solidification supersaturates Ti into the Cu matrix. Subsequent ageing at 470 °C promotes the formation of fine, coherent β′-Cu_4Ti precipitates, which provide significant strengthening without severely compromising electrical conductivity. This design pathway demonstrates that high-strength Cu-based alloys with retained conductivity can be fabricated using LB-DED, filling a critical gap for advanced electrical and thermal management applications. More broadly, the moderate-Ti/graphene strategy highlights the potential of coupling absorptivity modifiers with precipitation-strengthened systems, providing a generalisable framework that may be extended to other alloy systems to realise additively manufactured components with balanced structural and functional performance. Ongoing work on a reduced Ti composition (0.6 wt.%) aims to evaluate whether further lowering residual Ti in solid solution can enhance electrical conductivity while maintaining effective precipitation strengthening.

Chapter 9 Age-hardening Response of Cu-30Ni Alloys: The Role of Si Microalloying Additions

Cu–Ni alloys are extensively utilised in marine and chemical processing environments, where mechanical robustness, corrosion resistance, and long-term microstructural stability are essential for reliable service. To address Aim 5, the age hardening response of Cu-30Ni alloys is systematically investigated to elucidate the role of Si in microstructural evolution during age hardening heat treatments. Although Cu-Ni is well known to be a solid solution system, industrial alloys typically contain microalloying additions of Fe, Mn, Nb and/or Si, which invoke an age hardening response. However, an understanding of the microstructural evolution during age hardening heat treatments remains incomplete. While this study employs arc-melted Cu-30Ni alloys, the findings are directly relevant to CSAM, where alloy design and post-spray heat treatments are critical for achieving desired performance. In this study, ageing treatments are systematically conduced and the resulting hardness and microstructures are reported. The results show that Cu-30Ni alloy with Si aged at 650 °C for 6 h demonstrate significantly enhanced Vickers hardness, reaching ~201 HV_1 compared to 103 HV_1 for the as-homogenised sample. The microscopy experiments reveal the composition, size, and volume fraction of Si-rich clusters and γ′ precipitates, and we use this data to estimate their contribution to the improved strength. First-principles atomistic simulations elucidate the underlying formation mechanisms of these clusters and precipitates, highlighting the critical role of Si in driving their nucleation and growth. This study advances the design of high-strength Cu alloys with the potential for corrosion resistance in demanding maritime environments. This study provides valuable insights that advance the understanding of age hardening response in this alloy and guide the design of alloys with superior and tailored properties. This renewed scholarly attention not only aims

to bridge the historical knowledge gap but also seeks to integrate Cu-30Ni alloys into the exploration of advanced materials. The insights gained serve as a foundation for the development and optimisation of high-performance Cu-30Ni components produced via CSAM for use in demanding environments.

9.1 Results

9.1.1 Hardness variation under various heat treatment methods

Figure 9.1a–b shows Thermo-Calc simulations that analyse the changes of Ni mass fraction at 1000 °C over various durations (Figure 9.1a) and the equilibrium phase volume fractions across temperatures (Figure 9.1b). Ni distribution becomes increasingly uniform after over 16 h of homogenisation, facilitating sufficient Ni diffusion. During equilibrium solidification (Figure 9.1b), FCC α(Cu) phase with a Cu/Ni ratio of 3:1 nucleates and grows below 1240 °C, while an FCC γ′ phase emerges below 680 °C. Based on this simulation, the ageing temperature of 650 °C was selected to promote γ′ precipitate. Figure 9.1c–e shows the cross-sectional microstructure of the as-arc-melted, as-homogenised, and aged 0.5Si FA-FC samples. The EBSD random colour grain maps show columnar grains along the bottom-to-top direction (heat flow direction during arc-melting) for all samples, with fine grains and Ni-rich dendrites observed in the as-arc-melted sample (Figure 9.1c). These features disappear after homogenisation, yielding a compositional homogeneous microstructure (Figure 9.1d–e). No preferential crystallographic texture is evident in the EBSD maps, justifying the use of random colouring for grain orientation.

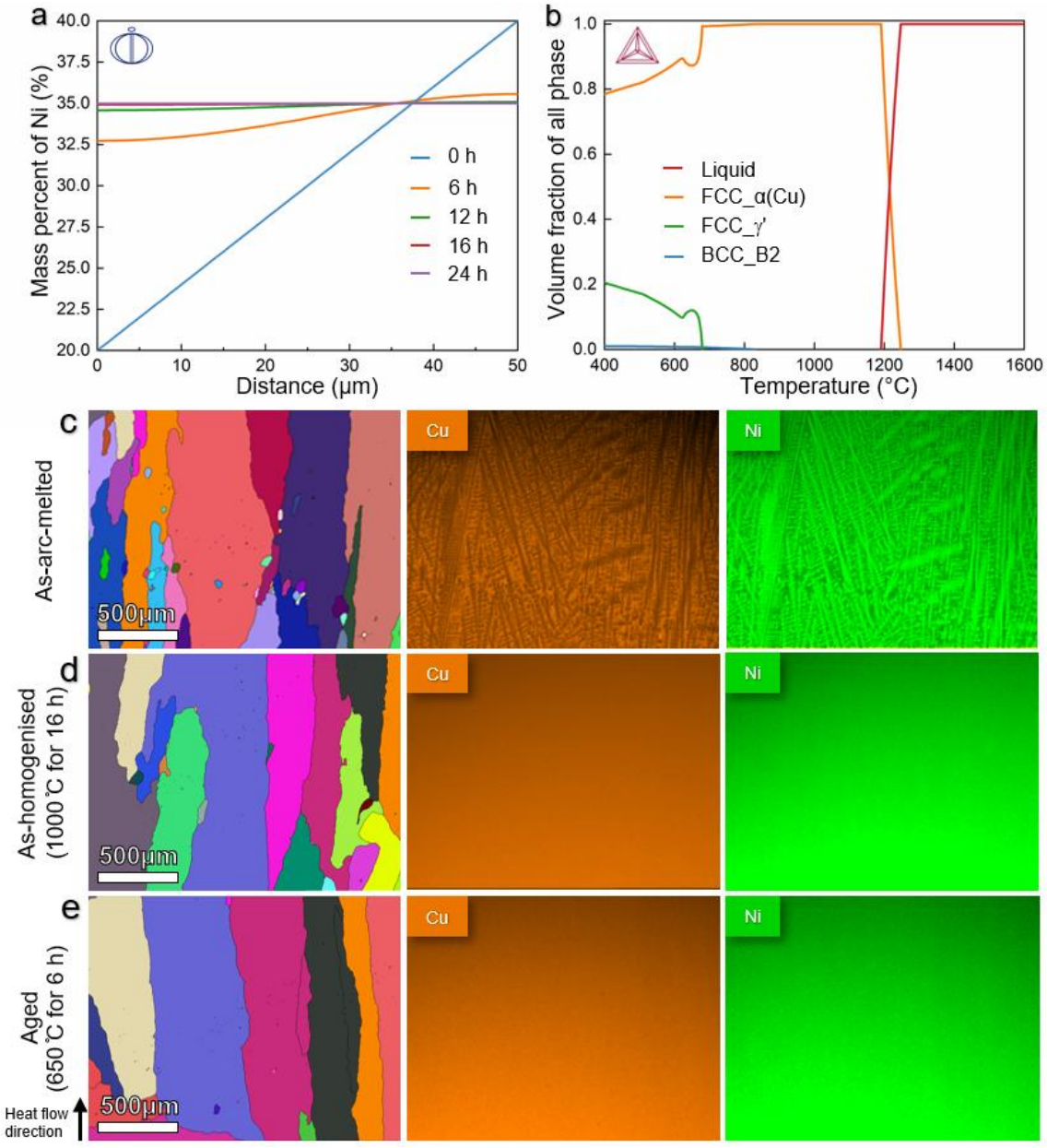

Figure 9.1: Phase analysis of Cu-30Ni with 0.5 wt.% Si using Thermo-Calc simulations, and microstructure analysis of the cross-sectional position of the as-arc-melted and heat-treated 0.5Si samples. (a) a single-phase diffusion simulation showing the concentration profile of Ni at 1000 °C over various diffusion times; (b) volume fraction of the stable phases as functions of temperature; and EBSD random colour grain maps of the as-arc-melted sample (c), as-homogenised sample at 1000 °C for 16 h (d), and aged sample at 650 °C for 6 h (e), along with EDXS elemental maps (Cu and Ni).

Figure 9.2 demonstrates the hardness evolution with ageing time for 0Si and 0.5Si alloys with various heat treatments. The 0.5Si FA-FC (furnace ageing followed by furnace cooling) samples show a pronounced hardening effect over time, with hardness increasing from 139

± 6 HV_1 at 0.1 h to 201 ± 1 HV_1 at 6 h, reaching a peak of 207 ± 3 HV_1 at 24 h, followed by a decrease to 190 ± 2 HV_1 at 100 h. In contrast, the 0Si FA-FC samples show negligible changes in hardness, fluctuating between 90 and 110 HV_1. The 0.5Si SB-Q (salt bath ageing followed by quenching) samples exhibit a similar trend of increasing hardness, though the hardness values are 10–15% lower than those of the 0.5Si FA-FC samples. Similarly, the hardness of the 0.5Si FA-Q (furnace ageing followed by quenching) sample is 13% lower than that of the 0.5Si FA-FC samples.

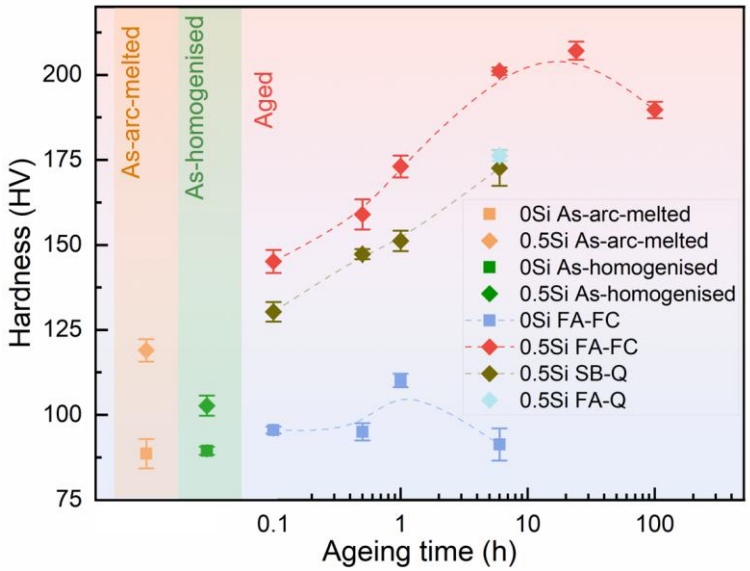

Figure 9.2: The age hardening response of the 0Si and 0.5Si samples, and the variations in hardness with ageing time at 650 °C under different age hardening treatments: furnace ageing followed by furnace cooling (FA-FC), furnace ageing followed by water quenching (FA-Q) and salt bath ageing followed by water quenching (SB-Q). The data points were fitted with B-spline curves. Initial hardness measurements for samples in the as-arc-melted and as-homogenised conditions are also included as baseline references. The 0.5Si FA-FC samples show significant age hardening, reaching a peak hardness of 207 ± 3 HV1 at 24 h, with a notable increase to 201 ± 1 HV1 at 6 h.

9.1.2 Microstructural Evolution

Figure 9.3 presents the microstructural evolution during ageing of the 0.5Si FA-FC samples at 650 °C for 0.1 h and 6 h, representing the early stage of ageing and a condition near peak hardness, respectively. At 6 h (Figure 9.3a–b), the HAADF-STEM images and

corresponding STEM-EDXS maps of Cu and Ni distributions confirm Ni enrichment, with particles also containing Mn, Si, Fe and Nb, consistent with the 1D concentration profiles. The bright-field TEM images and the corresponding selected area electron diffraction pattern (Figure 9.3c–d) reveal γ′ precipitates, oriented along [0 0 1] direction within the α(Cu) matrix. Figure 9.3d presents the selected area diffraction pattern acquired from a precipitate-containing region. In addition to the fundamental FCC reflections of the Cu matrix, distinct superlattice reflections are circled in yellow, confirming the formation of an ordered $L1_2$ structure corresponding to the γ′ precipitates. Based on the measured diffraction spot spacing, the lattice parameter of the precipitate phase was estimated and found to be consistent with reported values for the $L1_2$-structured γ′ phase, further supporting phase identification. Figure 9.3e displays a representative HAADF-STEM image, showing a coherent interface between the γ′ precipitate and the α(Cu) matrix. At 0.1 h, high-resolution TEM (HRTEM) (Figure 9.3f) and the corresponding FFT analysis (Figure 9.3g–h) reveal GP zone characteristics, including a set of diffraction spots and streak-like features [294, 295]. The area marked with a white square in Figure 9.3f is identified as a GP zone, which consists of solute clusters commonly found in under-aged Cu alloys [296]. The FFT pattern in Figure 9.3h, along with the circled weak spots, indicates the presence of the γ′ precipitates within the area marked with a yellow square in Figure 9.3f.

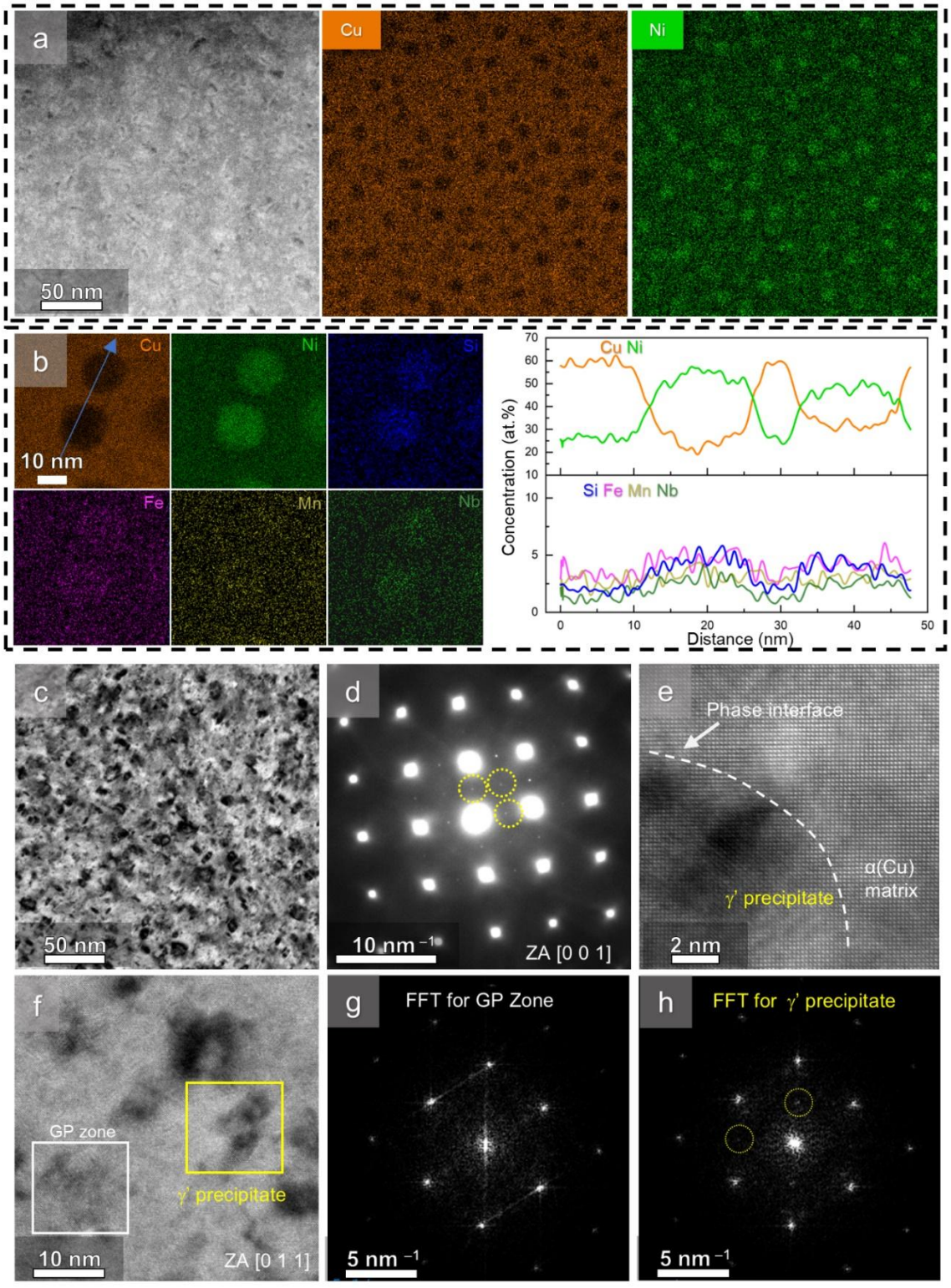

Figure 9.3: TEM microstructural observations of the 0.5Si FA-FC samples aged at 650 °C for 0.1 h and 6 h. (a) HAADF-STEM image showing the microstructure and EDXS elemental maps of Cu and Ni for the sample aged for 6 h; (b) EDXS elemental maps and 1D concentration profiles along the blue arrow; (c) bright-field TEM image of the sample aged for 6 h; (d) selected area electron diffraction pattern taken from the region in (c); (e) HAADF-STEM image showing the interface between the γ′ precipitate and the α(Cu) matrix in the sample aged for 6 h; (f) HRTEM images of the sample aged for 0.1 h showing the GP zone and γ′ precipitate; (g) and (h) are FFT patterns of the GP zone and precipitate, respectively, converted from the region in (f).

To gain deeper insights into the chemistry of the γ′ precipitates and their origin as solute clusters, APT was performed on the 0.5Si FA-FC samples aged at 650 °C for 0.1 h (Figure 9.4a) and 6 h (Figure 9.4b). The iso-density surfaces of Si were employed to visualise the γ′ precipitates within the reconstructed volume, which have average diameters of 6.9 nm for the 0.1 h sample and 10.1 nm for the 6 h sample. The number density of the γ′ precipitates is 1.76×10^{24} m^{-3} for the 0.1 h sample and 1.82×10^{23} m^{-3} for the 6 h sample. The volume fraction, calculated as the number of atoms within the precipitates divided by the total number of atoms in the APT datasets, is 0.31% for the 0.1 h sample and 4.68% for the 6 h sample. Meanwhile, the size and volume fraction of the solute clusters are measured to be 2.2 nm and 0.78% for the 0.1 h sample, and 2.8 nm and 0.09% for the 6 h sample, respectively (see Supplementary material for details of cluster analysis). Proxigram and cluster analysis reveal the compositional changes in the γ′ precipitates and solute clusters, as summarised in Table 9.1. In the 0.1 h sample, γ′ precipitates have a nominal composition of $Ni_{0.60}(Si_{0.17}Nb_{0.05})$; while after 6 h ageing, it evolves to $Ni_{0.73}(Si_{0.14}Nb_{0.07})$. Both samples also contain Fe (~0.3 at.%) and Mn (~2 at.%). In contrast, solute clusters are Si-rich, with compositions of $Ni_{0.24}(Si_{0.57}Nb_{0.01})$ for the 0.1 h sample and $Ni_{0.37}(Si_{0.51}Nb_{0.02})$ for the 6 h sample, respectively. The same proxigram and cluster analysis method was applied on the as-homogenised sample; however, no clusters or precipitates were detected (as shown in Figure 9.5), indicating that these microstructural features are induced by ageing. For reference, the 0Si FA-FC samples contain Ni-Nb precipitates (Figure 9.6) with nominal compositions of $Ni_{0.56}Nb_{0.09}$ for 0.1 h ageing and $Ni_{0.63}Nb_{0.09}$ for 6 h ageing.

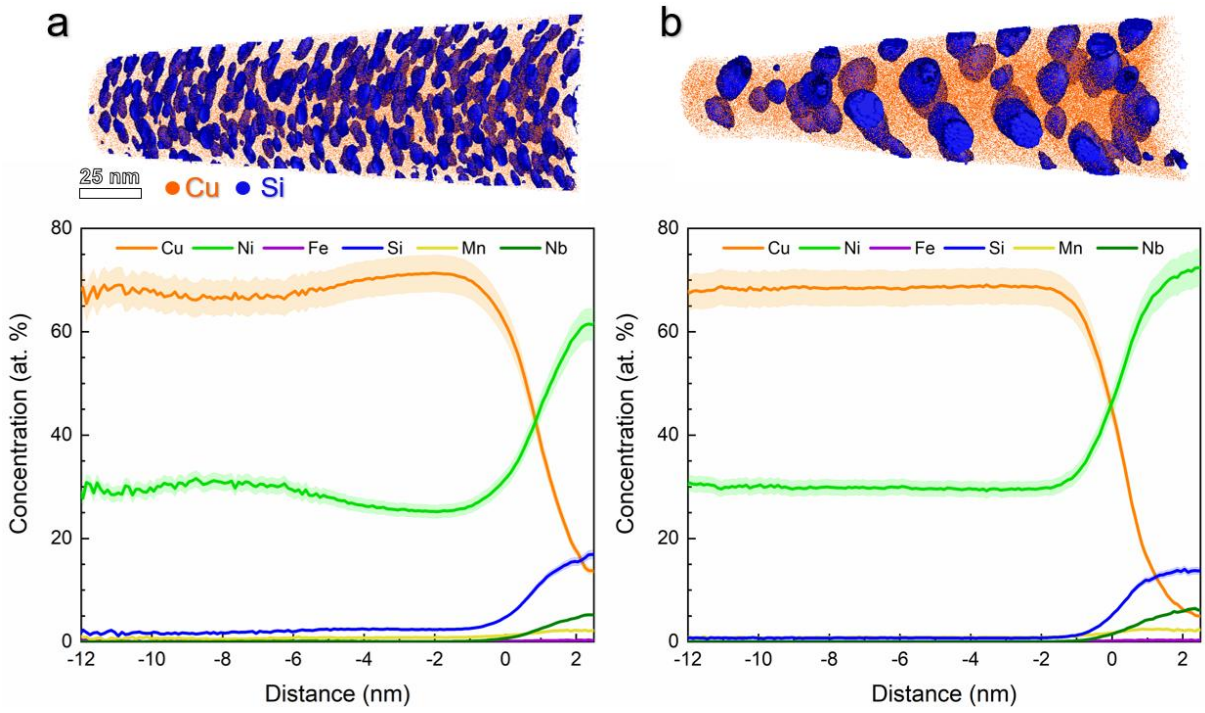

Figure 9.4: Atom probe tomography reveals three-dimensional atom map reconstructions with proxigram-based composition profiles derived from the Si iso-density surface for the 0.5Si FA-FC sample aged at 650 °C for (a) 0.1 h and (b) 6 h. The Si iso-density surface containing 2.4 atoms/nm^3 was applied to visualise γ′ precipitates. The shaded area represents a statistical error of the standard deviation.

Table 9.1: Chemical compositions (at.%) of the Si-rich clusters and γ′ precipitates in the 0.5Si FA-FC samples aged at 650 °C for 0.1 h and 6 h.

	Ni	Si	Nb
γ′ precipitates in the 0.1 h sample	60	17	5
γ′ precipitates in the 6 h sample	73	14	7
Si-rich clusters in the 0.1 h sample	24	57	1
Si-rich clusters in the 6 h sample	37	51	2

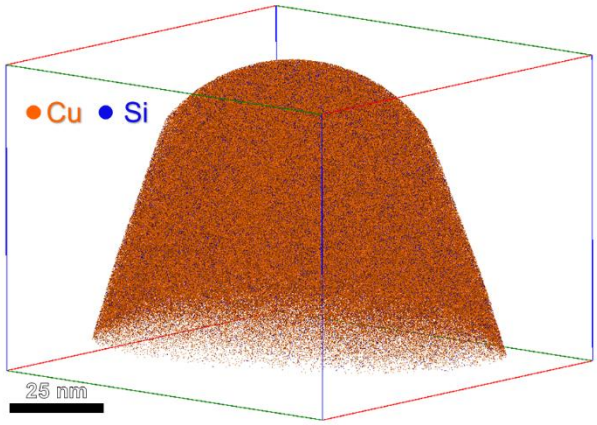

Figure 9.5: Three-dimensional atomic map acquired by atom probe displaying homogenised distribution of Cu and Si ions in the 0.5Si homogenised alloy.

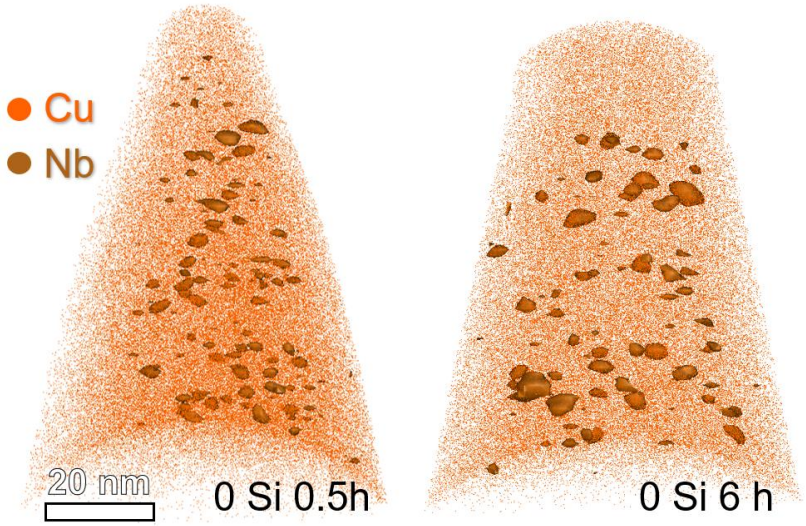

Figure 9.6: Three-dimensional atomic map acquired by atom probe displaying the Nb-rich Ni-Nb precipitate in 0Si sample aged at 650 °C for 0.1 h and 6 h.

9.2 Discussion

This study demonstrates the microstructural transformations during heat treatments and their consequent effects on the hardness of Cu-30Ni alloys with and without Si. As shown in Figure 9.2, adding 0.5 wt.% Si led to a substantial increase in hardness, and the 0.5Si FA-FC samples aged at 650 °C for 6 h and 24 h achieved nearly double the hardness

compared to the as-homogenised state. In addition, the hardness of the FA-FC samples was ~13% higher than that of the SB-Q and FA-Q samples, which is attributed to the extended cooling period for the FA-FC samples. The slower cooling in the furnace provides additional time for the diffusion of Ni, Si, and Nb and promotes precipitate growth during the final cooling step, thereby enhancing the formation of γ′ precipitates and increasing the hardness. While hardness after 24 h (207 HV_1) is slightly higher than after 6 h (201 HV_1), the increment is marginal for these durations. Thus, ageing for 6 h provides superior cost-time-performance efficiency. In contrast, the 0Si alloys did not show an increase in hardness after ageing, underscoring the critical role of Si in the hardness of the Cu-30Ni alloy. Based on these results, the remaining discussion in this study will focus only on the 0.5Si FA-FC sample.

9.2.1 Strengthening mechanism

The strength variations in the 0.5Si FA-FC samples are elucidated through microstructural examination. The as-arc-melted 0.5Si sample initially features large grains and Cu/Ni segregation (Figure 9.1c). After homogenising, the segregation is removed, while the grain structure remains largely unchanged, indicating minimal grain boundary strengthening. Solid solution strengthening, governed by the modulus and lattice mismatches, is primarily attributed to Ni dissolution in the α(Cu) matrix. However, it becomes less effective in the age-hardened state due to the reduction of solute atoms in the matrix. Unlike in a cold-rolled sample [297], ageing does not produce large populations of dislocations that lead to strengthening. These observations indicate that precipitation hardening [284] is the primary strengthening mechanism enabled by the addition of Si. APT analysis (Figure 9.4) determined the composition of the γ′ precipitate in the 0.5Si FA-FC samples as

$Ni_{0.60}(Si_{0.17}Nb_{0.05})$ for 0.1 h of ageing, and $Ni_{0.73}(Si_{0.14}Nb_{0.07})$ after 6 h. Solute clusters exhibited higher Si content with $Ni_{0.24}(Si_{0.57}Nb_{0.01})$ in the 0.1 h sample and $Ni_{0.37}(Si_{0.51}Nb_{0.02})$ in the 6 h sample. The higher Si concentration in solute clusters supports the hypothesis proposed in [298], in which Si atoms initially cluster together and aid nucleation before diffusing into the matrix. Although APT confirms that the precipitates are predominantly γ′ with an ordered $L1_2$ structure, minor elements such as Mn and Fe may substitute on the Ni sublattice due to their similar atomic size, while Nb may partially substitute on the Si sublattice or segregate at the interface; such limited substitution could slightly modify lattice misfit and coherency strain, but the primary strengthening mechanism remains governed by coherent γ′ precipitates.

The increase in hardness from the as-homogenised state was measured as 37 HV_1 for the 0.1 h sample and 99 HV_1 for the 6 h sample, corresponding to strength increase (Δσ) of 96 MPa and 257 MPa, respectively, using the strength-hardness relationship from [299]. To quantify the contribution of the γ′ precipitate strengthening, the increase in YS can be expressed by classical precipitation-strengthening models [300, 301]. As previously described, the volume fractions of the γ′ precipitates and Si-rich clusters were quantified using APT cluster analysis [171] and are summarised in Table 9.2. The result gives a precipitate-strengthening ($\Delta\sigma_{precipitates}$) of 76 MPa in the 0.1 h sample and 260 MPa in the 6 h sample, respectively (see Appendix D for details). Furthermore, hardening from the Si-rich clusters ($\Delta\sigma_{clusters}$) is calculated to be 61 MPa at 0.1 h and 26 MPa at 6 h. However, it is recognised that the strengthening contribution of clusters is difficult to quantify reliably, as it depends strongly on the details of dislocation–cluster interactions. According to Singh and Warner [302] the contribution of clusters or GP zones to strengthening is estimated as 8–33% of what the classical precipitation-strengthening model predicts due to their thin and coherent nature, which allows dislocations to loop around them with relatively low

resistance. Applying this estimation to the present study gives the $\Delta\sigma_{clusters}$ values of 5–20 MPa for the 0.1 h sample and 2–9 MPa for the 6 h sample. Consequently, the total strengthening from the γ′ precipitates and Si-rich clusters is therefore 81–96 MPa for the 0.1 h sample and 262–269 MPa for the 6 h sample. Further details of this calculation are provided in the Appendix D. These values align closely with the experimentally observed strength (Δσ), as shown in Table 9.2.

Table 9.2: Volume fraction of the Si-rich clusters and γ′ precipitates in the 0.5Si FA-FC samples aged at 650 °C for 0.1 h and 6 h as well as their contribution to strength.

Sample	Volume fraction of Si-rich clusters (%)	Volume fraction of γ′ precipitates (%)	Observed strengthening Δσ (MPa)	Strengthening of γ′ precipitates $\Delta\sigma_{precipitates}$ (MPa)	Strengthening of Si-rich clusters $\Delta\sigma_{clusters}$ (MPa)	Calculated total strengthening $\Delta\sigma_{precipitates} + \Delta\sigma_{clusters}$ (MPa)
0.1 h	0.78	0.31	96	76	5–20	81–96
6 h	0.09	4.68	257	260	2–9	262–269

In aged samples, dislocations tend to shear γ′ precipitates, contributing to strengthening mechanisms such as coherency strengthening [303], which occurs due to the stress field around coherent interfaces that hinders dislocation motion. Simulations suggest that for smaller precipitates (< 10 nm), coherency strengthening is dominant and intensifies with increasing coherency strain [304]. Classical precipitation strengthening mechanisms, including weak-pair coupling, strong-pair coupling, and the Orowan bypass mechanism, depend on precipitate size and volume fraction [300, 301]. As mentioned above, at 0.1 h, the Si-rich clusters with a volume fraction of 0.78% offer limited strengthening but still contribute alongside small γ′ precipitates, through weak-pair coupling. By 6 h, hardness rises to 201 HV_1 as the γ′ precipitates grow beyond 10 nm, and strong-pair coupling

becomes dominant, while the fraction of the Si-rich cluster drops to 0.09% (Figure 9.4b and Table 9.2). The interfaces remain coherent (Figure 9.3e), implying that coherency strengthening is still significant. Further prolonged ageing at 100 h leads to softer material due to precipitate coarsening and increased spacing [305] (Figure 9.2).

9.2.2 Formation mechanisms of Si-rich clusters and γ′ precipitates

To elucidate the formation mechanisms of the Si-rich clusters and γ′ precipitates, and their effect on the mechanical properties of Cu-30Ni, DFT and AIMD simulations [306] were conducted. Figure 9.7 summarises the relative total energy of pair-wise Ni-Ni, Si-Si, and Nb-Nb in Figure 9.7a and Ni-Si, Si-Nb and Nb-Ni interactions in Figure 9.7b, obtained from DFT calculations. The results suggest Ni and Cu distribute randomly, while Si avoids 1st nearest neighbour (1NN) positions. In contrast, Nb atoms strongly prefer 1NN configurations, forming close-packed clusters, with a binding energy of ~0.35 eV, exceeding values reported in Al-Si-Mg alloys [307]. All three solute pairs show attractive interactions, with Nb–Ni being strongest (~0.27 eV), followed by Ni–Si (~0.15 eV) and Si–Nb (~0.11 eV), favouring solute clustering and potential precipitate formation, as detected experimentally. These results suggest that the addition of Nb facilitates clustering with Ni, as the strong short-range Nb–Nb interactions encourage the early formation of stable nuclei. Consistent with these calculations, the Ni-Nb precipitates are observed in the 0Si FA-FC samples (Figure 9.6). In addition, AIMD simulations calculate the average solute diffusion coefficients of the solute elements at 427 °C and 627 °C, as shown in Table 9.3. The result suggests a consistent trend in solute relative diffusivities: Si > Ni > Nb. The calculated energetics and diffusivity help explain the observed composition of the Si-rich clusters and γ′ precipitates. Initially, strong Ni–Si–Nb interactions form small Ni–Si–Nb clusters with

high Si content (~55%) due to the fast diffusion of Si. As ageing progresses, Ni and Nb accumulate, Si becomes depleted, and the clusters grow into precipitates with lower Si and higher Ni and Nb concentrations.

The DFT results indicate strong Nb–Ni (and Nb–Si) interactions, supporting the formation of Nb-containing clusters at the early stages of ageing. This is consistent with the higher number density of Nb-rich clusters observed experimentally in the Si-free alloy and correlates with the initial hardness increase. In the Si-containing alloy, clustering preferentially evolves toward ordered $L1_2$ Ni_3Si (γ') precipitates, leading to a more sustained hardening response. These results link the atomic-scale role of trace elements to the experimentally observed ageing sequence and hardness evolution.

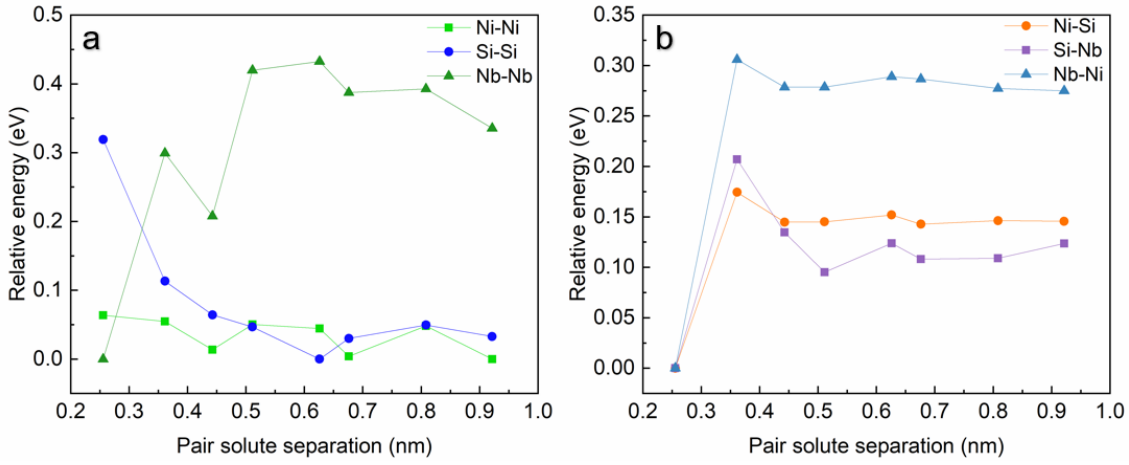

Figure 9.7: DFT calculated (a) single-species and (b) mixed-species solute-solute pair interactions using a 256-atom supercell. For each species, the lowest energy, corresponding to the most favourable configuration, is set as zero.

Table 9.3: Calculated solute average diffusion coefficients at concentrations of 1% solute in Cu at 427 °C and 627 °C based on AIMD simulations. The unit is in × 10^{-5} cm^2/s.

Solute	427 °C	627 °C
Ni	3.0	3.9
Si	6.5	7.6
Nb	1.8	2.4

To help understand the hardening effect of the Si-rich clusters and γ′ precipitates in Cu-30Ni, the elastic properties [308] of bulk Ni_3Si and Ni_3Nb, and bulk Cu (Table 9.4) were calculated. As shear and Young's moduli, along with Poisson's ratio, are reliable hardness indicators [308], the results suggest that the Ni_3Si is significantly harder than the Cu matrix, primarily due to the intrinsically strong Ni-Si bonding, highlighting the critical role of Si in hardening Cu-30Ni. In contrast, Ni_3Nb is predicted to be softer than the Cu matrix, mainly due to the low C_{44} elastic constant, which may enhance impact resistance.

Table 9.4: DFT calculated lattice constants (a, in nm), stiffness constants ($C_{i,j}$) and the corresponding bulk-, shear- and Young's moduli (in GPa) for bulk Ni_3Si, Ni_3Nb and Cu.

	a	C_{11}	C_{12}	C_{44}	Bulk modulus	Shear modulus	Young's modulus	Poisson's ratio
Ni_3Si	0.3506	313.5	159.8	130.0	211.0	105.3	270.9	0.286
Ni_3Nb	0.3694	248.0	174.2	16.1	198.8	22.5	65.1	0.445
Cu	0.3633	171.8	122.2	78.4	138.8	49.5	132.7	0.341

9.3 Summary

In summary, this study elucidates the microstructural transformations during heat treatments and their consequential impacts on the mechanical strength of Cu-30Ni alloys, with a particular focus on the effect of Si addition. The findings highlight the critical role of Si-rich clusters and γ′ precipitates in significantly enhancing the hardness. The presence of the Si-rich clusters in the early stages of ageing significantly contributes to the increased strength, underscoring the critical role of Si not only in initiating hardening but also in facilitating the formation of the γ′ precipitates. The insights into the ageing process and the formation mechanism of the Si-rich clusters and γ′ precipitates provide a valuable foundation for tailoring Cu-30Ni alloys to meet specific application requirements, particularly in environments that demand high-strength materials. Future work should explore the optimisation of Si concentration and heat treatment parameters to maximise mechanical properties and investigate the alloy's performance applied in different potential operating environments.

Chapter 10 Conclusions

This thesis investigated, Cu-10Sn, Cu-1Ti, and Cu-30Ni alloys, establishing robust powder–process–microstructure–property relationships that advance the understanding and capability of additive manufacturing of Cu alloys. These relationships enable microstructure control and the optimisation of mechanical and functional performance in these technologically important materials. Through a comprehensive suite of studies, spanning process parameter optimisation, powder characterisation, multiscale microscopy, mechanical/electrical testing, and thermodynamic/DFT simulations, this thesis addressed five major knowledge gaps identified in Chapter 2. The following conclusions correspond to the five ***Aims*** defined in Chapter 3.

Aim 1: Optimise printing parameters and investigate the effect of scan strategy in LB-PBF Cu-10Sn.

Conclusion 1: Printing parameters and scan strategy in LB-PBF Cu-10Sn were optimised, establishing the foundation for powder-structure-property studies presented in Chapter 6 and 7.

A systematic parameter sweep and four distinct scan strategies were employed to understand their role in defect formation, microstructure, and mechanical properties of LB-PBF Cu-10Sn (Chapter 5). For the LB-PBF system used in this study, key printing parameters included a P of 195 W, s of 860 mm/s, t of 25 μm and h of 75 μm. While all strategies produced broadly comparable ductility (~9–10%), the unidirectional alternating strategy achieved the highest strength (UTS ~512 MPa, YS ~408 MPa, hardness ~175 HV_1) due to a combination of minimal porosity and fine grains. Island-based strategies, in contrast, produced higher defect content and lower hardness. These results demonstrated

that scan strategy is a powerful lever for tuning defect content and strengthening mechanisms in Cu-10Sn.

Aim 2: Elucidate the formation mechanism, distribution, and strengthening contribution of the Sn-rich δ phase ($Cu_{41}Sn_{11}$) in LB-PBF Cu-10Sn.

Conclusion 2: The δ phase was elucidated as a non-equilibrium product that forms via metastable transformation, exhibits distinct morphologies at melt pool boundaries and interiors, and provides a measurable strengthening contribution without severely compromising ductility.

The formation and role of the Sn-rich δ ($Cu_{41}Sn_{11}$) phase under rapid solidification in LB-PBF Cu-10Sn were elucidated (Chapter 6). Multiscale characterisation revealed two morphologically distinct δ variants, whose size and distribution were governed by local solidification conditions. Contrary to conventional casting, where δ promotes brittleness, its submicron-scale dispersion in LB-PBF parts contributed positively to the YS and wear resistance without catastrophic loss of ductility. This highlights the non-equilibrium advantage of LB-PBF in re-purposing a traditionally deleterious phase into a strengthening feature.

Aim 3: Enhance the mechanical property of LB-PBF Cu-10Sn by investigating powders with varying characteristics.

Conclusion 3: Powder characteristics were shown to directly dictate porosity, microstructure, and properties, establishing a predictive powder–structure–property framework for Cu-10Sn.

LB-PBF Cu-10Sn samples fabricated using three batches of gas-atomised powders with distinct PSD, surface chemistries and flowability, were investigated (Chapter 7). Results showed bimodal PSD with surface enrichment of Sn or Zn enhance laser absorbance, packing density, and powder flowability, leading to more efficient melting, fewer defects, and superior mechanical performance. At the microstructural scale, the formation of dislocation cell walls combined with δ-phase precipitates, provides both strengthening and sustained plastic flow. These findings confirm that feedstock quality is a primary determinant of LB-PBF build outcomes, and that rational powder selection and design, particularly with respect to PSD, absorptivity, and surface chemistry, are essential for optimising the strength and ductility of Cu-10Sn alloys.

Aim 4: Develop processing strategies to balance high strength and electrical conductivity in Cu-based alloys, identifying composition and post-processing routes.

Conclusion 4: Processing strategies were established to achieve a balance of mechanical and functional properties in LB-DED Cu-1Ti, enabled by controlled precipitation and enhanced laser absorption.

A novel alloy design strategy that combined moderate Ti addition with graphene nanoplatelets was developed to overcome Cu's intrinsic processing limitations in LB-DED (Chapter 8). This approach improved laser absorptivity, enabled supersaturation of Ti in the Cu matrix, and facilitated subsequent precipitation hardening. Ageing at 470 °C promoted the formation of fine, coherent β′-Cu_4Ti precipitates, which progressively increased strength while reducing ductility with longer exposure times. The as-built alloy exhibited a YS of 167 MPa, UTS of 334 MPa, and elongation at fracture of 31%. After 3 h ageing, a YS of 315 MPA and UTS of 463 MPa were achieved at the expense of ductility (17%).

Electrical conductivity was ~12% IACS in the as-built condition, with incremental improvement after ageing (reaching values above 25% IACS). These results demonstrate that even at very low Ti concentrations, precipitation strengthening can be effectively activated while retaining useful conductivity. This confirms LB-DED Cu-1Ti as a promising pathway for designing Cu alloys that reconcile the longstanding strength–conductivity trade-off.

Aim 5: Investigate the age hardening response of Cu-30Ni alloys.

Conclusion 5: Si additions drive the formation of solute clustering and γ′–Ni_3Si precipitate as the main strengthening phase.

Age hardening response of Cu-30Ni with and without Si, with a particular focus on the precipitation behaviour, was investigated (Chapter 9). Various ageing treatments revealed that Si promotes the formation of solute clustering and fine γ′–Ni_3Si precipitates, significantly enhancing hardness while maintaining microstructural stability. The results clarify decades-old uncertainties regarding the role of Si in Cu-Ni alloys and provide a framework for tailoring post-spray heat treatments in CSAM builds, where precipitation strengthening is essential for property optimisation.

Overall, this thesis demonstrates that AM offers unique opportunities to re-engineer long-standing Cu alloys by exploiting rapid solidification, site-specific processing, and rational powder/alloy design. The work has shown that:

- Microstructure–property relationships in Cu alloys can be deliberately manipulated at scales ranging from powder attributes to nanoscale precipitates.

- Traditionally brittle phases (e.g., δ in Cu-10Sn) can be transformed into beneficial strengthening agents under AM conditions.
- Low-Ti Cu alloys can simultaneously deliver high strength and reasonable conductivity when designed with AM-specific processing routes.
- Precipitation engineering (γ′ in Cu-Ni, β′ in Cu-Ti) remains central to advancing high-performance Cu alloys for electrification and thermal management applications.

The findings of this thesis extend beyond fundamental metallurgy to enable application-specific pathways:

- Cu-10Sn (Bronze via LB-PBF): The transformation of δ into a refined strengthening agent positions AM Cu-10Sn for bearings, gears, and marine propellers, where both strength and wear resistance are essential. The demonstrated four-fold improvement in wear behaviour relative to cast bronzes directly supports deployment in rotating and sliding components under corrosive or abrasive service.
- Cu-1Ti (Low-Ti Cu alloy via LB-DED): The combination of high strength with retained conductivity makes this alloy attractive for electrical connectors, busbars, and EV charging infrastructure. The ability to fabricate robust, site-specific geometries with LB-DED further enables lightweight, mechanically reliable components for electrification and power-dense systems.
- Cu-30Ni (with Si): The clarified role of Si-rich clusters and γ′ precipitates supports the development of seawater-exposed systems (condensers, ship components) and chemical plant piping, where corrosion resistance must be complemented by higher strength. These results also inform the design of CSAM post-treatments, where

precipitation strengthening can be deliberately invoked to improve the durability of repaired or additively built structures in aggressive environments.

This thesis demonstrates that the behaviour of AM Cu alloys cannot be understood solely through conventional alloy design principles nor through generic AM frameworks. Rather, the observed microstructural features, defect mechanisms, and property evolutions emerge from the fundamental interaction between AM-specific thermal conditions and the intrinsic physical characteristics of copper, including its ultra-high thermal conductivity, reflectivity, and solute diffusivity. Across the Cu–Sn, Cu–Ti, and Cu–Ni systems investigated, it is shown that rapid solidification, steep thermal gradients, and cyclic reheating uniquely reshape phase formation pathways, segregation patterns, and precipitation behaviour. The thesis therefore establishes a mechanistic understanding of AM–Cu coupling. The insights established here provide not only immediate guidelines for industrial AM of Cu alloys but also a foundation for developing new strategies to deliberately tailor microstructure–property relationships. By linking processing optimisation, powder design, and post-processing to property optimisation, this thesis advances the vision of application-specific, high-performance copper components in Industry 4.0 and 5.0.

Chapter 11 Future work

The following future work is recommended for the continuation of this thesis:

1. Future work on scan strategy optimisation in LB-PBF Cu-10Sn should focus on reducing porosity, particularly at the boundaries of scan patterns. Although this thesis established the influence of scan strategy on density, microstructure, and properties, an optimisation of pattern boundaries remains underexplored. These regions often act as preferential sites for lack-of-fusion defects and stress concentration, limiting mechanical performance. Advanced scan path engineering, such as tailored vector rotations, adaptive stripe or island segmentation, and dynamic energy input at overlap regions, may offer effective routes to minimise boundary porosity. In addition, integrating real-time monitoring and closed-loop feedback could further stabilise melt pools and mitigate defect formation. A more comprehensive understanding of these effects will not only improve the intrinsic quality of LB-PBF Cu-10Sn parts but also expand the design space for reliable industrial implementation.
2. Residual stress (RS) remains another critical factor for the future development of LB-PBF Cu-10Sn. A common challenge in LB-PBF is the distortion of as-built components due to RS accumulation, which can strongly influence microstructure and mechanical performance. While residual stress was not quantitatively addressed in this thesis, follow-on studies, supported by the Australian Institute of Nuclear Science and Engineering (AINSE) Postgraduate Research Award program, have fabricated a gear-shaped sample and measured RS distributions using neutron diffraction. Future research will extend this approach by mapping RS across geometrically complex components and correlating it with microstructural

evolution and mechanical performance. Establishing robust RS–microstructure–property relationships will be vital for translating Cu-10Sn into demanding industrial applications, where dimensional stability, fatigue resistance, and service reliability are essential. These insights will also provide a foundation for process-intrinsic stress management strategies, including optimised scan strategies, substrate preheating, and post-build stress relief treatments.

3. For Cu–Ti alloys, future work should focus on enhancing the stability of the β′ precipitates, which remain metastable under extended thermal exposure. Since high-temperature structural and functional applications are increasingly demanding Cu alloys with both strength and conductivity, strategies to suppress β′ to β transformation and coarsening will be critical. One promising route lies in combining LB-DED processing with minor alloying additions such as Sc, Gd, or Zr, which have been shown in other studies to impede solute diffusion and stabilise metastable precipitates. By selectively tuning the Ti diffusion behaviour through these additions, it may be possible to extend the thermal stability of the β′ phase, thereby retaining strengthening effects at elevated temperatures without severely compromising electrical conductivity. Systematic investigation of such alloying-processing synergies will deepen the mechanistic understanding of β′ phase stability in Cu–Ti, and establish design principles for next-generation Cu alloys tailored for high-temperature service environments.
4. For Cu-30Ni alloys, future investigations should extend beyond the heat treatment optimisation conducted in this study. Here, the role of Si in promoting clustering and γ′ precipitation was clarified, but an important next step will be to evaluate whether these findings translate to Cu-30Ni fabricated by CSAM. Since CSAM introduces distinct microstructural features, such as work-hardened splat

boundaries and residual porosity, benchmarking the ageing response of CSAM-processed Cu-30Ni against the results obtained here will be essential for assessing applicability. Furthermore, given the well-established corrosion resistance of Cu-Ni alloys, it would be valuable to couple microstructural optimisation with rigorous corrosion testing, especially in simulated marine or chemically aggressive environments. These studies will confirm the transferability of the precipitation strengthening mechanisms and establish whether CSAM Cu-30Ni can achieve the combined performance of high strength and durability demanded for industrial service.

List of Figures

List of Tables

References

[1] M. Radetzki, Seven thousand years in the service of humanity—the history of copper, the red metal, Resources Policy 34(4) (2009) 176-184.
[2] D.E. Tyler, W.T. Black, Introduction to copper and copper alloys, Properties and selection: nonferrous alloys and special-purpose materials, ASM International1990, pp. 216-240.
[3] J.R. Davis, Copper and copper alloys, ASM international2001.
[4] S. Bonthula, S.R. Bonthula, R. Pothu, R.K. Srivastava, R. Boddula, A.B. Radwan, N. Al-Qahtani, Recent advances in copper-based materials for sustainable environmental applications, Sustainable Chemistry 4(3) (2023) 246-271.
[5] P. Nagrale, Copper & Copper Alloy Market Research Report Information By Product Type (Copper Foil, Brass Foil, Bronze Foil, Copper Nickel Foil, and Others), By Application (Construction, Electrical & Electronics, Industrial Machinery, Consumer Goods, and Others) And By Region (North America, Europe, Asia-Pacific, And Rest Of The World) –Market Forecast Till 2032 2025. https://www.marketresearchfuture.com/reports/copper-alloy-foils-market-3832. (Accessed 27/05 2025).
[6] B. Jones, R.J. Elliott, V. Nguyen-Tien, The EV revolution: The road ahead for critical raw materials demand, Applied Energy 280 (2020) 115072.
[7] K. Yang, Y. Wang, M. Guo, H. Wang, Y. Mo, X. Dong, H. Lou, Recent development of advanced precipitation-strengthened Cu alloys with high strength and conductivity: a review, Progress in Materials Science 138 (2023) 101141.
[8] H. Yang, Z. Ma, C. Lei, L. Meng, Y. Fang, J. Liu, H. Wang, High strength and high conductivity Cu alloys: A review, Science China Technological Sciences 63(12) (2020) 2505-2517.
[9] R. Mishnev, I. Shakhova, A. Belyakov, R. Kaibyshev, Deformation microstructures, strengthening mechanisms, and electrical conductivity in a Cu–Cr–Zr alloy, Materials Science and Engineering: A 629 (2015) 29-40.
[10] J. Li, H. Ding, B. Li, L. Wang, Microstructure evolution and properties of a Cu–Cr–Zr alloy with high strength and high conductivity, Materials Science and Engineering: A 819 (2021) 141464.
[11] R. Monzen, C. Watanabe, Microstructure and mechanical properties of Cu–Ni–Si alloys, Materials Science and Engineering: A 483 (2008) 117-119.
[12] S. Suzuki, N. Shibutani, K. Mimura, M. Isshiki, Y. Waseda, Improvement in strength and electrical conductivity of Cu–Ni–Si alloys by aging and cold rolling, Journal of Alloys and Compounds 417(1-2) (2006) 116-120.
[13] S. Nagarjuna, M. Srinivas, K. Balasubramanian, D. Sarma, On the variation of mechanical properties with solute content in Cu–Ti alloys, Materials Science and Engineering: A 259(1) (1999) 34-42.
[14] M. Elmer, The Rising Demand for Heat Exchangers in Data Centers and the Critical Role of Copper, 2025. https://blog.copper.org/hvac/r/the-rising-demand-for-heat-exchangers-in-data-centers-and-the-critical-role-of-copper. (Accessed 02/06 2025).
[15] R.P. Minneci, E.A. Lass, J.R. Bunn, H. Choo, C.J. Rawn, Copper-based alloys for structural high-heat-flux applications: a review of development, properties, and performance of Cu-rich Cu–Cr–Nb alloys, International materials reviews 66(6) (2021) 394-425.

[16] P.R. Gradl, T.W. Teasley, C.S. Protz, M.B. Garcia, D. Ellis, C. Kantzos, Advancing GRCop-based bimetallic additive manufacturing to optimize component design and applications for liquid rocket engines, AIAA Propulsion and Energy 2021 Forum, 2021, p. 3231.
[17] N. Saunders, A. Miodownik, The Cu-Sn (copper-tin) system, Bulletin of Alloy Phase Diagrams 11(3) (1990) 278-287.
[18] K. Chen, B. Lim, L. Zhang, B.X. Koo, S.P. Ringer, K. Nomoto, Formation mechanisms of Sn-rich δ phase and its role in strengthening Cu-10Sn manufactured by laser powder bed fusion, Additive Manufacturing 102 (2025) 104723.
[19] Y. Yu, W. Chen, L. Xie, Y. Song, Effect of heat treatment on microstructure evolution, phase transformation and mechanical properties of dual phase Cu-Zn alloy, Journal of Alloys and Compounds 904 (2022) 163960.
[20] A. Alfantazi, T. Ahmed, D. Tromans, Corrosion behavior of copper alloys in chloride media, Materials & Design 30(7) (2009) 2425-2430.
[21] W.A. Badawy, K.M. Ismail, A.M. Fathi, Effect of Ni content on the corrosion behavior of Cu–Ni alloys in neutral chloride solutions, Electrochimica acta 50(18) (2005) 3603-3608.
[22] T. De Terris, T. Baffie, C. Ribiere, Additive manufacturing of pure copper: a review and comparison of physical, microstructural, and mechanical properties of samples manufactured with Laser-Powder Bed Fusion (L-PBF), Electron Beam Melting (EBM) and Metal Fused Deposition Modelling (MFDM) technologies, International Journal of Material Forming 16(4) (2023) 32.
[23] I. Gibson, D. Rosen, B. Stucker, M. Khorasani, D. Rosen, B. Stucker, M. Khorasani, Additive manufacturing technologies, Springer2021.
[24] A. Inoue, Stabilization of metallic supercooled liquid and bulk amorphous alloys, Acta Materialia 48(1) (2000) 279-306.
[25] R. Vilar, Laser cladding, Journal of laser applications 11(2) (1999) 64-79.
[26] S. Qu, J. Ding, J. Fu, M. Fu, B. Zhang, X. Song, High-precision laser powder bed fusion processing of pure copper, Additive Manufacturing 48 (2021) 102417.
[27] T.J. Horn, D. Gamzina, Additive manufacturing of copper and copper alloys, Additive Manufacturing Processes, ASM International2020, pp. 388-418.
[28] S. Yadav, C. Paul, A. Jinoop, A. Rai, K. Bindra, Laser directed energy deposition based additive manufacturing of copper: process development and material characterizations, Journal of Manufacturing Processes 58 (2020) 984-997.
[29] S. Yin, P. Cavaliere, B. Aldwell, R. Jenkins, H. Liao, W. Li, R. Lupoi, Cold spray additive manufacturing and repair: Fundamentals and applications, Additive manufacturing 21 (2018) 628-650.
[30] L. Collini, Copper Alloys: Early Applications and Current Performance-Enhancing Processes, BoD–Books on Demand2012.
[31] K. Morshed-Behbahani, A. Aliyu, D.P. Bishop, A. Nasiri, Additive manufacturing of copper-based alloys for high-temperature aerospace applications: A review, Materials Today Communications 38 (2024) 108395.
[32] I.E. Agency, Total supply & demand for key minerals, 2025, pp. https://www.iea.org/data-and-statistics/data-tools/critical-minerals-data-explorer.
[33] F.C. Walsh, Electrode reactions in metal finishing, Transactions of the IMF 69(3) (1991) 107-110.
[34] U.S.B.o. Standards, Copper Wire Tables, U.S. Government Printing Office1914.
[35] L. Fan, J.M. Khodadadi, Thermal conductivity enhancement of phase change materials for thermal energy storage: a review, Renewable and sustainable energy reviews 15(1) (2011) 24-46.

[36] S. Chupradit, A.T. Jalil, Y. Enina, D.A. Neganov, M.S. Alhassan, S. Aravindhan, A. Davarpanah, Use of organic and copper-based nanoparticles on the turbulator installment in a shell tube heat exchanger: a CFD-based simulation approach by using nanofluids, Journal of Nanomaterials 2021(1) (2021) 3250058.
[37] C.Y. Ho, R.W. Powell, P.E. Liley, Thermal conductivity of the elements, Journal of physical and chemical reference data 1(2) (1972) 279-421.
[38] Z. Mao, D.Z. Zhang, J. Jiang, G. Fu, P. Zhang, Processing optimisation, mechanical properties and microstructural evolution during selective laser melting of Cu-15Sn high-tin bronze, Materials Science and Engineering: A 721 (2018) 125-134.
[39] M. Parvizi, A. Aladjem, J. Castle, Behaviour of 90–10 cupronickel in sea water, International Materials Reviews 33(1) (1988) 169-200.
[40] W. Soffa, D. Laughlin, High-strength age hardening copper–titanium alloys: redivivus, Progress in Materials Science 49(3-4) (2004) 347-366.
[41] D. Zhao, Q. Dong, P. Liu, B. Kang, J. Huang, Z. Jin, Structure and strength of the age hardened Cu–Ni–Si alloy, Materials Chemistry and Physics 79(1) (2003) 81-86.
[42] S. Ford, M. Despeisse, Additive manufacturing and sustainability: an exploratory study of the advantages and challenges, Journal of cleaner Production 137 (2016) 1573-1587.
[43] S.A. Tofail, E.P. Koumoulos, A. Bandyopadhyay, S. Bose, L. O'Donoghue, C. Charitidis, Additive manufacturing: scientific and technological challenges, market uptake and opportunities, Materials today 21(1) (2018) 22-37.
[44] D.D. Gu, W. Meiners, K. Wissenbach, R. Poprawe, Laser additive manufacturing of metallic components: materials, processes and mechanisms, International materials reviews 57(3) (2012) 133-164.
[45] S.D. Jadhav, L.R. Goossens, Y. Kinds, B. Van Hooreweder, K. Vanmeensel, Laser-based powder bed fusion additive manufacturing of pure copper, Additive Manufacturing 42 (2021) 101990.
[46] W. Abd-Elaziem, S. Elkatatny, T.A. Sebaey, M.A. Darwish, M.A. Abd El-Baky, Machine learning for advancing laser powder bed fusion of stainless steel, Journal of Materials Research and Technology 30 (2024) 4986-5016.
[47] R. Shrestha, J. Simsiriwong, N. Shamsaei, Fatigue behavior of additive manufactured 316L stainless steel parts: Effects of layer orientation and surface roughness, Additive Manufacturing 28 (2019) 23-38.
[48] M. Muhammad, P. Nezhadfar, S. Thompson, A. Saharan, N. Phan, N. Shamsaei, A comparative investigation on the microstructure and mechanical properties of additively manufactured aluminum alloys, International Journal of Fatigue 146 (2021) 106165.
[49] J. Rogers, J. Elambasseril, C. Wallbrink, B. Krieg, M. Qian, M. Brandt, M. Leary, The impact of surface orientation on surface roughness and fatigue life of laser-based powder bed fusion Ti-6Al-4V, Additive Manufacturing 85 (2024) 104149.
[50] A.P. Jirandehi, B. Hajshirmohammadi, P. Carrion, M. Khonsari, N. Shamsaei, S. Shao, Strain energy-based fatigue failure analyses of LB-PBF Inconel 718: Effect of build orientation, Additive Manufacturing 52 (2022) 102661.
[51] Selective Laser Melting. https://www.empa.ch/web/coating-competence-center/selective-laser-melting.
[52] R. Guschlbauer, A.K. Burkhardt, Z. Fu, C. Körner, Effect of the oxygen content of pure copper powder on selective electron beam melting, Materials Science and Engineering: A 779 (2020) 139106.
[53] S.J. Raab, R. Guschlbauer, M.A. Lodes, C. Körner, Thermal and electrical conductivity of 99.9% pure copper processed via selective electron beam melting, Advanced Engineering Materials 18(9) (2016) 1661-1666.

[54] C. Silbernagel, L. Gargalis, I. Ashcroft, R. Hague, M. Galea, P. Dickens, Electrical resistivity of pure copper processed by medium-powered laser powder bed fusion additive manufacturing for use in electromagnetic applications, Additive Manufacturing 29 (2019) 100831.
[55] M. Zavala-Arredondo, N. Boone, J. Willmott, D.T.D. Childs, P. Ivanov, K.M. Groom, K. Mumtaz, Laser diode area melting for high speed additive manufacturing of metallic components, Materials & Design 117 (2017) 305-315.
[56] P. Wagenblast, A. Myrell, M. Thielmann, T. Scherbaum, D. Coupek, Additive manufacturing with green disk lasers, Laser 3D Manufacturing VII, SPIE, 2020, pp. 39-45.
[57] M.B. Schäfle, J. Gärtner, F. Nahr, E. Bruder, M. Schmidt, E. Kirchner, Process development for green laser LPBF of pure Cu using dimensionless numbers, Progress in Additive Manufacturing (2025) 1-18.
[58] K. Takenaka, Y. Sato, N. Yoshida, M. Yoshitani, M. Heya, M. Tsukamoto, Additive manufactured of pure copper by blue diode laser induced selective laser melting, Journal of Laser Applications 34(4) (2022).
[59] D. Tiberto, U.E. Klotz, F. Held, G. Wolf, Additive manufacturing of copper alloys: influence of process parameters and alloying elements, Materials science and technology 35(8) (2019) 969-977.
[60] Q. Mao, Y. Liu, Y. Zhao, A review on copper alloys with high strength and high electrical conductivity, Journal of Alloys and Compounds (2024) 174456.
[61] Y. Liu, J. Zhang, Q. Sun, M. Li, M. Yan, X. Cheng, M. Li, M.-X. Zhang, Laser powder bed fusion of copper matrix iron particle reinforced nanocomposite with high strength and high conductivity, Journal of Materials Science & Technology 134 (2023) 50-59.
[62] Y. Liu, J. Zhang, Q. Tan, Y. Yin, S. Liu, M. Li, M. Li, Q. Liu, Y. Zhou, T. Wu, F. Wang, M.-X. Zhang, Additive manufacturing of high strength copper alloy with heterogeneous grain structure through laser powder bed fusion, Acta Materialia 220 (2021) 117311.
[63] Y. Liu, J. Zhang, R. Niu, M. Bayat, Y. Zhou, Y. Yin, Q. Tan, S. Liu, J.H. Hattel, M. Li, Manufacturing of high strength and high conductivity copper with laser powder bed fusion, Nature Communications 15(1) (2024) 1283.
[64] S. Qu, L. Wang, S. Zhang, C. Yang, H.Y. Chia, G. Wu, Z. Hu, J. Ding, W. Yan, Y. Zhang, Oxide-dispersion-enabled laser additive manufacturing of high-resolution copper, Nature Communications 16(1) (2025) 3234.
[65] S.D. Jadhav, L.R. Goossens, Y. Kinds, B.V. Hooreweder, K. Vanmeensel, Laser-based powder bed fusion additive manufacturing of pure copper, Additive Manufacturing 42 (2021) 101990.
[66] S.D. Jadhav, S. Dadbakhsh, L. Goossens, J.P. Kruth, J. Van Humbeeck, K. Vanmeensel, Influence of selective laser melting process parameters on texture evolution in pure copper, Journal of Materials Processing Technology 270 (2019) 47-58.
[67] P. Mair, J. Braun, L. Kaserer, L. March, D. Schimbaeck, I. Letofsky-Papst, G. Leichtfried, Unique microstructure evolution of a novel Ti-modified Al-Cu alloy processed using laser powder bed fusion, Materials Today Communications 31 (2022) 103353.
[68] Z. Hu, Z. Ma, L. Yu, Y. Liu, Functionally graded materials with grain-size gradients and heterogeneous microstructures achieved by additive manufacturing, Scripta Materialia 226 (2023) 115197.
[69] M.R. Jandaghi, H. Pouraliakbar, S.H. Shim, V. Fallah, S.I. Hong, M. Pavese, In-situ alloying of stainless steel 316L by co-inoculation of Ti and Mn using LPBF additive

manufacturing: Microstructural evolution and mechanical properties, Materials Science and Engineering: A 857 (2022) 144114.
[70] G. Marchese, S. Parizia, M. Rashidi, A. Saboori, D. Manfredi, D. Ugues, M. Lombardi, E. Hryha, S. Biamino, The role of texturing and microstructure evolution on the tensile behavior of heat-treated Inconel 625 produced via laser powder bed fusion, Materials Science and Engineering: A 769 (2020) 138500.
[71] H. Wang, Z. Zhu, H. Chen, A. Wang, J. Liu, H. Liu, R. Zheng, S. Nai, S. Primig, S. Babu, Effect of cyclic rapid thermal loadings on the microstructural evolution of a CrMnFeCoNi high-entropy alloy manufactured by selective laser melting, Acta Materialia 196 (2020) 609-625.
[72] R. Ghomashchi, S. Nafisi, Solidification of Al12Si melt Pool in laser powder bed fusion, Journal of Materials Engineering and Performance 32(23) (2023) 10943-10955.
[73] A. Shrivastava, S.A. Kumar, S. Rao, Postprocessing challenges in metal AM: Strategies for achieving homogeneous microstructure in Ni-based superalloys, Advances in Metal Additive Manufacturing, Elsevier2023, pp. 179-202.
[74] S. Kou, Welding metallurgy, New York1987.
[75] S.H. Baghjari, S.A.A. AkbariMousavi, Experimental investigation on dissimilar pulsed Nd:YAG laser welding of AISI 420 stainless steel to kovar alloy, Materials & Design 57 (2014) 128-134.
[76] Z. Li, S. Sui, X. Ma, H. Tan, C. Zhong, G. Bi, A.T. Clare, A. Gasser, J. Chen, High deposition rate powder-and wire-based laser directed energy deposition of metallic materials: A review, International Journal of Machine Tools and Manufacture 181 (2022) 103942.
[77] W.E. Frazier, Metal additive manufacturing: a review, Journal of Materials Engineering and performance 23(6) (2014) 1917-1928.
[78] S.-H. Li, P. Kumar, S. Chandra, U. Ramamurty, Directed energy deposition of metals: processing, microstructures, and mechanical properties, International Materials Reviews 68(6) (2023) 605-647.
[79] S.W. Williams, F. Martina, A.C. Addison, J. Ding, G. Pardal, P. Colegrove, Wire+ arc additive manufacturing, Materials science and technology 32(7) (2016) 641-647.
[80] J.-S. Lim, W.-J. Oh, C.-M. Lee, D.-H. Kim, Selection of effective manufacturing conditions for directed energy deposition process using machine learning methods, Scientific Reports 11(1) (2021) 24169.
[81] B. Zhang, Z. Gao, H. Xiao, X. Yang, Y. Li, H. Zhu, Size effects and optimization during laser directed energy deposition on high thermal conductivity copper alloys, Journal of Materials Research and Technology 33 (2024) 4389-4399.
[82] G. Demeneghi, B. Barnes, P. Gradl, D. Ellis, J.R. Mayeur, K. Hazeli, Directed energy deposition GRCop-42 copper alloy: Characterization and size effects, Materials & Design 222 (2022) 111035.
[83] W. Zhang, H. Liao, Z. Hu, S. Zhang, B. Chen, H. Yang, Y. Wang, H. Zhu, Interfacial characteristics and mechanical properties of additive manufacturing martensite stainless steel on the Cu-Cr alloy substrate by directed energy deposition, Journal of Materials Science & Technology 90 (2021) 121-132.
[84] B. Li, H. Zheng, C. Han, K. Zhou, Nanotwins-containing microstructure and superior mechanical strength of a Cu–9Al–5Fe–5Ni alloy additively manufactured by laser metal deposition, Additive Manufacturing 39 (2021) 101825.
[85] D. Svetlizky, M. Das, B. Zheng, A.L. Vyatskikh, S. Bose, A. Bandyopadhyay, J.M. Schoenung, E.J. Lavernia, N. Eliaz, Directed energy deposition (DED) additive manufacturing: Physical characteristics, defects, challenges and applications, Materials Today 49 (2021) 271-295.

[86] D.D. Singh, S. Arjula, A.R. Reddy, Functionally graded materials manufactured by direct energy deposition: a review, Materials Today: Proceedings 47 (2021) 2450-2456.
[87] G. Prashar, H. Vasudev, A comprehensive review on sustainable cold spray additive manufacturing: State of the art, challenges and future challenges, Journal of Cleaner Production 310 (2021) 127606.
[88] R. Raoelison, C. Verdy, H. Liao, Cold gas dynamic spray additive manufacturing today: Deposit possibilities, technological solutions and viable applications, Materials & Design 133 (2017) 266-287.
[89] A. Papyrin, V. Kosarev, S. Klinkov, A. Alkhimov, V.M. Fomin, Cold spray technology, Elsevier2006.
[90] Y. Zou, Cold Spray Additive Manufacturing: Microstructure Evolution and Bonding Features, Accounts of Materials Research 2(11) (2021) 1071-1081.
[91] J. Karthikeyan, Development of oxidation resistant coatings on GRCop-84 substrates by cold spray process, 2007.
[92] L. Cui, K. Fang, J. Cao, E. Hao, J. Zhu, G. Liu, J. Hao, A practical method to improve mechanical and electrical properties of ADS copper prepared by cold spray additive manufacturing through powder pretreatment, Journal of Alloys and Compounds 965 (2023) 171319.
[93] C. Chen, Y. Xie, S. Yin, W. Li, X. Luo, X. Xie, R. Zhao, C. Deng, J. Wang, H. Liao, M. Liu, Z. Ren, Ductile and high strength Cu fabricated by solid-state cold spray additive manufacturing, Journal of Materials Science & Technology 134 (2023) 234-243.
[94] N. Hutasoit, R.A.R. Rashid, S. Palanisamy, A. Duguid, Effect of build orientation and post-build heat treatment on the mechanical properties of cold spray additively manufactured copper parts, The International Journal of Advanced Manufacturing Technology 110(9) (2020) 2341-2357.
[95] Z.L. Zhang, M. Afrasiabi, M. Bambach, A meshless computational framework for studying cold spray additive manufacturing including large numbers of powder particles with diverse characteristics, Scientific Reports 14(1) (2024) 11393.
[96] L. Cui, G. Xu, K. Liu, J. Hao, J. Zhao, J. Cui, G. Liu, E. Hao, J. Zou, Influence of feedpowder morphology on microstructure and mechanical properties of Tantalum produced by cold spray additive manufacturing, International Journal of Refractory Metals and Hard Materials 131 (2025) 107203.
[97] W.Y. Li, C. Zhang, H.T. Wang, X.P. Guo, H.L. Liao, C.J. Li, C. Coddet, Significant influences of metal reactivity and oxide films at particle surfaces on coating microstructure in cold spraying, Applied Surface Science 253(7) (2007) 3557-3562.
[98] W. Li, K. Yang, S. Yin, X. Yang, Y. Xu, R. Lupoi, Solid-state additive manufacturing and repairing by cold spraying: A review, Journal of materials science & technology 34(3) (2018) 440-457.
[99] T.T.T. Tran, K. Krishnan, Antimicrobial property, corrosion resistance and tarnish resistance of cold-sprayed additive manufactured copper-nickel alloy, Progress in Additive Manufacturing 9(4) (2024) 1253-1264.
[100] Copper Alloys Market Size, Share & Trend Analysis Report, By Type (Brass, Bronze), By End Use (Building & Construction, Automotive & Transportation), By Region, And Segment Forecasts, 2024 - 2030. https://www.grandviewresearch.com/industry-analysis/copper-alloys-market-report. 2025).
[101] O. Salman, F. Brenne, T. Niendorf, J. Eckert, K. Prashanth, T. He, S. Scudino, Impact of the scanning strategy on the mechanical behavior of 316L steel synthesized by selective laser melting, Journal of Manufacturing Processes 45 (2019) 255-261.

[102] T. Bhardwaj, M. Shukla, Effect of laser scanning strategies on texture, physical and mechanical properties of laser sintered maraging steel, Materials Science and Engineering: A 734 (2018) 102-109.
[103] N. Nadammal, T. Mishurova, T. Fritsch, I. Serrano-Munoz, A. Kromm, C. Haberland, P.D. Portella, G. Bruno, Critical role of scan strategies on the development of microstructure, texture, and residual stresses during laser powder bed fusion additive manufacturing, Additive Manufacturing 38 (2021) 101792.
[104] L.N. Carter, C. Martin, P.J. Withers, M.M. Attallah, The influence of the laser scan strategy on grain structure and cracking behaviour in SLM powder-bed fabricated nickel superalloy, Journal of Alloys and Compounds 615 (2014) 338-347.
[105] M.C. Lam, S.C.V. Lim, H. Song, Y. Zhu, X. Wu, A. Huang, Scanning strategy induced cracking and anisotropic weakening in grain texture of additively manufactured superalloys, Additive Manufacturing 52 (2022) 102660.
[106] A. Mehta, L. Zhou, H. Hyer, T. Huynh, B. Lu, K. Graydon, E.J. Drobner, S.H. Park, Y. Sohn, Microstructural characteristics and mechanical properties of additively manufactured Cu–10Sn alloys by laser powder bed fusion, Materials Science and Engineering: A 838 (2022) 142775.
[107] P. Yang, D. He, W. Shao, Z. Tan, X. Guo, S. Lu, K. Anton, Study of the microstructure and mechanical properties of Cu–Sn alloys formed by selective laser melting with different Sn contents, Journal of Materials Research and Technology 24 (2023) 5476-5485.
[108] F. Kohler, T. Campanella, S. Nakanishi, M. Rappaz, Application of single pan thermal analysis to Cu–Sn peritectic alloys, Acta Materialia 56(7) (2008) 1519-1528.
[109] W. Zhai, W. Wang, D. Geng, B. Wei, A DSC analysis of thermodynamic properties and solidification characteristics for binary Cu–Sn alloys, Acta Materialia 60(19) (2012) 6518-6527.
[110] S. Scudino, C. Unterdörfer, K. Prashanth, H. Attar, N. Ellendt, V. Uhlenwinkel, J. Eckert, Additive manufacturing of Cu–10Sn bronze, Materials Letters 156 (2015) 202-204.
[111] C. Zeng, B. Zhang, A.H. Ettefagh, H. Wen, H. Yao, W. Meng, S. Guo, Mechanical, thermal, and corrosion properties of Cu-10Sn alloy prepared by laser-powder-bed-fusion additive manufacturing, Additive Manufacturing 35 (2020) 101411.
[112] G. Karthik, P. Sathiyamoorthi, A. Zargaran, J.M. Park, P. Asghari-Rad, S. Son, S.H. Park, H.S. Kim, Novel precipitation and enhanced tensile properties in selective laser melted Cu-Sn alloy, Materialia 13 (2020) 100861.
[113] P. Yang, D. He, Z. Wang, Z. Tan, H. Fu, W. Shao, X. Guo, Investigation of selective laser melting process for Cu-5Sn alloy on surface roughness, microstructure and mechanical property, Rapid Prototyping Journal 28(1) (2022) 10-20.
[114] J.S. Park, C.W. Park, K.J. Lee, Implication of peritectic composition in historical high-tin bronze metallurgy, Materials characterization 60(11) (2009) 1268-1275.
[115] S. Fürtauer, D. Li, D. Cupid, H. Flandorfer, The Cu–Sn phase diagram, Part I: new experimental results, Intermetallics 34 (2013) 142-147.
[116] N. Bosco, F. Zok, Strength of joints produced by transient liquid phase bonding in the Cu–Sn system, Acta materialia 53(7) (2005) 2019-2027.
[117] X. Li, T. Ivas, A.B. Spierings, K. Wegener, C. Leinenbach, Phase and microstructure formation in rapidly solidified Cu-Sn and Cu-Sn-Ti alloys, Journal of Alloys and Compounds 735 (2018) 1374-1382.
[118] T. Watanabe, Nano plating-microstructure formation theory of plated films and a database of plated films, Elsevier2004.

[119] Q. Zhai, Y. Yang, J. Xu, X. Guo, Microstructural morphology and phase structure of rapidly solidified Cu-Sn alloy, CHINESE JOURNAL OF NONFERROUS METALS 16(8) (2006) 1374.
[120] C. Pleass, S. Jothi, Influence of powder characteristics and additive manufacturing process parameters on the microstructure and mechanical behaviour of Inconel 625 fabricated by Selective Laser Melting, Additive Manufacturing 24 (2018) 419-431.
[121] A. Mussatto, R. Groarke, A. O'Neill, M.A. Obeidi, Y. Delaure, D. Brabazon, Influences of powder morphology and spreading parameters on the powder bed topography uniformity in powder bed fusion metal additive manufacturing, Additive Manufacturing 38 (2021) 101807.
[122] K. Jin, H. Wang, P. Chen, T. Hong, J. Cheng, Effects of powder particle size distribution on the microstructure and properties of Laser powder bed fusion CuSn10 alloy, Materials Science and Technology 0(0) 02670836251350244.
[123] P. Ren, Y. Ouyang, J. Mu, S. Luo, Z. Tang, Y. Wu, C.L.A. Leung, J.P. Oliveira, Y. Zou, H. Wang, H. Wang, Metal powder atomization preparation, modification, and reuse for additive manufacturing: A review, Progress in Materials Science 152 (2025) 101449.
[124] A.B. Spierings, G. Levy, Comparison of density of stainless steel 316L parts produced with selective laser melting using different powder grades, (2009).
[125] X. Zhou, X. Liu, D. Zhang, Z. Shen, W. Liu, Balling phenomena in selective laser melted tungsten, Journal of Materials Processing Technology 222 (2015) 33-42.
[126] K. Jin, H. Wang, P. Chen, T. Hong, J. Cheng, Effects of powder particle size distribution on the microstructure and properties of Laser powder bed fusion CuSn10 alloy, Materials Science and Technology (2024) 02670836251350244.
[127] B. Liu, R. Wildman, C. Tuck, I. Ashcroft, R. Hague, Investigation the effect of particle size distribution on processing parameters optimisation in selective laser melting process, (2011).
[128] C.L.A. Leung, S. Marussi, M. Towrie, R.C. Atwood, P.J. Withers, P.D. Lee, The effect of powder oxidation on defect formation in laser additive manufacturing, Acta Materialia 166 (2019) 294-305.
[129] B.C. Hornbuckle, J.A. Smeltzer, S. Sharma, S. Nagar, C.J. Marvel, P.R. Cantwell, M.P. Harmer, K. Solanki, K.A. Darling, A high-temperature nanostructured Cu-Ta-Li alloy with complexion-stabilized precipitates, Science 387(6741) (2025) 1413-1417.
[130] M.S. Palm, M. Horn, A. Bachmann, G. Schlick, M.F. Zaeh, G. Reinhart, Influence of contaminants on part quality during Laser-Based Powder Bed Fusion of nickel base alloys, Procedia CIRP 94 (2020) 233-238.
[131] Q. Liu, C. Ren, Z. Song, X. Dan, J. Ju, T. Yang, S. Ni, J. Lu, L. Liu, J. Pan, High-strength and high-conductivity additively manufactured Cu-O alloy enabled by cellular microstructure, Additive Manufacturing (2024) 104244.
[132] Y.M. Wang, T. Voisin, J.T. McKeown, J. Ye, N.P. Calta, Z. Li, Z. Zeng, Y. Zhang, W. Chen, T.T. Roehling, R.T. Ott, M.K. Santala, Philip J. Depond, M.J. Matthews, A.V. Hamza, T. Zhu, Additively manufactured hierarchical stainless steels with high strength and ductility, Nature Materials 17(1) (2018) 63-71.
[133] S.E. Brika, M. Letenneur, C.A. Dion, V. Brailovski, Influence of particle morphology and size distribution on the powder flowability and laser powder bed fusion manufacturability of Ti-6Al-4V alloy, Additive Manufacturing 31 (2020) 100929.
[134] A. Strondl, O. Lyckfeldt, H. Brodin, U. Ackelid, Characterization and Control of Powder Properties for Additive Manufacturing, JOM 67(3) (2015) 549-554.
[135] P. Ren, Y. Ouyang, J. Mu, S. Luo, Z. Tang, Y. Wu, C.L.A. Leung, J. Oliveira, Y. Zou, H. Wang, Metal powder atomization preparation, modification, and reuse for additive manufacturing: A review, Progress in Materials Science (2025) 101449.

[136] R. Gu, X. Yao, D. Wang, H. Wang, M. Yan, K.S. Wong, Selective Laser Melting of Cu–10Sn–0.4P: Processing, Microstructure, Properties, and Brief Comparison with Additively Manufactured Cu–10Sn, Advanced Engineering Materials 24(2) (2022) 2100716.
[137] C. Kittel, P. McEuen, Introduction to solid state physics, John Wiley & Sons2018.
[138] S. Qu, J. Ding, J. Fu, M. Fu, X. Song, Anisotropic material properties of pure copper with fine-grained microstructure fabricated by laser powder bed fusion process, Additive Manufacturing 59 (2022) 103082.
[139] G. Ghosh, J. Miyake, M. Fine, The systems-based design of high-strength, high-conductivity alloys, Jom 49(3) (1997) 56-60.
[140] A. Datta, W. Soffa, The structure and properties of age hardened Cu-Ti alloys, Acta Metallurgica 24(11) (1976) 987-1001.
[141] S. Nagarjuna, M. Srinivas, K. Balasubramanian, D. Sarma, The alloy content and grain size dependence of flow stress in Cu Ti alloys, Acta materialia 44(6) (1996) 2285-2293.
[142] S. Chen, Y.-H. Duan, B. Huang, W.-C. Hu, Structural properties, phase stability, elastic properties and electronic structures of Cu–Ti intermetallics, Philosophical Magazine 95(32) (2015) 3535-3553.
[143] Y. Fu, G. Xie, F. Zhao, J. Wan, X. Meng, X. Liu, R. Wang, X. Liu, Precipitation behaviors and property variations of Cu-3.0 wt% Ti fabricated by a novel short-processing non-vacuum heating-cooling combined mold continuous casting, Journal of Alloys and Compounds 921 (2022) 166059.
[144] D.E. Laughlin, J.W. Cahn, The crystal structure of the metastable precipitate in copper-based copper-titanium alloys, Scripta Metallurgica 8(1) (1974) 75-78.
[145] D.E. Laughlin, J.W. Cahn, Spinodal decomposition in age hardening copper-titanium alloys, Acta Metallurgica 23(3) (1975) 329-339.
[146] Y. Liao, C. Guo, C. Zhou, W. Xie, B. Yang, H. Wang, Stability of the metastable β'-Cu4Ti phase in CuTi alloys: Role of the Ti content, Materials Characterization 203 (2023) 113164.
[147] S. Semboshi, M. Ishikuro, S. Sato, K. Wagatsuma, T. Takasugi, Extraction of precipitates from age-hardenable Cu–Ti alloys, Materials characterization 82 (2013) 23-31.
[148] A.W. Thompson, J.C. Williams, Age hardening in Cu-2.5 wt pct Ti, Metallurgical Transactions A 15(5) (1984) 931-937.
[149] Y. Liao, C. Guo, C. Zhou, W. Xie, B. Yang, H. Wang, Strengthening of Cu-Ti alloys by stabilization of metastable β′ phase with addition of Gd element, Materials Today Communications 39 (2024) 108671.
[150] Q. Liu, S. Jin, C. Ren, D. Zhang, Z. Pu, H. Wen, Y. Ran, X. Dan, X. Chen, S. Ni, Reducing solidification cracks and enhancing mechanical performance in additively manufactured Cu-Ti alloys via chemical fluctuation manipulation, Virtual and Physical Prototyping 20(1) (2025) e2522274.
[151] K. Sadayappan, M. Sahoo, H.T. Michels, Copper and Copper Alloy Castings, in: S. Viswanathan, D. Apelian, R.J. Donahue, B. DasGupta, M. Gywn, J.L. Jorstad, R.W. Monroe, M. Sahoo, T.E. Prucha, D. Twarog (Eds.), Casting, ASM International 2008, p. 1088.
[152] J.L. Everhart, Copper-Base Nickel Alloys, in: J.L. Everhart (Ed.), Engineering Properties of Nickel and Nickel Alloys, Springer US, Boston, MA, 1971, pp. 100-128.
[153] B. Shepherd, Cast 70–30 cupro-nickel: inherent characteristics, Modern Castings 37 (1960) 120.

[154] A.M.S. El Din, Copper alloys for desalination plants, Desalination 93(1) (1993) 499-516.
[155] W.J. Barnett, The age hardening of copper-manganese-nickel alloys, (1946).
[156] W. Stewart, F. LaQue, Corrosion resisting characteristics of iron modified 90: 10 cupro nickel alloy, Corrosion 8(8) (1952) 259-277.
[157] S. Gupta, A. Johnson, K. Mukherjee, E. Imbembo, Age hardening in a cupronickel alloy containing 1 wt.% silicon, Materials Science and Engineering 6(6) (1970) 395-396.
[158] S. Gupta, A. Johnson, K. Mukherjee, An electron microscopic investigation of precipitation in a Cupronickel alloy containing 1 wt.% Si, Materials Science and Engineering 9 (1972) 97-100.
[159] C. Kokkinoplitis, Precipitation behaviour of the Cu-30% Ni-2% Nb-4% Fe alloy, Thesis (1986).
[160] Q. Lei, Z. Li, T. Xiao, Y. Pang, Z. Xiang, W. Qiu, Z. Xiao, A new ultrahigh strength Cu–Ni–Si alloy, Intermetallics 42 (2013) 77-84.
[161] S.P. Gupta, S.P. Kodali, The Bauschinger Effect in an Age Hardenable Cu–30Ni–1Si Alloy, Transactions of the Japan Institute of Metals 17(5) (1976) 261-266.
[162] M. Sahoo, J.O. Edwards, A. Couture, Forty Years of Investigation, Research and Technology Development on Copper Base Alloys at The Physical Metallurgy Research Laboratories (PMRL), Canadian Metallurgical Quarterly 22(2) (1983) 247-255.
[163] G. Bailey, Copper-nickel-iron alloys resistant to sea-water corrosion, J INST MET 79 (1951) 243-292.
[164] W.J. Braun, F.W. Fink, G.L. Ericson, THE CORROSION OF MONEL AND 70-30 CUPRONICKEL IN HYDROFLUORIC ACID, United States, 1957.
[165] C.A. Schneider, W.S. Rasband, K.W. Eliceiri, NIH Image to ImageJ: 25 years of image analysis, Nature methods 9(7) (2012) 671-675.
[166] L. Orefice, J. Remmelgas, A. Neveu, F. Francqui, J.G. Khinast, A novel methodology for data analysis of dynamic angle of repose tests and powder flow classification, Powder Technology 435 (2024) 119425.
[167] B.H. Toby, R.B. Von Dreele, GSAS-II: the genesis of a modern open-source all purpose crystallography software package, Applied Crystallography 46(2) (2013) 544-549.
[168] A. Mehta, N. Eriksson, R. Newell, L. Zhou, E. Schulz, W. Sprowes, F. Betancor, Y. Park, D.D. Keiser Jr, Y. Sohn, Phase transformations and microstructural development in the U-10 Wt pct Mo alloy with varying Zr contents after heat treatments relevant to the monolithic fuel plate fabrication process, Metallurgical and Materials Transactions A 50(1) (2019) 72-96.
[169] D.B. Williams, C.B. Carter, The transmission electron microscope, Transmission electron microscopy: a textbook for materials science, Springer1996, pp. 3-17.
[170] B. Gault, M.P. Moody, J.M. Cairney, S.P. Ringer, Atom probe microscopy, Springer Science & Business Media2012.
[171] R.K.W. Marceau, L.T. Stephenson, C.R. Hutchinson, S.P. Ringer, Quantitative atom probe analysis of nanostructure containing clusters and precipitates with multiple length scales, Ultramicroscopy 111(6) (2011) 738-742.
[172] S. Mukherjee, I.B. Timokhina, C. Zhu, S.P. Ringer, P.D. Hodgson, Three-dimensional atom probe microscopy study of interphase precipitation and nanoclusters in thermomechanically treated titanium–molybdenum steels, Acta Materialia 61(7) (2013) 2521-2530.
[173] M.W. Zandbergen, Q. Xu, A. Cerezo, G.D.W. Smith, Study of precipitation in Al–Mg–Si alloys by Atom Probe Tomography I. Microstructural changes as a function of ageing temperature, Acta Materialia 101 (2015) 136-148.

[174] C.A. Williams, D. Haley, E.A. Marquis, G.D. Smith, M.P. Moody, Defining clusters in APT reconstructions of ODS steels, Ultramicroscopy 132 (2013) 271-278.
[175] R.K.W. Marceau, G. Sha, R. Ferragut, A. Dupasquier, S.P. Ringer, Solute clustering in Al–Cu–Mg alloys during the early stages of elevated temperature ageing, Acta Materialia 58(15) (2010) 4923-4939.
[176] S. Dhara, R.K.W. Marceau, K. Wood, T. Dorin, I.B. Timokhina, P.D. Hodgson, Atom probe tomography data analysis procedure for precipitate and cluster identification in a Ti-Mo steel, Data in Brief 18 (2018) 968-982.
[177] E. ASTM, Standard test methods for tension testing of metallic materials, Annual book of ASTM standards. ASTM, 2001.
[178] G. ASTM, 99; Standard Test Method for Wear and Friction Testing with a Pin-on-Disk or Ball-on-Disk Apparatus, ASTM International: West Conshohocken, PA, USA (2023).
[179] A. Standard, ASTM E92–17, 2017a, Standard test methods for vickers hardness and knoop hardness of metallic materials, West Conshohocken, PA, USA: ASTM International (2017).
[180] A. Standard, E384, Standard test method for microindentation hardness of materials, West Conshohocken, PA: ASTM International (2000).
[181] J.P. Perdew, K. Burke, M. Ernzerhof, Generalized gradient approximation made simple, Physical review letters 77(18) (1996) 3865.
[182] P.E. Blöchl, Projector augmented-wave method, Physical review B 50(24) (1994) 17953.
[183] G. Kresse, J. Furthmüller, Efficient iterative schemes for ab initio total-energy calculations using a plane-wave basis set, Physical review B 54(16) (1996) 11169.
[184] S. Nosé, A unified formulation of the constant temperature molecular dynamics methods, The Journal of chemical physics 81(1) (1984) 511-519.
[185] C. Cepeda-Jiménez, F. Potenza, E. Magalini, V. Luchin, A. Molinari, M. Pérez-Prado, Effect of energy density on the microstructure and texture evolution of Ti-6Al-4V manufactured by laser powder bed fusion, Mater. Charact. 163 (2020) 110238.
[186] C. Wu, W. Zai, H.C. Man, Additive manufacturing of ZK60 magnesium alloy by selective laser melting: Parameter optimization, microstructure and biodegradability, Materials Today Communications 26 (2021) 101922.
[187] Q. Deng, X. Wang, Q. Lan, Z. Chang, Z. Liu, N. Su, Y. Wu, D. Liu, L. Peng, W. Ding, Limitations of linear energy density for laser powder bed fusion of Mg-15Gd-1Zn-0.4 Zr alloy, Mater. Charact. 190 (2022) 112071.
[188] K. Moussaoui, W. Rubio, M. Mousseigne, T. Sultan, F. Rezai, Effects of Selective Laser Melting additive manufacturing parameters of Inconel 718 on porosity, microstructure and mechanical properties, Materials Science and Engineering: A 735 (2018) 182-190.
[189] U.S. Bertoli, A.J. Wolfer, M.J. Matthews, J.-P.R. Delplanque, J.M. Schoenung, On the limitations of volumetric energy density as a design parameter for selective laser melting, Mater. Des. 113 (2017) 331-340.
[190] Q. Deng, Y. Wu, Y. Luo, N. Su, X. Xue, Z. Chang, Q. Wu, Y. Xue, L. Peng, Fabrication of high-strength Mg-Gd-Zn-Zr alloy via selective laser melting, Mater. Charact. 165 (2020) 110377.
[191] Q. Guo, C. Zhao, M. Qu, L. Xiong, L.I. Escano, S.M.H. Hojjatzadeh, N.D. Parab, K. Fezzaa, W. Everhart, T. Sun, In-situ characterization and quantification of melt pool variation under constant input energy density in laser powder bed fusion additive manufacturing process, Addit. Manuf. 28 (2019) 600-609.

[192] D. Dai, D. Gu, H. Zhang, J. Xiong, C. Ma, C. Hong, R. Poprawe, Influence of scan strategy and molten pool configuration on microstructures and tensile properties of selective laser melting additive manufactured aluminum based parts, Optics & Laser Technology 99 (2018) 91-100.
[193] H. Zhang, D. Gu, D. Dai, C. Ma, Y. Li, R. Peng, S. Li, G. Liu, B. Yang, Influence of scanning strategy and parameter on microstructural feature, residual stress and performance of Sc and Zr modified Al–Mg alloy produced by selective laser melting, Materials Science and Engineering: A 788 (2020) 139593.
[194] T. DebRoy, H.L. Wei, J.S. Zuback, T. Mukherjee, J.W. Elmer, J.O. Milewski, A.M. Beese, A. Wilson-Heid, A. De, W. Zhang, Additive manufacturing of metallic components – Process, structure and properties, Progress in Materials Science 92 (2018) 112-224.
[195] W. Zhang, H. Wang, B.J. Kooi, Y. Pei, Additive manufacturing of interstitial-strengthened high entropy alloy: Scanning strategy dependent anisotropic mechanical properties, Materials Science and Engineering: A 872 (2023) 144978.
[196] L. Mugwagwa, D. Dimitrov, S. Matope, I. Yadroitsev, Evaluation of the impact of scanning strategies on residual stresses in selective laser melting, The International Journal of Advanced Manufacturing Technology 102(5) (2019) 2441-2450.
[197] Y. Liu, Y. Yang, D. Wang, A study on the residual stress during selective laser melting (SLM) of metallic powder, The International Journal of Advanced Manufacturing Technology 87(1) (2016) 647-656.
[198] J. Wu, L. Li, L. Dai, W. Zhang, L. Huang, X. Meng, H. Zhang, P. Li, S. Huang, J. Zhou, Influence of scanning strategies on microstructure and mechanical properties of laser powder bed fusion 2195 Al-Li alloy, Journal of Alloys and Compounds 1004 (2024) 175841.
[199] Z. Hu, Z. Yang, Z. Du, J. Wu, J. Dong, H. Wang, Z. Ma, Effect of scanning strategy on the anisotropy in microstructure and properties of Cu-Cr-Zr alloy manufactured by laser powder bed fusion, Journal of Alloys and Compounds 920 (2022) 165957.
[200] A. Kudzal, B. McWilliams, C. Hofmeister, F. Kellogg, J. Yu, J. Taggart-Scarff, J. Liang, Effect of scan pattern on the microstructure and mechanical properties of Powder Bed Fusion additive manufactured 17-4 stainless steel, Materials & Design 133 (2017) 205-215.
[201] M.N. Doğu, S. Ozer, M.A. Yalçın, K. Davut, M.A. Obeidi, C. Simsir, H. Gu, C. Teng, D. Brabazon, A comprehensive study of the effect of scanning strategy on IN939 fabricated by powder bed fusion-laser beam, Journal of Materials Research and Technology 33 (2024) 5457-5481.
[202] L. Liu, D. Wang, Y. Yang, Z. Wang, Z. Qian, S. Wu, J. Tang, C. Han, C. Tan, Effect of scanning strategies on the microstructure and mechanical properties of inconel 718 alloy fabricated by laser powder bed fusion, Advanced Engineering Materials 25(5) (2023) 2200492.
[203] X. Liu, R. Hu, H. Zou, C. Yang, X. Luo, J. Bai, R. Ma, Investigation of cracking mechanism and yield strength associated with scanning strategy for an additively manufactured nickel-based superalloy, Journal of Alloys and Compounds 938 (2023) 168532.
[204] E.A. Gadallah, M.A. Ghanem, M. El-Hamid, A.E. El-Nikhaily, Effect of tin content and ECAP passes on the mechanical properties of Cu/Sn alloys as bearing materials, Port-Said Eng. Res. J 18 (2014) 79-89.
[205] A.Ç. Kılınç, A.A. Göktaş, Ö.Y. Keskin, S. Köktaş, K.C. Tekin, Comparison of wear and mechanical properties of cast and 3D printed CuSn10 bronze alloy, Materials Testing 65(5) (2023) 764-773.

[206] S.-M. So, K.-Y. Kim, S.-J. Lee, Y.-J. Yu, H.-A. Lim, M.-S. Oh, Effects of Sn content and hot deformation on microstructure and mechanical properties of binary high Sn content Cu–Sn alloys, Materials Science and Engineering: A 796 (2020) 140054.
[207] X. Yan, C. Chang, D. Dong, S. Gao, W. Ma, M. Liu, H. Liao, S. Yin, Microstructure and mechanical properties of pure copper manufactured by selective laser melting, Materials Science and Engineering: A 789 (2020) 139615.
[208] S.D. Jadhav, J. Vleugels, J.P. Kruth, J. Van Humbeeck, K. Vanmeensel, Mechanical and electrical properties of selective laser-melted parts produced from surface-oxidized copper powder, Material Design & Processing Communications 2(2) (2020) e94.
[209] C. Deng, J. Kang, T. Feng, Y. Feng, X. Wang, P. Wu, Study on the selective laser melting of CuSn10 powder, Materials 11(4) (2018) 614.
[210] H. Wang, L. Guo, Z. Nie, Q. Lyu, Q. Zhang, Processing Technologies and Properties of Cu-10Sn Formed by Selective Laser Melting Combined with Heat Treatment, 3D Printing and Additive Manufacturing 8(1) (2021) 13-22.
[211] R. Gu, X. Yao, D. Wang, H. Wang, M. Yan, K.S. Wong, Selective laser melting of Cu–10Sn–0.4 P: Processing, microstructure, properties, and brief comparison with additively manufactured Cu–10Sn, Advanced Engineering Materials 24(2) (2022) 2100716.
[212] Z. Li, Y. Cui, W. Yan, D. Zhang, Y. Fang, Y. Chen, Q. Yu, G. Wang, H. Ouyang, C. Fan, Enhanced strengthening and hardening via self-stabilized dislocation network in additively manufactured metals, Materials Today 50 (2021) 79-88.
[213] A.R. Kini, D. Maischner, A. Weisheit, D. Ponge, B. Gault, E.A. Jägle, D. Raabe, In-situ synthesis via laser metal deposition of a lean Cu–3.4 Cr–0.6 Nb (at%) conductive alloy hardened by Cr nano-scale precipitates and by Laves phase micro-particles, Acta Materialia 197 (2020) 330-340.
[214] J. Wang, X. Zhou, J. Li, M. Brochu, Y.F. Zhao, Microstructures and properties of SLM-manufactured Cu-15Ni-8Sn alloy, Additive Manufacturing 31 (2020) 100921.
[215] T. Blanton, S. Misture, N. Dontula, S. Zdzieszynski, In situ high-temperature X-ray diffraction characterization of silver sulfide, Ag2S, Powder Diffraction 26(2) (2011) 114-118.
[216] W. Jones, N.H. March, Theoretical solid state physics, Courier Corporation1985.
[217] C. Wei, H. Gu, Q. Li, Z. Sun, Y.-h. Chueh, Z. Liu, L. Li, Understanding of process and material behaviours in additive manufacturing of Invar36/Cu10Sn multiple material components via laser-based powder bed fusion, Additive Manufacturing 37 (2021) 101683.
[218] Y. Li, L. Li, B. Geng, Q. Wang, R. Zhou, X. Wu, H. Xiao, Microstructure characteristics and strengthening mechanism of semisolid CuSn10P1 alloys, Materials Characterization 172 (2021) 110898.
[219] A. Shyam, A. Plotkowski, S. Bahl, K. Sisco, L. Allard, Y. Yang, J.A. Haynes, R. Dehoff, An additively manufactured AlCuMnZr alloy microstructure and tensile mechanical properties, Materialia 12 (2020) 100758.
[220] J.R. Croteau, S. Griffiths, M.D. Rossell, C. Leinenbach, C. Kenel, V. Jansen, D.N. Seidman, D.C. Dunand, N.Q. Vo, Microstructure and mechanical properties of Al-Mg-Zr alloys processed by selective laser melting, Acta Materialia 153 (2018) 35-44.
[221] H. Zhang, H. Zhu, X. Nie, J. Yin, Z. Hu, X. Zeng, Effect of Zirconium addition on crack, microstructure and mechanical behavior of selective laser melted Al-Cu-Mg alloy, Scripta Materialia 134 (2017) 6-10.
[222] N. Ciftci, N. Ellendt, G. Coulthard, E. Soares Barreto, L. Mädler, V. Uhlenwinkel, Novel cooling rate correlations in molten metal gas atomization, Metallurgical and Materials Transactions B 50(2) (2019) 666-677.

[223] E. Li, H. Shen, L. Wang, G. Wang, Z. Zhou, Laser shape variation influence on melt pool dynamics and solidification microstructure in laser powder bed fusion, Additive Manufacturing Letters 6 (2023) 100141.
[224] P. He, R.F. Webster, V. Yakubov, H. Kong, Q. Yang, S. Huang, M. Ferry, J.J. Kruzic, X. Li, Fatigue and dynamic aging behavior of a high strength Al-5024 alloy fabricated by laser powder bed fusion additive manufacturing, Acta Materialia 220 (2021) 117312.
[225] D.A. Porter, K.E. Easterling, Phase transformations in metals and alloys (revised reprint), CRC press2009.
[226] M. Easton, D. StJohn, Grain refinement of aluminum alloys: Part I. the nucleant and solute paradigms—a review of the literature, Metallurgical and Materials Transactions A 30(6) (1999) 1613-1623.
[227] P. Liu, Z. Wang, Y. Xiao, M.F. Horstemeyer, X. Cui, L. Chen, Insight into the mechanisms of columnar to equiaxed grain transition during metallic additive manufacturing, Additive Manufacturing 26 (2019) 22-29.
[228] J. Li, T. Cheng, Y. Liu, Y. Yang, W. Li, Q. Wei, Simultaneously enhanced strength and ductility of Cu-15Ni-8Sn alloy with periodic heterogeneous microstructures fabricated by laser powder bed fusion, Additive Manufacturing 54 (2022) 102726.
[229] M. Mabuchi, K. Higashi, Strengthening mechanisms of Mg□ Si alloys, Acta Materialia 44(11) (1996) 4611-4618.
[230] H. Jung, J. Lee, G.H. Gu, H. Lee, S.-M. Seo, A. Zargaran, H.S. Kim, S.S. Sohn, Multiscale defects enable synergetic improvement in yield strength of CrCoNi-based medium-entropy alloy fabricated via laser-powder bed fusion, Additive Manufacturing 61 (2023) 103360.
[231] R. Aikin Jr, L. Christodoulou, The role of equiaxed particles on the yield stress of composites, Scripta metallurgica et materialia 25(ISSN: 0956-716X) (1991).
[232] Y. Liu, Z. Li, Y. Jiang, Y. Zhang, Z. Zhou, Q. Lei, The microstructure evolution and properties of a Cu–Cr–Ag alloy during thermal-mechanical treatment, Journal of Materials Research 32(7) (2017) 1324-1332.
[233] T. Gladman, Precipitation hardening in metals, Materials science and technology 15(1) (1999) 30-36.
[234] G. Le Roy, J. Embury, G. Edwards, M. Ashby, A model of ductile fracture based on the nucleation and growth of voids, Acta Metallurgica 29(8) (1981) 1509-1522.
[235] S. Qu, S. Gao, L. Wang, J. Ding, Y. Lu, Y. Wen, X. Qu, B. Zhang, X. Song, Full-composition-gradient in-situ alloying of Cu–Ni through laser powder bed fusion, Additive Manufacturing 85 (2024) 104166.
[236] C.-C. Chang, Y.-T. Hsiao, Y.-L. Chen, C.-Y. Tsai, Y.-J. Lee, P.-H. Ko, S.-Y. Chang, Lattice distortion or cocktail effect dominates the performance of Tantalum-based high-entropy nitride coatings, Applied Surface Science 577 (2022) 151894.
[237] A.P. Zhilyaev, I. Shakhova, A. Belyakov, R. Kaibyshev, T.G. Langdon, Wear resistance and electroconductivity in copper processed by severe plastic deformation, Wear 305(1-2) (2013) 89-99.
[238] A. Moharrami, A. Razaghian, M. Emamy, R. Taghiabadi, Effect of tool pin profile on the microstructure and tribological properties of friction stir processed Al-20 wt% Mg2Si composite, Journal of Tribology 141(12) (2019) 122202.
[239] A. Moharami, Improving the dry sliding-wear resistance of as-cast Cu-10Sn-1P alloy through accumulative back extrusion (ABE) process, Journal of Materials Research and Technology 9(5) (2020) 10091-10096.
[240] J. Krell, A. Röttger, U. Ziesing, W. Theisen, Influence of precipitation hardening on the high-temperature sliding wear resistance of an aluminium alloyed iron-nickel base alloy, Tribology International 148 (2020) 106342.

[241] G. Pürçek, T. Savaşkan, T. Küçükömeroğlu, S. Murphy, Dry sliding friction and wear properties of zinc-based alloys, Wear 252(11-12) (2002) 894-901.
[242] S. Scudino, C. Unterdörfer, K.G. Prashanth, H. Attar, N. Ellendt, V. Uhlenwinkel, J. Eckert, Additive manufacturing of Cu–10Sn bronze, Materials Letters 156 (2015) 202-204.
[243] P. Yang, D. He, X. Guo, S. Lu, S. Chen, F. Shang, D. Oleksandr, L. Chen, Effect of Printing Orientation on the Mechanical Properties of 3D-Printed Cu–10Sn Alloys by Laser Powder Bed Fusion Technology, Metals 14(6) (2024) 660.
[244] J. Kim, J. Won, W. Lee, Microstructure and Mechanical Properties of Laser Powder Bed Fusion 3D-Printed Cu-10Sn Alloy, Journal of Powder Materials 31(5) (2024) 422-430.
[245] EFFECT OF TIN CONTENT AND ECAP PASSES ON THE MECHANICAL PROPERTIES OF Cu/Sn ALLOYS AS BEARING MATERIALS, Port-Said Engineering Research Journal 18(1) (2014) 79-89.
[246] J.A. Muñiz-Lerma, A. Nommeots-Nomm, K.E. Waters, M. Brochu, A comprehensive approach to powder feedstock characterization for powder bed fusion additive manufacturing: a case study on AlSi7Mg, Materials 11(12) (2018) 2386.
[247] J. Yang, J. Han, H. Yu, J. Yin, M. Gao, Z. Wang, X. Zeng, Role of molten pool mode on formability, microstructure and mechanical properties of selective laser melted Ti-6Al-4V alloy, Materials & Design 110 (2016) 558-570.
[248] D. Field, P. Trivedi, S. Wright, M. Kumar, Analysis of local orientation gradients in deformed single crystals, Ultramicroscopy 103(1) (2005) 33-39.
[249] K. Mingard, B. Roebuck, E. Bennett, M. Gee, H. Nordenstrom, G. Sweetman, P. Chan, Comparison of EBSD and conventional methods of grain size measurement of hardmetals, International Journal of Refractory Metals and Hard Materials 27(2) (2009) 213-223.
[250] A. Keshavarzkermani, E. Marzbanrad, R. Esmaeilizadeh, Y. Mahmoodkhani, U. Ali, P.D. Enrique, N.Y. Zhou, A. Bonakdar, E. Toyserkani, An investigation into the effect of process parameters on melt pool geometry, cell spacing, and grain refinement during laser powder bed fusion, Optics & Laser Technology 116 (2019) 83-91.
[251] P.A. Hooper, Melt pool temperature and cooling rates in laser powder bed fusion, Additive Manufacturing 22 (2018) 548-559.
[252] T. Qi, H. Zhu, H. Zhang, J. Yin, L. Ke, X. Zeng, Selective laser melting of Al7050 powder: Melting mode transition and comparison of the characteristics between the keyhole and conduction mode, Materials & Design 135 (2017) 257-266.
[253] S.D. Jadhav, D. Fu, M. Deprez, K. Ramharter, D. Willems, B. Van Hooreweder, K. Vanmeensel, Highly conductive and strong CuSn0.3 alloy processed via laser powder bed fusion starting from a tin-coated copper powder, Additive Manufacturing 36 (2020) 101607.
[254] Y. Zhou, J. Wang, Y. Yang, M. Yang, H. Zheng, D. Xie, D. Wang, L. Shen, Laser additive manufacturing of zinc targeting for biomedical application, International Journal of Bioprinting 8(1) (2022).
[255] T. Carney, An X-ray photoelectron spectroscopy study of rapidly solidified aluminium alloy powders, University of Surrey (United Kingdom)1990.
[256] C.D. Boley, S.A. Khairallah, A.M. Rubenchik, Calculation of laser absorption by metal powders in additive manufacturing, Appl. Opt. 54(9) (2015) 2477-2482.
[257] B. Brandau, A. Da Silva, C. Wilsnack, F. Brueckner, A.F.H. Kaplan, Absorbance study of powder conditions for laser additive manufacturing, Materials & Design 216 (2022) 110591.

[258] H.-C. Tran, Y.-L. Lo, M.-H. Huang, Analysis of scattering and absorption characteristics of metal powder layer for selective laser sintering, IEEE/ASME Transactions On Mechatronics 22(4) (2017) 1807-1817.
[259] J. Zhang, D. Gu, Y. Yang, H. Zhang, H. Chen, D. Dai, K. Lin, Influence of particle size on laser absorption and scanning track formation mechanisms of pure tungsten powder during selective laser melting, Engineering 5(4) (2019) 736-745.
[260] M. Asta, C. Beckermann, A. Karma, W. Kurz, R. Napolitano, M. Plapp, G. Purdy, M. Rappaz, R. Trivedi, Solidification microstructures and solid-state parallels: Recent developments, future directions, Acta Materialia 57(4) (2009) 941-971.
[261] N. Chakraborty, The effects of turbulence on molten pool transport during melting and solidification processes in continuous conduction mode laser welding of copper–nickel dissimilar couple, Applied Thermal Engineering 29(17-18) (2009) 3618-3631.
[262] M. Habibnejad-korayem, J. Zhang, Y. Zou, Effect of particle size distribution on the flowability of plasma atomized Ti-6Al-4V powders, Powder Technology 392 (2021) 536-543.
[263] M.C. Flemings, Solidification processing, Metallurgical and Materials Transactions B 5 (1974) 2121-2134.
[264] K. Masubuchi, Analysis of welded structures: residual stresses, distortion, and their consequences, Elsevier2013.
[265] D. Kuhlmann-Wilsdorf, Theory of plastic deformation:-properties of low energy dislocation structures, Materials Science and Engineering: A 113 (1989) 1-41.
[266] H. Wang, Z.G. Zhu, H. Chen, A.G. Wang, J.Q. Liu, H.W. Liu, R.K. Zheng, S.M.L. Nai, S. Primig, S.S. Babu, S.P. Ringer, X.Z. Liao, Effect of cyclic rapid thermal loadings on the microstructural evolution of a CrMnFeCoNi high-entropy alloy manufactured by selective laser melting, Acta Materialia 196 (2020) 609-625.
[267] L. Liu, Q. Ding, Y. Zhong, J. Zou, J. Wu, Y.-L. Chiu, J. Li, Z. Zhang, Q. Yu, Z. Shen, Dislocation network in additive manufactured steel breaks strength–ductility trade-off, Materials Today 21(4) (2018) 354-361.
[268] J. Wu, X. Wang, W. Wang, M. Attallah, M. Loretto, Microstructure and strength of selectively laser melted AlSi10Mg, Acta Materialia 117 (2016) 311-320.
[269] Q. Wang, H. Shao, X. Zhang, K. Wang, S. Liu, C. Yang, W. Wang, Study of thermal behavior and microstructure formation mechanism of CuCrZr alloy melted by laser powder bed fusion, Materials Characterization 198 (2023) 112721.
[270] K. Prashanth, J. Eckert, Formation of metastable cellular microstructures in selective laser melted alloys, Journal of Alloys and Compounds 707 (2017) 27-34.
[271] C.L. Mendis, K. Oh-ishi, Y. Kawamura, T. Honma, S. Kamado, K. Hono, Precipitation-hardenable Mg–2.4Zn–0.1Ag–0.1Ca–0.16Zr (at.%) wrought magnesium alloy, Acta Materialia 57(3) (2009) 749-760.
[272] D. Ramirez, L. Murr, E. Martinez, D. Hernandez, J. Martinez, B.I. Machado, F. Medina, P. Frigola, R. Wicker, Novel precipitate–microstructural architecture developed in the fabrication of solid copper components by additive manufacturing using electron beam melting, Acta Materialia 59(10) (2011) 4088-4099.
[273] H. Wen, T.D. Topping, D. Isheim, D.N. Seidman, E.J. Lavernia, Strengthening mechanisms in a high-strength bulk nanostructured Cu–Zn–Al alloy processed via cryomilling and spark plasma sintering, Acta Materialia 61(8) (2013) 2769-2782.
[274] J. Gao, S. Jiang, H. Zhang, Y. Huang, D. Guan, Y. Xu, S. Guan, L.A. Bendersky, A.V. Davydov, Y. Wu, Facile route to bulk ultrafine-grain steels for high strength and ductility, Nature 590(7845) (2021) 262-267.

[275] S.D. Jadhav, P.P. Dhekne, S. Dadbakhsh, J.-P. Kruth, J. Van Humbeeck, K. Vanmeensel, Surface modified copper alloy powder for reliable laser-based additive manufacturing, Additive Manufacturing 35 (2020) 101418.
[276] J. Huang, X. Yan, C. Chang, Y. Xie, W. Ma, R. Huang, R. Zhao, S. Li, M. Liu, H. Liao, Pure copper components fabricated by cold spray (CS) and selective laser melting (SLM) technology, Surface and Coatings Technology 395 (2020) 125936.
[277] P. Guan, X. Chen, P. Liu, F. Sun, C. Zhu, H. Zhou, S. Fu, Z. Wu, Y. Zhu, Effect of selective laser melting process parameters and aging heat treatment on properties of CuCrZr alloy, Materials Research Express 6(11) (2019) 1165c1.
[278] J. Wang, X. Zhou, J. Li, Evolution of microstructures and properties of SLM-manufactured Cu–15Ni–8Sn alloy during heat treatment, Additive Manufacturing 37 (2021) 101599.
[279] A.P. Ventura, C.J. Marvel, G. Pawlikowski, M. Bayes, M. Watanabe, R.P. Vinci, W.Z. Misiolek, The effect of aging on the microstructure of selective laser melted Cu-Ni-Si, Metallurgical and Materials Transactions A 48(12) (2017) 6070-6082.
[280] S.D. Jadhav, S. Dadbakhsh, J. Vleugels, J. Hofkens, P. Van Puyvelde, S. Yang, J.-P. Kruth, J. Van Humbeeck, K. Vanmeensel, Influence of carbon nanoparticle addition (and impurities) on selective laser melting of pure copper, Materials 12(15) (2019) 2469.
[281] X. Zhang, Y. Xu, M. Wang, E. Liu, N. Zhao, C. Shi, D. Lin, F. Zhu, C. He, A powder-metallurgy-based strategy toward three-dimensional graphene-like network for reinforcing copper matrix composites, Nature communications 11(1) (2020) 2775.
[282] A.P. Ventura, C.A. Wade, G. Pawlikowski, M. Bayes, M. Watanabe, W.Z. Misiolek, Mechanical properties and microstructural characterization of Cu-4.3 Pct Sn fabricated by selective laser melting, Metallurgical and Materials Transactions A 48(1) (2017) 178-187.
[283] X. Tang, X. Chen, F. Sun, L. Li, P. Liu, H. Zhou, S. Fu, A. Li, A study on the mechanical and electrical properties of high-strength CuCrZr alloy fabricated using laser powder bed fusion, Journal of Alloys and Compounds 924 (2022) 166627.
[284] Z. Zhao, Z. Xiao, Z. Li, M. Ma, J. Dai, Effect of magnesium on microstructure and properties of Cu-Cr alloy, Journal of Alloys and Compounds 752 (2018) 191-197.
[285] J.Y. He, H. Wang, H.L. Huang, X.D. Xu, M.W. Chen, Y. Wu, X.J. Liu, T.G. Nieh, K. An, Z.P. Lu, A precipitation-hardened high-entropy alloy with outstanding tensile properties, Acta Materialia 102 (2016) 187-196.
[286] C. Booth-Morrison, D.C. Dunand, D.N. Seidman, Coarsening resistance at 400°C of precipitation-strengthened Al–Zr–Sc–Er alloys, Acta Materialia 59(18) (2011) 7029-7042.
[287] A.J. Ardell, Precipitation hardening, Metallurgical Transactions A 16(12) (1985) 2131-2165.
[288] N. Hong, Y. Liao, H. Chen, C. Zhou, W. Xie, H. Wang, B. Yang, Precipitation behavior and strengthening mechanism in a Cu-3.5Ti-0.1 Tm alloy, Materials Science and Engineering: A 914 (2024) 147136.
[289] W. Soboyejo, Mechanical properties of engineered materials, CRC press2002.
[290] Q. Liu, C. Ren, Z. Song, X. Dan, J. Ju, T. Yang, S. Ni, J. Lu, L. Liu, J. Pan, High-strength and high-conductivity additively manufactured Cu-O alloy enabled by cellular microstructure, Additive Manufacturing 88 (2024) 104244.
[291] S. Riedel, J. Röber, T. Geßner, Electrical properties of copper films produced by MOCVD, Microelectronic Engineering 33(1-4) (1997) 165-172.
[292] S. Semboshi, Y. Kaneno, T. Takasugi, S.Z. Han, N. Masahashi, Effect of composition on the strength and electrical conductivity of Cu-Ti binary alloy wires fabricated by aging and intense drawing, Metallurgical and Materials Transactions A 50(3) (2019) 1389-1396.

[293] S. Semboshi, Y. Kaneno, T. Takasugi, N. Masahashi, High strength and high electrical conductivity Cu-Ti alloy wires fabricated by aging and severe drawing, Metallurgical and Materials Transactions A 49(10) (2018) 4956-4965.
[294] X. Guoliang, W. Qiangsong, M. Xujun, X. Baiqing, P. Lijun, The precipitation behavior and strengthening of a Cu–2.0 wt% Be alloy, Materials Science and Engineering: A 558 (2012) 326-330.
[295] T. Konno, K. Hiraga, M. Kawasaki, Guinier-Preston (GP) zone revisited: atomic level observation by HAADF-TEM technique, Scripta materialia 44(8-9) (2001) 2303-2307.
[296] L. Peng, H. Xie, G. Huang, G. Xu, X. Yin, X. Feng, X. Mi, Z. Yang, The phase transformation and strengthening of a Cu-0.71 wt% Cr alloy, Journal of Alloys and Compounds 708 (2017) 1096-1102.
[297] G. Wang, H. Liu, K. Song, Y. Zhou, C. Cheng, H. Guo, Y. Guo, J. Tian, Aging process and strengthening mechanism of Cu–Cr–Ni alloy with superior stress relaxation resistance, Journal of Materials Research and Technology 19 (2022) 3579-3591.
[298] J.H. Jang, C.-H. Lee, Y.-U. Heo, D.-W. Suh, Stability of (Ti, M) C (M= Nb, V, Mo and W) carbide in steels using first-principles calculations, Acta Materialia 60(1) (2012) 208-217.
[299] S.C. Krishna, N.K. Gangwar, A.K. Jha, B. Pant, On the prediction of strength from hardness for copper alloys, Journal of Materials 2013(1) (2013) 352578.
[300] Q. Fang, L. Li, J. Li, H. Wu, Z. Huang, B. Liu, Y. Liu, P.K. Liaw, A statistical theory of probability-dependent precipitation strengthening in metals and alloys, Journal of the Mechanics and Physics of Solids 122 (2019) 177-189.
[301] Q. Fang, Z. Huang, L. Li, Z. Huang, B. Liu, Y. Liu, J. Li, P.K. Liaw, Modeling the competition between solid solution and precipitate strengthening of alloys in a 3D space, International Journal of Plasticity 149 (2022) 103152.
[302] C.V. Singh, D.H. Warner, Mechanisms of Guinier–Preston zone hardening in the athermal limit, Acta Materialia 58(17) (2010) 5797-5805.
[303] Y. Wang, Y. Song, Y. Fan, H. Zhao, Z. Hong, K. Song, X. Dong, C. Guo, Double-peak precipitation hardening in the Cu-Fe-Ti alloy, Scripta Materialia 232 (2023) 115478.
[304] H. Fan, A.H.W. Ngan, K. Gan, J.A. El-Awady, Origin of double-peak precipitation hardening in metallic alloys, International Journal of Plasticity 111 (2018) 152-167.
[305] D.N. Seidman, E.A. Marquis, D.C. Dunand, Precipitation strengthening at ambient and elevated temperatures of heat-treatable Al (Sc) alloys, Acta Materialia 50(16) (2002) 4021-4035.
[306] X.-Y. Cui, S.P. Ringer, On the nexus between atom probe microscopy and density functional theory simulations, Materials characterization 146 (2018) 347-358.
[307] S. Zhu, X. Cui, Y. Aruga, H. Liu, S.P. Ringer, Precipitation strengthening and thermal stability in a conventionally non-heat treatable AA3xxx aluminium alloy, Acta Materialia 272 (2024) 119909.
[308] B. Fulcher, X. Cui, B. Delley, C. Stampfl, Hardness analysis of cubic metal mononitrides from first principles, Physical Review B—Condensed Matter and Materials Physics 85(18) (2012) 184106.
[309] FLOW-3D Users Site, Flow Science, Inc., 2023.
[310] T. Mao, B. Xiufang, X. Xue, Z. Yanning, Correlation between viscosity of molten Cu–Sn alloys and phase diagram, Physica B: Condensed Matter 387(1-2) (2007) 1-5.
[311] B.J. Monaghan, J.G.J. Neale, L. Chapman, Some Thermal Properties of a Copper–Tin Alloy, International Journal of Thermophysics 20(4) (1999) 1051-1060.
[312] J. Lee, W. Shimoda, T. Tanaka, Surface Tension and its Temperature Coefficient of Liquid Sn-X (X=Ag, Cu) Alloys, Materials Transactions 45(9) (2004) 2864-2870.

[313] D. Li, P. Franke, S. Fürtauer, D. Cupid, H. Flandorfer, The Cu–Sn phase diagram part II: New thermodynamic assessment, Intermetallics 32 (2013) 148-158.
[314] UNS C52400 Phosphor Bronze, MakeItFrom.com, 2020.
[315] FLOW-3D, FLOW-3D Users Site, Flow Science, Inc., 2023.
[316] Q. Lei, Z. Xiao, W. Hu, B. Derby, Z. Li, Phase transformation behaviors and properties of a high strength Cu-Ni-Si alloy, Materials Science and Engineering: A 697 (2017) 37-47.
[317] J. Li, T. Cheng, Y. Liu, Y. Yang, W. Li, Q. Wei, Simultaneously enhanced strength and ductility of Cu-15Ni-8Sn alloy with periodic heterogeneous microstructures fabricated by laser powder bed fusion, Addit. Manuf. 54 (2022) 102726.
[318] G. Gottstein, Physical foundations of materials science, Springer2004.
[319] Y. Liu, Z. Li, Y. Jiang, Y. Zhang, Z. Zhou, Q. Lei, The microstructure evolution and properties of a Cu–Cr–Ag alloy during thermal-mechanical treatment, J. Mater. Res. 32(7) (2017) 1324-1332.
[320] T.H. Courtney, Mechanical behavior of materials, Waveland Press2005.
[321] M. Aksoy, V. Kuzucu, H. Turhan, A note on the effect of phosphorus on the microstructure and mechanical properties of leaded-tin bronze, Journal of Materials Processing Technology 124(1-2) (2002) 113-119.
[322] J.-S. Zhang, High temperature deformation and fracture of materials, Elsevier2010.
[323] L. Liu, L. Chen, Y. Jiang, C. He, G. Xu, Y. Wen, Temperature effects on the elastic constants, stacking fault energy and twinnability of Ni3Si and Ni3Ge: a first-principles study, Crystals 8(9) (2018) 364.

Appendix A

FLOW3D-AM simulation

To simulate the sequential stages of the real LB-PBF process, three separate models – Powder Settling, Powder Spreading, and Melt and Solidification – were employed. The output of one model was fed into another as input. Detailed model parameters are described as follows.

Powder Settling Model

The powder settling model generates a uniformly distributed cloud of particles above a baseplate and then simulates the settling of those particles into a static layer over the baseplate under the force of gravity. Figure A.1 shows the baseplate design with a rectangular prism measuring 2500 × 800 × 50 μm. The depression for the powder bed was left open on two sides, as a wall boundary condition could be set in the missing walls' place. One of the elevated platforms outside the depression was made larger than the other. This is because, in the next modelling step, we planned to use a blade to sweep particles sitting outside of the depression into and over the depression. We designed a large platform before the approach of the blade towards the depression which would hold a large number of particles to model the clumping effect of particles on the blade. The particle sizes and the particle size distribution (Table A.1) are also set in this model. The PSD was based on relative size frequencies measured from the powder size distribution of Cu-10Sn powder measured by the laser diffraction particle size analyser. The output of the settling model produced a layer of powder of relatively constant thickness on top of the baseplate, as shown in Figure A.2.

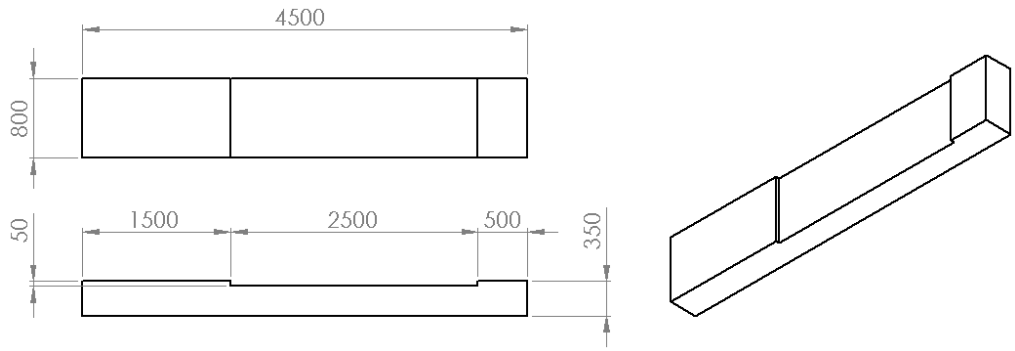

Figure A.1: Baseplate design in FLOW3D-AM simulation. All dimensions shown are in μm.

Table A.1: Powder size distribution of Cu-10Sn powder.

Particle Size (μm)	Distribution (%)
12	13.8
16	20.7
20	13.8
24	7.4
28	7.9
32	10.9
36	17.0
40	8.5

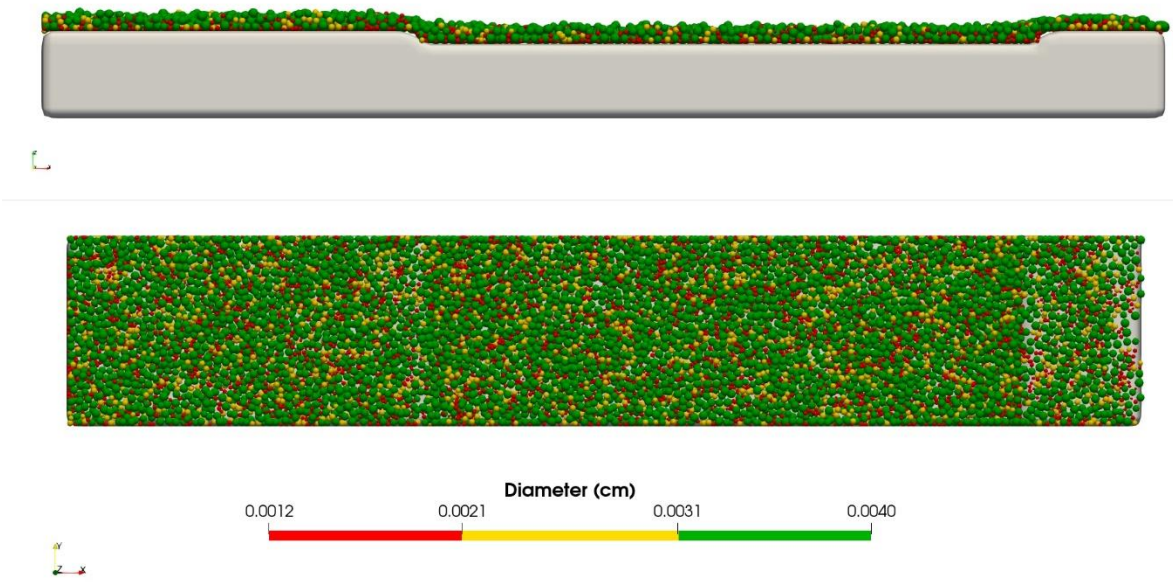

Figure A.2: Cu-10Sn particles settled in a thin layer over the baseplate.

Powder Spreading Model

The powder spreading model simulates the action of a blade over the build platform to create a smooth powder bed of relatively constant thickness. Table A.2 and A.3 summarise the parameters used in this model. The friction option in FLOW-3D DEM is set to "vertical force dependent" due to the long contact time of the particle. As the powder is deposited in a uniform vertical downward direction onto the build platform from rest, elastic forces caused by the contacts between powder are negligible. Hence, the more elaborate "vertical force dependent elastic force" option is not selected to reduce computational time [309].

Table A.2: Summary of Linear Spring Dashpot Parameters.

Parameter	Value
Spring Constant	20
Coefficient of restitution (normal direction)	0.3
Coefficient of restitution (tangential direction)	0.3

Table A.3: Summary of Friction Parameters.

Parameter	Value
Particle static friction coefficient	0.2
Particle dynamic friction coefficient	0.15
Wall static friction coefficient	0.2
Wall dynamic friction coefficient	0.15

Melt and Solidification Model

The metal and solidification model simulates the laser beam passing over the powder bed which melts due to the intense heat and then solidifies again. The material properties and laser parameters that are relevant to melting and solidification are summarised as follows.

- Temperature-dependent Viscosity

The viscosity of Cu-10Sn melt increases as the temperature decreases. This phenomenon can be accurately described by the Arrhenius equation [310]. The temperature-dependent viscosity was calculated over a range of temperatures from 920 °C to 1700 °C (Figure A.3).

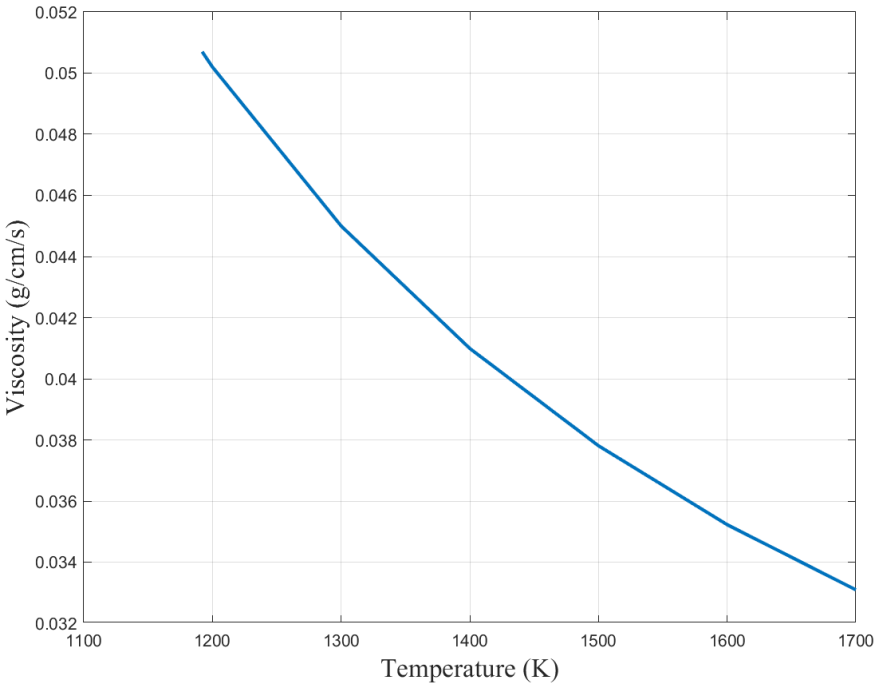

Figure A.3: A MATLAB generated plot that illustrates the temperature-dependent viscosity of liquid Cu-10Sn.

- Temperature-dependent Thermal Conductivity

Temperature-dependent thermal conductivity values for Cu-10Sn [311] were extracted using PlotDigitizer Pro, and they were reproduced as in Figure A.4.

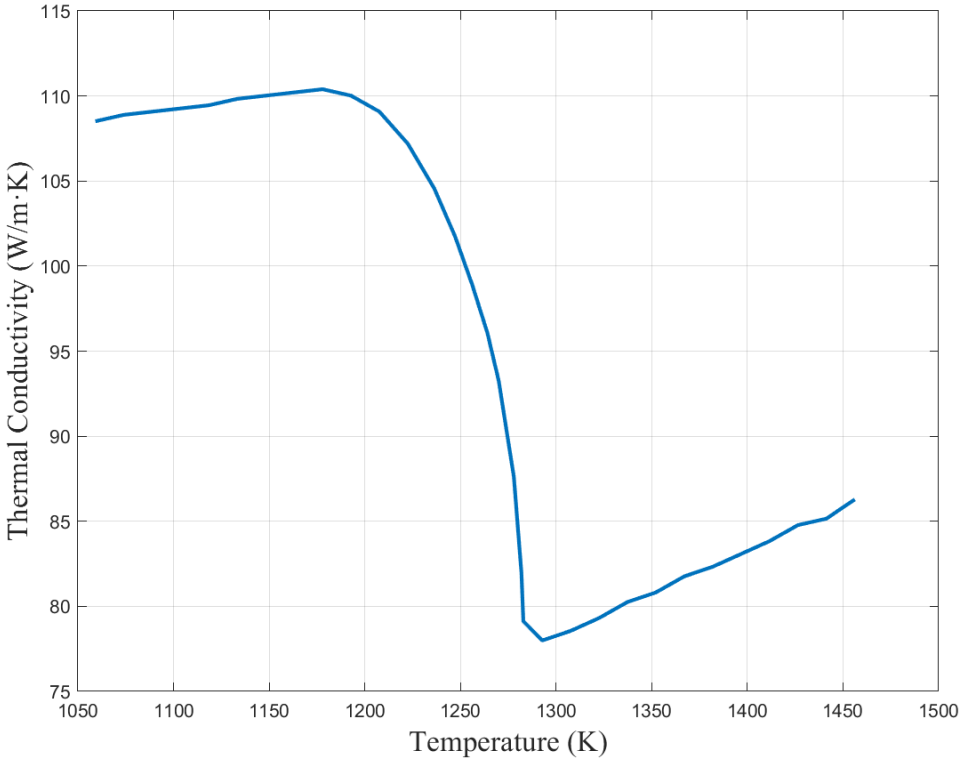

Figure A.4: A MATLAB generated plot that illustrates the temperature-dependent thermal conductivity of liquid Cu-10Sn.

- Temperature-dependent Specific Heat Capacity

The specific heat capacity (C_p) of the liquid phase of Cu-10Sn was observed to exhibit temperature independence, consistently retaining a value of 0.505 J/g·K [311].

- Surface Tension Coefficient

The surface tension force plays a pivotal role in LB-PBF by influencing the behaviour of molten materials. As the temperature increases, the surface tension force decreases. Significant Marangoni flows within the melt pool are driven by high thermal gradients. The relationship governing the surface tension coefficient for Cu-10Sn in relation to its temperature is specifically described by [312]:

$$\sigma(T) = 1076 - 0.064T$$

- Solidification Parameters

Summarised in Table A. 4.

Table A.4: Summary of Solidification Parameters.

Parameter	Value	Unit	Ref.
Solidus temperature	1071	K	[115],[313]
Liquids temperature	1191	K	[115],[313]
Solidification drag coefficient	1.06721e+7	1/s	
Fraction of solid at coherency point	0.33		
Critical fraction of solid	0.67		
Latent heat of fusion	1.9e+9	erg/g	[314]

- Solidification Drag Coefficients

The solidification drag coefficient (TSDRG) is important in simulating the LB-PBF process. It represents the resistance encountered by the solidification front as it progresses through the mushy phase during the cooling and solidification of the material. The TSDRG is mathematically described by [315]:

$$TSDRG = \frac{180\mu}{{\lambda_1}^2 \rho}$$

Where λ_1 is the characteristic dimension for flow. We used the dendrite arm spacing here.

In the computation of the TSDRG, two assumptions are made. Firstly, there is an assumption of a dendrite arm spacing of 5 μm. Secondly, the viscosity and density values are considered as averages, calculated based on the solidus and liquidus temperatures.

$$TSDRG = \frac{180 \times \left(\frac{7.9734 + 7.9109}{2}\right)}{(0.0005)^2 \times \left(\frac{0.0573 + 0.0507}{2}\right)} \approx 4.895399860239 \times 10^7$$

- Solidified Fluid Parameters

Summarised in Table A.5.

Table A.5: Summary of Solidified Fluid Parameters.

Parameter	Value	Unit	Ref.
Density	8.77999	g/cm^3	
Specific heat capacity	3.8e+6	erg/g/K	[314]
Thermal conductivity	4.1e+6	erg/cm/s/K	[314]

- Laser Parameters

The laser printing parameters (Table A.6) were set based on the best parameters that led to the highest material density. When the scanning velocity is 860 mm/s, it takes 11.6 ms for the laser to complete a 10 mm long track (length for the actual as-built sample in this study). We set the start of the second and third laser scans to be 11.6 ms to replicate actual conditions, and the laser track paths are shown in Figure A.5. As each 2000 μm long laser track is timed to be 11.6 ms apart and there are three tracks, the simulation time was set to 30 ms. This would allow for $30 - 2 \times 11.6 - 2.33 = 4.47$ ms of cooling time after each laser track is finished. The track length could not be feasibly lengthened in our model as this comes with significant computational cost.

Table A.6: Laser parameters set in melt and solidification model.

Parameter	Value	Unit
Laser Power	195	W
Scanning Velocity	860	mm/s
Spot Diameter	50	μm
Focal Distance	9.65	mm
Hatching Distance	75	μm
Track Length	2000	μm

Scanning Time/Track	2.33	ms
Number of Tracks	3	-

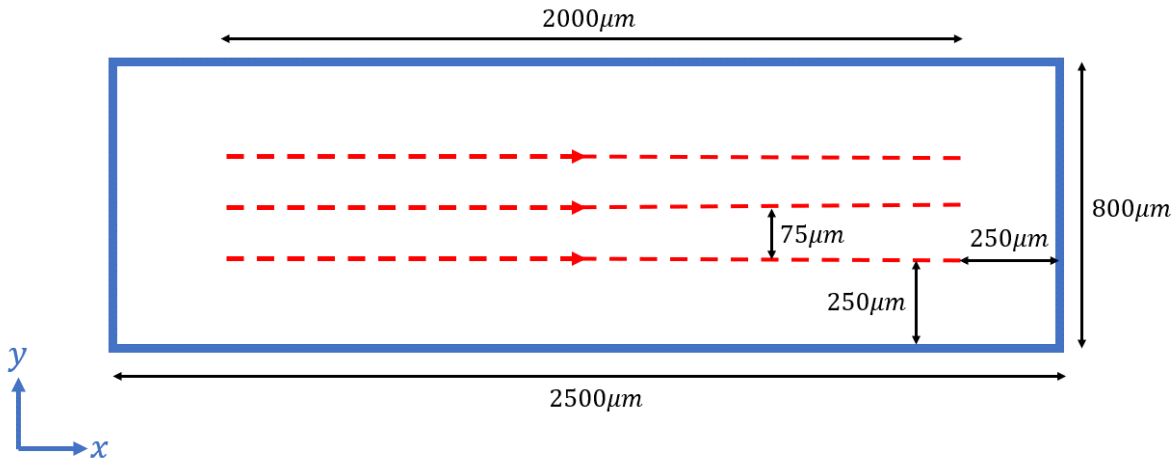

Figure A.5: Top-down view of the powder bed with red dotted-line arrows indicating paths of the laser tracks.

- Melting and Solidification Model Parameters

Nested sub meshing was used in our melt and solidification model to improve the powder bed geometry resolution without incurring significant computational costs. Table A.7 shows the meshing setup. A smaller "fine" mesh was fully contained within the "coarse" mesh that defined our computational domain. The heat loss was modelled from the fluid to its surroundings by activating heat transfer to the walls of the mesh block and heat transfer to a void region above the fluid region. The heat transfer coefficients used for each type of heat transfer are stated in Table A.8.

Table A.7: Mesh setup for melt and solidification. All units are in μm.

Parameter	Cell size	X min	X max	Y min	Y max	Z min	Z max
Fine Mesh	8	1650	3850	150	500	260	360
Coarse Mesh	16	1500	4000	0	650	100	400

Table A.8: Key Model Parameters for melt and solidification.

Parameter	Value	Unit
Simulation Time	30	ms
Wall Heat Transfer Coefficient	4.1e+6	erg/s/cm^2/K
Heat Transfer to Void	1e+5	erg/s/cm^2/K

Model Output

The solidified melt pool geometry is shown in Figure A.6. The depth of the melt pool was approximately 50 μm, and the width across all three tracks was 263 μm. As the hatching distance was set to 75 μm, an individual track's width can be estimated as $263 - 2 \times 75 = 113$ μm. The profile of each individual track's melt pool is roughly tubular, with a high level of inter-track melting. Inter-layer melting is significant as the melt region deeply extends into the bulk beneath the powder bed, as indicated by the horizontal slice in Figure S11 which shows a significant melted region without interior gaps. This suggests that the once-solidified region undergoes cyclical melting and heating, as the laser passes nearby, which supports the phase transformation pathway to the δ phase during cyclic thermal loading.

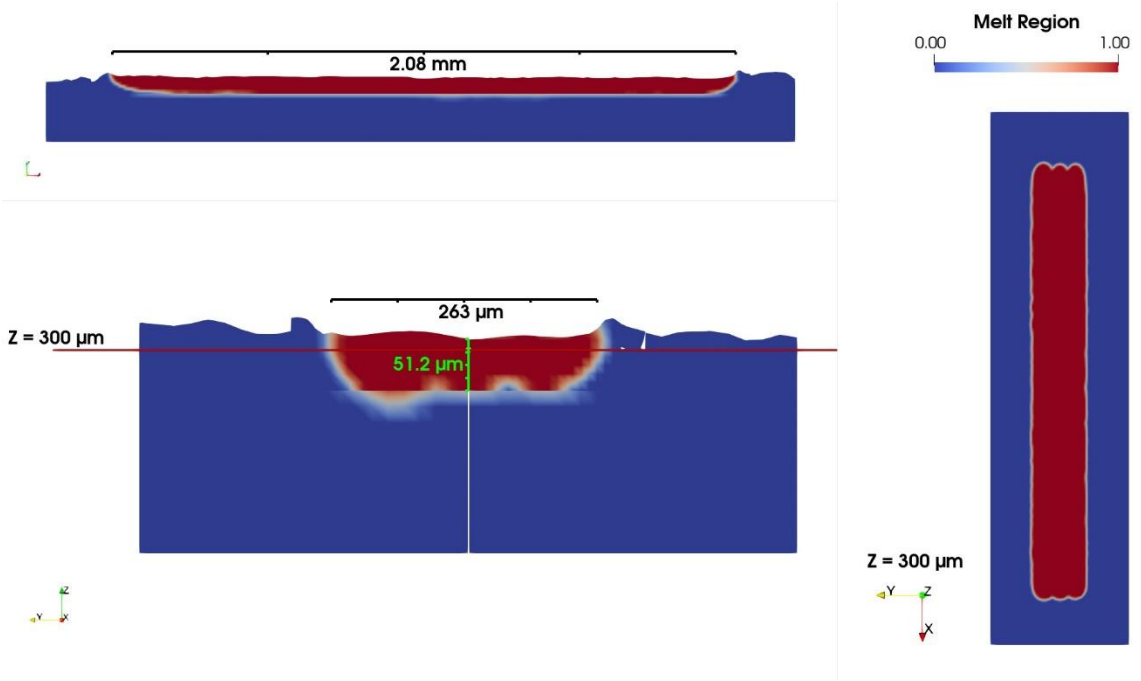

Figure A.6: The length, depth and width of the melted region. A flat slice is shown on the right at a height of 300 µm, the level where the powder meets the bulk material. This level is also indicated by a red line in the slice on the lower left.

Figure A.7 shows the isosurfaces representing solidus, liquidus, and saturation temperatures during a laser scan. The result indicates that the material solidifies rapidly after being scanned, leaving little room for fluid flow. A thin layer of solidus temperature isosurface is observed at the bottom of the melt pool. Figure A.8 depicts the thermal gradient in a plane normal to the scan direction. The results indicate that the melt pool boundaries experience the largest thermal gradient, resulting a higher G:R ratio, as compared to that in the case of the centre. This observation is consistent with the presence of finer grains at the melt pool boundary, where the higher G/R is considered to be the contributing factor.

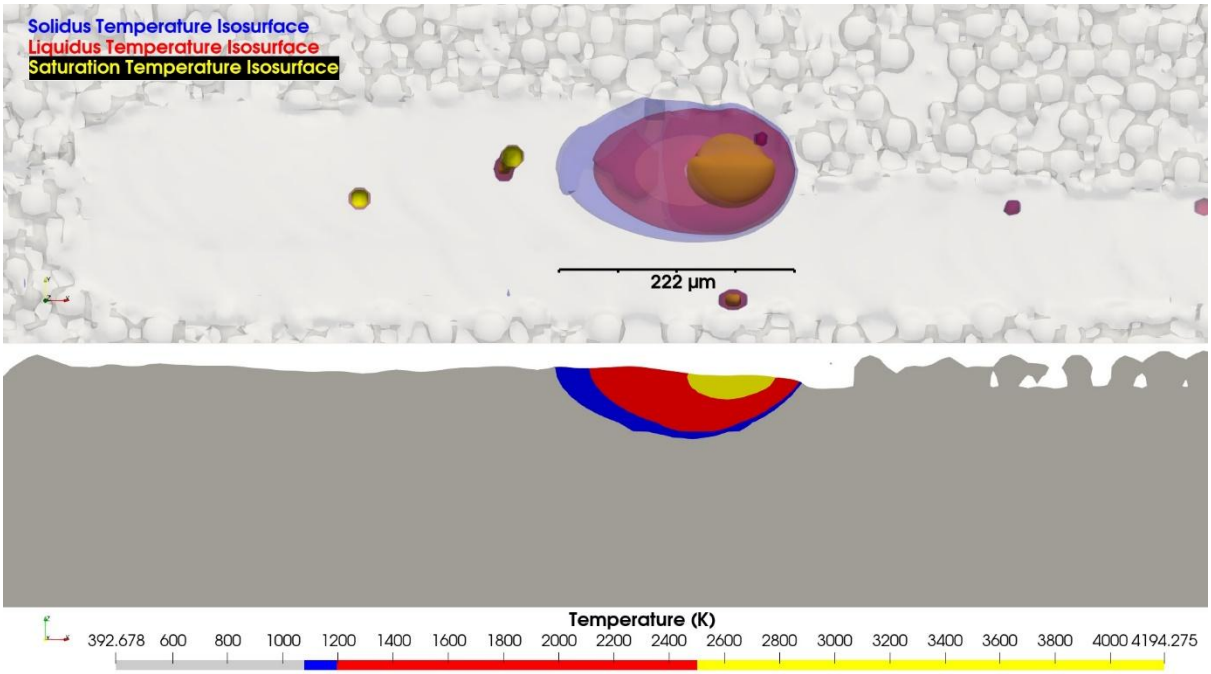

Figure A.7: The liquid/mushy region during a laser scan, sectioning isosurfaces between saturation temperature (yellow), liquidus temperature (red), and solidus temperature (blue).

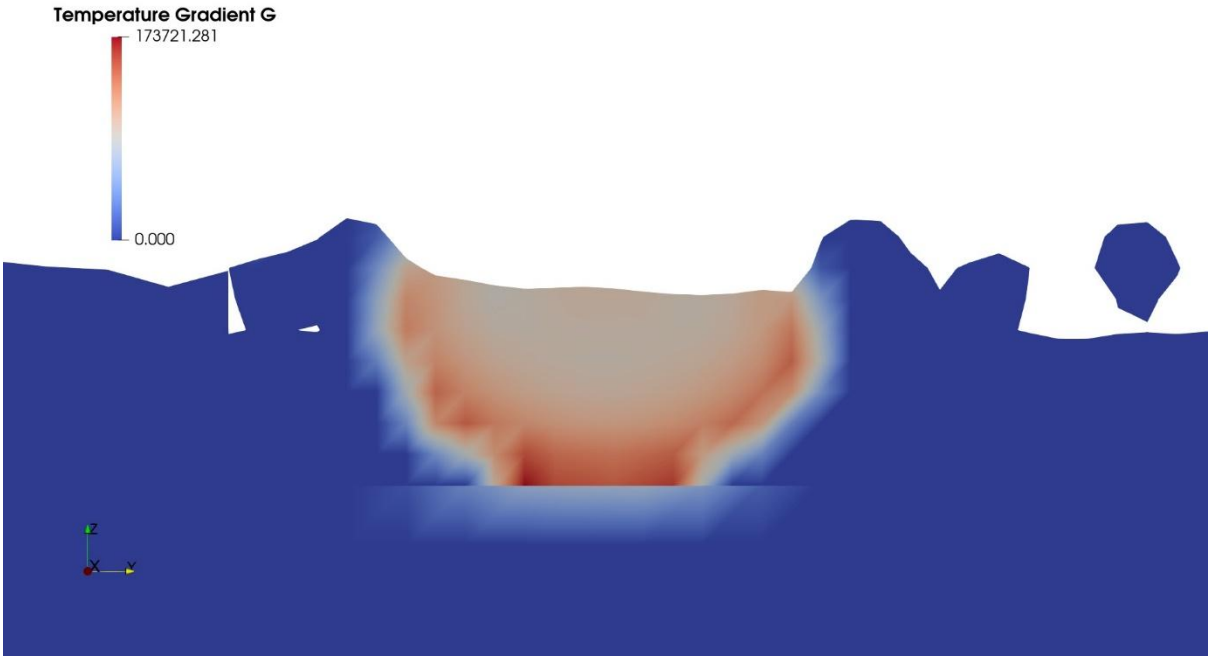

Figure A.8: The thermal gradient at a point on the first track. Within the fluid the gradient is increasing towards the centre of the track.

Appendix B

Strengthening mechanisms

The strengthening of the LB-PBF Cu-10Sn can be attributed to the intrinsic yield strength of Cu matrix (σ_0), solid solution strengthening (σ_{SSS}), grain boundary strengthening (σ_{GBS}), dislocation strengthening (σ_{DS}), and precipitation strengthening (σ_{PS}). Therefore, the YS (σ_Y) can be expressed by:

$$\sigma_Y = \sigma_0 + \sigma_{SSS} + \sigma_{GBS} + \sigma_{DS} + \sigma_{PS}$$

where σ_0 is the intrinsic yield strength of Cu matrix estimated to be 52 MPa [316].

The σ_{SSS} is mainly due to the modulus mismatch and lattice mismatch between the solute and solvent atoms. In this study, the contribution from σ_{SSS} is mainly derived from the abundant solid solution Sn atoms in the α(Cu) matrix. Previous study [106] estimated σ_{SSS} to be 10.2 MPa, which is small towards the overall strengthening of the alloy, as observed in the case of Cu-15Ni-8Sn alloy, wherein Sn exhibits significant solid solubility in α matrix [317].

Grain refinement is an effective method to improve strength and ductility because dislocation slip in polycrystalline alloys needs to overcome the grain boundary resistance. The relationship between the contribution from σ_{GBS} and the grain size can be calculated by the Hall-Petch formula below [318]:

$$\sigma_{GBS} = \frac{k}{\sqrt{d}}$$

where k is the strengthening coefficient related to Cu alloys (0.18 MPa$\sqrt{m}$) [319], and d represents the average grain size (4.9 μm) for the as-built sample. Therefore, the increase in the YS due to Hall-Petch strengthening is estimated to be 81.3 MPa.

A high density of dislocations interacts and entangles with each other, which impedes their own motion. The σ_{DS} contribution can be estimated using Baily-Hirsh relationship [273, 320]:

$$\sigma_{DS} = M\alpha Gb\sqrt{\rho}$$

where M is the Taylor factor of Cu (3.1) [319], α is the constant for FCC alloy (0.2) [273], G is the shear modulus (48.3 GPa) [233], b is the Burgers vector of Cu (2.56×10^{-10} m) [317], and ρ is the dislocation density (5.26×10^{14} /m^2) given by EBSD results. Therefore, the strengthening contribution from the dislocation interaction was calculated to be 175.8 MPa.

Exceptionally, the Cu_3P embedded in δ holds potential influence for strengthening effects as this phase is a hard and brittle intermetallic compound [321] and can also serve as dispersoids. However, the contribution from this phase is considered negligible because both the fraction and size of Cu_3P are much smaller than those of δ.

Appendix C

Strengthening mechanisms

The strengthening of the LB-PBF Cu-10Sn can be attributed to the intrinsic yield strength of Cu matrix (σ_0), solid solution strengthening (σ_{SSS}), grain boundary strengthening (σ_{GBS}), dislocation strengthening (σ_{DS}), and precipitation strengthening (σ_{PS}). The σ_0 is the intrinsic yield strength of Cu matrix estimated to be 52 MPa [316]. Previous study [106] estimated σ_{SSS} to be 10.2 MPa, which is small towards the overall strengthening of the alloy, as observed in the case of Cu-15Ni-8Sn alloy, wherein Sn exhibits significant solid solubility in α matrix [317].

Grain refinement is an effective method to improve strength and ductility because dislocation slip in polycrystalline alloys needs to overcome the grain boundary resistance. The relationship between the contribution from σ_{GBS} and the grain size can be calculated by the Hall-Petch formula below [318]:

$$\sigma_{GBS} = \frac{k}{\sqrt{d}}$$

where *k* is the strengthening coefficient related to Cu alloys (0.18 MPa$\sqrt{m}$) [319], and *d* represents the average grain size (3.4 μm, 3.4 μm, and 3.7 μm) for the as-built samples A, B and C, respectively. Therefore, the increase in the YS due to Hall-Petch strengthening is estimated to be 98 MPa, 98 MPa, and 94 MPa, respectively.

A high density of dislocations interacts and entangles with each other, which impedes their own motion. The σ_{DS} contribution can be estimated using Baily-Hirsh relationship [273, 320]:

$$\sigma_{DS} = M\alpha Gb\sqrt{\rho}$$

where M is the Taylor factor of Cu (3.1) [319], α is the constant for FCC alloy (0.2) [273], G is the shear modulus (48.3 GPa) [233], b is the Burgers vector of Cu (2.56×10^{-10} m) [317], and ρ is the dislocation density given by EBSD results. The mean GND densities for samples A, B, and C are 6.27 ± 2.6, 6.15 ± 3.0, and 5.26 ± 2.1 (($\times 10^{14}$ m^{-2}), respectively. Therefore, the strengthening contribution from the dislocation interaction was calculated to be 192MPa, 190MPa, and 176 MPa.

The main source of the precipitation strengthening (σ_{PS}) is the dislocation-particle interaction by the Orowan process [229]. In this case, the δ phase particles act as dispersoids, requiring dislocations to bow around them, resulting in an increase in YS [230]. Therefore, the σ_{PS} contribution can be calculated by the Ashby–Orowan equation [231]:

$$\sigma_{PS} = \frac{0.81 M G_s b}{2\pi(1 - v)^{1/2}} \frac{\ln(d_p / b)}{(\lambda - d_p)}$$

where M is the Taylor factor of Cu (3.1) [232], Gs is the shear modulus (48.3 GPa) [233], b is the Burgers vector of Cu (2.56 × 10-10 m) [228], υ is the Poisson's ratio of Cu (0.34) [232] and dp is the average diameter of δ (the average diameters of samples A, B, and C were measured as 121 nm, 118 nm and 176 nm, respectively). Furthermore, λ is the interspacing between precipitates and related to their diameters (dp) and volume fractions (fp) as follows [234]:

$$\lambda = \frac{1}{2} d_p \sqrt{\frac{3\pi}{2 f_p}}$$

The volume fraction was estimated to be 7.1 vol.% in sample A, 8.0 vol.% in sample B and 9.6 vol.% in sample C. As a result, the σ_{PS} of samples A, B, and C were calculated at 101 MPa, 110 MPa, and 93 MPa.

Appendix D

Precipitate strengthening calculation of age-hardened Cu-30Ni alloy

The classical precipitation strengthening is established on the interaction between the precipitate and dislocation. According to the previous study [301] [300], the classical model considers the movement of dislocation pairs through precipitates, forming and subsequently removing an anti-phase boundary (APB) as they pass. When a dislocation shears an ordered precipitate an APB is created on the slip lane [322], and this APB formation and elimination by leading and trailing dislocations help maintain the ordered structure, influencing the alloy's strength. Their strengthening mechanism involves weak-pair coupling, strong-pair coupling and Orowan mechanism, depending on the APB energy, precipitate size and volume fraction. In weak-pair coupling, where the spacing between dislocations in the pair is large relative to the precipitate diameter, the trailing dislocation lags, leaving faulted regions within small precipitates. Strong-pair coupling, by contrast, occurs when the spacing is similar to the particle diameter, with dislocations closely paired within the larger precipitate. When the precipitate size exceeds the critical radius, the stress required for a dislocation to cut through the precipitate is greater than that needed for the dislocation to bypass the precipitate, forming an Orowan loop. Therefore, the Orowan bypassing mechanism becomes operative.

In our current research, we applied the same analytical approach, as demonstrated in Figure D.1a–d, which illustrates the correlation among these three strengthening mechanisms in a 0.5Si FA-FC sample aged at 650 °C for 0.1h and 6h.

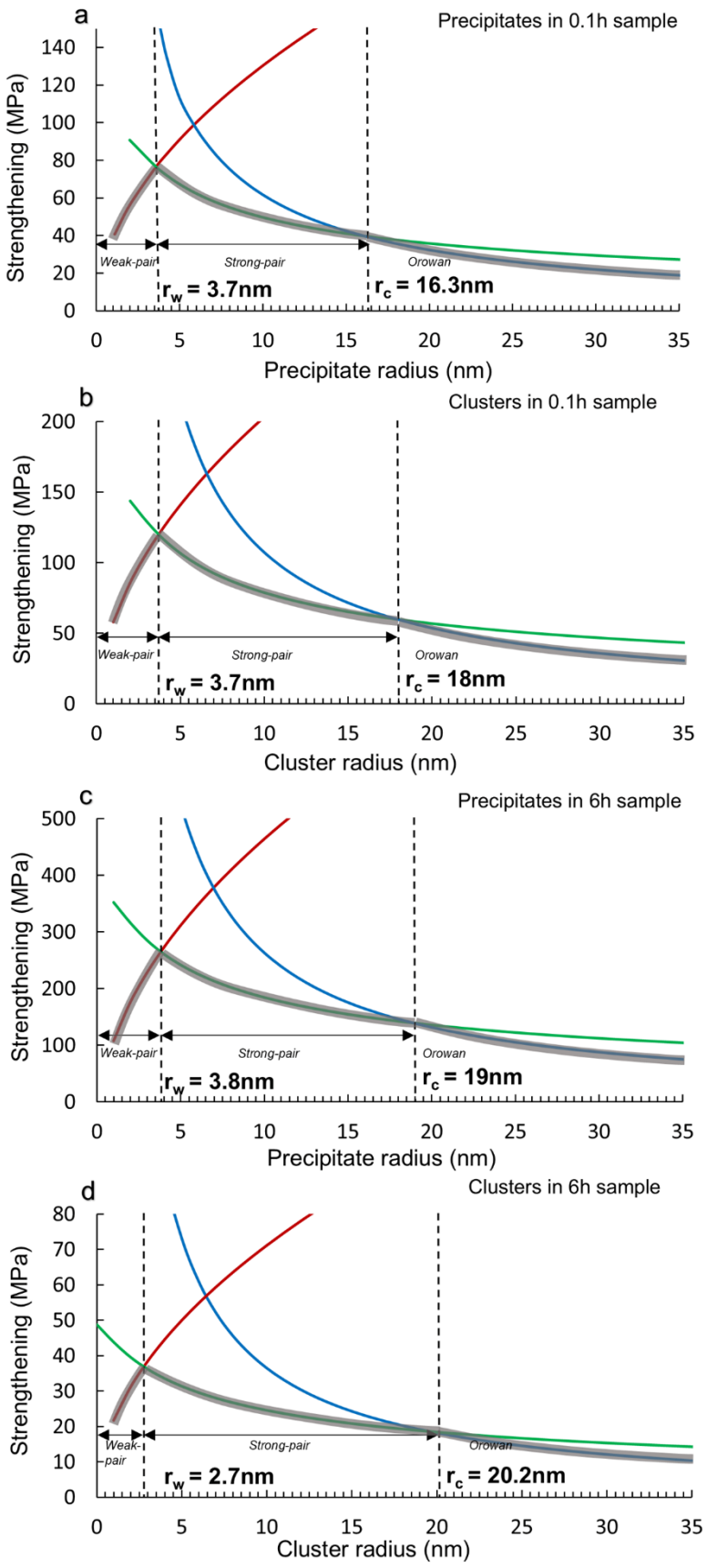

Figure D.1: The size-strengthening relationship of precipitates and clusters in 0.5Si FA-FC sample aged at 650 °C for (a–b) 0.1h and (c–d) 6h. In this figure, the red line represents the weak-pair coupling

mechanism, the green line indicates the strong-pair coupling mechanism, and the blue line corresponds to the Orowan mechanism. The symbol r_w denotes the critical size for the transition from weak-pair to strong-pair coupling, while r_c indicates the critical size for the transition from the cutting to the Orowan mechanism. The shaded lines represent the effective contributions from the weak-pair coupling, strong-pair coupling, and Orowan mechanisms. The unshaded lines illustrate the ineffective parts of these mechanisms.

When the precipitate radius $r < r_w$ (critical size for the transformation from the weak-pair to strong-pair coupling), the weak-pair coupling is the dominant mechanism, which can be expressed by:

$$\sigma_{weak-pair} = \frac{\gamma_{APB}}{2b}\left[\left(\frac{6\gamma_{APB}fr}{\pi Gb^2}\right)^{1/2} - f\right] \quad (1)$$

where:

γ_{APB}: Anti-phase boundary energy, 0.62 [323]

G: Shear modulus, 45910 MPa [316]

b: Burger's vector, 0.2557 nm [228]

f: volume fraction of precipitates

r: radius of precipitates

When the precipitate radius $r_w < r < r_c$ (critical size for the transformation from the strong pair to Orowan mechanism), the strong-pair coupling is the dominant mechanism, which can be expressed by:

$$\sigma_{strong-pair} = \sqrt{\frac{3}{2}}\left(\frac{Gb}{r}\right)\frac{f^{1/2}}{\pi^{3/2}}\left(\frac{2\pi\gamma_{APB}}{Gb^2} - 1\right)^{1/2} \quad (2)$$

When the precipitate radius $r_c < r$, the Orowan mechanism is the dominant mechanism, which can be expressed by:

$$\sigma_{Orowan} = \frac{3Gb}{2r}\left(\frac{2\pi}{3f}\right)^{-1/2} \quad (3)$$

For the 0.5Si sample aged for 0.1 hours, the effective contributions to strengthening from weak-pair coupling, strong-pair coupling, and the Orowan mechanisms are highlighted as shaded areas in Figure D.1a and b. The critical radii $r_{w \text{ and }} r_c$ for γ′ precipitates were determined as 3.7 and 16.3 nm from Figure D.1a. The average precipitate radius in this study was was determined to be approximately 3.5 nm, calculated as half of the measured precipitate diameter, and the volume fraction were estimated as 0.31%. As a result, the dominant strengthening mechanism is weak-pair coupling, which contributes a strengthening effect of 76 MPa. Similarly, the average Si-rich cluster radius and volume fraction were estimated to be 1.1 nm and 0.78%, respectively. Then, the $r_{w \text{ and }} r_c$ for clusters is determined by plotting the size-strengthening relationship figure for clusters (Figure D.1b), revealing that weak-pair coupling also dominates the strengthening, contributing 61 MPa. However, Singh and Warner [302] previously estimated that the contribution of the clusters or GP zones to the strength is approximately 25% of what the classical precipitation-strengthening model predicts. Therefore, the strengthening from clusters is adjusted to 15 MPa, resulting in the total predicted strengthening of 91 MPa.

For the 0.5Si sample aged for 6 hours, we employed the same method to quantify the strengthening contributions from precipitates and clusters. The average precipitate radius and volume fraction were estimated to be 5.1 nm and 4.68%, respectively. The dominant strengthening mechanism was identified as strong-pair coupling from Figure D.1c, resulting in a strengthening effect of 260 MPa. For the clusters, the radius and volume fraction were estimated to be 1.4 nm and 0.09%, respectively. Here, the strengthening is primarily due to weak-pair coupling as shown in Figure D.1d, contributing 26 MPa.

Subsequently, the cluster strengthening was adjusted to 7 MPa, representing 25% of the predicted value. The total predicted strengthening is therefore 267 MPa.

Appendix E PhD Candidature Outcomes

Publications

Chapter 6 of this thesis contains material from the published work:

"Chen, K., Lim, B., Zhang, L., Koo, B. X., Ringer, S. P., & Nomoto, K. (2025). Formation mechanisms of Sn-rich δ phase and its role in strengthening Cu-10Sn manufactured by laser powder bed fusion. **Additive Manufacturing**, 102, 104723."

Manuscripts in submission and preparation

Chapter 9 of this thesis contains material currently under peer review in **Scripta Materialia**:

"Chen, K., Cui, X. Y., Lim, B., Tran, T., Duguid, A., Camilleri, S., Ringer, S. P., & Nomoto, K. (2025). Age hardening response of Cu-30Ni alloys: The role of Si microalloying additions."

Chapter 7 of this thesis contains material currently in manuscript preparation:

"Chen, K., Li, B., Kruzic, J. J., Ringer, S. P., & Nomoto, K. Enhancing Strength and Ductility of As-Built Cu-10Sn via Powder–Structure–Property Control in Laser Beam Powder Bed Fusion."

Grants and awards

2025: Postgraduate research support scheme (PRSS), The University of Sydney.

2025: Asia-Pacific International Conference on Additive Manufacturing (APICAM) 2025 Student Bursaries, Materials Australia

2024: AINSE Technical Skills Scholarship, The Australian Institute of Nuclear Science and Engineering, Aug 2024.

2024: AINSE post graduate research award (PGRA), The Australian Institute of Nuclear Science and Engineering, Jun 2024, Thin-wall effects and residual stress of additively manufactured Cu-10Sn.

2024: Postgraduate research support scheme (PRSS), The University of Sydney.

2023: Best Oral Presentation Awards (conference), 20th International Microscopy Congress, Busan, Korea, Sep 2023, Effect of laser powder bed fusion process and powder characteristics for Cu-10Sn alloy on microstructure and mechanical property.

2023: Postgraduate research support scheme (PRSS), The University of Sydney.

Conference attendance

2025: (Oral) The 4th Asia-Pacific International Conference on Additive Manufacturing, Melbourne, Australia, June 2025, K. Chen, S.P. Ringer, K. Nomoto, Cu-10Sn alloys manufactured by laser powder bed fusion: from powder characteristics to performance.

2025: (Poster contest) The Minerals, Metals & Materials Society 2025 Annual Meeting & Exhibition, Las Vegas, USA, Mar 2025, K. Chen, S.P. Ringer, K. Nomoto, Unravelling the powder-microstructure-property relationship in Cu-10Sn manufactured by laser powder bed fusion.

2024: (Oral) The Conference of Combined Australian Materials Societies (CAMS) 2024, Adelaide, Australia, Dec 2024, K. Chen, S.P. Ringer, K. Nomoto, Unravelling the powder-microstructure-property relationship in Cu-10Sn manufactured by laser powder bed fusion.

2024: (Oral) The Minerals, Metals & Materials Society 2024 Annual Meeting & Exhibition, Orlando, USA, Mar 2024, K. Chen, S.P. Ringer, K. Nomoto, Formation mechanisms of Sn-rich δ phases and their role in strengthening of additively manufactured Cu-10Sn.

2023: (Oral) 20th International Microscopy Congress, Busan, Korea, Sep 2023, K. Chen, S.P. Ringer, K. Nomoto, Effect of laser powder bed fusion process and powder characteristics for Cu-10Sn alloy on microstructure and mechanical property.

2023: (Oral) The 3rd Asia-Pacific International Conference on Additive Manufacturing, Sydney, Australia, Jun 2023, K. Chen, S.P. Ringer, K. Nomoto, Unveiling the formation mechanism of Sn-rich phases and enhancing mechanical properties of Cu-10Sn via LPBF.

2023: (Poster) The Minerals, Metals & Materials Society 2023 Annual Meeting & Exhibition, San Diego, USA, Mar 2023, K. Chen, S.P. Ringer, K. Nomoto, Effect of laser powder bed fusion process and powder characteristics for Cu-10Sn alloy on microstructure and mechanical property.

2023: (Oral) 27th Australian Conference on Microscopy and Microanalysis, Perth, Australia, Feb 2023 K. Chen, S.P. Ringer, K. Nomoto, Characterisation of Cu alloy powders for Additive Manufacturing.